How tests of geoengineering can win public support p. 20

Vinyl acetate unites the catalyst kingdoms pp. 29 & 49

Programmable mRNA sensor wins BII & *Science* Prize p. 40

Science

$15
4 APRIL 2025
science.org

AAAS

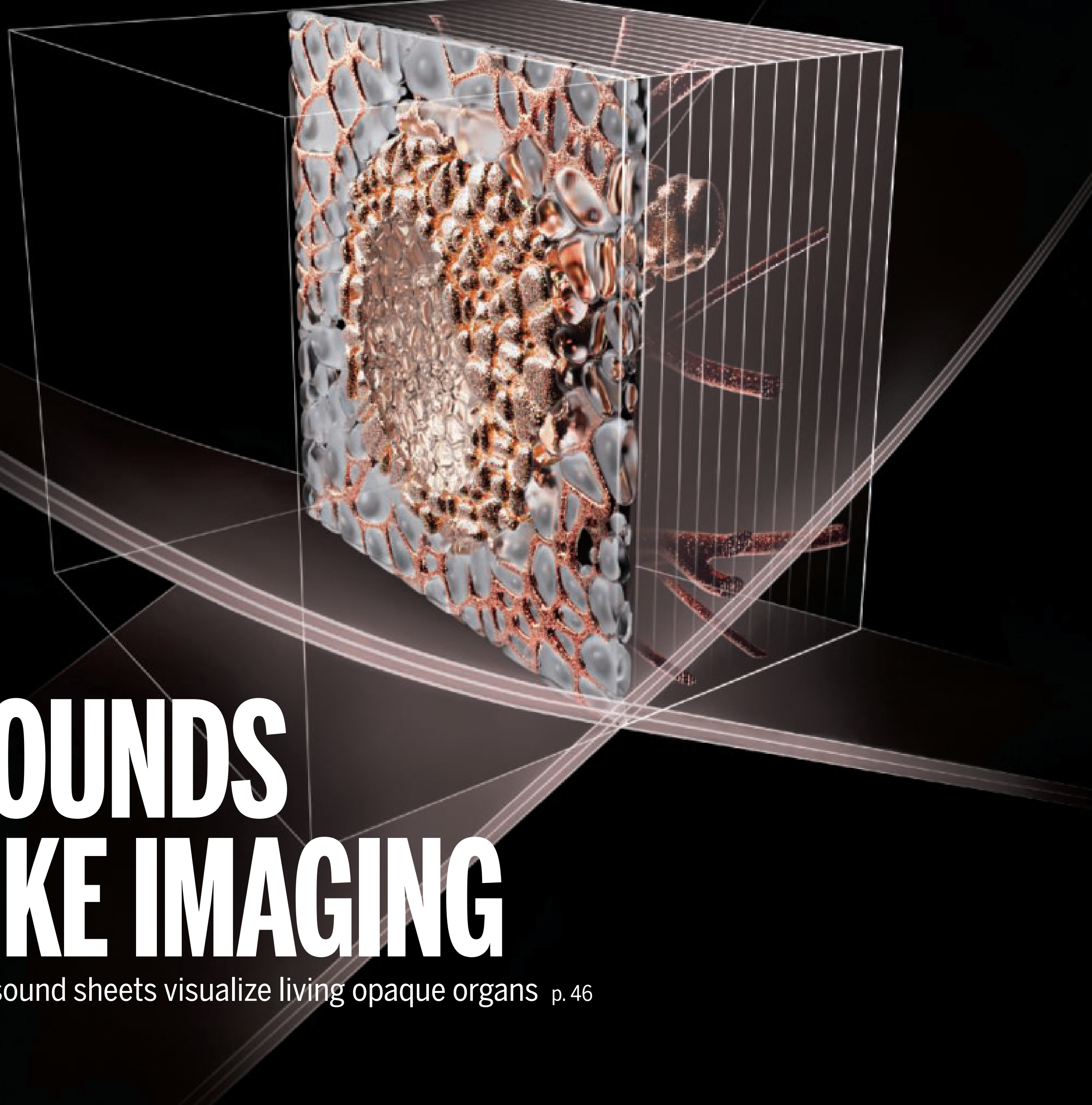

SOUNDS LIKE IMAGING

Thin sound sheets visualize living opaque organs p. 46

Your bridge to successful innovation.

NEB's Customized Solutions Team is here to help, and serves as a bridge to the support and resources you need to ensure your success.

Creating the right partnership is essential when pioneering a new life science product. Every aspect of development – technical expertise, reagent optimization, manufacturing scale, turnaround time, reagent quality, and comprehensive logistical support – is vital for achieving your objectives. And in the regulated markets landscape, these challenges magnify, demanding an even more specialized approach.

Your Bridge to Successful Innovation

- Leverage NEB's 50 years of experience in enzymology and reagent manufacturing
- As an extension of your team, we prioritize a deep understanding of your objectives, work with you on an optimal solution, and help to anticipate your future needs
- Benefit from our ISO 9001- and 13485-certified processes and commitment to quality, as well as our GMP-grade* production facility, and specialized lyophilization facility for the highest quality production standards
- Access unparalleled support from our dedicated account managers, program managers, technical scientists and production teams
- We work closely with you on inventory management and global distribution through our network of NEB-owned subsidiaries, to ensure successful commercialization

NEB's Customized Solutions Team will help you access novel products, meet quality specifications, speed time to market, and streamline your supply chain, allowing you to focus more on what matters most — innovation.

Ready to start the discussion? Learn more at
www.neb.com/customizedsolutions.

NEW ENGLAND
Biolabs®

* *"GMP-grade" is a branding term NEB uses to describe products manufactured or finished at NEB's Rowley facility. The Rowley facility was designed to manufacture products under more rigorous infrastructure and process controls to achieve more stringent product specifications and customer requirements. Products manufactured at NEB's Rowley facility are manufactured in compliance with ISO 9001 and ISO 13485 quality management system standards. However, at this time, NEB does not manufacture or sell products known as Active Pharmaceutical Ingredients (APIs), nor does NEB manufacture its products in compliance with all of the Current Good Manufacturing Practice regulations.*

CONTENTS

4 APRIL 2025 • VOLUME 388 • ISSUE 6742

20
Researchers run a test of cloud-brightening technology over the Great Barrier Reef.

NEWS

IN BRIEF

10 News at a glance

IN DEPTH

12 Killed NIH grants could waste billions of dollars
More than $1.4 billion in sunk research costs may produce few results, analysis suggests *By S. Reardon*

13 NSF has awarded almost 50% fewer grants
An analysis shows a drastic falloff since Trump took office. The finding conflicts with the director's claims *By J. Mervis*

14 Stellarators, once fusion's dark horse, hit their stride
Multiple companies aim to build pilot plants using twisted magnets *By D. Clery*

16 NIH cancels research grants for COVID-19 and future pandemics
Scientists reject claim that the work is no longer needed *By J. Cohen*

17 International scientists rethink U.S. conferences
Opposition to Trump administration and fears of customs run-ins are shifting travel plans
By K. Langin

18 Ancient DNA illuminates 'green Sahara' dwellers
Skeletons from an ancient, lush interlude offer genetic peek at a lost population
By A. Curry

19 'Uniquely human' language capacity found in bonobos
Study is the first to show an animal combining different calls to make new meanings *By C. O'Grady*
RESEARCH ARTICLE P. 104

FEATURES

20 Failure to communicate
Geoengineering could be crucial in the fight against climate change. But first scientists need to learn how to talk to the public about it *By R. White*
PODCAST

INSIGHTS

PERSPECTIVES

26 Saving the cultural legacy of wild animals
Loss of biodiversity threatens the study of tool use and other cultural behaviors in animals
By A. K. Kalan and L. V. Luncz

28 Archaea go multicellular under pressure
A microbe from the Dead Sea switches to a tissue-like form when compressed
By E. K. Pillai and T. Brunet
RESEARCH ARTICLE p. 109

29 Catalysis at the crossroads
Homogeneous and heterogeneous catalysis work concurrently in a chemical process
By C. L. Tway and S. V. Filip
RESEARCH ARTICLE p. 49

30 Beyond wear and tear at the joint
Bile acid metabolism meets glucagon-like peptide 1 signaling in osteoarthritis
By C. Liu
RESEARCH ARTICLE p. 48

POLICY FORUM

32 Rubella and measles: The beginning of the endgame
Benchmarks must be established and progress tracked to set a global target and take action
By M. J. Ferrari and W. J. Moss

LETTERS

35 NextGen Voices: Science safeguards

BOOKS ET AL.

38 Convince me, control me
A historian probes the origins and evolution of psychological manipulation *By K. Joice*

39 When trainees seek other paths
A new book offers advice for mentoring those who do not aspire to follow in faculty's footsteps *By J. Wai*

PHOTOS: (TOP TO BOTTOM) BRENDAN KELAHER/SOUTHERN CROSS UNIVERSITY; ASH ADAMS/*THE NEW YORK TIMES* VIA REDUX

Science &
SciLifeLab
PRIZE
For Young Scientists

Recent PhD?

How about $30,000 US, having your essay published in *Science*, and being celebrated with a week of festivities in Stockholm, Sweden?

Apply now to the *Science* & SciLifeLab Prize for Young Scientists!

A global award aimed at young researchers

Every year, four early-career scientists from across the globe are awarded the *Science* & SciLifeLab Prize for Young Scientists for outstanding research they have conducted as part of their PhD.

The selected winners receive up to $30, 000 US in prize money for their accomplishments. In addition, all four winners are published in *Science* and invited by SciLifeLab to Sweden in December to participate in a unique week filled with events in honor of science. Here, they will be given the opportunity to meet with leading scientists in their field of research and create life-long connections to support their career.

Categories

The award is available in four categories:

- Cell and Molecular Biology
- Genomics, Proteomics and Systems Biology Approaches
- Ecology and Environment
- Molecular Medicine

More information

More information: scienceprize.scilifelab.se
Questions: scilifelabprize@aaas.org
Application deadline: July 15, 2025
Eligibility: applicants must have received their PhD between January 1, 2023 and December 31, 2024.

Enabled by the generous support of the Knut and Alice Wallenberg Foundation.

Knut and Alice
Wallenberg
Foundation

Science
AAAS

SciLifeLab

RESEARCH

IN BRIEF

REVIEW

RESEARCH ARTICLES

DEPARTMENTS

ON THE COVER

A cross-propagating ultrasound wave exposes a thin tissue section that contains blood vessels feeding a tumor. The wave interacts with sound-scattering probes (displayed in orange gold) that are genetically expressed in cancer cells or are injected in the bloodstream to reveal capillary vessels. White contour lines indicate previously scanned tissue sections and the total volume explored by this sound-sheet microscopy technique. See page 46. *Credit: N. Burgess/Science*

PHOTO: MARTIN SURBECK

SCIENCE (ISSN 0036-8075) is published weekly on Friday, except last week in December, by the American Association for the Advancement of Science, 1200 New York Avenue, NW, Washington, DC 20005. Periodicals mail postage (publication No. 484460) paid at Washington, DC, and additional mailing offices. Copyright © 2025 by the American Association for the Advancement of Science. The title SCIENCE is a registered trademark of the AAAS. Domestic individual membership, including subscription (12 months): $165 ($74 allocated to subscription). Domestic institutional subscription (51 issues): $2865; Foreign postage extra: Air assist delivery: $135. First class, airmail, student, and emeritus rates on request. Canadian rates with GST available upon request, GST #125488122. Publications Mail Agreement Number 1069624. **Printed in the U.S.A.**

Change of address: Allow 4 weeks, giving old and new addresses and 8-digit account number. **Postmaster:** Send change of address to AAAS, P.O. Box 96178, Washington, DC 20090–6178. **Single-copy sales:** $15 each plus shipping and handling available from backissues.science.org; bulk rate on request. **Authorization to reproduce** material for internal or personal use under circumstances not falling within the fair use provisions of the Copyright Act can be obtained through the Copyright Clearance Center (CCC), www.copyright.com. The identification code for *Science* is 0036-8075. *Science* is indexed in the *Reader's Guide to Periodical Literature* and in several specialized indexes.

Science AAAS

Editor-in-Chief Holden Thorp, hthorp@aaas.org

Executive Editor Valda Vinson

Editor, Research Jake S. Yeston **Editor, Insights** Lisa D. Chong **Deputy Executive Editor** Lauren Kmec

DEPUTY EDITORS Stella M. Hurtley (UK), Phillip D. Szuromi, Sacha Vignieri **SR. EDITORS** Caroline Ash (UK), Michael A. Funk, Angela Hessler, Di Jiang, Priscilla N. Kelly, Marc S. Lavine (Canada), Sarah Lempriere (UK), Mattia Maroso, Yevgeniya Nusinovich, Ian S. Osborne (UK), L. Bryan Ray, H. Jesse Smith, Keith T. Smith (UK), Jelena Stajic, Peter Stern (UK), Yury V. Suleymanov, Valerie B. Thompson, Brad Wible **ASSOCIATE EDITORS** Jack Huang, Sumin Jin, Bianca Lopez, Sarah Ross (UK), Madeleine Seale (UK), Corinne Simonti, Ekeoma Uzogara **SENIOR LETTERS EDITOR** Jennifer Sills **NEWSLETTER EDITOR** Christie Wilcox **RESEARCH & DATA ANALYST** Jessica L. Slater **LEAD CONTENT PRODUCTION EDITORS** Chris Filiatreau, Harry Jach **SR. CONTENT PRODUCTION EDITOR** Amelia Beyna **CONTENT PRODUCTION EDITORS** Anne Abraham, Robert French, Julia Haber-Katris, Nida Masiulis, Abigail Shashikanth, Suzanne M. White **SR. EDITORIAL MANAGER** Beverly Shields **SR. PROGRAM ASSOCIATE** Maryrose Madrid **EDITORIAL ASSOCIATES** Aneera Dobbins, Joi S. Granger, Lisa Johnson, Jerry Richardson, Anita Wynn **SR. EDITORIAL COORDINATORS** Alexander Kief, Ronmel Navas, Isabel Schnaidt, Alice Whaley (UK), Brian White **EDITORIAL COORDINATORS** Clair Goodhead (UK), Kat Kirkman, Samantha Price **ADMINISTRATIVE COORDINATOR** Karalee P. Rogers **ASI DIRECTOR, OPERATIONS** Janet Clements (UK) **ASI OFFICE MANAGER** Victoria Smith **ASI SR. OFFICE ADMINISTRATORS** Dawn Titheridge (UK), Jessica Waldock (UK) **COMMUNICATIONS DIRECTOR** Meagan Phelan **DEPUTY DIRECTOR** Matthew Wright **SENIOR WRITERS** Walter Beckwith, Joseph Cariz **WRITERS** Abigail Eisenstadt, Mahathi Ramaswamy **SENIOR COMMUNICATIONS ASSOCIATES** Zachary Graber, Sarah Woods **COMMUNICATIONS ASSOCIATES** Kiara Brooks, Haley Riley, Mackenzie Williams

News Editor Tim Appenzeller

NEWS MANAGING EDITOR John Travis **INTERNATIONAL EDITOR** David Malakoff **DEPUTY NEWS EDITORS** Rachel Bernstein, Shraddha Chakradhar, Martin Enserink, David Grimm, Eric Hand, Michael Price Kelly Servick, Matt Warren (Europe) **SR. CORRESPONDENTS** Daniel Clery (UK), Jon Cohen, Jeffrey Mervis **ASSOCIATE EDITORS** Jeffrey Brainard, Michael Greshko, Katie Langin **NEWS REPORTERS** Adrian Cho, Jennifer Couzin-Frankel, Phie Jacobs, Jocelyn Kaiser, Rodrigo Pérez Ortega (Mexico City), Robert F. Service, Erik Stokstad, Paul Voosen, Meredith Wadman **CONSULTING EDITOR** Elizabeth Culotta **CONTRIBUTING CORRESPONDENTS** Vaishnavi Chandrashekhar, Dan Charles, Warren Cornwall, Andrew Curry (Berlin), Ann Gibbons, Sam Kean, Kai Kupferschmidt (Berlin), Andrew Lawler, Mitch Leslie, Virginia Morell, Dennis Normile (Tokyo), Cathleen O'Grady, Elisabeth Pain (Careers), Charles Piller, Sara Reardon, Richard Stone (Senior Asia Correspondent), Gretchen Vogel (Berlin), Lizzie Wade (Mexico City) **INTERNS** Alexa Robles-Gil **COPY EDITORS** Julia Cole (Senior Copy Editor), Hannah Knighton, Cyra Master (Copy Chief) **ADMINISTRATIVE SUPPORT** Meagan Weiland

Creative Director Beth Rakouskas

DESIGN MANAGING EDITOR Chrystal Smith **GRAPHICS MANAGING EDITOR** Chris Bickel **PHOTOGRAPHY MANAGING EDITOR** Emily Petersen **MULTIMEDIA MANAGING PRODUCER** Kevin McLean **DIGITAL DIRECTOR** Kara Estelle-Powers **DESIGN EDITOR** Marcy Atarod **DESIGNER** Noelle Jessup **SENIOR SCIENTIFIC ILLUSTRATOR** Noelle Burgess **SCIENTIFIC ILLUSTRATORS** Austin Fisher, Kellie Holoski, Ashley Mastin **SENIOR GRAPHICS EDITOR** Monica Hersher **GRAPHICS EDITOR** Veronica Penney **SENIOR PHOTO EDITOR** Charles Borst **PHOTO EDITOR** Elizabeth Billman **SENIOR PODCAST PRODUCER** Sarah Crespi **SENIOR VIDEO PRODUCER** Meagan Cantwell **SOCIAL MEDIA STRATEGIST** Jessica Hubbard **SOCIAL MEDIA PRODUCER** Sabrina Jenkins **WEB DESIGNER** Jennie Pajerowski

Chief Executive Officer and Executive Publisher Sudip Parikh

Publisher, Science Family of Journals Bill Moran

DIRECTOR, BUSINESS SYSTEMS AND FINANCIAL ANALYSIS Randy Yi **DIRECTOR, BUSINESS OPERATIONS & ANALYSIS** Eric Knott **MANAGER, BUSINESS OPERATIONS** Jessica Tierney **MANAGER, BUSINESS ANALYSIS** Cory Lipman **BUSINESS ANALYSTS** Kurt Ennis, Maggie Clark, Isacco Fusi **BUSINESS OPERATIONS ADMINISTRATOR** Taylor Fisher **DIGITAL SPECIALIST** Marissa Zuckerman **SENIOR PRODUCTION MANAGER** Jason Hillman **SENIOR MANAGER, PUBLISHING AND CONTENT SYSTEMS** Marcus Spiegler **CONTENT OPERATIONS MANAGER** Rebecca Doshi **PUBLISHING PLATFORM MANAGER** Jessica Loayza **PUBLISHING SYSTEMS SPECIALIST, PROJECT COORDINATOR** Jacob Hedrick **SENIOR PRODUCTION SPECIALIST** Kristin Wowk **PRODUCTION SPECIALISTS** Kelsey Cartelli, Audrey Diggs **SPECIAL PROJECTS ASSOCIATE** Shantel Agnew

MARKETING DIRECTOR Sharice Collins **ASSOCIATE DIRECTOR, MARKETING** Justin Sawyers **GLOBAL MARKETING MANAGER** Allison Pritchard **ASSOCIATE DIRECTOR, MARKETING SYSTEMS & STRATEGY** Aimee Aponte **SENIOR MARKETING MANAGER** Shawana Arnold **MARKETING MANAGER** Ashley Evans **MARKETING ASSOCIATES** Hugues Beaulieu, Ashley Hylton, Lorena Chirinos Rodriguez, Jenna Voris **MARKETING ASSISTANT** Courtney Ford **SENIOR DESIGNER** Kim Huynh

DIRECTOR AND SENIOR EDITOR, CUSTOM PUBLISHING Erika Gebel Berg **ADVERTISING PRODUCTION OPERATIONS MANAGER** Deborah Tompkins **DESIGNER, CUSTOM PUBLISHING** Jeremy Huntsinger **SR. TRAFFIC ASSOCIATE** Christine Hall

DIRECTOR, PRODUCT MANAGEMENT Kris Bishop **PRODUCT DEVELOPMENT MANAGER** Scott Chernoff **ASSOCIATE DIRECTOR, PUBLISHING INTELLIGENCE** Rasmus Andersen **SR. PRODUCT ASSOCIATE** Robert Koepke **PRODUCT ASSOCIATES** Caroline Breul, Anne Mason

ASSOCIATE DIRECTOR, INSTITUTIONAL LICENSING MARKETING Kess Knight **ASSOCIATE DIRECTOR, INSTITUTIONAL LICENSING SALES** Ryan Rexroth **INSTITUTIONAL LICENSING MANAGER** Nazim Mohammedi, Claudia Paulsen-Young **SENIOR MANAGER, INSTITUTIONAL LICENSING OPERATIONS** Judy Lillibridge **MANAGER, RENEWAL & RETENTION** Lana Guz **SYSTEMS & OPERATIONS ANALYST** Ben Teincuff **FULFILLMENT ANALYST** Aminta Reyes

ASSOCIATE DIRECTOR, INTERNATIONAL Roger Goncalves **ASSOCIATE DIRECTOR, US ADVERTISING** Stephanie O'Connor **US MID WEST, MID ATLANTIC AND SOUTH EAST SALES MANAGER** Chris Hoag **DIRECTOR, OUTREACH AND STRATEGIC PARTNERSHIPS, ASIA** Shoupeng Liu **SALES REP, ROW** Sarah Lelarge **SALES ADMIN ASSISTANT, ROW** Victoria Glasbey **DIRECTOR OF GLOBAL COLLABORATION AND ACADEMIC PUBLISHING RELATIONS, ASIA** Xiaoying Chu **ASSOCIATE DIRECTOR, INTERNATIONAL COLLABORATION** Grace Yao **SALES MANAGER** Danny Zhao **MARKETING MANAGER** Kilo Lan **ASCA CORPORATION, JAPAN** Rie Rambelli (Tokyo), Miyuki Tani (Osaka)

DIRECTOR, COPYRIGHT, LICENSING AND SPECIAL PROJECTS Emilie David **RIGHTS AND PERMISSIONS ASSOCIATE** Elizabeth Sandler **LICENSING ASSOCIATE** Virginia Warren **RIGHTS AND LICENSING COORDINATOR** Dana James **CONTRACT SUPPORT SPECIALIST** Michael Wheeler

EDITORIAL
science_editors@aaas.org

NEWS
science_news@aaas.org

INFORMATION FOR AUTHORS
science.org/authors/science-information-authors

REPRINTS AND PERMISSIONS
science.org/help/reprints-and-permissions

MULTIMEDIA CONTACTS
SciencePodcast@aaas.org
ScienceVideo@aaas.org

MEDIA CONTACTS
scipak@aaas.org

PRODUCT ADVERTISING & CUSTOM PUBLISHING
advertising.science.org
science_advertising@aaas.org

CLASSIFIED ADVERTISING
advertising.science.org/science-careers
advertise@sciencecareers.org

JOB POSTING CUSTOMER SERVICE
employers.sciencecareers.org
support@sciencecareers.org

MEMBERSHIP AND INDIVIDUAL SUBSCRIPTIONS
science.org/subscriptions

MEMBER BENEFITS
aaas.org/membership/benefits

INSTITUTIONAL SALES AND SITE LICENSES
science.org/librarian

AAAS BOARD OF DIRECTORS
CHAIR Gilda A. Barabino
PRESIDENT Keith R. Yamamoto
PRESIDENT-ELECT Willie E. May

TREASURER Carolyn N. Ainslie

CHIEF EXECUTIVE OFFICER
Sudip Parikh

BOARD Cynthia M. Beall
Janine Austin Clayton
Kaye Husbands Fealing
Kathleen Hall Jamieson
Jane Maienschein
Robert B. Millard
Babak Parviz
William D. Provine
Juan S. Ramírez Lugo
Susan M. Rosenberg
Vassiliki Betty Smocovitis

EDITORIAL

Don’t quit the long game

Living cells that produce biofuel; robots that assist factory workers; intelligent machines that guide drug discovery—these technologies are “deep” in that they achieve something extraordinary—often thought impossible—and push society forward. Indeed, so-called “deep tech” powers the future of medical breakthroughs, resilient energy grids, and clean industrial processes, among other frontiers. But deep tech requires more of everything to become a reality—research and development, specialized talent, time, risk-taking, and funding. The US government has been the world’s largest investor in this enterprise. Yet cuts to federal support for deep tech threaten this entrepreneurial engine at its source—university labs. Without sustained federal support, the country risks losing its technological edge, threatening economic competitiveness and national security.

Deep tech ventures are launched by scientist-entrepreneurs and thrive in ecosystems where labs, highly trained individuals, government funding, and risk capital intersect. Universities are key to cultivating deep-tech innovations by supplying the talent, infrastructure, and intellectual freedom essential for the long-term, high-risk research required. Cuts to major sources of support, including the National Science Foundation, National Institutes of Health, and Department of Defense, now endanger this innovation environment.

Translational research funding is crucial for moving discoveries and early-stage technologies from labs to real-world applications. Government support gives scientists the time to refine nascent technologies, which can be a long and uncertain process. But this approach has had substantial payoffs. Boston Metal, founded by researchers at the Massachusetts Institute of Technology, developed a cleaner, cost-effective steel production process using molten oxide electrolysis. Early grant support advanced the idea to technology, positioning the company to transform one of the world’s most carbon-intensive industries.

Unlike software startups, deep tech depends on specialized equipment and prototyping facilities to incubate ideas and convert intellectual capital into tangible products. Losing federal funds for university equipment and labs will deprive scientist-entrepreneurs of the resources needed to navigate this leap. Pascal, a startup developing solid refrigerants to replace harmful greenhouse gases in heating, ventilation, and air conditioning systems, made its breakthrough at Harvard University, where the labs and expertise were essential to advancing the technology.

The United States has long attracted top talent in engineering and science, offering opportunities for academic and entrepreneurial excellence, along with flexible early-stage funding through government and university programs that align with a project’s needs as it progresses through technological milestones. It is a serious concern that as government support declines, fewer scientists will have the resources to pursue entrepreneurship, stifling innovation and reversing the trend of PhDs and postdocs entering startups. The cuts to research support across higher education institutions are provoking scientists in the US to seek opportunities in other countries with stronger public support for science, signaling the onset of a brain drain. For example, the Max Planck Society in Germany has seen a recent surge in applications from US researchers and is expanding its programs to accommodate them. Other countries in Europe with burgeoning innovation ecosystems, including ETH Zurich and the University of Oxford, will also likely benefit from the movement of top-tier talent from the United States. This is undermining decades of US research investment.

> “The cuts to research support…are provoking scientists in the US to seek opportunities in other countries…”

The current funding cuts are not just an academic issue—they are also an economic and national security concern. The United States built its technological dominance by investing in the long game, in areas such as semiconductors, aerospace technology, and mRNA vaccines. The government, philanthropists, and universities funded the frontiers of knowledge, seeding deep-tech breakthroughs. Venture capital, corporations, and government customers then drove the growth of these endeavors. US leadership has also placed the country at the forefront of developing policies and regulations for new technologies. It now risks losing a prominent seat at this table as well.

Replacing or restoring federal support will be a formidable challenge. But universities must take decisive steps now—diversifying funding sources, strengthening private-sector collaborations, and engaging in policy dialogue—to preserve an ecosystem that has shaped the world in revolutionary ways.

–Stefan Raff-Heinen and Fiona E. Murray

Stefan Raff-Heinen is a professor at the Institute for Digital Technology Management, Bern University of Applied Sciences, Bern, Switzerland, and a research affiliate at the MIT Sloan School of Management, Massachusetts Institute of Technology, Cambridge, MA, USA. stera127@mit.edu

Fiona E. Murray is the associate dean of innovation and the William Porter (1967) Professor of Entrepreneurship at the MIT Sloan School of Management, Massachusetts Institute of Technology, Cambridge, MA, USA, and vice chair of the NATO Innovation Fund. fmurray@mit.edu

10.1126/science.adx8118

NEWS

> “[I]t has become clear that the Secretary wishes subservient confirmation of his misinformation and lies.”

Former U.S. Food and Drug Administration official Peter Marks, who oversaw vaccine approvals, referring to Department of Health and Human Services Secretary Robert F. Kennedy Jr.’s criticisms of vaccines, in a letter of resignation last week.

IN BRIEF

Edited by
Jeffrey Brainard

HHS workers line up outside their office in Washington, D.C., on 1 April, when many were fired. Some staffers learned of this only when they were barred from the building.

PHOTO: KEVIN LAMARQUE/REUTERS

TRUMP TRACKER

Mass firings at health agencies, grant solicitations vetted, and autism revisited

HEALTH LEADERS AXED
President Donald Trump’s administration this week began an expected—and sweeping—purge of senior officials and other workers at U.S. federal health agencies. As *Science* went to press, at least five directors of the National Institutes of Health’s (NIH’s) 27 institutes and centers were told they are being reassigned. Several center directors at the Food and Drug Administration (FDA) were also removed. Some were given 1 day to decide whether they are willing to move to jobs in Oklahoma, Alaska, or other states. In all, the U.S. Department of Health and Human Services (HHS) said it plans to fire 1200 employees at NIH—about 6% of its workforce when Trump took office in January—as well as 3500 at FDA and 2400 at the Centers for Disease Control and Prevention (CDC). The cuts at CDC included many staff members in its HIV prevention division. Although the administration said last week that many of the positions to be eliminated across HHS agencies were likely to be administrative, multiple tenured scientists who worked for in-house research programs at one large institute were let go, sources told *Science*. HHS says the moves are intended to save money and increase efficiency, but some outsiders decried a large, sudden loss of institutional memory. Adding this week’s removals to resignations since Trump was sworn in, most of FDA’s leaders “with a deep understanding of product development and safety are no longer employed,” Robert Califf, who led the agency under former President Joe Biden, wrote on LinkedIn. “FDA as we’ve known it is finished.”

POLITICAL REVIEW HHS and the White House Department of Government Efficiency plan to review each of NIH’s draft solicitations for grant proposals, *Science* has learned. The reviews, intended to ensure the funding will align with Trump’s priorities, represent unprecedented political interference with NIH’s grantmaking process. An agency employee familiar with the matter worries Trump administration officials reviewing the Notices of Funding Opportunities (NOFOs) may lack the scientific background required to understand why certain topics are important to fund. NIH has developed a large backlog of unpublished NOFOs because the administration paused them. The agency has withdrawn dozens of previously issued NOFOs that involved topics such as gender minorities because Trump’s executive orders ban them from receiving federal funds.

VACCINE-AUTISM STUDY HHS Secretary Robert F. Kennedy Jr. has tapped a controversial figure, David Geier, to lead a new government study about whether vaccines cause autism, *The Washington Post* reported. Kennedy has supported the connection despite extensive research findings dating back at least 2 decades that show no credible link. Geier, who holds only a bachelor’s degree, and his father, Mark Geier, a physician, have published papers suggesting a link between autism and thimerosal, a mercury-containing preservative—studies the Institute of Medicine characterized as having “serious methodological flaws.” The Geiers misled parents that a regimen they developed to treat autism in children was approved, according to a 2011 investigation by the Maryland Board of Physicians.

SCIENTISTS’ WARNING The Trump administration’s avalanche of policy changes and funding cuts are wrecking the nation’s scientific enterprise, nearly 2000 of the 8000-plus members of the U.S. National Academies warn in a letter released on 31 March. It faults the administration for firing federal scientists, terminating grants in fields it finds objectionable, and withholding research funding from certain universities. The signers include Nobel laureates, medical school deans, and researchers in fields ranging from astronomy to zoology.

SCIENCE POLICY DIRECTOR The U.S. Senate has confirmed Michael Kratsios to lead the White House Office of Science and Technology Policy (OSTP), with the technology executive winning much more support from Democrats than Trump's controversial picks to lead federal health agencies. Twenty-one Democrats joined all 53 Republicans last week in confirming Kratsios, who some U.S. researchers hope will make the case for the importance of academic research in fostering innovation as the administration slashes spending and fires scientists. Kratsios is the first OSTP director without a science Ph.D. or extensive research experience. He served as U.S. chief technology officer during Trump's first term. For the past 3 years Kratsios has been managing director of Scale AI, an artificial intelligence infrastructure company.

KEY VACCINE GRANT AXED The administration has ended most grants by the U.S. Agency for International Development, according to a list it released last week, including a $2.6 billion award to Gavi, the Vaccine Alliance, a global nonprofit that helps provide inoculations in poor countries. Gavi says its work has saved an estimated 19 million lives since its inception in 2000. According to the list, released after multiple requests from grantees and lawsuit plaintiffs, 5341 grants with $28 billion in unobligated funds have been terminated, including programs aimed at treating severe malnutrition in children and stopping the spillover of viruses from animals to humans. Nearly 900 programs with $8 billion in unobligated funds remain active.

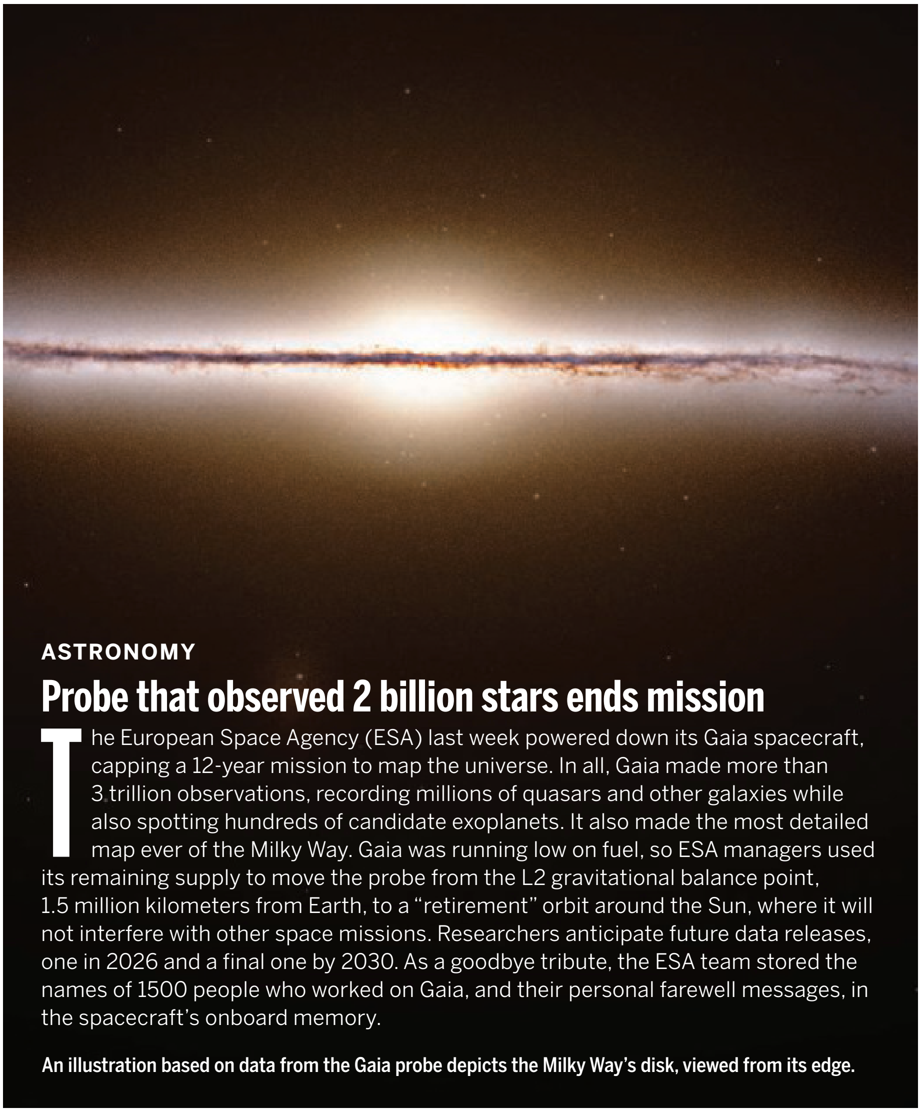

ASTRONOMY

Probe that observed 2 billion stars ends mission

The European Space Agency (ESA) last week powered down its Gaia spacecraft, capping a 12-year mission to map the universe. In all, Gaia made more than 3 trillion observations, recording millions of quasars and other galaxies while also spotting hundreds of candidate exoplanets. It also made the most detailed map ever of the Milky Way. Gaia was running low on fuel, so ESA managers used its remaining supply to move the probe from the L2 gravitational balance point, 1.5 million kilometers from Earth, to a "retirement" orbit around the Sun, where it will not interfere with other space missions. Researchers anticipate future data releases, one in 2026 and a final one by 2030. As a goodbye tribute, the ESA team stored the names of 1500 people who worked on Gaia, and their personal farewell messages, in the spacecraft's onboard memory.

An illustration based on data from the Gaia probe depicts the Milky Way's disk, viewed from its edge.

IMAGE: ESA/GAIA/DPAC; STEFAN PAYNE-WARDENAAR

African cancer database debuts

DIVERSITY | A genomics research company in Ghana has received support from the pharmaceutical giant Roche to sequence the whole genomes of people in Africa who have cancer, in hopes of improving treatments for those populations. African people are among the most genetically diverse and are about 17% of global population but make up less than 2% of participants in genetic studies. The African Cancer Atlas aims to collect genomic and clinical data from up to 7500 patients with diverse types of cancer, including breast, prostate, and lung, to better understand cancer biology, identify biomarkers, and develop targeted therapies. Roche and its Ghanaian partner, Yemaachi Biotech, say they will make the database freely accessible to researchers based in Africa. The companies declined to disclose the amount of their funding.

Judge blocks FDA on lab tests

BIOMEDICINE | A U.S. District Court judge in Texas this week struck down a rule adopted by the Food and Drug Administration (FDA) that had allowed it to regulate laboratory-developed tests as medical devices, ruling that the agency lacked this statutory authority. The agency's rule covered tests—including some prenatal screening tests and gene sequencing of tumors, for example—designed by a single lab for patient care. (FDA already vets in vitro diagnostic tests, such as continuous glucose monitors, that are developed by and used across multiple labs.) Such tests are often marketed nationwide, and regulators and scientists have said many are not well validated and can put patients at risk. But organizations representing laboratories and pathologists had said this oversight would raise costs and stymie innovation, and sued FDA.

IN DEPTH

A study of ways to improve vaccine uptake in Native Alaskans had already spent half its funds before being ended abruptly by the National Institutes of Health.

PHOTO: ASH ADAMS/*THE NEW YORK TIMES* VIA REDUX

TRUMP ADMINISTRATION

Killed NIH grants could waste billions of dollars

More than $1.4 billion in sunk research costs may produce few results, analysis suggests

By **Sara Reardon**

Since 2022, sexual health researcher Jeremy Goldbach has spent about $2 million of the U.S. government's money studying whether a peer-mentoring program could alleviate anxiety and depression among transgender and gender-minority teenagers. The 3-year project, funded by the National Institutes of Health (NIH), had recruited some 200 students from 20 schools in the Los Angeles area and was scheduled to wrap up in September.

But all that effort—and money—might now be for naught. On 28 February, Goldbach, who works at Washington University in St. Louis, received an email from NIH saying the agency no longer supports "research based on gender identity." The letter, which arrived following several related executive orders by President Donald Trump, told Goldbach to immediately stop work and informed him that NIH was rescinding approximately $500,000 remaining in his grant. He had planned to use the money to recruit students from an additional four to eight schools.

Without those participants, Goldbach says he doesn't have enough teenagers to draw solid conclusions. "We'll still probably try to look at the data, but I don't have a ton of faith" that they will be statistically significant, he says. His team probably won't publish any results. "We spent all this money on this research and we're not even going to be able to give taxpayers the outcomes."

Among the hundreds of grants NIH has canceled since Trump's inauguration, such wasted spending appears to be common, a *Science* analysis of a small sample of them shows. Trump's Department of Government Efficiency (DOGE), effectively headed by billionaire Elon Musk, claims it has saved taxpayer money by systematically slashing funding for research on politicized topics including transgender health; diversity, equity, and inclusion; and vaccine hesitancy, and for work at universities and institutions the administration is targeting.

Until last week, the DOGE website claimed it had "saved" the entire sums of recently terminated grants like the one awarded to Goldbach. But NIH-funded researchers are typically reimbursed incrementally as they complete project milestones, often across multiple years. In a move unexplained on its website, DOGE now only claims as "savings" the remaining amount of money on a grant.

But that accounting does not note the hundreds of millions of dollars that had already been spent on canceled grants—and the potential loss of effort and data. The wave of cancellations, Goldbach says, "is rendering a lot of studies' data basically completely useless. It's creating waste, and I don't think that it's saving the kind of money that [DOGE] believe that it is."

Science's analysis drew on a list of 477 canceled NIH grants from an independent database compiled by researchers at Harvard University, who used data from Department of Health and Human Services data and scientists' own accounts of grants they know to be terminated. More than half of those grants have used up 50% of their total funds, according to a federal database that tracks such outlays. In total, the grants included in this sample have already spent $1.4 billion of the $2.8 billion NIH had promised their investigators.*

The analysis has limitations: Among others, the reports represent only a subset of the terminations, some terminations only affect one subsection of a grant, and some outlays are not publicly listed or are out of date. Most importantly, not all the spent money will be lost; unlike Goldbach, some researchers will be able to analyze or publish their existing data. But the numbers illustrate how wasteful DOGE's strategy is, says biochemist Jeremy Berg, former director of the National Institute of General Medical Sciences and former editor-in-chief of *Science*.

DOGE, he notes, contends these grants were worthless anyway. In that light, "Any money you don't spend on them is money saved," Berg says. "But if you actually believed the grants had value in the first place, what they're doing is throwing away the money that's already been invested."

Ethan Moitra, a clinical psychologist at Brown University, worries that will be the fate of nearly $1.5 million NIH awarded him. He was studying the mental health impact of the COVID-19 pandemic on LGBTQ+ individuals with anxiety and depression. When Moitra received NIH's termination letter on 28 February, he had spent about two-thirds of his $2.36 million grant assessing whether two counseling sessions could improve participants' mental health, and his team had completed follow-up interviews with 190 of the participants. The remaining 50 would have given his results statistical significance. "The timing is so awful," Moitra says.

Even if Moitra finds alternative funding to interview the final 50 participants, he's not sure whether he could continue because the NIH letter ordered him to stop all study activities. Moreover, any rescue funding may come too late: Too much time might have elapsed between the counseling sessions and the follow-up interviews.

A multimillion-dollar NIH project led by Annie Collier, a clinical psychologist at the University of Colorado Anschutz Medical Campus, to study vaccine hesitancy among Alaska Native and American Indian people and test strategies to promote vaccination was also cut short, terminated on 10 March. "It's really confusing and disturbing," she says, noting that vaccination rates among these populations are low and that people in these groups are more likely to die of diseases such as COVID-19.

Working with dozens of partners from Alaskan tribes, Collier and her colleagues developed culturally appropriate visuals and storytelling strategies for "community advocates" to use when talking about vaccines to other tribal members. The team was just about to start testing the strategies when they got the bad news. "We basically have about half of the funds wasted," Collier says.

Some of the scientists or their institutions are appealing the cancellations. Others may try to restructure their projects to remove them from the administration's target lists. But the researchers *Science* spoke with—several of whom declined to be quoted because of pending appeals or concern about their other grants—said they are getting little guidance from their NIH program officers. (Some of those NIH staff tell *Science* they had little to no input into the termination decisions and don't know the potential for reversing them.)

Ophthalmologist Nisha Acharya of the University of California San Francisco says she will nevertheless appeal the termination of her $3.3 million grant to study how people with ocular shingles infections react to the new shingles vaccine. The cancellation has effectively shut down her lab and forced her to lay off her employees.

Acharya had already spent $1.5 million of the grant. She hopes she can publish at least some of her lab's partially finished projects analyzing millions of medical records. But now that she's the only team member remaining, she worries she won't have the programming expertise to perform any additional analyses that peer reviewers might request. "I can't be doing every single part of the job, it's not possible," she says. If the grant is restored after her former employees find new positions, she would need to spend additional time and money training new programmers. For now, she says, the grant termination is "psychologically devastating."

Ironically, Acharya says, the wasted work might have appealed to the vaccine-skeptical Trump administration. She believes her grant was targeted as "vaccine hesitancy" in error. Its abstract says many eye specialists report "hesitancy" to recommend the new shingles vaccine to people with ocular shingles because the jab might cause inflammation.

Acharya's past research supports the idea that these vaccines—which the Centers for Disease Control and Prevention recommends for everyone over age 50—are not always safe. This is exactly the kind of research NIH would want to prioritize, Acharya believes. "You're not going to have [vaccine manufacturers] fund this." ■

---

*The analyzed sample excludes grants that were canceled at Columbia University because of the administration's contention that the school allowed antisemitic protests on its campus. Columbia is currently involved in negotiations with the government. It also excludes some supplements that were canceled and grants for which no outlay information was available.

TRUMP ADMINISTRATION

NSF has awarded almost 50% fewer grants

An analysis shows a drastic falloff since Trump took office. The finding conflicts with the director's claims

By **Jeffrey Mervis**

The number of new grants handed out by the National Science Foundation (NSF) since President Donald Trump took office has fallen by nearly 50% compared with the same 2-month period 1 year ago. The drop-off—which has reduced the funds awarded to researchers by more than $400 million—is even steeper for engineering, education, computing sciences, as well as NSF's new technology directorate.

The finding, revealed by an independent analysis of NSF's publicly available database, contrasts with NSF's public claims. On 11 March, NSF Director Sethuraman Panchanathan posted a letter to the research community saying the $9 billion agency was "continuing to advance the scientific enterprise" despite the slew of executive orders and actions by the Trump administration targeting government spending and the federal workforce.

"My priorities have not changed," Panchanathan wrote in the letter. The agency, he asserted, "has continued to make significant progress and has issued 95% of our funding as compared to the same time last year."

That figure, however, refers to the money handed out since the start of this fiscal year on 1 October 2024. But the analysis, based on data for the 2 months following Trump's inauguration on 20 January, tells a starkly different story.

The $1.1 billion education directorate, for example, has made only 12 new awards between 21 January and 27 March compared with 120 during the same period in 2024. The difference in dollars is equally staggering: $6 million versus $64 million. The $1 billion engineering directorate made

63 awards, down from 351, totaling $20 million versus $133 million. The computing directorate has seen the number of new awards fall from 264 to 115, although the dollar gap—from $71 million to $48 million—is smaller. And the 3-year-old Directorate for Technology, Innovation, and Partnerships has obligated only $19 million this year, one-tenth of the 2024 amount, with the number of new awards falling by roughly half, from 174 to 83.

Those numbers come from an analysis by David Miller, an NSF-funded research psychologist who studies science education. He found that NSF made 919 new awards across its eight directorates between when Trump returned to the White House and 27 March, compared with 1707 in the same period of 2024. This year's grants obligated a total of $312 million versus $761 million a year earlier. (Obligations refer to the initial funding of a grant; a 3-year award may be made entirely up front, for example, or parceled out in annual increments.)

> **The budget and finance office is "where things have broken down ... and nobody knows why."**
>
> National Science Foundation program officer

NSF provided *Science* with data that show a smaller downturn, although its analysis stops on 28 February and includes all financial obligations, including additional payments on current grants. The agency says it passed out $405 million during the initial 6 weeks of Trump's second term. Miller's number for all financial obligations over the same period is $172 million, compared with $501 million in 2024.

Panchanathan, who was appointed during Trump's first term for a 6-year term ending in June 2026, has declined repeated requests from *Science* to discuss the slowing of NSF's grantmaking machinery. But several sources inside the agency attribute the bottleneck to the office that handles the final step of the long process of winning an NSF grant.

That process begins with a scientist submitting a proposal, which then undergoes peer review. If the idea gets high marks, a program officer recommends it for funding—and often tells the applicant that things are looking good. Once a division director signs off on the recommendation, the paperwork goes to the budget and finance office.

"That's where things have broken down," says one program officer who requested anonymity because they are not authorized to speak for the agency. "And nobody knows why."

NSF's data show that two $1.6 billion directorates—geosciences (GEO) and math/physical sciences (MPS)—have not only weathered the storm, but appear to have been more active than in 2024. They show MPS has handed out $138 million since Trump took office, compared with $98 million for the comparable period in 2024, and GEO has obligated $116 million versus $64 million in 2024. But the independent analysis doesn't support that rosy picture, a variance that might be due to NSF's use of a different yardstick.

Unlike Miller's analysis, NSF's numbers include money handed out as part of what it calls "postaward actions," that is, fresh rounds of funding for a project, center, or facility that NSF has been supporting. For example, this year's GEO total includes the latest tranche of money—$49 million—for the National Center for Atmospheric Research, which NSF has been funding since 1960. And MPS's total includes $41 million to continue operating three NSF-built facilities—the Gemini telescope, the Laser Interferometer Gravitational-Wave Observatory, and the National High Magnetic Field Laboratory. Compared with additional support for existing grants, new awards require more time and effort by NSF employees, a politically sensitive issue given Trump's efforts to shrink the federal workforce. That's why Miller chose to focus on new awards.

On 28 February, Democrats on the science committee in the U.S. House of Representatives wrote to NSF's oversight body, the National Science Board, asking it to investigate rumors that NSF's grantmaking process had been disrupted under the new administration. "We request that you and your colleagues immediately undertake a review of NSF's capacity to fulfill its mission ... and do everything in your power to stop the ongoing destruction of the National Science Foundation," the legislators wrote in a letter signed by the panel's ranking member, Representative Zoe Lofgren (D–CA), and Representative Haley Stevens (MI), the top Democrat on its research subcommittee.

The board's 14 March reply suggested all was well. "The Board has looked closely at the capacity of NSF to perform its mission," wrote back Dario Gil, board chair, and "we are happy to be able to report ... that the Director is doing everything in his power" to advance NSF's mission, citing the numbers in his 11 March letter. Gil, head of research at IBM, is awaiting a Senate hearing on his nomination to be undersecretary of science and innovation at the Department of Energy. He declined further comment. ■

ENERGY

Stellarators, once fusion's dark horse, hit their stride

Multiple companies aim to build pilot plants using twisted magnets

By **Daniel Clery**

A dark horse reactor design has emerged as a contender in the race to develop a commercial fusion reactor. Doughnut-shaped machines called tokamaks have long been the favorites of scientists hoping to fuse atoms to generate energy. Their twistier cousins, stellarators, had gotten less attention—and funding—because they didn't perform as well and their complex geometries are harder to design and build. But stellarators have properties that could, in the long run, make them better as power plants.

Now, equipped with an improved grasp of the needed physics and more powerful supercomputers, several startup companies have published designs for prototype machines they think could generate electricity before the end of the next decade. One has also tested a novel magnet technology to make building them easier.

"People are coming to realize the stellarator maybe is the way to go," says theorist Chris Hegna, vice president of Type One Energy, a firm whose scientists last week published seven papers in the *Journal of Plasma Physics* describing in detail its proposed pilot plant, Infinity Two.

The ultimate test of stellarators and all the other designs fusion companies are touting is to get their fuel to temperatures and pressures high enough for nuclei to fuse and release more energy than was needed to spark the reaction. So far no reactor has achieved that, except in the brief laser flashes at the National Ignition Facility in California.

But stellarators are a promising avenue, even some tokamak researchers say. "I'm quite excited actually about the stellarators," says Dennis Whyte, former director of the Plasma Science and Fusion Center at the Massachusetts Institute of Technology. "What stellarators provide is operational simplification as compared to a tokamak."

A key challenge for any fusion device is confining its superheated fuel, a roiling plasma of hydrogen ions and electrons. A temperature of 100 million degrees Celsius—hot enough to destroy any material—is needed to make the ions fuse. Tokamaks use a strong magnetic field to cage the plasma and then heat it with microwaves and particle beams. A series of magnet coils loop around the doughnut vertically and horizontally, a geometry that drives the plasma to flow around the doughnut. That plasma "current" creates a magnetic field of its own, causing the plasma to follow a helical, candy cane path around the vessel. Since the 1960s, most fusion funding has gone into this approach, culminating in the globally backed €25 billion ITER tokomak under construction in France.

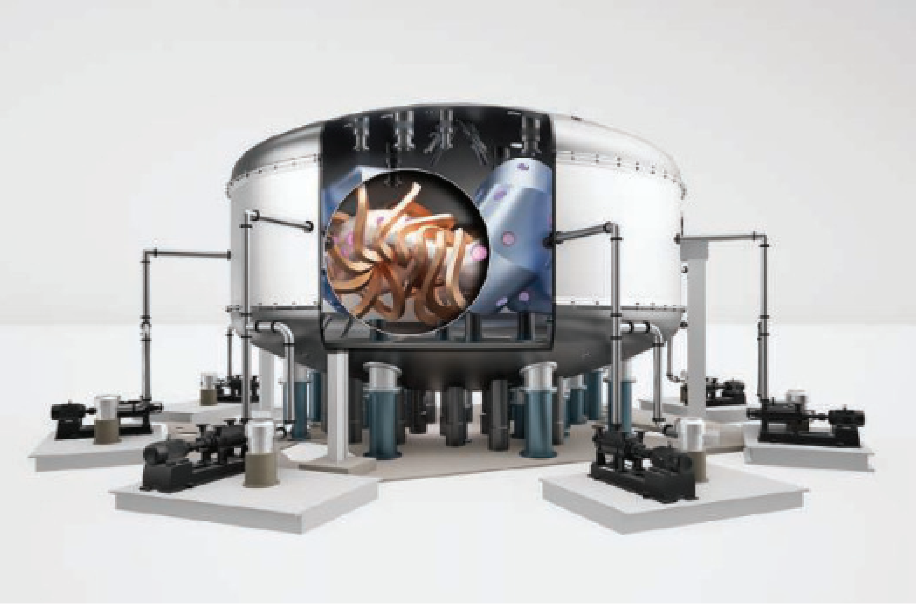

Type One Energy's first stellarator, Infinity One, will use an odd geometry of magnets (gold) to confine plasma.

IMAGE: TYPE ONE ENERGY

Tokamaks are good at keeping particles and their heat contained, but they have Achilles' heels. The electromagnet at the tokamak's center that drives the plasma current around the loop can't do so indefinitely and must occasionally be paused and reset. Tokamaks are also prone to "disruptions," breakdowns in the plasma's flow that cause its particles to veer off course, potentially damaging the wall of the vessel. Disruptions can also generate electron beams capable of burning a hole right through the wall.

Stellarators behave better. Like tokamaks they're doughnut shaped, but stellarator magnets are arranged to confine the plasma without needing a plasma current. As a result, they don't suffer from disruptions and don't need a reset. In theory, you "can turn [it] on once and just leave on forever," Whyte says. But early stellarator designs underperformed because colliding particles diffused out of the plasma, cooling it and making it impossible to reach fusion temperatures.

In the 1980s and 1990s, however, a better understanding of plasma physics and more powerful supercomputers enabled stellarator designers to calculate magnetic field shapes that would limit the heat-sapping particle collisions. They also devised the magnet geometries needed to produce those fields—a process known as optimization. The required magnets often had weirdly distorted shapes, making the machines difficult and expensive to build, but in 2015 the Max Planck Institute for Plasma Physics (IPP) debuted the first large-scale optimized stellarator, Wendelstein 7-X (W7-X [*Science*, 23 October 2015, p. 369]). "It's been a real success … for plasma theory that we can actually predict things in a very cogent way," Hegna says.

Over the past decade, the length of W7-X's runs and its plasma temperature have grown to rival those of tokamaks. "W7-X demonstrated … the stellarator was ready to go for a path towards a pilot plant design," says Novimir Pablant, head of stellarator experiments at the Princeton Plasma Physics Laboratory (PPPL) and a collaborator with W7-X. Investors paid heed. A report last year from the Fusion Industry Association listed eight companies working on stellarators compared with six on tokamaks.

Type One, which Axios this week reported is seeking $200 million in investment on top of the $82 million raised last year, is finalizing the design for its first machine, Infinity One. Its aim "is to essentially fill in the gaps where we need a little more validation work," Hegna says. Construction is set to begin next year. Infinity Two, which Hegna says is the company's focus now and could fire up next decade, is a true fusion pilot plant.

Type One says that machine will span nearly 14 meters and generate 800 megawatts of heat, resulting in 350 MW of electricity. In February, it signed an agreement with the Tennessee Valley Authority, a U.S. electrical utility, to build its reactors at the retired Bull Run power plant. Like tokamak competitors, Type One plans to use high-temperature superconductors in its magnets, allowing them to generate stronger fields while keeping the machine compact.

Last month, Proxima Fusion—a spinout company from W7-X's creator IPP—published a paper in *Fusion Engineering and Design* describing a design for another stellarator pilot plant, dubbed Stellaris. Similar in size to Type One's machine, Stellaris is also targeting electricity production in the 2030s. The company says it will build a test magnet from high-temperature superconductors in 2027 and a demo stellarator in 2031 before embarking on Stellaris. One of the challenges for such efforts is making complex magnet geometries at a reasonable cost. "Proxima invested quite heavily in computational design in the beginning to deal with these complexities," says Felix Warmer, head of the recently created stellarator reactor studies group at IPP.

Another stellarator company, Thea Energy—a spinout from PPPL—hopes to dispense with the complex magnet shapes entirely: Instead, it will shape its fields with a series of simple circular coils oriented at different angles and then finetune the fields with hundreds of controllable flat magnets—dubbed magnetic pixels—covering the outside of the reactor. Last week, the company posted a preprint on arXiv describing tests of a 3x3 array of magnetic pixels made from a high-temperature superconductor, which showed they could produce different field shapes by powering up and down the individual pixels. "It just worked the first time we turned it on. So it was very rewarding in that regard," says Thea co-founder David Gates.

All of these developments are creating a new confidence among stellaratormakers. "The sheer fact that tokamaks look simpler to build, I think that's fading away," says W7-X director Thomas Klinger.

The use of artificial intelligence and large-scale 3D printing for magnet design and manufacturing could further erode tokamaks' advantages. Stellarators, Whyte says, are catching up fast. "There's a really good chance that they can get there." ■

Mass vaccination sites are no longer needed for COVID-19, but vaccines could still be improved.

PHOTO: LINDSEY WASSON/REUTERS

INFECTIOUS DISEASES

NIH cancels research grants for COVID-19 and future pandemics

Scientists reject claim that the work is no longer needed

By **Jon Cohen**

The White House appears to have a new target for its cuts to research funding: grants linked to COVID-19, which President Donald Trump and his appointees have decided are a waste of money because the pandemic is "over." Infectious disease scientists are aghast at the move, which they say will cripple attempts to improve COVID-19 medicines and will make society more vulnerable to future pandemics.

On the night of 24 March, a batch of 29 grant termination letters went out from the National Institute of Allergy and Infectious Diseases (NIAID). "The end of the pandemic provides cause to terminate COVID-related grant funds," the notifications stated. "These grant funds were issued for a limited purpose: to ameliorate the effects of the pandemic. Now that the pandemic is over, the grant funds are no longer necessary."

The terminated projects included many that focus specifically on COVID-19 but also some that study Long Covid, the mysterious chronic affliction that can develop after a COVID-19 infection. They also include nine grants under a $577 million program aimed in part at delivering antiviral drugs to prevent future pandemics. The cancellations, researchers say, will likely eliminate more than research programs: Graduate students and postdocs may lose jobs because many labs depend on grants to pay their salaries.

NIAID's parent agency, the Department of Health and Human Services (HHS), championed the cuts. "HHS will no longer waste billions of taxpayer dollars responding to a non-existent pandemic that Americans moved on from years ago," Andrew Nixon, a Trump appointee who is now the agency's head spokesperson, emailed *Science*. "HHS is prioritizing funding projects that will deliver on President Trump's mandate to address our chronic disease epidemic and Make America Healthy Again."

The nine Antiviral Drug Discovery Centers for Pathogens of Pandemic Concern eliminated last week were founded in 2022 to develop drugs to better treat COVID-19. They also aimed to design antivirals for entire families of disease-causing viruses, including bunyaviruses (Rift Valley fever), filoviruses (Ebola, Marburg), flaviviruses (yellow fever, dengue, Zika), paramyxoviruses (measles), picornaviruses (common cold), and togaviruses (chikungunya).

The centers' termination has a "misleading rationale" and is a "pointless, ill-advised move that will hurt U.S. science and pandemic readiness," says Charles Rice, a Nobel Prize–winning virologist at Rockefeller University who co-leads one center.

Other terminated grants supported research to improve COVID-19 vaccines. "The research is being treated like we already have all the answers we will need in the future and that the current vaccines work well enough and don't need improvement, which we know is not true," says an investigator involved with one of the NIAID grants who asked not to be named for fear of retribution. Some of the studies being canceled were attempting to make a pancoronavirus vaccine, effective against many different coronaviruses. A broad-spectrum vaccine "would hopefully be available the next time a novel coronavirus jumps species into humans," the investigator says.

Several canceled grants were part of the Researching COVID to Enhance Recovery (RECOVER) initiative, which studies the drivers of Long Covid and potential treatments. Congress had set up the program with a $1.15 billion appropriation in 2021 and the National Institutes of Health (NIH) subsequently committed another $662 million to it. After an outcry, the RECOVER grant terminations were rescinded.

Science has learned that the terminations also include at least two of the eight federally funded Serological Sciences Centers of Excellence. This network was set up to study immune responses to SARS-CoV-2, what leads to its transmission between people, and what drives disease progression in the infected. The U.S. National Cancer Institute–organized program involved 26 institutions, from academic labs to hospitals, and had been authorized to receive more than $150 million from an emergency congressional appropriation made in 2020.

On top of the terminated NIH research grants, the U.S. Centers for Disease Control and Prevention has begun cutting $11.4 billion in pandemic response funds allocated to state and country health departments and nongovernmental organizations.

The NIAID grant termination letter Rice and colleagues received told the researchers they could appeal, but said that would be pointless. "Although 'NIH generally will suspend (rather than immediately terminate) a grant and allow the recipient an opportunity to take appropriate corrective action before NIH makes a termination decision,' no corrective action is possible here," the termination notice said. "The premise of this award is incompatible with agency priorities, and no modification of the project could align the project with agency priorities." ■

SCIENTIFIC COMMUNITY

International scientists rethink U.S. conferences

Opposition to Trump administration and fears of customs run-ins are shifting travel plans

By **Kate Langin**

Marco Prado has rarely missed a meeting of the International Society for Neurochemistry in 30 years. "I have deep ties to the society," the Canada research chair and University of Western Ontario professor says. But after U.S. President Donald Trump began announcing tariffs on Canadian goods and repeatedly referring to the sovereign nation as the "51st state," Prado says he scrapped his lab's plans to attend the society's next conference this August in New York City. (The team opted instead for an Alzheimer's disease meeting in Toronto.) "It's like our neighbor is trying to attack us. … I cannot [bring] myself morally to spend Canadian taxpayers' money in attending U.S. conferences," he says.

Thousands of researchers from outside the United States attend scientific meetings there each year to present work, network, and build collaborations. But some are reassessing their travel plans because of objections to U.S. policy and fears of being interrogated or detained by customs officials. None of the scientific societies *Science* reached out to reported an uptick in cancellations from foreign scientists for recent or upcoming meetings. But some noted they are keeping an eye on the situation. "We have heard from some members with concerns, and we're continuing to listen and learn how we can best support them," says a spokesperson for the American Physical Society (APS), which held a Global Physics Summit in Los Angeles last month that drew 15,000 attendees, including 4000 from outside the country.

Border crossings into the U.S. have created particular anxiety. "I think that not many students would like to come to U.S. nowadays," a professor at a university in China told *Science* last month at the APS meeting. She asked to remain anonymous for fear of jeopardizing her ability to obtain a U.S. visa in the future. The researcher, who did a postdoc in the U.S. and currently holds a 10-year multiple entry visa, had no problems on this trip. But she knows a Ph.D. student from China who was questioned by U.S. customs for more than 1 hour about his work and ties to the Chinese government before being let through. Fearing she'll have a similar problem—or worse—as the Trump administration moves to tighten border security, she now wonders whether she should take a break from meetings on U.S. soil.

Last month, a space researcher from CNRS, France's national research agency, made headlines after being detained while en route to attend a conference in Texas. The scientist, who has not been publicly identified, was held for a day, his devices were confiscated and searched, and he was put on a plane home. Philippe Baptiste, France's higher education and research minister, claimed the researcher was denied entry because his phone contained exchanges in which he shared personal views of the Trump administration's research policy. The U.S. Department of Homeland Security denied politics was a factor, instead saying the researcher's device contained confidential information from the U.S.'s Los Alamos National Laboratory.

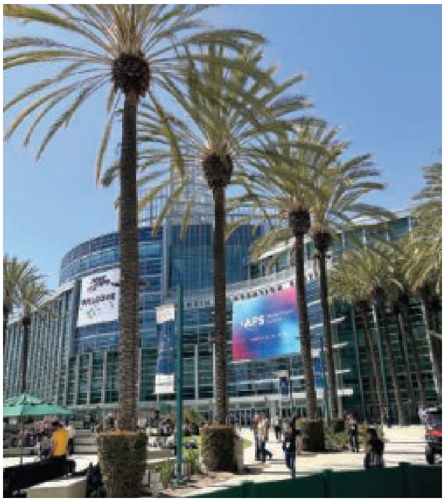
Thousands of foreign scientists flock annually to U.S. conferences like last month's Global Physics Summit.

French researchers at multiple institutions have since received emails from their employers advising them to consider traveling with a laptop empty of emails and sensitive documents. *Science* has seen two of the notices, which state that the advisory came at the request of French security officials.

The incident has had a chilling effect. One physical scientist who was scheduled to fly from France to the U.S. last week for a meeting chose to cancel his trip at the last moment. "I didn't want to take the risk to be detained," says the scientist, who wished to remain anonymous because he has ongoing collaborations with U.S. researchers and may still need to travel to the U.S. He was able to give a virtual talk instead. "But unfortunately, it cannot replace contacts with other scientists."

The cost of opting out can be especially high for early-career researchers. "I am at a point in my career where building new collaborative relationships is critical," says one Canadian biologist, an assistant professor who is scheduled to be an invited speaker and sessions organizer at two upcoming U.S. meetings, and who also asked to remain anonymous. She may decide not to go, and has asked the organizers to arrange remote attendance, but she says they haven't been receptive.

International students and scholars working in the U.S. face a different risk: If they travel to attend meetings in other countries, they could have problems returning. "Current U.S. immigration policy is unpredictable and subject to rapid change," reads a 6 March advisory from the University of California, Berkeley's international office, one of several that has recommended foreign students avoid leaving the U.S.

"I feel scared to leave the city I'm in, let alone the country," a student from India pursuing a Ph.D. at a U.S. university told *Science* on the condition of anonymity. "It's definitely impairing what career opportunities I can access."

Even some U.S. citizens working abroad are avoiding meeting travel. Jennifer Love, a University of Calgary chemistry professor whose Bluesky profile reads "American by chance, Canadian by choice," recently turned down an invitation to the International Chemical Congress of Pacific Basin Societies in December in Honolulu. She fears that because of her vocal support of diversity, equity, and inclusion initiatives—a target of the Trump administration—she will be hassled by border guards.

Love also does not want to support a country whose policies she objects to. But, "I feel badly that I'm turning down colleagues and friends," she says. "I don't want to penalize them or the scientific community. Science is supposed to be international." ■

With reporting by Adrian Cho.

PHOTO: CHRIS VANDE LUNE

POPULATION GENETICS

Ancient DNA illuminates 'green Sahara' dwellers

Skeletons from an ancient, lush interlude offer genetic peek at a lost population

By **Andrew Curry**

Today, the Sahara Desert is a sea of sand, but 7000 years ago it was a lush savanna full of hippos, crocodiles, elephants, and giraffes. During a humid, monsoon-heavy interval that spanned more than 5 millennia, people hunted, fished, and eventually herded livestock in a landscape now covered by shifting dunes.

But who were they? Many archaeologists believed migrants from south of the Sahara mingled there with people from the Mediterranean. But the idea was hard to test: The hot, dry conditions that have dominated the Sahara since then have left little DNA preserved in ancient bones. Now, a team of geneticists and archaeologists has at last succeeded in gleaning genetic data from early Saharans: two women buried in a cave in southern Libya. "It's the first time ancient genomes have come out from anywhere in the Sahara," says University of Oxford archaeologist Peter Mitchell. "It's very exciting."

The findings, reported in a paper this week in *Nature*, reveal a previously unknown population, entirely disconnected from people living in sub-Saharan Africa at the time. "It's surprising," says Eugenia D'Atanasio, a population geneticist at the Sapienza University of Rome who was not involved in the research. "I would have expected more gene flow across the green Sahara."

Between 2003 and 2006, a team of archaeologists excavated a rock shelter called Takarkori in southwestern Libya, near the Algerian border. Although the site "is now in the middle of the desert," says archaeologist and excavation leader Savino di Lernia of Sapienza, the people living here 7000 years ago would have looked out over a lake year-round.

The site yielded pottery sherds impregnated with milk fats, the oldest evidence of dairying in Africa, and some of the first signs of wild cereal domestication on the continent. Nearby caves are richly decorated with rock art depicting hunting and herding scenes. It also concealed the remains of 15 women and children who were buried between 8000 and 400 years ago.

The view today from the Takarkori rock shelter in Libya is arid desert, but it once looked out over a lake.

Two of them—both women in their 40s—died around 5000 B.C.E., after shifting climate patterns ended the Sahara's green period. Their bodies were naturally mummified by the dry desert conditions and contained enough preserved DNA for researchers to reconstruct their genomes and compare their ancestry with databases of modern and ancient populations. "We were very fortunate to have samples preserved at this level," says co-author Nada Salem, a paleogeneticist at the Max Planck Institute for Evolutionary Anthropology (EVA).

Based on archaeological findings and previous genomic studies, researchers previously hypothesized that migrants from northern Africa populated the green Sahara, and later mixed with people from sub-Saharan Africa and the eastern Mediterranean. "People said this was a corridor," says co-author Johannes Krause, a geneticist at EVA. "After all, animals came in from the sub-Saharan savanna more than 10,000 years ago."

Instead, the DNA suggests their ancestors were distinct from sub-Saharan Africans. Another clue revealed they didn't come from the Levant, either. The genomes of people from that region—and much of the world outside Africa—contain DNA derived from Neanderthals, acquired when modern humans began to move out of Africa and swap genes with our close cousins, some 50,000 to 60,000 years ago. But the genome of the woman with the best preserved DNA had only a vanishingly small amount of Neanderthal ancestry, 10 times less than people living outside sub-Saharan Africa today.

Meanwhile, the women's mitochondrial DNA, which is passed down along the maternal line, suggested their ancestors came from an African population that provided some of the earliest modern human migrants to Europe. That population has now vanished from both continents. "It's a population that's separate from sub-Saharan Africa," Salem says, "but also distinct from people outside Africa today."

Mysteries remain. Pottery found at Takarkori resembles that made across North Africa. That suggests contact with people outside the Sahara. Yet the genes don't show any mixing with new populations, even when new technologies—such as herding cattle and goats—were introduced about 8300 years ago. Such technological and cultural shifts in other places are often accompanied an influx of new people. "The green Sahara wasn't a corridor for the movement of people, but for sure it was a corridor for ideas and technology," di Lernia says.

Although the ancestry of these women offers a good start to the story of those who occupied this fleeting green Sahara, much more work is needed, Mitchell says. Since di Lernia's excavations at Takarkori 20 years ago, political tensions and violence have made working in the region dangerous. "Exciting as this is, it's difficult to be absolutely sure how much to make of it based on two data points," Mitchell says. "Maybe if we had DNA from other burials in the Sahara, we'd see a more complicated picture." ■

PHOTO: SAPIENZA UNIVERSITY OF ROME

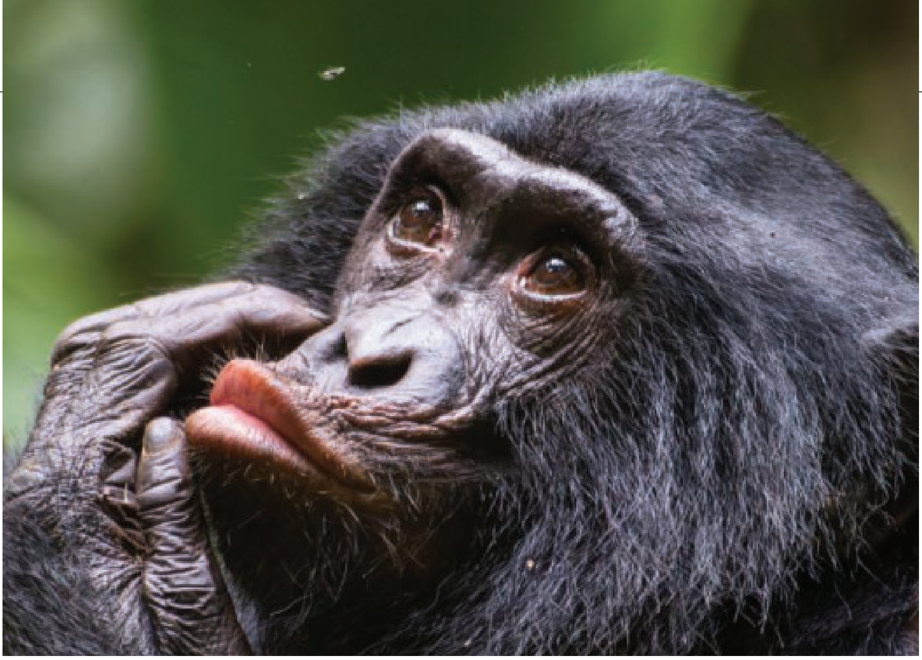

Researchers spent 8 months following wild bonobos and recording their vocalizations.

PHOTO: ROLAND HILGARTNER

ANIMAL BEHAVIOR

‘Uniquely human’ language capacity found in bonobos

Study is the first to show an animal combining different calls to make new meanings

By **Cathleen O’Grady**

Human language can combine words to create an infinite number of meanings—an ability that gives language its expressive power and sets it apart from the communication of other animals. Now, researchers have found a more modest version of this ability in bonobos, our closest living relative. The apes can combine different calls to create new meanings, the team reports this week in *Science* (p. 104).

It’s a “pivotal” study that “will change the face of the field,” says Maël Leroux, an evolutionary biologist at the University of Rennes who was not involved with the work. The finding is “compelling evidence for abilities that were assumed to be uniquely human.”

Previous studies have found that other animal species can combine their calls, but only in “trivial” combinations that simply add the meanings together. Human language is much more powerful: Speakers can combine words into more than the sum of their parts. For instance, “tall cook” is a trivial combination—it means someone who is tall and a cook. But “good cook” is not someone who is good and a cook: They might be good at cooking, but terrible in other areas—perhaps a dangerous driver. This combination of words generates a new meaning.

To find out whether bonobos are capable of making these “nontrivial” combinations, University of Zürich (UZH) animal communication researcher Mélissa Berthet spent 8 months following wild bonobo groups in the Kokolopori Bonobo Reserve in the Democratic Republic of the Congo. Every day, she and her guides set out at about 4 a.m. to find the bonobos before they left their overnight nests, then tracked them all day. Whenever she had a clear view of their activities, she recorded every vocalization, along with all its context: who made it, what they were doing, how other animals responded, and even what the weather was like. Any number of more than 300 contextual features could be linked with each call. Eventually, Berthet started to understand some of what the animals were communicating: “You see a vocalization and then everybody moves … and it’s very satisfying to be like, ‘Ah, I think I start to get it,’” she says.

Berthet recorded 700 different vocalizations, many of which were combinations of two distinct calls, like “whistle and peep” or “high hoot and low hoot.” To see whether the animals were creating new meanings from these combinations, the team borrowed an approach from human language studies, statistically analyzing how much context the vocalizations shared with each other. (In human language, words that occur in similar contexts tend to be more closely related in meaning.)

Three combinations stood out: Their meanings appeared different enough from those of their constituent calls that they seemed to count as nontrivial combinations. “High hoot and low hoot” was one of these. “Low hoot,” the team found, is often used in situations of high excitement, and appears to mean something like “I am excited.” “High hoot” is used when bonobos want to alert others to their presence and may mean “Pay attention to me.” But the combination of the two calls doesn’t simply mean “I am excited, pay attention to me”; instead, it conveys a more nuanced message. It is used specifically when another individual is putting on an aggressive display. The bonobo using this call combination might be trying to stop the other individual from displaying or get others in the group to pay attention to the caller, the authors suggest.

The findings suggest bonobos have a “precursor” to the human capacity to combine units of language to create new meanings, says senior author Simon Townsend, a primate communication researcher at UZH. Both bonobos and humans may have inherited the ability from our common ancestor some 7 million years ago, he says.

Even more exciting than the results, Leroux says, is the method Berthet and her colleagues used for defining and comparing the potential meanings of different calls. Past animal communication studies have described general contexts for particular calls, but have not been this systematic or specific in documenting the circumstances. The team’s approach is “revolutionary” and has “fantastic potential” for studying communication in other species, says Gal Badihi, an animal communication researcher at the University of St. Andrews.

It also suggests a new direction for studying primate communication, says Cedric Boeckx, an evolutionary linguist at the Catalan Institution for Research and Advanced Studies. Communication research in great apes has often focused on their gestures, but this study shows that bonobos’ vocal calls also have rich meanings, he says. Future experiments with other primate species—including chimpanzees but also gibbons and marmosets—could shed new light on the complexities of other communication systems.

Leroux agrees: “We have so much to do now, thanks to them.” ■

FEATURES

FAILURE TO COMMUNICATE

Geoengineering could be crucial in the fight against climate change. But first scientists need to learn how to talk to the public about it *By* **Rebekah White**

PHOTO: IAN C. BATES/*THE NEW YORK TIMES* VIA REDUX

When Marilyn Ezzy Ashcraft, mayor of Alameda, California, scrolled through *The New York Times* on a Saturday morning in April 2024, a story about a controversial experiment caught her eye. Researchers from Washington state were trialing a machine that looked like a big snow cannon, which they hoped could one day be used to brighten clouds to reflect more of the Sun's rays. They'd been spraying tiny salt particles into the air over the San Francisco Bay.

At first, Ashcraft wondered which neighboring town was hosting the test. But as she read, she was shocked to learn that the researchers were conducting their experiment right there in Alameda.

Ashcraft texted her acting city manager, who was equally surprised. The story revealed that the researchers had kept the test a secret to limit protests. "It wasn't just an oversight that they forgot to tell the city," Ashcraft says. "They chose not to." Concerned about the safety of the test, city staff investigated. Though a report concluded it was harmless, the council eventually voted to ban it, discomfited by the researchers' lack of transparency.

Ashcraft hoped this would be a "teachable moment" for the research team. "Maybe they were just in such a hurry, or maybe they thought they could get by without being noticed," she says. "Whatever it was, it didn't work well for them. It really backfired."

The technology being trialed in Alameda was one of a suite of new geoengineering tools—many still in the earliest stages of development—that aim to modify the atmosphere or the ocean in order to fight climate change. Some of these tools are designed to remove carbon dioxide (CO_2) from the atmosphere, a step that, along with drastic emissions cuts, scientists agree will be essential for limiting global warming to 1.5°C. Others—such as cloud brightening—don't counter the drivers of climate change, but aim to limit warming, protecting vulnerable ecosystems such as coral reefs.

One thing these technologies have in com-

Scientists spray salt particles into the air above the deck of the *USS Hornet*, docked in Alameda, California.

mon, however, is that they're at risk of being stopped before they can even be tested in the field. Researchers' ability to conduct even the most basic field tests depends on the goodwill of nearby communities, but critics charge that many project leaders treat public engagement as a check-box exercise—or forgo it entirely. In the past 3 years, public outcry has thwarted several climate engineering projects.

Others, however, have built enough trust to proceed. Their success has taught some key lessons—as has a flurry of studies by social scientists. These researchers have explored the kinds of concerns people hold about climate engineering, how to have productive public discussions about it, and even where to run experiments. Yet their findings are rarely incorporated into the groundwork for field tests.

"It's really, really hard to be taken seriously," says social scientist Sikina Jinnah of the University of California, Santa Cruz. "There's a handful of scientists who I think bend over backwards to support social science and to advocate for the inclusion of social scientists and their perspectives, but they're few and far between."

GEOENGINEERING—deliberately altering the workings of the planet—sounds ambitious, even arrogant. Perhaps inevitably it invites concerns about meddling with nature, and poses tricky questions about who decides when and where the technologies should be deployed.

It comes in two main flavors (see graphic, p. 22). Solar radiation modification describes techniques for deflecting the Sun's rays, from painting buildings white, to brightening clouds, to injecting tiny reflective particles into the stratosphere. The international shipping fleet has been inadvertently geoengineering the planet for decades with emissions from ships' stacks: When new shipping regulations restricted sulfur dioxide emissions in 2020, the resulting rise in sea-surface temperatures suggested the pollution had been brightening clouds above the sea.

Carbon removal, on the other hand, describes ways to reduce the level of CO_2 in the atmosphere, from low-tech strategies such as planting trees and restoring wetlands to new methods such as changing the chemistry of the ocean to absorb more CO_2 or vacuuming the gas out of the air with giant filters. Currently, carbon-removal efforts soak up about 2 gigatons of CO_2 from the atmosphere each year, mostly through the planting of new forests. That amount would likely need to quadruple by 2050 in order to limit warming to 1.5°C, according to a 2024 report from the University of Oxford, requiring the rapid scale-up of new carbon-removal methods. "It's got to go from something that most people have never heard of to the biggest industry the world has ever seen in a really short time," says climate scientist David Ho, a professor at the University of Hawaii at Manoa.

Because carbon-removal technologies are so new and unfamiliar, public perceptions of them have not yet hardened. But many worry researchers are squandering the opportunity this presents. When it comes to ocean-based carbon removal, for instance, "I just feel like we're at a really vulnerable stage from a public perception standpoint," says Sara Nawaz, who directs research at American University's Institute for Responsible Carbon Removal Law and Policy. "I think that there's totally the risk that one or several projects that get really stigmatized can just delay things or even just totally kind of take it off the table."

FORGOING PUBLIC engagement has already had fatal consequences for solar geoengineering projects—with ramifications for the entire field.

In 2021, the Harvard University–backed Stratospheric Controlled Perturbation Experiment (SCoPEx) project was planning to launch a balloon in Sweden to study stratospheric aerosol injection, the theory that releasing tiny particles of calcium carbonate or sulfur dioxide into the stratosphere will reflect enough sunlight to temporarily cool the planet. The balloon flight would simply test whether SCoPEx's equipment worked as intended, not release particles.

In the lead-up to the test flight, SCoPEx's advisory committee debated the need for public engagement. Some members argued the test flight bore little difference to atmospheric research routinely carried out without public consultation, whereas others advocated for transparency and dialogue. In the end, the committee ruled that public outreach wasn't necessary.

But, as with the Alameda project, the intention of the research was more important to people than what was actually taking place, and after objections from the Saami Council, a local Indigenous group, as well as local and international campaigners, the flight was halted. "These experiments and these technologies have much deeper meaning than just whether or not there's particles in the air," says Jinnah, who co-authored a paper describing SCoPEx's governance challenges and joined the advisory committee following the launch cancellation.

The debates continued as the team planned its next moves. Should the researchers only engage with the community at the launch site, or with the global public, which stood to benefit from planetary cooling? And should engagement simply involve informing people, or should it be a process of building relationships with communities and incorporating their concerns into research? Most guidelines for public engagement assume a project will continue for a significant length of time. SCoPEx wanted to launch a balloon and leave.

The advisory committee could not agree on a plan, and the project leaders ultimately decided to pull the plug in 2024. In an interview with *MIT Technology Review*, SCoPEx co-leader David Keith said the project's prominent failure would make this branch of research more difficult.

A turbulent history

Scientists have suggested using geoengineering to combat climate change since the late 20th century. **Solar radiation modification** (●) includes proposals to reflect sunlight away from Earth, whereas **marine carbon dioxide removal** (●) includes technologies for changing the chemistry of the ocean to speed up its absorption of carbon. Field trials of the technologies have accelerated in the past 5 years, but public perception remains fraught and many projects have foundered.

1974
Soviet climatologist proposes **releasing sulfur aerosols** in the stratosphere to deflect sunlight.

SEPTEMBER 1990
British cloud physicist suggests **spraying saltwater droplets into clouds** to make them more reflective.

APRIL 2004
A study suggests **iron fertilization** in the Southern Ocean could **increase carbon dioxide uptake**.

MAY 2008
United Nations puts a **moratorium on ocean-fertilization** experiments in the open ocean.

MAY 2012
A U.K. stratospheric **aerosol injection** test is **canceled** following conflict-of-interest issues and public protests.

APRIL 2017
A Canadian nonprofit sparks **protests** after applying for permits to **dump iron** near Chile.

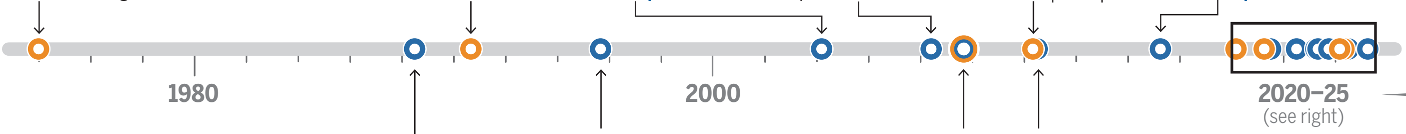

JULY 1988
Oceanographer John Martin **sparks interest in fertilizing the ocean** with iron to produce blooms of phytoplankton that consume carbon dioxide.

SEPTEMBER 1995
A paper **proposes** sequestering carbon dioxide by **increasing ocean alkalinity**.

SEPTEMBER 2009
A Royal Society report spurs interest in **carbon removal** and **solar geoengineering**.

JULY 2012
U.S. entrepreneur Russ George **slammed for dumping iron** into the open ocean to revive a fishery.

CLIMATE ENGINEERING can be even more unsettling to the public than other controversial technologies such as genetic engineering. It involves tinkering with complex natural systems—the sea, the sky—which largely renders it irreversible: It isn't possible to retrieve sulfur dioxide particles from the stratosphere or grains of CO_2-absorbing mineral sand from the seabed. And exactly how the technologies will be deployed and regulated is unclear.

"You're not just asking people, what do they think of this technology or this field trial or this sort of machinery or activity," Nawaz says. "You're asking people to contemplate different potential futures that could arise. So you're asking them to think through, what do you want the world to look like?"

Such outreach often meets with scepticism. In a study led by Livia Fritz, a social scientist at Aarhus University, hundreds of people across 22 countries in the Global North and Global South spoke in focus groups about how they believed geoengineering projects should be discussed. Most expressed disillusionment with engagement—not because they didn't want to be consulted, but because they had experienced bad-faith consultations in the past that sought to convince rather than to listen.

Some participants didn't believe the public should be involved in decision-making, citing concerns about people being manipulated by misinformation, then making consequential decisions, Fritz says. "Brexit, for example, was mentioned a lot here." She says the results point to the need for open consultation on climate engineering that isn't limited to issuing or denying permission for particular projects, but that allows people to consider and debate the technologies more broadly.

Solar radiation modification research rouses other suspicions: Studies have found a strong overlap between online discussion of the technology and long-standing conspiracy theories, such as the idea that condensation trails from airplanes are in fact chemicals released for an unknown but nefarious purpose. These conspiracy theories and other misunderstandings are partly behind moves to ban or restrict solar geoengineering: There are bills passing through the legislature in 28 U.S. states to limit research or deployment of the technology, most of which were introduced in this year.

Yet engagement offers one form of inoculation against the spread of misinformation, according to a National Academies of Sciences, Engineering, and Medicine report from 2017. Transparent communication builds trust, the report concludes, such as when scientists disclose funding sources or potential conflicts of interest or demonstrate a willingness to listen to public concerns.

Jinnah says some scientists believe engagement isn't necessary because they feel the importance of the research should override public concerns, and because some people will be opposed to it no matter what outreach takes place. But engagement can lead

Solar radiation modification

Researchers have proposed various methods to curb the effects of climate change by reflecting sunlight away from the planet.

Stratospheric aerosol injection
Balloons or aircraft would release tiny sulfur dioxide or calcium carbonate particles into the stratosphere to reflect solar radiation.

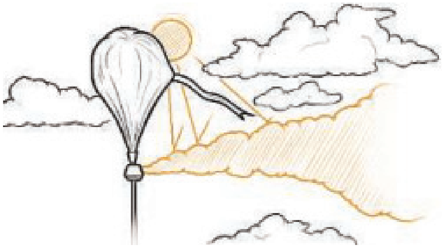

Marine cloud brightening
Ships would spray a fog of sea salt particles into low-lying clouds to brighten them, causing them to reflect more sunlight.

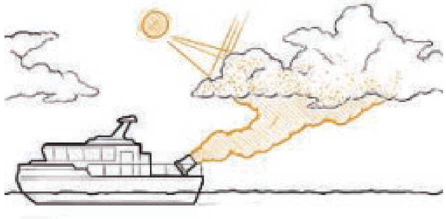

Marine carbon dioxide removal

Technologies that boost the removal of carbon dioxide from the atmosphere (gray arrows) by changing the chemistry of the ocean could help limit global warming.

Ocean fertilization
Adding iron sulfate or other nutrients would produce blooms of phytoplankton, which would absorb carbon dioxide and take it to the ocean floor when they die.

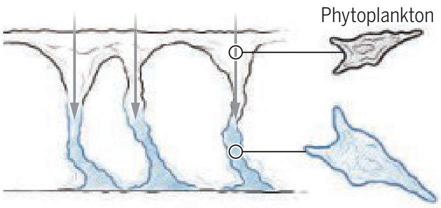

Ocean alkalinity enhancement
Alkaline minerals would be released from ships or outflow pipes, or spread along the beach to dissolve in the water, enhancing alkalinity and increasing carbon dioxide uptake.

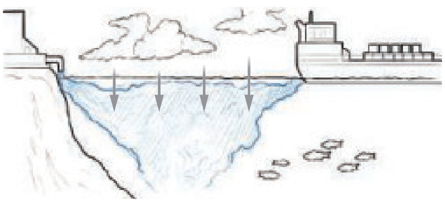

CREDITS: (GRAPHIC) A. FISHER/*SCIENCE*; (TIMELINE) M. HERSHER/*SCIENCE*

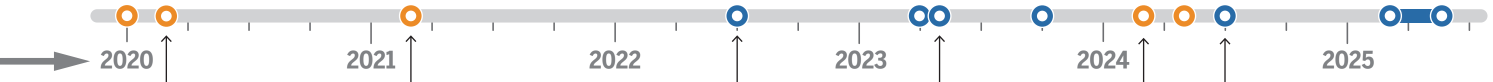

JANUARY 2020
New shipping regulations restrict sulfur emissions; later studies suggest ships' pollution had inadvertently been brightening clouds.

MARCH 2020
Australian scientists begin testing cloud-brightening equipment over the Great Barrier Reef.

MARCH 2021
SCoPEx cloud-brightening test flight in Sweden canceled after public protest.

JULY 2022
Vesta conducts an ocean alkalinity enhancement test, spreading olivine sand at Little Peconic Bay on Long Island with public support.

APRIL 2023
First public protest is held over Planetary Technologies's ocean alkalinity enhancement tests in Cornwall, England; the project is later put on hold.

MAY 2023
A NOAA special report suggests there is still potential in ocean iron fertilization.

OCTOBER 2023
Planetary Technologies field tests take place in Halifax, Canada.

MARCH 2024
The entire SCoPEx project is canceled.

MAY 2024
Alameda, California, cloud-brightening equipment test halted after council outcry.

JULY 2024
Vesta conducts a field test in Duck, North Carolina.

SPRING 2025
Planetary Technologies is conducting public engagement ahead of field trials in Vancouver, Canada.

to greater flexibility in people's viewpoints by defusing tensions and resolving objections, says Rob Bellamy, a social scientist at the University of Manchester. "People often display something that's called reluctant acceptance," he says. "They're actually quite happy for you to go ahead and do your experiments because they recognize through the deliberative process that … we're at a point now where we need to start considering these more controversial ideas."

Researchers, too, may learn something by listening: Local people know their area better than anyone, and might raise potential complications that aren't even on scientists' radars. Cardiff University social scientist Emily Cox says research on carbon removal in the United Kingdom consistently finds that no one is entirely opposed to it. Rather, people want to know whether the large arrays of energy-hungry machines might create competition for electric power, or increase housing pressures by occupying much-needed land.

"Not all technologies that are developed should go on to be deployed," Bellamy says. "I'm certain there will be some technologies that won't go on to be deployed for very good reasons. And public participation helps us feed into those decisions."

THE ATTEMPTS SO FAR HAVE ALSO taught some lessons about public engagement, including a sobering one: Success isn't guaranteed. Social license can be lost overnight, as Planetary Technologies learned on 1 March 2023, when it presented its research plan to people in the coastal town of Hayle, near the western tip of Cornwall in England.

Planetary was preparing to conduct a trial of ocean-alkalinity enhancement—a nascent carbon-removal method that entails changing the pH of seawater to accelerate CO_2 uptake from the atmosphere. After a long search for a test site, the Canadian startup had landed on St. Ives Bay, where it was to partner with a local utility company to add magnesium hydroxide to an outflow pipe. The chemicals would be discharged into the bay, where they would be stirred up by Atlantic Ocean currents.

The meeting was at capacity. CEO Mike Kelland asked whether anyone was worried about the climate crisis. The room bristled. Cornwall is known for its environmentalism; it's part of the region's identity.

When a member of the public asked what would happen if something went wrong, Kelland said Planetary would go out of business. It seemed to more than one attendee that he hadn't considered what might happen to the bay. They were concerned by what they saw as attempts to downplay the chemical the company was using by describing it as "an antacid for the sea."

The meeting was "dreadful," says Sue Sayer, a researcher who studies the seal colony in the bay and directs the nonprofit Cornwall Seal Group Research Trust. "They did 20 minutes for discussion, and then it was pasties and wine. And everyone refused to leave for pasties and wine and said, 'We're not leaving until you answer all our questions.'"

Within the month, St. Ives town councilor Senara Wilson Hodges had launched a protest movement, Keep Our Sea Chemical Free. "It was just feeling like something's being done to you with zero consultation," she says.

Kelland had obtained an environmental safety review. He'd been meeting stakeholders all over the region. Even the mayor of Hayle was in support. What he was missing was an understanding of the region's history and identity. In Cornwall, people have a reason to be skeptical of the use of chemicals in the sea. In 1967, a tanker foundering on the coast caused one of the world's largest oil spills, and in recent years beaches have been polluted by sewage discharged by the same utility company that was to be Planetary's partner. "I think a lot of it is doing your homework in advance and understanding what you're getting yourself into, which I don't think we did very well in that location," Kelland says.

Planetary's work in Cornwall never resumed; the trial planned in 2023 remains on hold.

THE CORNWALL PROJECT demonstrates that large-scale projects will only succeed if they're a good match for the local culture, social scientists say. "It's not all about engagement," Cox says. "It's also about place-technology fit. You've got to do the right thing in the right place, and you've got to understand the culture and history of the local area, and then work with that."

Fritz and others have found that people from the Global South are generally more open to solar geoengineering than those in the Global North, perhaps because they are presently bearing the brunt of climate impacts. Global South participants in Fritz's research were more likely to have experienced a major natural disaster in the past 3 years and to expect that climate change would harm them personally. Younger and more vulnerable groups, who likewise stand to be more affected by climate change, also tend to be more supportive of climate interventions.

At the same time, at least in the United States, people in more deprived areas may be more skeptical of untested technologies, as they are often still facing the consequences of prior industrial pollution. These regions—which often have existing infrastructure and an underemployed workforce—are good candidates for running operations once the technology has become more established, a 2023 document from Lawrence Livermore

National Laboratory concludes, whereas areas with higher socioeconomic status may be better suited for collaborating on early trials.

Who's in charge can also make a big difference. In a collaboration with Cox, Bellamy has found that people were more likely to say they'd oppose a hypothetical ocean alkalinity enhancement project if told it will be run by companies funded by private investment—but they're much more open to the technology when they're told it will be operated by local cooperatives. "The specifics matter," Nawaz says. "The specifics not only of the technology that you're talking about, but also what exactly that looks like in practice in a given ecosystem or geographic context."

Some projects have succeeded in finding the right fit. Planetary has received much more public support for field tests in its home of Halifax, Canada, than it did in Cornwall. The company has a trusted collaborator in Dalhousie, the local university, and its approach to public engagement has evolved. "We move at the speed of trust," says Diana Philip, a community-engagement practitioner who joined Planetary in September 2024. Now, she says, the company's first step is to try to understand a community and its needs. "We have to move from just informing to, 'How do we collaborate? How can this be more beneficial to you?'"

Meanwhile, in the U.S., a startup called Vesta was able to run its first field trial on New York state's Long Island after the local community invited the company to come and pitch the experiment to them. Vesta aims to boost marine carbon removal by spreading highly alkaline sand made of olivine, a greenish rock, in the tidal zone, where waves will erode it, releasing its alkalinity. Residents of the small community bordering what is arguably the world's first geoengineered beach are enthusiastic about their role in testing a potential climate solution.

DESPITE THE MISSTEPS in Alameda and Sweden, there is one place where solar geoengineering has broad public support. For the past 5 years, oceanographer Daniel Harrison of Southern Cross University has been leading a cloud brightening project off the northeastern coast of Australia—without local or international protest.

On a ship over the Great Barrier Reef, the scientists have been spraying a fine plume of saltwater particles into the sky, on and off, since 2020. When the tiny particles reach existing clouds, they attract water vapor and swell to 500,000 times their size, forming visible droplets.

The project aims to find out whether the salt particles will increase the clouds' reflectivity, bouncing more sunlight back into space before it hits the water. If it succeeds, the technology might cool the ocean enough to prevent the death of the Great Barrier Reef.

This is a big operation. Below decks are three shipping containers' worth of machinery to suck up seawater and generate saltwater spray. A second ship carries a lab that measures the size and distribution of the salt particles, while an aircraft, nicknamed Bruce, samples clouds to measure the particles that reach them. A drone takes on the role of a weather balloon, as these are banned in this highly regulated patch of ocean: Balloons burst, fall to the surface, and become oceanborne waste.

Protesters campaign against a planned trial by Planetary Technologies in England's St. Ives Bay.

PHOTO: LIZARDFISH TV

The Great Barrier Reef is traditionally owned by more than 70 Indigenous groups, and the researchers obtained permission from every group whose sea country overlapped with their proposed testing area. "We have a self-imposed rule," Harrison says. "We don't do any research on sea country without the express prior permission of traditional owners. We've never been refused for cloud brightening, but if we were, we'd have to go do it somewhere else."

The marine cloud brightening project also ran 1 year's worth of community engagement panels in Townsville, a nearby city, and invited the public to share ideas and concerns. "What we strive towards is codesigned research," Harrison says. "So it's not as simple as just going and asking them for permission. We ask for their input, we ask for their opinions, we invite them to be part of the process."

People identified risks that Harrison and his team hadn't considered. Would salt be carried over the crop fields of northeastern Queensland? Would it rust all the cars in Townsville? The researchers investigated, and learned that the amount of salt they produced was minuscule compared with the quantity that naturally blows in from the sea.

In 2024, an independent survey of the project found a majority of people Australia-wide support it, a view Harrison attributes to the project's clear purpose and limited scope. "We're not just doing science for the sake of doing science. We're doing science to try and find solutions for the reef."

By winning over the public, Harrison's effort has become the first solar geo-engineering project to stage a real world test, 3 decades after cloud brightening was proposed. "We're the first ones to ever go and test anything outside," he says.

THOUGH RESEARCH POINTS the way, scientists agree there's no recipe book for climate-tech engagement that can be used for each new project. But some structural changes would make the process a whole lot easier, social scientists say. "We tend to say, 'There's a project here, let's go and talk to people about what they want,'" Nawaz says. "The project level is a deeply flawed way to do engagement. We need to be thinking about what the impacts are at scale."

Instead of communities being consulted over and over again for different climate engineering projects, Nawaz proposes that an independent authority could oversee a single consultation across an entire region, to get a bird's-eye picture of the area's history, culture, ecosystems, and resources, and figure out—with public input—the types of projects that would best suit the area. Geo-engineering tests could be combined with the development of other climate-related infrastructure, such as the additional renewable energy sources that will be required by some technologies.

One thing is clear: Effective technology and good intentions will never be enough to get climate engineering off the ground. "There's no point having a technological solution if you don't have the social license to use it," Harrison says. "If the community and the public don't support this, then it's never going to happen." ■

Rebekah White is a science journalist based in New Zealand.

eppendorf
& Science
PRIZE FOR
NEURO
BIOLOGY

2024 Winner
Laura Seeholzer, Ph.D.
University of California San Francisco,
School of Medicine, USA

For research on airway
neuroendocrine cells responding
to external threats

Application Deadline
June 15, 2025

Call for Entries 2025

Eppendorf & Science Prize for Neurobiology
The annual Eppendorf & Science Prize for Neurobiology is an international prize which honors young scientists for outstanding neurobiological research based on methods of molecular, cellular, systems, or organismic biology. If you are 35 years of age or younger and doing great research, now is the time to submit an entry for this prize.
It’s easy to apply! Write a 1,000-word essay and tell the world about your work.

eppendorf.com/prize

As the winner, you could be next to receive
> Prize money of US$25,000
> Publication of your work in *Science*
> Full support to attend the Prize Ceremony held in conjunction with the Annual Meeting of the Society for Neuroscience in the USA
> 10-year AAAS membership and online subscription to *Science*
> Complimentary products worth US$1,000 from Eppendorf
> An invitation to visit Eppendorf in Hamburg, Germany

eppendorf
Science
AAAS

AAAS® and Science® are registered trademarks of the American Association for the Advancement of Science, USA. Eppendorf® and the Eppendorf Brand Design are registered trademarks of Eppendorf SE, Germany.
All rights reserved, including graphics and images. Copyright © 2025 by Eppendorf SE. Photography: Brian Carey, figMedia

A long-tailed macaque uses a stone to open a shell (Koram Island, Thailand), an example of behavioral culture in wild animals.

PHOTO: CYRIL RUOSO/NPL/MINDEN PICTURES

ANIMAL BEHAVIOR

Saving the cultural legacy of wild animals

Loss of biodiversity threatens the study of tool use and other cultural behaviors in animals

By **Ammie K. Kalan**[1] *and* **Lydia V. Luncz**[2]

Biodiversity is increasingly declining in response to the effects of human activities on Earth's climate, geological processes, and ecosystems. This includes the degradation of behavioral and cultural diversity of animals (*1*–*4*). Cultural behaviors—the activities and skills acquired through social learning—can contribute to a species' ability to adapt to environmental changes, which can enhance the overall health and functionality of ecosystems (*5*). Some cultural behaviors involve tool use to access resources such as food, water, and mates, thereby contributing to the long-term survival of a species. These tool-use behaviors leave behind physical artifacts and sites that provide material evidence of nonhuman cultural activity (*6*). Comparative research on diverse animal material cultures can offer insights into the evolutionary origins of behaviors and improve comprehension of human evolution. However, a steep decline in population sizes worldwide is threatening progress in understanding the behavioral diversity of wild animals.

Some behavioral diversity observed in wild animals (including whales, dolphins, and some birds) has been identified as cultural, whereby culture is broadly defined as behavioral traditions that are learned and transmitted across generations through social means such as observing, copying, and interacting with others (*5*). Animals with rich cultural repertoires are better equipped to innovate and adapt, using learned behaviors to exploit new resources or navigate new challenges (*4*). In this way, cultural diversity acts as a form of ecological insurance, enabling populations to respond to unpredictable changes in their surroundings. This has broadened our understanding of the capacity and importance of behavioral and cultural plasticity in responding to major threats imposed by humans (*5*). Moreover, examining how cultural practices vary across species can provide a deeper understanding of the similarities and differences in social behaviors and cognitive abilities between species, including humans.

Identifying culture in wild animals can be challenging because of the limitations of

---

[1] GAB Lab, Department of Anthropology, University of Victoria, Victoria, BC, Canada. [2] Technological Primates Research Group, Max Planck Institute for Evolutionary Anthropology, Leipzig, Germany. Email: lydia_luncz@eva.mpg.de

observational methods and diverse ways in which culture manifests in different species. Some behaviors may be subtle and harder to recognize and define, such as play and communication signals. Only through comparisons across multiple groups of the same species can cultural diversity be understood and socially learned behaviors be teased apart from largely genetically driven responses (*5*). Technological advances in applied animal behavior research, such as camera traps, audio sensors, and genetic analyses, have effectively documented cultural behavior in animals (*5*, *7*, *8*). Cultural traditions in animals include variable socially transmitted behaviors such as the songs of humpback whales, prey preferences of orcas, and migratory routes of bighorn sheep (*5*). These cultural behaviors contribute to the social cohesion and resilience of animal societies, enhancing their collective ability to thrive in diverse environments (*4*). However, one of the most reliable ways to identify behavioral and cultural diversity focuses on tool use because of its conspicuous and tangible nature. Tool use leaves behind physical artifacts that can be examined to reconstruct an animal's behavior as well as facilitate the identification of cultural variation such as differences in tool selection, function, or frequency of use (*3*, *5–8*).

Habitual tool use is rare in animals (*9*). Where it does occur, most tools are made from vegetation that is ephemeral because of its organic nature. Only a few nonhuman species regularly use durable stone material as tools. For example, stone-tool use is observed in otters and seabirds to break open various marine prey (*9*). Some of the closest living primate relatives to humans exhibit myriad ways in which stones are used as hammers, anvils, and sometimes for sociocommunicative purposes (*3*, *6*, *7*, *9–11*). Yet much of the stone-tool use observed in nonhuman primates is for percussive foraging behaviors such as pounding open various nuts and shellfish (*3*, *6*, *7*, *10*). Three primate taxa demonstrate habitual stone-tool use in the wild, with evidence for social learning and culture: chimpanzees (*Pan troglodytes verus*) in West Africa, capuchins (*Sapajus libidinosus*, *Cebus capucinus*) in Central and South America, and macaques (*Macaca fascicularis*) in Southeast Asia. Unlike most animal tool use, these stone-tool behaviors leave behind a high concentration of durable artifacts because of their repeated use at the same location and extensive modifications of the raw material (*6*). Over time, these concentrations of artifacts create conspicuous technological landscapes that are amenable to archaeological inquiry (*3*, *10*, *12*, *13*). Moreover, the use of archaeological methods has shown that primate tool-use behavior demonstrates intergenerational transmission of cultural knowledge that has existed for thousands of years (*12*, *13*). Yet the very existence of these material cultures is under threat, given that many nonhuman primates face extinction.

By examining nonhuman primates as living models of an evolutionary history shared with humans, it is possible to gain new insights into the origins of human technology and culture. Nonhuman primate material cultures, in combination with observed behavior, provide an unprecedented opportunity to interpret the static hominin record (stone tools of extinct human species), where stone material is the only evidence left to infer past behavior (*6*). Recent discoveries show that nonhuman primate stone artifacts can challenge long-standing interpretations of tool use in hominins. For instance, the first production of sharp cutting stone flakes attributed to human ancestors was thought to require advanced cognitive skills, foresight, and understanding of fracture mechanics and material properties. However, recent research shows that nonhuman primates unintentionally produce stone flakes that are indistinguishable from the tools of early human ancestors (*14*). These findings raise questions about the detection of intentional behavior in hominins but also highlight potential misinterpretations of human evolutionary history. Similarly, the material remains of anvils used by marine animals for foraging indicate that interpreting coastal archaeological assemblages as evidence solely of human activity should be taken with caution (*15*). Hence, it is critical to confidently differentiate archaeological remains as nonhuman or human in origin. Substantial comparative research both within and across species should clarify those features that identify material culture as nonhuman. It should also advance understanding of the social and environmental factors that may promote tool use as a convergent evolutionary adaptation.

Tools are part of present-day cultural landscapes and ecological niches of technological species. The presence of the tools along with specific sites where these tools are used help to encourage cultural transmission within and across generations by facilitating opportunities to socially learn the behavior (*6*, *12*, *13*). Animals that use tools are therefore part of ecosystems where the physical removal of artifacts for research purposes could endanger the very behavior we seek to understand. Although temporary removal of tools may be required for research purposes, complete removal and interference with physical materials should be limited, given the potential impact on the cultural behavior of these wild animals. Digital solutions are required, particularly when raw material sources may be limited in the wild. Visualization technologies, such as portable laser scanning, photogrammetry, and three-dimensional modeling software, have revolutionized the ability to create digitized collections of artifacts. For example, it is now possible to record, analyze, and preserve tools digitally with high resolution (*14*). Digital collections of animal material cultures further facilitate accessibility, scientific transparency, and future opportunities for collaborative comparative research across space, time, and species.

Presently, there is no concentrated effort to explicitly preserve or protect animal material culture beyond its fortuitous inclusion within a protected area or national park. To secure the intergenerational transmission of cultural behaviors, tool-using animals must continue to have access to the materials needed to carry out these behaviors. Protecting the living cultural landscapes of animal stone-tool-use sites involves preserving the environments where these behaviors occur and recognizing the intrinsic value of animal cultures (*1*, *2*, *4*). This not only expands our knowledge base of animal behavior and evolution but also contributes to the broader goal of preserving biodiversity and promoting more inclusive conservation strategies. For example, the United Nations Convention on the Conservation of Migratory Species approved Concerted Actions to specifically protect chimpanzee and sperm whale cultures (*4*). This reflects the growing importance of incorporating cultural and social knowledge of wildlife into conservation efforts (*1*, *2*, *5*).

With the continued rates of human disturbance to the natural world, there is no certainty that animals and their cultural legacies will persist. It is paramount to acknowledge that cultural heritage is not limited to humans but extends to the material culture of other animals too. Humans are responsible for protecting and preserving animal cultures not only for research and education but also for their contributions to a richer and more holistic understanding of humans' shared evolutionary heritage with nonhumans. ■

REFERENCES AND NOTES

1. H. S. Kühl *et al.*, *Science* **363**, 1453 (2019).
2. P. Brakes *et al.*, *Science* **363**, 1032 (2019).
3. A. Presotto *et al.*, *Int. J. Primatol.* **41**, 596 (2020).
4. P. Brakes *et al.*, *Proc. R. Soc. London Ser. B* **288**, 20202718 (2021).
5. A. Whiten, *Science* **372**, eabe6514 (2021).
6. A. Pascual-Garrido *et al.*, *Am. J. Biol. Anthropol.* **183**, e24835 (2024).
7. L. V. Luncz *et al.*, *Curr. Biol.* **22**, 922 (2012).
8. C. Boesch *et al.*, *Nat. Hum. Behav.* **4**, 910 (2020).
9. R. W. Shumaker *et al.*, *Animal Tool Behavior: The Use and Manufacture of Tools by Animals* (JHU Press, 2011).
10. L. V. Luncz *et al.*, *eLife* **8**, e46961 (2019).
11. A. K. Kalan *et al.*, *Biol. Lett.* **15**, 20190747 (2019).
12. T. Falótico *et al.*, *Nat. Ecol. Evol.* **3**, 1034 (2019).
13. J. Mercader *et al.*, *Proc. Natl. Acad. Sci. U.S.A.* **104**, 3043 (2007).
14. T. Proffitt *et al.*, *Sci. Adv.* **9**, eade8159 (2023).
15. J. M. Erlandson, M. L. Moss, *Am. Antiq.* **66**, 413 (2001).

10.1126/science.adj3716

CELL BIOLOGY

Archaea go multicellular under pressure

A microbe from the Dead Sea switches to a tissue-like form when compressed

By **Eva K. Pillai**[1,2,3] *and* **Thibaut Brunet**[3]

During the 3.5-billion-year history of life on Earth, some events, like the origin of life, of the eukaryotic cell, and of animals, occurred only once; however, the transition to multicellularity happened numerous times independently in slightly different ways. A recent census counted 45 independent such events in eukaryotes (*1*)—three of which gave rise to the respective ancestors of animals, land plants, and fungi (*2*). By contrast, multicellularity seems to be rare in Archaea—a group of prokaryotic microbes from which eukaryotes originated (*3*). On page 109 of this issue, Rados *et al.* (*4*) describe multicellular development in an archaeon, *Haloferax volcanii*, with an unexpected twist: Multicellularity is induced by mechanical pressure.

H. volcanii is a member of Haloarchaea, a group of archaea that are hypersaline extremophiles. This species was isolated from the Dead Sea and has been extensively studied for its highly variable cell shape, which ranges from triangles to rods and disks (*5*), and for its deformability in response to external forces: *H. volcanii* is not encased in a rigid cell wall but, like almost all archaea, has a flexible protein coat called an S-layer (*3*). Usually, *H. volcanii* undergoes normal binary cell division to produce two separate daughter cells. Rados *et al.* confined single-cell *H. volcanii* under an agar pad and found that they stopped dividing but continued to grow and replicate their DNA. This resulted in large, dome-shaped structures with genetic material housed within multiple nucleoids. After 12 hours, these cells underwent fragmentation into multiple smaller cells (cellularization) by growth and fusion of membranes from the periphery to the center. This resulted in a cellular polygonal network that the authors described as “tissue-like.” Notably, cells within tissue-like structures had two phenotypes: tall and narrow in the center of the dome, and flatter and broader at the periphery (see the figure).

Through genetic and biophysical manipulations, Rados *et al.* showed that this multicellular development involved repurposing of the *H. volcanii* cytoskeleton. Notably, the archaeal homolog of the eukaryotic cytoskeletal protein actin formed vertical “pillars” that were required for the tissue-like structures to gain their full height and resist compression. By contrast, the cell division protein FtsZ (a prokaryotic homolog of the cytoskeletal protein tubulin), although necessary for membrane constriction in ordinary cell division, was not needed for cellularization (*6*). Instead, cellularization was triggered when membrane tension (measured using membrane fluidity as a proxy) crossed a critical threshold.

The process observed by Rados *et al.* resembles cellularization of coenocytes in the multicellular development of some eukaryotes. Coenocytes are multinucleated structures enclosed by a single membrane that form by nuclear proliferation without cell division. They occur in fly embryos, in fungi, and in some unicellular relatives of animals (*7*). By contrast, no such structure seems to have been previously reported in bacteria or Archaea, with the most comparable phenomenon perhaps being the septation of coenocytic filaments named hyphae in the bacterium *Streptomyces* (*8*). Is tissue-like development in *H. volcanii* a passive effect of confinement, or does it involve a dedicated mechanotransduction pathway? Several observations made by Rados *et al.* suggest the latter. Notably, expression of volactin is upregulated under compression and contributes to active cellular remodeling and the mechanical resistance of these structures.

What could be the function of this dramatic response to confinement? Rados *et al.* show that haloarchaeal species that cannot undergo tissue-like development show reduced viability under confinement and little ability to escape into nonconfined spaces. This suggests that ordinary cell division mechanisms are inoperant or inefficient under confinement—perhaps owing to geometrical constraints—and that coenocyte-like growth followed by cellularization might be activated as an alternative proliferation mechanism. Whether “tissue”-forming and non-“tissue”-forming archaea inhabit different natural environments or have different

Adapting to confinement

Uncompressed *Haloferax volcanii* undergoes repeated rounds of binary cell division, which require the cell division protein FTsZ and result in individual daughter cells. When compressed, *H. volcanii* ceases cell division but continues to grow and replicate its DNA, producing a coenocyte-like cell. Membranes then grow inward from the edge of the cell to create compartments, resulting in a tissue-like polygonal network of smaller cells: tall, thin scutoid cells in the center and flatter, broader peripheral cells. The cytoskeletal protein volactin forms pillars that support these tissue-like structures, but FtsZ is not required.

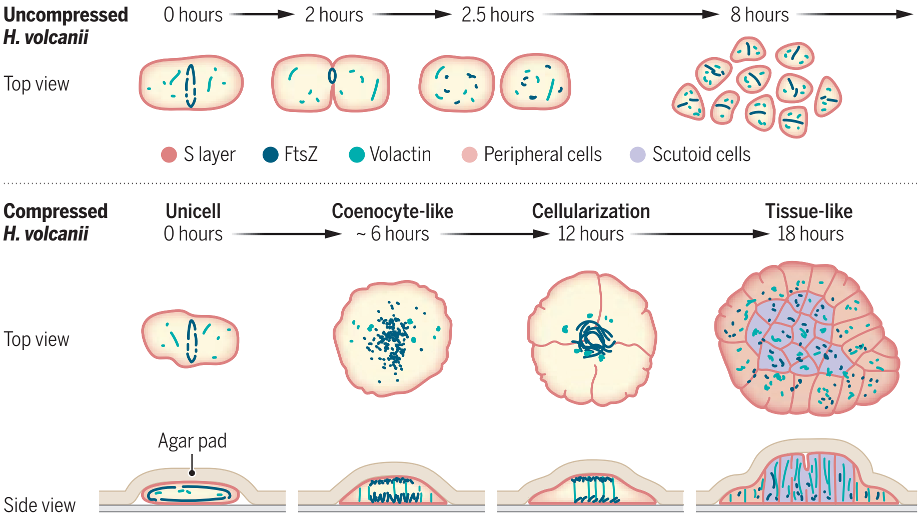

GRAPHIC: K. HOLOSKI/*SCIENCE*

---

[1]Cell Biology and Biophysics Unit, European Molecular Biology Laboratory, Heidelberg, Germany. [2]Developmental Biology Unit, European Molecular Biology Laboratory, Heidelberg, Germany. [3]Evolutionary Cell Biology and Evolution of Morphogenesis Unit, Institut Pasteur, Université Paris-Cité, CNRS UMR3691, Paris, France. Email: thibaut.brunet@pasteur.fr

genetic toolkits remains unclear. Notably, *H. volcanii* cells naturally contain many copies of their genome (*9*) within a diffuse nucleoid (*5*). In addition, the plane of normal cell division seems to be determined by a self-organized reaction-diffusion mechanism (*5*). Such features might facilitate radical evolutionary remodeling of cell division under geometric constraints.

If the suppression of cell division and the subsequent cellularization is an active and adaptive response to confinement, the same may not be true of maintenance of the final tissue-like morphology. Although it could involve specific cell-cell or cell-matrix adhesion (as in animals and plants), polygonal geometries can also passively arise through packing constraints, as seen in the amoeba *Naegleria* (*10*). This interpretation aligns with hypotheses that suggest that generic physical effects had an important role at the evolutionary beginnings of multicellular morphogenesis (*11*). Recent research supports this view, showing that multicellular geometry in "simple" forms, such as the microscopic alga *Volvox,* might emerge spontaneously from randomness in cell packing (*12*). These observations reinforce the concept that the evolution of multicellularity lies on a continuum, where the formation of multicellular groups resulting from simple biophysical changes preceded the emergence of heritable collective adaptations during the evolution of integrated multicellular organisms (*13*).

The discovery of tissue-like development in *H. volcanii* also raises questions. For example, where might *H. volcanii* naturally encounter conditions that induce multicellularity? Furthermore, whether the two final cell phenotypes express different genes remains unclear. With this study, Rados *et al.* have shown that even well-studied organisms can be surprising and that humble archaea can display unexpected resourcefulness under pressure. ■

REFERENCES AND NOTES

1. Ł. Lamża, *Biol. Rev. Camb. Philos. Soc.* **98**, 2188 (2023).
2. T. Brunet, N. King, *Dev. Cell* **43**, 124 (2017).
3. M. van Wolferen, A. A. Pulschen, B. Baum, S. Gribaldo, S.-V. Albers, *Nat. Microbiol.* **7**, 1744 (2022).
4. T. Rados *et al.*, *Science* **388**, 109 (2025).
5. J. C. Walsh *et al.*, *Mol. Microbiol.* **112**, 785 (2019).
6. H. Schiller *et al.*, *Nat. Commun.* **15**, 1414 (2024).
7. B. McCartney, O. Dudin, *Curr. Opin. Cell Biol.* **80**, 102157 (2023).
8. D. Claessen, D. E. Rozen, O. P. Kuipers, L. Søgaard-Andersen, G. P. van Wezel, *Nat. Rev. Microbiol.* **12**, 115 (2014).
9. S. Breuert, T. Allers, G. Spohn, J. Soppa, *PLOS ONE* **1**, e92 (2006).
10. E. N. Willmer, *Cytology and Evolution* (Acad. Press, ed. 3, 1970).
11. S. A. Newman, G. B. Müller, *J. Exp. Zool.* **288**, 304 (2000).
12. T. C. Day *et al.*, *eLife* **11**, e72707 (2022).
13. C. J. Rose, K. Hammerschmidt, *Front. Ecol. Evol.* **9**, 730714 (2021).

10.1126/science.adw6689

CHEMISTRY

Catalysis at the crossroads

Homogeneous and heterogeneous catalysis work concurrently in a chemical process

By **Cathy L. Tway**[1] and **Sorin V. Filip**[2]

Approximately 90% of industrial chemical products use catalysts during manufacturing to speed up a reaction, minimize energy consumption, and reduce waste products (*1*). They are classified into two main types. Homogeneous catalysts that are in the same phase as the reactants decrease the activation energy by direct binding. By contrast, heterogeneous catalysts are in a different phase than the reactants and work by surface reactions (*2*). Both mechanisms have long been considered distinct from each other. Consequently, catalysis discovery efforts do not attempt to encompass both homogeneous and heterogeneous catalysts concurrently. On page 49 of this issue, Harraz *et al.* (*3*) report an interconversion between homogeneous and heterogeneous catalysts within the same catalytic cycle of vinyl acetate synthesis. This finding could usher in new approaches for designing catalytic processes that combine the high efficiency of homogeneous catalysts with the facile operation of heterogeneous catalysts for broad industrial applications.

Vinyl acetate is an industrial intermediate that is widely used in applications such as coatings and adhesives (*4*). For more than five decades, this organic compound has been primarily produced from ethylene, acetic acid, and oxygen (reactants) using a heterogeneously catalyzed vapor-phase process (*5*). In one proposed mechanism for vinyl acetate production, the reactants are coadsorbed and activated on a supported palladium heterogeneous catalyst, subsequently forming a palladium-ethylene-acetate intermediate. The resulting vinyl acetate is released, and the catalyst surface is oxidized again for further reactions. Another frequently proposed mechanism suggests that under reaction conditions, a liquid film that is developed on the catalyst surface causes oxidized palladium to dissolve then function as a homogeneous catalyst. Thus, the reaction proceeds through a homogeneous-catalyzed pathway rather than a heterogeneous one (*6*). Similar dissolu-

---

[1]bp America, Chicago, IL, USA. [2]BP p.l.c., Pangbourne, UK. Email: cathy.tway@bp.com; sorin.filip@uk.bp.com

Infinite loop of homogeneous-heterogeneous catalysis

Solid palladium (Pd^0) is activated by oxygen gas to produce Pd^{2+} through a heterogeneous catalysis scheme. The Pd^{2+} then goes into solution in the liquid acetic acid film and catalyzes the reaction between acetic acid and ethylene by a homogeneous mechanism to produce vinyl acetate. The deactivated Pd^0 intermediate regenerates into active sites of solid Pd for subsequent catalysis reactions.

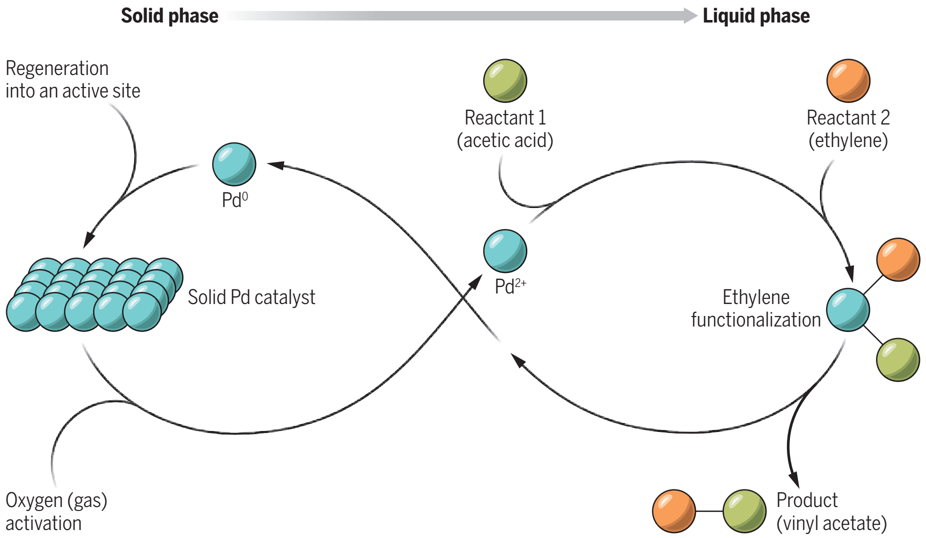

GRAPHIC: A. FISHER/SCIENCE

tion of palladium from a metal-supported catalyst into the surrounding solution resulting in homogeneous catalysis has also been observed in chemical reactions other than vinyl acetate (*7*) and with metal catalysts other than palladium (*8*). Given the fast nature of catalytic reactions, it is difficult to identify the catalyst phase in play during the reaction, even with a battery of characterization techniques (*8*).

Harraz *et al.* performed a rigorous electrochemical analysis to unravel a dynamic interconversion between heterogeneous and homogeneous palladium catalyst phases in the vinyl acetate reaction. Metallic palladium nanoparticles (heterogeneous) were corroded in a liquid acetic acid film to form oxidized palladium species (homogeneous) that catalyzed the reaction of ethylene and acetic acid to form vinyl acetate. After the catalysis, molecular palladium was regenerated into metallic palladium active sites for subsequent reactions. This bifunctional nature of palladium catalysts with both homogeneous and heterogeneous phases promoted a collaboration between the two catalysis schemes within the same reaction cycle (see the figure). A similar bifunctional system was described between two separate heterogeneous catalysts (*9*). A physical mixture of separate palladium and gold heterogeneous catalysts cooperatively enhanced the removal of hydrogen atoms from an alcohol and the subsequent oxidation of the aldehyde intermediate. However, both palladium and gold heterogeneously catalyzed the reaction, and the potential for a heterogeneous-homogeneous cooperative effect was not proposed (*9*). The findings of Harraz *et al.* are distinctive because they demonstrate how homogeneous and heterogeneous catalysts can work simultaneously within the same reaction system.

> **“…collaboration between catalysis communities has often driven the development of sustainable technologies.”**

An interesting observation of Harraz *et al.* is the balance between interconversion rates of the homogeneous and heterogeneous catalysis mechanisms. This prevents the regenerated palladium from agglomerating, which could deactivate the catalyst. However, the performance of liquid-phase catalysts depends on various factors such as catalyst composition, substrate material, and reaction conditions (*10*). In addition, the liquid film must be uniformly spread on the support to allow efficient mass transfer between reactants and products (*11*). Thus, detailed characterization of the relationship between the acetic acid film and catalytic activities for vinyl acetate synthesis is needed. For example, advanced methods such as high-temperature and high-pressure magic angle spinning nuclear magnetic resonance (*12*) could detail the evolution of the liquid film under industrially relevant reaction conditions.

Industries are seeking catalytic solutions to improve sustainability and energy efficiency. For example, chemical sectors are moving from batch production to continuous flow processes in which products are simultaneously generated and removed from an ongoing chemical reaction. This can reduce operation costs by more than 40% and speed up manufacturing (*13*). However, dissolution and loss of metal from heterogeneous catalysts leading to catalytic deactivation and product contamination challenge the adoption of continuous processes (*14*). Integrating techniques to balance the homogeneous-heterogeneous interconversion processes could help overcome these issues. Moreover, computational simulations could help identify other catalytic reactions that benefit from a bifunctional scheme (*15*). Cross-disciplinary collaboration between catalysis communities has often driven the development of sustainable technologies. As demonstrated by Harraz *et al.*, revisiting mature technologies with new approaches could yield valuable insights. ■

REFERENCES AND NOTES

1. M. W. Yoneyama, *Catalysts: Petroleum and Chemical Process* (SRI Consulting, 2010).
2. J. Hagen, *Industrial Catalysis: A Practical Approach* (Wiley, 2015).
3. D. M. Harraz, K. M. Lodaya, B. Y. Tang, Y. Surendranath, *Science* **388**, eads7913 (2025).
4. H. A. Wittcoff, B. G. Reuben, J. S. Plotkin, *Industrial Organic Chemicals* (Wiley, ed. 2, 2004).
5. L. Hornig, H. Fernholz, H.-J. Schmidt, F. Wunder, T. Quadflieg, “Process for preparing vinyl acetate,” US Patent 3658888 (1972).
6. C. R. Reilly, J. J. Lerou, *Catal. Today* **41**, 433 (1998).
7. M. Pagliaro, V. Pandarus, R. Ciriminna, F. Béland, P. Demma Carà, *ChemCatChem* **4**, 432 (2012).
8. J. A. Widegren, R. G. Finke, *J. Mol. Catal. Chem.* **198**, 317 (2003).
9. X. Huang *et al.*, *Nature* **603**, 271 (2022).
10. W. D. Provine, P. L. Mills, J. J. Lerou, in *11th International Congress on Catalysis – 40th Anniversary*, J. W. Hightower *et al.*, Eds. (Elsevier, 1996), pp. 191–200.
11. M. Haumann, P. Wasserscheid, in *Applied Homogeneous Catalysis with Organometallic Compounds*, B. Cornils *et al.*, Eds. (Wiley, 2018), chap. 14.
12. A. Chamas *et al.*, *Magn. Reson. Imaging* **56**, 37 (2019).
13. R. L. Hartman, *Curr. Opin. Chem. Eng.* **29**, 42 (2020).
14. R. Ciriminna, M. Pagliaro, R. Luque, *Green Energy Environ.* **6**, 161 (2021).
15. J. Jover, M. García-Ratés, N. López, *ACS Catal.* **6**, 4135 (2016).

10.1126/science.adw5529

BIOMEDICINE

Beyond wear and tear at the joint

Bile acid metabolism meets glucagon-like peptide 1 signaling in osteoarthritis

By **Chuan-ju Liu**

Osteoarthritis is the most prevalent joint disorder worldwide and a leading cause of chronic pain and disability in older adults. Traditionally, it has been regarded as a degenerative disease driven by mechanical wear and tear (*1*, *2*). However, emerging evidence highlights the role of metabolic pathways in the pathogenesis of osteoarthritis (*3*, *4*). For instance, obesity predisposes individuals to osteoarthritis even in non–weight-bearing joints, indicating that chronic metabolic inflammation and altered lipid metabolism—rather than mechanical overload alone—can drive cartilage breakdown. However, mechanisms underlying the links between metabolism and disease progression remain poorly understood, limiting the ability to develop new therapeutic approaches. On page 48 of this issue, Yang *et al.* (*5*) report compelling evidence for a gut-joint axis involving bile acid metabolism and glucagon-like peptide 1 (GLP-1) signaling in osteoarthritis development, advancing the understanding of osteoarthritis pathogenesis and opening new avenues for therapy.

Historically, osteoarthritis research has focused on cartilage degeneration resulting from mechanical stress (*1*, *2*). However, systemic factors, such as lipid metabolism and gut-derived metabolites, are gaining increasing attention in this disease (*6*, *7*). Yang *et al.* observed that disruptions in bile acid metabolism—specifically reduced amounts of glycoursodeoxycholic acid (GUDCA)—drive osteoarthritis progression. GUDCA supplementation ameliorated osteoarthritis progression in mice primarily by inhibiting intestinal farnesoid X receptor (FXR). FXR regulates the balance of bile acid synthesis, conjugation, and transport as well as lipid and glucose

---

Department of Orthopaedics and Rehabilitation, Yale School of Medicine, New Haven, CT, USA. Email: chuan-ju.liu@yale.edu

metabolism. FXR blockade or deletion in intestinal stem cells enhanced stem cell proliferation and led to an increased number of intestinal enteroendocrine cells that produce GLP-1 (called L cells) and increased serum GLP-1 concentration. GLP-1 is secreted by L cells, enters the circulation, and reaches the joints. It likely protects against osteoarthritis by regulating cells bearing the GLP-1 receptor, including cartilage-producing chondrocytes, synovial fibroblasts, and infiltrating immune cells such as macrophages (see the figure). Given the substantial differences in the number of these cell types in the joints, their contributions to osteoarthritis warrant further investigation in mouse models that are genetically engineered to lack the GLP-1 receptor in these cells.

The gut-joint axis influences osteoarthritis

In the mouse gut, *Clostridium bolteae* influences bile acid metabolism, with ursodeoxycholic acid (UDCA) and glycoursodeoxycholic acid (GUDCA) inhibiting farnesoid X receptor (FXR) in intestinal stem cells. This promotes their proliferation and differentiation into L cells, which secrete glucagon-like peptide 1 (GLP-1). GLP-1 reaches the joints through blood vessels, where it ameliorates osteoarthritis by interacting with GLP-1 receptor (GLP-1R)–bearing cells, including chondrocytes and potentially synovial fibroblasts and infiltrating immune cells.

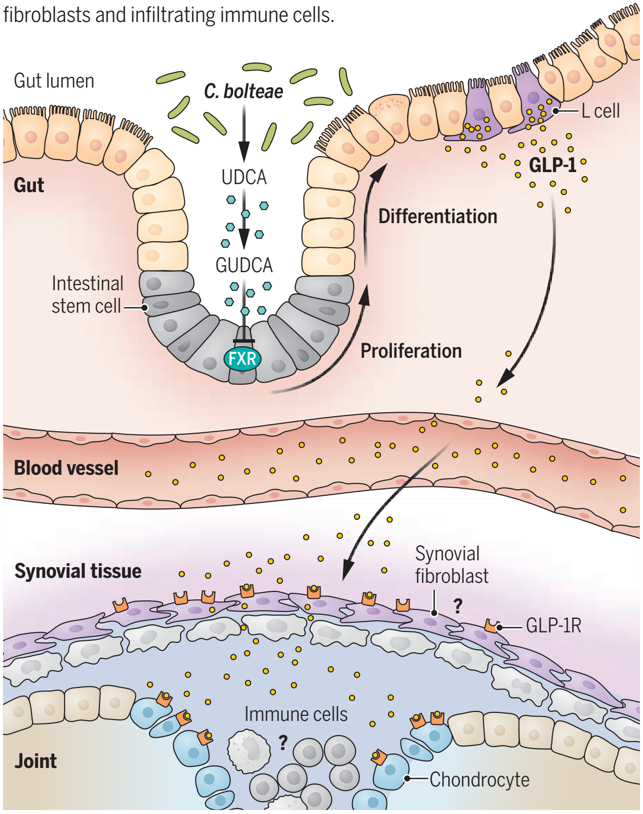

GRAPHIC: K. HOLOSKI/*SCIENCE*

The study of Yang *et al.* also highlights the role of the bacterium *Clostridium bolteae*, a constituent of the gut microbiome, in FXR signaling and GLP-1 modulation. Using fecal microbiota and metabolomic profiling, the authors demonstrate that in mice, *C. bolteae* disrupts bile acid balance, affects GLP-1 secretion, and alters osteoarthritis progression. These findings underscore the intricate connection between the gut microbiome and joint disease—the so-called gut-joint axis. Moreover, Yang *et al.* provide strong preclinical evidence that supplementation with ursodeoxycholic acid (UDCA), a precursor of GUDCA and a clinically approved drug for liver disorders, has protective effects on joints by restoring bile acid composition and increasing GLP-1 amounts, thus reducing joint inflammation and cartilage degradation. Given that UDCA is already in clinical use, these findings offer an exciting path for clinical translation (*8*). Notably, Yang *et al.* show that supplementation with UDCA was associated with a reduced risk of osteoarthritis-related joint replacement in a cohort of 5972 individuals.

GLP-1 receptor agonists, such as semaglutide and liraglutide, are widely used for treating diabetes and obesity (*9*, *10*). Recent studies have suggested a potential role in treating osteoarthritis, with some evidence that semaglutide alleviates osteoarthritis-related pain (*11*, *12*). However, the effects on cartilage integrity and joint structure are unclear. Given the strong preclinical and clinical evidence linking GLP-1 signaling to osteoarthritis protection, large-scale randomized controlled trials should be conducted to evaluate whether GLP-1 receptor agonists can not only reduce symptoms but also slow disease progression.

Although UDCA has shown promise in mitigating osteoarthritis progression in preclinical and observational human studies, determining its long-term safety and efficacy in osteoarthritis patients is imperative. Key questions include what the optimal dosing and duration of UDCA treatment for osteoarthritis should be, whether UDCA has any unintended metabolic effects on joint tissues, and whether certain patient subgroups are more likely to benefit owing to the composition of their gut microbiome. Future studies should incorporate longitudinal clinical trials and metabolomic profiling to assess interindividual variability in UDCA response and to refine patient selection criteria.

The concept of a gut-joint axis raises intriguing possibilities beyond osteoarthritis. Could a similar gut-mediated GUDCA–GLP-1 axis contribute to other joint disorders, such as rheumatoid arthritis or spondyloarthritis (*13*, *14*)? The interplay among gut microbiota, bile acids, glucose homeostasis, and systemic immune responses is an emerging field that may uncover common therapeutic targets across multiple musculoskeletal diseases. If intestinal FXR inhibition and GLP-1 modulation regulate joint inflammation in general, then targeting these pathways may offer new therapeutic opportunities for rheumatoid arthritis and other systemic inflammatory diseases and conditions.

The findings of Yang *et al.* also raise the possibility that *C. bolteae* and other gut microbiome constituents that stimulate the gut-joint axis might be suitable for development into live biotherapeutic products for joint diseases, such as osteoarthritis. However, the gut microbiome is very complex, and numerous microbial-derived metabolites likely affect joint health and inflammation. Future research using comprehensive multi-omics approaches is warranted, including metagenomics to identify other microbial species involved in osteoarthritis pathogenesis; metabolomics to analyze bile acid and GLP-1–related metabolic pathways; and transcriptomics to assess the impact of gut-derived signals on joint cells, particularly chondrocytes and synovial cells. ■

REFERENCES AND NOTES

1. M. Kloppenburg, M. Namane, F. Cicuttini, *Lancet* **405**, 71 (2025).
2. J. N. Katz, K. R. Arant, R. F. Loeser, *JAMA* **325**, 568 (2021).
3. W. Fu *et al.*, *Nature* **625**, 557 (2024).
4. R. Zhou, W. Fu, D. Vasylyev, S. G. Waxman, C. J. Liu, *Nat. Rev. Rheumatol.* **20**, 545 (2024).
5. Y. Yang *et al.*, *Science* **388**, eadt0548 (2025).
6. E. Sanchez-Lopez, R. Coras, A. Torres, N. E. Lane, M. Guma, *Nat. Rev. Rheumatol.* **18**, 258 (2022).
7. W.-S. Choi *et al.*, *Nature* **566**, 254 (2019).
8. T. Brevini *et al.*, *Nature* **615**, 134 (2023).
9. K. A. Gudzune, R. F. Kushner, *JAMA* **332**, 571 (2024).
10. D. J. Drucker, *Science* **385**, 258 (2024).
11. H. Bliddal *et al.*, *N. Engl. J. Med.* **391**, 1573 (2024).
12. D. T. Felson, *N. Engl. J. Med.* **391**, 1643 (2024).
13. W. Tang *et al.*, *Science* **332**, 478 (2011).
14. V. Navarro-Compán, A. Sepriano, D. Capelusnik, X. Baraliakos, *Lancet* **405**, 159 (2025).

ACKNOWLEDGMENTS

The author thanks Z. Yuan for assistance with the figure and acknowledges support from the National Institutes of Health (R01AR078035, R01AR062207, R01AR076900, and R01NS070328).

10.1126/science.adw4656

POLICY FORUM

A vaccination is prepared in Gedaref, Sudan, during a campaign against measles and rubella in January 2024.

PHOTO: AFP/GETTY IMAGES

INFECTIOUS DISEASE

Rubella and measles: The beginning of the endgame

Benchmarks must be established and progress tracked to set a global target and take action

By **Matthew J. Ferrari**[1] *and* **William J. Moss**[2]

A September 2024 recommendation from the World Health Organization (WHO) for universal introduction of rubella-containing vaccines (RCVs) into childhood vaccination programs in all countries paves the way to dramatically reduce, and ultimately eradicate, congenital rubella syndrome (CRS), which affects tens of thousands of families each year (*1*). It removes a critical barrier to the introduction of rubella vaccination in most of the remaining 19 countries yet to do so. Because rubella vaccine is delivered in combination with measles vaccine and introduction will involve large campaigns to vaccinate all children under 15 years of age, this recommendation provides an opportunity to move much closer to the ultimate goal: a world without measles or rubella. With planning for this goal currently paused, the programmatic, operational, and research communities must come together to establish empirical benchmarks that countries have progressed far enough for a global target to be set and the "endgame" to begin.

Although usually a mild infection in both children and adults, rubella virus can cause CRS in infants if contracted by the mother during the first trimester of pregnancy. CRS can result in hearing impairment, cataracts or glaucoma, heart defects, and developmental delays. One-third of infants born with CRS will die before their first birthday (*2*). Vaccination provides direct protection to mothers and their babies, but reducing circulating rubella virus means that the unvaccinated are more likely to be exposed to rubella virus later in life, including during pregnancy. In rare specific settings, this can lead to a paradoxical effect in which CRS rates in partially vaccinated populations are higher than in unvaccinated populations (*3*). This effect manifests 10 or more years after vaccine introduction precisely because the vaccine decreases the rate of rubella virus infections among unvaccinated individuals (*2*, *3*). Concern over this phenomenon led the WHO, in 2000, to recommend against introducing rubella vaccination into national programs that could not achieve 80% vaccine coverage (*2*).

New epidemiological, modeling, and operational evidence presented to the WHO Strategic Advisory Group of Experts on Immunization (SAGE) made the case that the prior 80% threshold was overly conservative and that universal introduction of RCV could avert tens of thousands of cases of CRS annually at current coverage levels (*1*). Their September 2024 recommendation—which is the first of many political, financial, and operational steps necessary to introduce rubella vaccine in the remaining countries—represents a triumph of evidence-based policy-making.

Rubella vaccination is delivered in a combined dose together with measles vaccine [in many countries, this is a measles-mumps-rubella (MMR) vaccine, but in lower-income countries, this is a measles-rubella (MR) vaccine only]. The current WHO guidance for introduction of rubella vaccination (switching from measles-only to MR vaccine) recommends an initial vaccination campaign that includes all children between 9 months and 15 years of age (*2*). These wide-age-range campaigns with MR vaccine present an unprecedented opportunity to dramatically reduce the prevalence of two viruses, rubella and measles. Coordinated action to accelerate introduction of RCV through wide-age range campaigns in the remaining 19 countries, 6 with and 13 without current plans to introduce in place (see the box), means that the highest level of global population immunity to both measles and rubella viruses in human history could be realized by 2030.

If done well, the campaigns could transform the epidemiology of measles in the African continent [which accounted for 70% of the 107,482 deaths due to measles in 2023 (*4*)] and move the region an order of magnitude closer to the levels of protection from measles seen in most of the rest of the world. This represents a huge step forward in efforts to eliminate these diseases and could be the beginning of the end [the endgame (*5*)] for the second and third human pathogens to be eradicated after smallpox.

The public health and economic value of measles eradication has been well established, but there are powerful arguments against setting an eradication goal without

---

[1] Center for Infectious Disease Dynamics, The Pennsylvania State University, University Park, PA, USA. [2] International Vaccine Access Center, Johns Hopkins University, Baltimore, MD, USA. Email: mjf283@psu.edu

a well-planned, well-resourced, realistic, and sustainable endgame (*6*). Timing is critical, and the endgame should not start until clear benchmarks are met that indicate measles eradication is achievable in a reasonable timeframe. Such concerns should not blind us to the real possibility of rubella eradication; the lower transmission rate for rubella virus suggests that eradication is feasible and sustainable at lower vaccination coverage levels than for measles virus (*7*). Eradication, the permanent reduction to zero of the worldwide incidence of infection caused by a specific pathogen as a result of deliberate efforts (*8*), is the only public health outcome for which intervention measures, and the financial costs they incur, are no longer needed (for example, the cessation of smallpox vaccination). But eradication requires enormous global coordination, effort, and expense, especially as the pathogen becomes rare, which may divert resources from other societal needs for marginal immediate health benefits.

Currently, all six WHO regions have set independent elimination goals for measles (*4*), and all but the Eastern Mediterranean region have set elimination goals for rubella (*9*). There is a profound difference between regional elimination [defined as interruption of endemic transmission in a region for 12 months (*9*)] and eradication. No region that has achieved elimination has yet maintained 12 months with no reported cases of measles or rubella, highlighting the continued risk of reintroduction in a highly connected world. The arguments for and against setting a rubella and measles eradication goal are worth debating; however, that debate is a double-edged sword. Delaying the programmatic and operational planning necessary to capitalize on the distinct opportunity that will follow universal RCV introduction while we debate the merits incurs economic, ethical, and epidemiological costs to all regions as a result of continued virus transmission (*5*). Thus, we should identify and strive to achieve benchmarks in our progress toward endgame scenarios, when eradication will be realistic and achievable within a specified timeframe. This risks some wasted investment if debate ultimately results in a decision to not pursue eradication but preserves the option to do so.

Many critical steps are necessary to make the best use of this generational opportunity. First and foremost, the remaining 19 countries should introduce RCV with the support of the international community. This process has already begun in earnest but requires additional high-level diplomacy to maintain momentum, financial and technical assistance, and logistical support, recognizing the challenges posed by recent changes in funding priorities.

Although many countries have already introduced RCV, and done so using domestic resources, there are other countries for which domestic capacity is insufficient; thus, they have depended on external funding, primarily from Gavi, the Vaccine Alliance; United Nations Children's Fund (UNICEF); WHO; and the World Bank. Of the 19 countries that have not completed RCV introduction at the national level, five have applied and been approved for funding from Gavi, and one (South Africa) is self-funding introduction. The remaining 13 countries have not met the 80% coverage criterion under the old SAGE guidance, and funders were not willing to approve proposals for funding for RCV introduction that were contraindicated by a SAGE recommendation. The updated SAGE recommendation removes one barrier for this latter group. But each country must be convinced of the benefit of RCV introduction in the near term relative to other national priorities.

Status of rubella-containing vaccine (RCV) introduction

Of the 19 countries that have not completed national RCV introduction, 5 have been approved for funding from Gavi and one (South Africa) is self-funding introduction. The updated World Health Organization recommendation removes one barrier for the remaining 13 countries.

Plan	Countries	Potential population impact (annual births 2023)
Current plan for rubella vaccine introduction **with** Gavi funding	Democratic Republic of the Congo, Guinea Bissau, Mali, Nigeria, and Sudan	14.4 million
Current plan for rubella vaccine introduction **without** Gavi funding	South Africa	1.2 million
No current plan for rubella vaccine introduction and **eligible** for Gavi funding	Afghanistan, Central African Republic, Djibouti, Ethiopia, Guinea, Liberia, Madagascar, Niger, Somalia, South Sudan, and Tchad	10.7 million
No current plan for rubella vaccine introduction and **ineligible** for Gavi funding	Equatorial Guinea and Gabon	100,000

Because eradication is a global good, the international community—with leadership from the Measles & Rubella Partnership, WHO African and Eastern Mediterranean Regional Offices, as well as international nongovernmental organizations (NGOs) such as International Committee of the Red Cross—must collaborate to make this case and provide the appropriate incentives to ensure high-quality introductory campaigns. Importantly, three countries (South Africa, Gabon, and Equatorial Guinea) are not eligible for funding from Gavi because their gross annual national income per capita exceeds US$2300. Gavi and its donors should develop a plan to support introduction in these three countries, perhaps using the same application process, so that their failure to introduce does not provide a refuge for rubella and measles viruses that could spark outbreaks elsewhere.

Technical assistance is critical to assure efficient and effective introduction of RCV. This should be organized as a multilateral engagement to support county-led initiatives, transferring expertise among the 19 countries, with those further along in the process serving as mentors for their peers, aligning with the Lusaka Agenda's call for shifts in the long-term evolution of global health initiatives (*10*). This could include guidance in developing applications for Gavi funding to support RCV introduction; developing microplans to guide vaccination campaigns and strengthen routine immunization; and organizing campaign logistics, with leadership comprising a team of regional experts from countries that have recently introduced RCV.

The logistics and project management of such an effort should not be underestimated, and external support will be needed. Funding and administrative support from external partners such as US Centers for Disease Control and Prevention, the Gates Foundation, and WHO would allow national resources to be focused on technical assistance rather than meetings and travel logistics. Campaign logistics should specifically focus on anticipating the challenges of reaching the populations hardest to reach, which will benefit from the engagement of international organizations such as Medecins Sans Frontieres and civil society organizations within each country and drawing on lessons learned from other eradication programs (*8*).

Integrated activities to ensure that routine immunization systems are strengthened during the introduction of RCV will ensure a durable impact and prevent, or slow, backsliding of population immunity after introduction. Such improvements will leave countries stronger after the campaign than before, leveraging RCV introduction to achieve broad improvements across all vaccines, including the strengthening of cold chain capacity to transport and store vaccines, microplanning to enumerate target populations and identify missed communities, educating health professionals and the public, as well as strengthening disease surveillance systems and outbreak response. Such integration should be led by national immunization programs with support from WHO and other technical partners, building on existing global guidance and experience on what works best in the local context. Most importantly, and in line with the concept of "measles as a tracer," an effort to identify children who have received no vaccines and qualitative methods to identify structural reasons for nonvaccination can drive robust systematic improvements in coverage across all childhood vaccines (*11*).

Even with a successful RCV introduction over the coming 5 years, there remains a parallel set of tasks specifically focused on planning for the eradication endgame. Even before an eradication goal is set, this process should be undertaken to best plan for the endgame scenarios, including the immunization and communication strategies, vaccine supply requirements, and necessary financial and personnel resources. Moss *et al.* have argued that benchmarks for setting a measles and rubella elimination goal be developed by using a "consultative process with key stakeholders, including representatives from countries, regions, donors, industry, Civil Society Organizations, the M&RI partners, and the public, informed by rigorous analyses and modeling" [(*12*), p. 3557]. Successful introduction of RCV sets the stage for such a determination but is not sufficient. Developing clear and measurable benchmarks and developing a consensus among stakeholders of the criteria necessary for a global eradication goal will take time. This is precisely why this process should begin now so that we may identify and take steps to achieve these benchmarks that will allow us to capitalize on the historic population immunity that will follow RCV introduction.

Successful RCV introduction will necessitate a dramatic scale-up of existing MR vaccine supply, leveraging Gavi's leadership in market development. New technologies, currently in the pipeline, could increase the feasibility of eradication efforts and should be prioritized by academic and philanthropic organizations, such as the Gates Foundation, to accelerate their development. Microarray patches (MR-MAPs), a thermostable and needle-free delivery mechanism for measles and rubella vaccines, are in phase 2 trials and could make future access to "last-mile" communities much easier. The high population immunity generated through rubella vaccine introduction through conventional vaccines could dramatically reduce risk in accessible communities, allowing MR-MAPs to be initially deployed in those communities where they are most needed. Expansion of measles and rubella rapid diagnostic tests (RDTs) could speed up outbreak detection and response to prevent reestablishment of transmission in communities that have reached zero cases. How best to deploy these new technologies depends on the success of the introduction campaigns in the coming years and the future commitment from countries and NGOs for eradication versus elimination efforts. The academic research and modeling community—for example, through the recently established Gates Foundation–funded Measles Analytics Hub—should be engaged to evaluate strategies for optimal deployment of MAPs and RDTs to guide evidence-based rollout as these technologies come online. These products are already in trial phase, and the accelerated investment, streamlined regulatory approval processes, and development of markets and supply chains to ensure they are available at the scale necessary for eradication are critical. Even in the absence of a future eradication initiative, these investments will pay dividends for other vaccine initiatives and pandemic preparedness for children, adolescents, and adults (*13*).

Last, the role of the Pan American Health Organization (PAHO) as an exemplar, partner, and beneficiary of rubella and measles elimination planning cannot be overstated. PAHO's success with regional elimination of both measles and rubella viruses serves as an inspiration for success elsewhere (*14*). There is enthusiasm for measles and rubella elimination across the other global regions, and these regions will benefit from the experience of PAHO's success (*15*). The risk of reestablishment of rubella and measles virus transmission in the Western Hemisphere as a result of waning support for vaccination, US withdrawal from the WHO, and recent US threats to eliminate international health funding looms as a dark cloud on the horizon that could undermine the potential for a monumental human achievement. Civil society organizations such as the American Red Cross and Lions Clubs International, which played an outsized role in support for measles elimination in the United States, need to unite to ensure continued vigilance and support for rubella and measles elimination at the highest levels of national governments.

RCV introduction through wide-age-range campaigns will result in a massive, hopefully coordinated increase in population immunity against both rubella and measles viruses in many countries at greatest risk of outbreaks. Imperfect routine vaccination systems mean that this population immunity will rapidly begin to erode upon the completion of the last campaign. Despite disagreement among partners about the timing and feasibility of an eradication agenda for either rubella or measles, a short-term investment now would bring Africa an order of magnitude closer to achieving measles and rubella elimination, lead to a major global reduction in deaths and disability from measles and CRS, reduce the risk (and cost) of outbreaks and the reestablishment of transmission in eliminated countries, and at least leave the door open for capitalizing on the high population immunity that will result from RCV introduction. If we wait to further garner support and develop plans for eradication until after scaling up vaccination against rubella, we will be racing against the clock to make decisions and plans before it is too late and the opportunity has passed. We are in the rare position of knowing that the conditions for eradication will improve, even before we have decided to take it. If we wait until 2030 to have this discussion about the endgame, we will lose ground and miss this distinct opportunity. ■

REFERENCES AND NOTES

1. WHO, *Wkly. Epidemiol. Rec.* **99**, 719 (2024).
2. WHO, *Wkly. Epidemiol. Rec.* **95**, 30624 (2020).
3. C. J. E. Metcalf, J. Lessler, P. Klepac, F. Cutts, B. T. Grenfell, *Epidemiol. Infect.* **140**, 2290 (2012).
4. A. A. Minta *et al.*, *MMWR Morb. Mortal. Wkly. Rep.* **73**, 1036 (2024).
5. D. N. Durrheim, *Lancet Infect. Dis.* **20**, e138 (2020).
6. A. K. Winter, W. J. Moss, *Vaccines* **12**, 814 (2024).
7. A. K. Winter *et al.*, *Lancet Glob. Health* **10**, e1412 (2022).
8. J. Breman, J. K. Andrus, Eds., *The Principles and Practice of Disease Eradication* (Oxford Univ. Press, 2024).
9. P. O'Connor *et al.*, *Vaccines* **12**, 947 (2024).
10. World Health Organization Regional Office for Africa, "Roadmap for implementation of the Lusaka Agenda in Africa," 23 September 2024; https://iris.who.int/handle/10665/379013.
11. Immunization Agenda 2030 Partners, *Vaccine* **42**, S5 (2024).
12. W. J. Moss *et al.*, *Vaccine* **39**, 3544 (2021).
13. P. L. Raghunathan, W. Orenstein, *Lancet Glob. Health* **10**, e1363 (2022).
14. J. K. Andrus *et al.*, *Rev. Panam. Salud Publica* **48**, 1 (2024).
15. D. N. Durrheim *et al.*, *Vaccines* **12**, 699 (2024).

ACKNOWLEDGMENTS

The authors are thankful to N. Crowcroft for helpful discussions in framing this work. W.J.M. is a member of the WHO Immunization and vaccines related implementation research advisory committee (IVIR-AC).

10.1126/science.adv7588

NEXTGEN VOICES

Science safeguards

In 1975, scientists and lawyers met in Asilomar, California, to discuss the risks of recombinant DNA research and possible safeguards. Fifty years later, in the 31 January issue of *Science*, an Editorial (S. Parthasarathy, p. 454), Policy Forum (J. B. Hurlbut, p. 468), and Books Essay (L. A. Campos, p. 480) reflected on the meeting's long-term impacts on scientists' self-regulation, equity, and sense of obligation to the public. We gave young scientists this prompt: **If you gave a keynote speech at a meeting similar to the Asilomar conference today, what would you identify as the biggest risk posed by research in your field, and what action would you suggest to address it?** Read a selection of the responses here, and follow NextGen Voices on social media with hashtag #NextGenSci. **—Jennifer Sills**

Battery technology

Half a century after Asilomar's pioneers grappled with biotechnology's Pandora's box, we face our own reckoning. The lithium-ion revolution brought forth the dangerous myth that higher recycling percentages equal planetary salvation. But our attempts to solve one problem have created another: In places like Kolkata, children near shredding facilities suffer from exposure to toxic chemicals. This challenge demands Asilomar-level courage. We must redesign batteries to promote pollution-free recyclability, and we must evaluate every recycling technology for environmental harm, including greenhouse gases, water toxicity, and particulate emissions.

Zhen Wang
International School of Low Carbon Studies, Shandong University of Finance and Economics, Jinan, Shandong, China.
Email: janewang@sdufe.edu.cn

Plant virology

Cutting-edge innovations in plant virology could revolutionize agriculture, boosting crop resilience, combating diseases, and enhancing productivity. Engineered plant viral vectors could serve as powerful tools for gene delivery and crop improvement, but they could also recombine with natural viruses or behave unpredictably, risking ecological disruption and the emergence of new viral strains. Before field applications become a reality, we must prioritize comprehensive biosafety evaluations, develop containment strategies, and conduct long-term ecological studies. Collaboration across disciplines, including virology, ecology, and policy, will be key to building robust guidelines.

Sara Shakir
Biology of Fruit and Pathology, Joint Research Unit (UMR) 1332, French National Research Institute for Agriculture and Environment (INRAE), Villenave d'Ornon, Nouvelle-Aquitaine, France.
Email: sara.shakir@inrae.fr

Cognitive science

It is now possible to replace animal models with human-derived neurons in increasingly advanced microscale devices. However, attempts to mimic human

ILLUSTRATION: ROBERT NUEBECKER

cognition come with the risk of misunderstandings. We need a clear roadmap with criteria that define levels of cognition, intelligence, and consciousness, as well as guidelines to apply these thresholds to human-derived samples.

Bram Servais
Department of Biomedical Engineering, The University of Melbourne, Melbourne, VIC, Australia. Email: bservais@student.unimelb.edu.au

Biomedical engineering

Brain-computer interfaces have the potential to restore movement to paralyzed limbs and vision to unseeing eyes. But history warns us that technology rarely stays confined to its original purpose. Without strict oversight, corporations could exploit brain-computer interfaces to influence emotions and decisions, shaping consumer choices and even political beliefs. To prevent misuse, we need clear ethical policies enforced by independent oversight bodies. Success isn't just about innovation, it's about protecting human autonomy before profit-driven interests take over.

Safaa Osman Abuzaid Osman
Department of Biomedical Engineering and Health Sciences, University of Technology Malaysia, Johor Bahru, Malaysia. Email: safaa.o.abuzaid@gmail.com

Clinical medicine

A critical challenge as the field of medicine incorporates artificial intelligence (AI) is the growing risk to patient data privacy. Data breaches could hurt patient trust, compromise sensitive health information, and hinder the adoption of life-saving AI innovations. To tackle this challenge, we must prioritize data security by implementing encryption, enforcing strict access controls, conducting regular staff training, and collaborating with IT experts.

Yutong Hu
Division of Life Sciences and Medicine, University of Science and Technology of China, Hefei, Anhui, China. Email: hyt241188@mail.ustc.edu.cn

Nuclear physics

The misuse of nuclear and quantum research for military applications could have devastating consequences for global security. Strengthening international regulations and ethical guidelines will ensure that our discoveries serve humanity rather than threaten it. Scientists, policy-makers, and institutions must collaborate to uphold these standards. Only through collective responsibility can we safeguard the future of scientific progress and facilitate global peace.

Yumna Gamal Awad
Department of Physics, University of Mansoura, Mansoura, Dakahlia, Egypt.
Email: yumnagamal@std.mans.edu.eg

Biotechnology

Biotechnology has revolutionized medicine, agriculture, and industry, but ethical dilemmas persist. One emerging concern is the widening gap between those who can afford gene therapies and those who cannot. As gene-editing technologies such as CRISPR advance, wealthy individuals may gain access to enhancements that improve intelligence, immunity, or longevity, creating a genetic elite. Another dilemma involves synthetic life forms. If synthetic microbes escape into the wild, they could disrupt ecosystems or evolve unpredictably. Who takes responsibility if something goes wrong? Lastly, bioweapons disguised as research pose a moral risk. Gene editing can cure diseases, but it could also be used to engineer deadly pathogens. Regulating research without stifling innovation is a delicate balance. Biotechnology holds immense promise, but without ethical oversight, it risks deepening social divides and creating unforeseen threats.

Malk Elshrief
Department of Biotechnology, University of Tanta, Tanta, Egypt. Email: malkelshrief732@gmail.com

Nanotechnology

Imagine a world where cancer treatments target diseased cells precisely, agriculture thrives without pesticides, and self-repairing materials extend infrastructure's life span. This is nanotechnology's promise, but it comes with risk. Engineered nanoparticles, smaller than a virus, can breach biological barriers, accumulate in ecosystems, and trigger unforeseen toxicity. Scientists, ethicists, and policy-makers must collaborate to establish global, standardized safety regulations before the commercialization of nanotechnology, not after a disaster occurs. We need rigorous risk assessments, environmental monitoring, and ethical oversight. Success is not just patents, but public trust, environmental security, and responsible innovation.

Karen Jacqueline Cloete
College of Graduate Studies, University of South Africa, Pretoria, Gauteng, South Africa.
Email: kaboutercloete@gmail.com

Sociology

One of the greatest risks in social research is the unequal application of ethical standards. Marginalized, resource-dependent societies often become the subjects of research without the safeguards put in place in high-income regions. This selective oversight leads to exploitation and deepens inequalities and injustice. To address this, we must enforce ethical regulations equally across all research settings. Establishing independent oversight committees will ensure compliance, thus preventing bias and favoritism. In addition, artificial intelligence that has been trained in ethical principles can analyze research proposals, ensuring that guidelines are applied fairly to all communities. The implementation of universal ethical review standards and increased accountability will improve trust between researchers and communities.

Alaa Mostafa
Alexandria, Alexandria Governorate, Egypt.
Email: alaamos2017@yahoo.com

Neurobiology

Autism research has advanced rapidly, uncovering genetic and neurobiological factors that shape neurodevelopment, but the misuse of genetic and biomarker research could fuel stigmatization, discrimination, and even selective reproduction practices. If we don't proceed carefully, autism could be seen as a condition to be eliminated rather than understood, and individuals on the spectrum could be denied opportunities based on genetic predictions rather than on their actual abilities. We must establish strong ethical guidelines and policy safeguards ensuring that autism research is used to support and empower neurodivergent individuals, not marginalize them. Scientists must work alongside ethicists, advocates, and policymakers to ensure that research findings lead to better services, inclusive policies, and respect for neurodiversity.

Julio Santos
Laboratory of Experimental Neurology, University of Southern Santa Catarina, Criciuma, Santa Catarina, Brazil. Email: drjuliosantosc@gmail.com

Power computing

As we dive into the exciting world of power computing synergy, one of the biggest risks we face is the integration of computational models with real-time power systems. These complex systems, although promising, create vulnerabilities that could undermine the stability and security of our power grids. If these models fail to work as intended or are compromised by external threats, then the entire infrastructure could be at risk, leading to power outages, inefficiencies, and financial losses. To mitigate this risk, we must prioritize the development of robust cybersecurity protocols alongside real-time monitoring systems. By integrating these safeguards, we can ensure that our models and grids work seamlessly without exposing them to unnecessary threats.

Yuanxing Xia
College of Electrical and Power Engineering, Hohai University, Nanjing, Jiangsu Province, China. Email: eexyx@hhu.edu.cn

Biomedicine

Science thrives on data, but when only a fraction of the world's population is represented by those data, we fail those who need our innovations most. In biosensing, sensors are often developed, calibrated, and tested using a narrow demographic sample. As a result, these devices may misdiagnose members of marginalized communities. For example, a glucose sensor fails for patients with darker skin tones, a lactate monitor cannot account for genetic variations in metabolism, and a heart rate tracker ignores non-Western baseline vitals. We must dismantle this echo chamber by building an open-source, global calibration framework for biosensors. Validation across diverse human populations not only reduces bias, but also improves reliability and trust in medical technology. We must empower communities to contribute physiological data through decentralized, participatory biosensing, allowing real-world diversity to inform the next generation of diagnostics.

Caitlyn X. Chen
Department of Chemistry, University of Pennsylvania, Philadelphia, PA, USA.
Email: caitchen@upenn.edu

Aquatic genetics

The advancements in genetically improved aquatic organisms promise not only to revolutionize aquaculture but also to address the growing global demand for sustainable food sources. However, we must acknowledge a substantial risk that threatens the future of our field: the loss of genetic diversity due to an overreliance on genetically improved strains. As we selectively breed for desirable traits, we may inadvertently narrow the genetic pool, making our cultivated species more vulnerable to disease outbreaks, environmental changes, and other unforeseen challenges. This genetic bottleneck poses a risk to the resilience of aquaculture and could undermine the long-term sustainability of global food systems. To mitigate this risk, we must integrate a broader range of genetic material from wild populations into our breeding programs. By maintaining a diverse genetic reservoir, we can enhance the adaptability of farmed species, ensuring that they are better equipped to face the uncertainties of the future.

Fengbo Li
National Genetic Breeding Center for Giant Freshwater Prawn, Zhejiang Institute of Freshwater Fisheries, Huzhou, Zhejiang, China.
Email: fengboli@hotmail.com

Geophysics

Geophysical exploration is a vital tool for understanding the Earth, but activities such as drilling and seismic surveys can destroy habitats and pollute water and air. These effects can lead to environmental imbalances and biodiversity loss. Scientists should focus on conducting comprehensive environmental assessments before any geophysical activity. By adopting noninvasive techniques such as remote sensing and using less harmful equipment, we can substantially reduce the environmental impact of our work.

Ibrahem Hamed Ibrahem Hilal
Dirb Najm, Al Sharqiah Governorate, Egypt.
Email: ihamed091@gmail.com

Energy-efficient AI

Our quest for ever more advanced artificial intelligence (AI) models risks destroying the very society that these systems are intended to enhance. Training large language models demands enormous amounts of energy, almost 10 times the lifetime carbon emissions of an average car. Important ecosystems are directly threatened by this unsustainable consumption. Before launching large-scale AI initiatives, the AI community must come together to develop standardized risk assessment frameworks that incorporate comprehensive energy audits, life-cycle analyses, and incentives for creating energy-efficient algorithms.

Ahmed Ezzat Elsayed
Helsinki, Uusima, Finland.
Email: ahmed.ezzat@mentorna.com

Solar energy

Solar energy stands at the forefront of the global transition to sustainable power, but we cannot ignore the risks associated with solar panel waste. As photovoltaic installations grow exponentially, so does the volume of end-of-life panels. Without proper disposal, toxic materials such as lead and cadmium can leach into the environment, threatening soil, water, and entire ecosystems. If we fail to act, this waste could undermine the very sustainability that we strive to achieve. However, there is a solution: a worldwide commitment to solar panel recycling. By enforcing standardized recycling programs, we can reclaim valuable materials, minimize waste, and prevent environmental harm. Countries leading in solar adoption must also lead in responsible disposal. With innovation, policy, and cooperation, we can close the loop on solar sustainability.

Yousef Abdallatif
Department of Energy Systems Engineering, Necmettin Erbakan University, Meram, Konya, Turkey. Email: youseflatif@hotmail.com

Geological hydrogen

We stand at the precipice of an energy revolution: geological hydrogen production. However, if we mismanage hydrogen extraction, we could contaminate groundwater, trigger seismic activity, and deplete natural hydrogen reservoirs. Such consequences could stall progress, erode public trust, and set back clean energy innovation by decades. To mitigate this risk, we must prioritize rigorous site assessment and monitoring standards before extraction begins. Scientists must collaborate to develop precise models of hydrogen flow, test pilot projects in diverse geological settings, and enforce strict environmental safeguards.

Hao Zhang
Department of Materials Science and Engineering, Massachusetts Institute of Technology, Cambridge, MA, USA.
Email: hzhchem@mit.edu

Qualitative research

Qualitative research, which often complements quantitative methods in social science, is vulnerable to privacy threats. Qualitative methods can unearth highly sensitive information about study participants, with the potential to put individuals and their affiliated communities and organizations in jeopardy. In response to the reproducibility crisis, qualitative researchers are expected to adhere to strict standards of data transparency, but data openness and accountability requirements can backfire without the appropriate guardrails in place. Cryptography based on zero-knowledge proofs, which has anonymized medical records to protect citizens under authoritarian regimes, could help. Informed by practices of risk modeling, interoperable zero-knowledge cryptographic protocols should be integrated into qualitative research software to remedy the lack of cybersecurity standards in social science.

Fotis Tsiroukis
Department of Science, Technology, and Society, School of Social Sciences and Technology, Technical University of Munich, Munich, Bavaria, Germany. Email: fotis.tsiroukis@tum.de

10.1126/science.adx0308

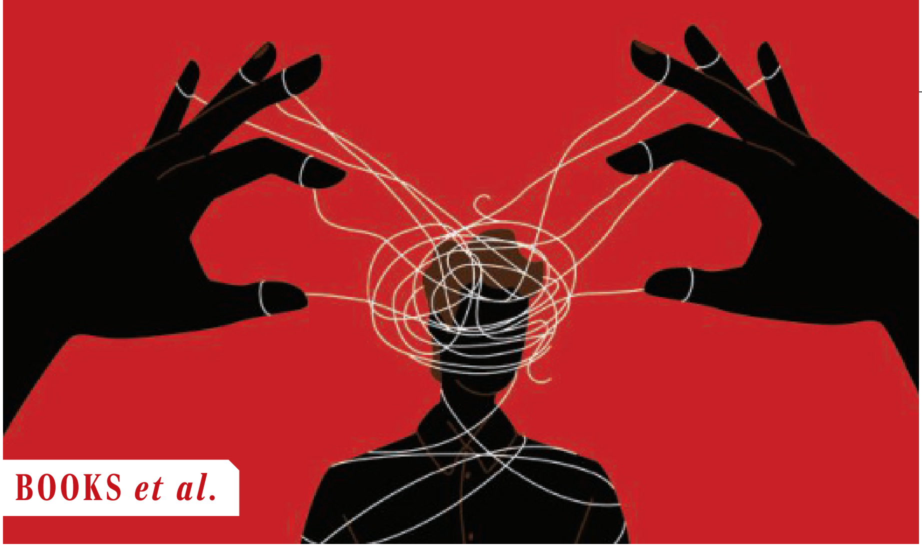

Lemov draws parallels between early brainwashing experiments and more modern forms of persuasion.

ILLUSTRATION: TATIANAZAETS/ISTOCK

PSYCHOLOGY

Convince me, control me

A historian probes the origins and evolution of psychological manipulation

By **Katie Joice**

"Brainwashed" has always been a kind of slur. Brainwashing is something that happens to other people: the politically untethered, the mentally unhinged, loners, dupes, screen addicts. In her new book, *The Instability of Truth*, historian Rebecca Lemov argues that it can happen, and is potentially happening, to all of us.

As anxiety about disinformation, alternative media, and online surveillance intensifies, the malleability of our minds has become a newly relevant problem. *The Instability of Truth* joins a burgeoning literature on this subject, including Daniel Pick's *Brainwashed: A New History of Thought Control* (2022) and Andreas Killen's *Nervous Systems: Brain Science in the Early Cold War* (2023).

Although her core material overlaps with these works, Lemov's arguments are shaped by her expertise in mid-century behavioral science, a decade of teaching the subject at Harvard University, and personal reflections on human vulnerability and trauma. The book's central claim is that a detailed understanding of postwar experiments in psychological manipulation will make us vigilant to the endless demands on our own attention, desires, and political affiliations.

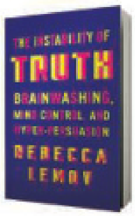

The Instability of Truth: Brainwashing, Mind Control, and Hyper-Persuasion
Rebecca Lemov
Norton, 2025. 464 pp.

Lemov's story begins in familiar territory, with what she terms "the great brainwashing crisis" of the 1950s and early 1960s. The concept first emerged during the Korean War to describe the psychological breakdown of a group of US soldiers held in Maoist prison camps. A subsequent media-fueled panic about the vulnerability of the American psyche led to the creation of a clandestine government-sponsored brainwashing industry. Programs such as MKULTRA and SERE were created to define and prevent mind control by enemy agents but ultimately became playgrounds for experimentation involving hallucinogenic drugs, hypnosis, sleep deprivation, and psychosurgery.

Lemov is at her strongest when telling the strange tales that emerge from the confrontation between fragile individuals and malign technologies. A particularly compelling example is found in the story of Leonard Kille, the brilliant and irascible working-class engineer who played a role in the development of the Polaroid camera and subsequently became the victim of his own inventions when he was used as an experimental subject for imaging and cauterizing brain matter. By interweaving the motivations of the manipulated and the manipulator, Lemov suggests that brainwashing, rather than being an either/or state, is an open-ended process involving risk and curiosity, messy human attachments, and the pragmatic need to survive. For this reason, it has always resisted scientific or legal definition.

Alongside her retellings of key episodes in the history of brainwashing, Lemov poses a series of difficult questions about scientific discovery and the nature of selfhood, although at times these lines of inquiry get subsumed under the weight of historical and ethnographic detail. In the latter part of the book, these "empirically driven" portraits—particularly the legal intricacies of the Patty Hearst kidnapping case and the niche online world of Astro-cryptocurrency—threaten to topple the story over.

Throughout her career, Lemov has been fascinated by scientists' attempts to stabilize arational phenomena, such as dreams and psychosis, with hyperrationalized recording and archival practices. Just as brainwashing should be thought of as a flux state rather than a personality transplant, she reminds readers that at its leading edge, science is itself uncertain and undefined, inviting them to reflect on the fact that both scientists and their human subjects are always being "done over" by experience.

Lemov asserts repeatedly that the long-term effects of emotional and physical trauma have been rightly acknowledged in the past decade and that it is this type of suffering, rather than "rational, cognitive malfunction," that makes us susceptible to brainwashing. This is a convincing and compassionate argument. Yet it remains unclear whether the vulnerability to which she refers precedes the manipulation or is generated by the cruelties of the conversion process itself.

As the book's narrative unfolds—and the 20th century progresses—the sites where brainwashing takes place become more diffuse: from prison camps and secret laboratories to psychiatric clinics and cult headquarters, and most recently to our kitchen nooks and living rooms. Violent coercion and surgical interventions have made way for online nudging and coaxing, a brave new world of soft control that feeds on narcissism and dopamine hits (although Elon Musk's Neuralink program, which connects brains directly to the internet, involves a real implant).

Brainwashing may be a capacious idea, but I am not entirely convinced that we can draw a true line of evolution between these different forms of persuasion. Other terms such as propaganda, mass culture, and digital capitalism are perhaps more salient. Ultimately, however, *The Instability of Truth* is a sensitively written, albeit uneven, book that will leave readers puzzling over how much we resist, submit to, or even desire to be "done over" by external influences. ■

10.1126/science.adw2209

The reviewer is at the School of Historical Studies, Birkbeck, University of London, London, UK.
Email: kjoice01@mail.bbk.ac.uk

PROFESSIONAL DEVELOPMENT

When trainees seek other paths

A new book offers advice for mentoring those who do not aspire to follow in faculty's footsteps

How to Mentor Anyone in Academia
Maria LaMonaca Wisdom
Princeton University Press, 2025. 280 pp.

By **Jonathan Wai**

The elephant in the room for many university students is that their personal goals may not always align with their mentor's incentives. In *How to Mentor Anyone in Academia*, Maria LaMonaca Wisdom gets to the heart of this issue with a question for potential advisers: "How do you mentor someone who isn't like you, and perhaps doesn't want to become you?" From there, she takes the perspective of a professional coach, drawing on insights gained from more than a thousand conversations with faculty and students across various disciplines. As she explains in the book's first chapter, "I uphold a definition of mentoring that foregrounds the needs of the mentee, in the service of their continuous learning and growth."

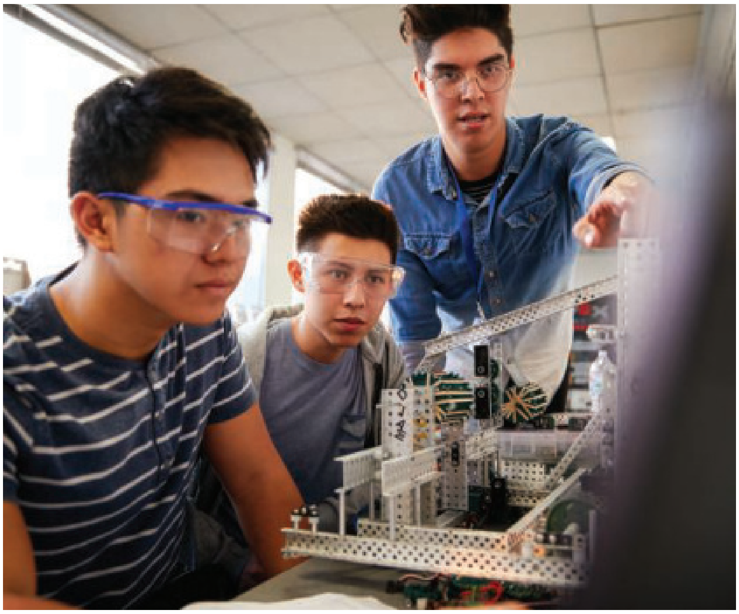

Faculty are often ill-equipped to advise those with aspirations outside academia.

PHOTO: MONKEYBUSINESSIMAGES/ISTOCK

Wisdom advocates taking mentors off of their metaphorical pedestals, explaining that although many faculty training panels feature "successful" faculty in a particular area, they can be intimidating and ultimately demoralizing to trainees. She then addresses the importance of holding mentees to high standards while also creating nurturing spaces for failure and growth, framing one-on-one academic mentoring as a marathon rather than a sprint. She encourages mentors to think of their advisees as having two selves: "Self 1," the inner critic, and "Self 2," the one who carries out the actions. Helping trainees quiet Self 1 and grow into and develop Self 2 is part of a mentor's job, she maintains.

In chapter 3, "Mentoring with Heart," Wisdom notes that "academia attracts narcissists, and its culture often reinforces and rewards their behaviors, to the detriment of everyone." Here, she argues that mentors should bridge differences, honor their mentees' values and vision, and offer them unconditional positive regard.

In chapter 5, Wisdom discusses power dynamics, writing: "Much has changed for graduate students in the past couple of decades, especially developments around issues of compensation, benefits, and employment status." Even so, mentors and students "still operate within a hierarchical academic structure," and we should all be aware of the different types of power involved and work to create psychological safety while acknowledging factors we cannot control.

Cultures of informal mentorship, including peer mentorship, can be just as, if not more, important than one-on-one academic mentoring relationships. But Wisdom notes that the "hypercompetitive and siloed research university" environment can be antithetical to the inclination to offer someone help without strings attached.

In chapter 7, Wisdom introduces the idea of helping trainees prepare for careers across and beyond higher education. This is one of the most important things research-oriented faculty simply may not know how to do, but probably need to figure out fast, given downward trends in funding and hiring at research-intensive universities.

Wisdom herself followed an unconventional academic path that informs her broad and open-minded perspective on opportunities both within and outside academia. She recalls a discussion with a department chair who told her that she was lucky to get an interview because she did not know how to write a cover letter to a teaching institution. In that moment, Wisdom realized that her mentors had taught her to value research (which mattered in their jobs) but failed to convey, or themselves appreciate, the importance of teaching.

Wisdom points out that graduate students seeking nonacademic jobs will often try to frame their research, project management, or other skills as "transferable" to the position they are seeking. However, she notes, it is often much better for a job seeker to actually have relevant experience in the area in which they are applying and to network with the people who have those jobs.

If faculty do not take care of themselves first, they are unlikely to be good mentors to anyone, observes Wisdom. And yet, incentives in the "up or out" tenure track system mean that triaging is always a necessity. Wisdom does not offer solutions to this broader structural problem but stresses the need to take care of oneself, to manage time effectively, and to leave room for play.

Wisdom concludes that we must learn to be mentors in the world as it is rather than how we would like it to be. "Do not underestimate how threatening or difficult change is for many people," she cautions. Her observations raise an important question for academia: What should graduate school look like when most students will not go on to become versions of their advisers? This broader topic falls outside the scope of Wisdom's book, but her framework for improving mentoring in academia is a good place to start. ■

The reviewer is at the Department of Education Reform and Department of Psychology, University of Arkansas, Fayetteville, AR, USA. Email: jwai@uark.edu

10.1126/science.adw0718

PRIZE ESSAY

GRAND PRIZE WINNER

Xiaojing Gao

Xiaojing Gao received an undergraduate degree from Peking University and a PhD from Stanford University. After completing his postdoctoral fellowship at the California Institute of Technology, he started his laboratory in the Department of Chemical Engineering at Stanford University in 2020. His research creates biomolecular tools for human health applications. **www.science.org/doi/10.1126/science.adw0397**

BII Science | Prize for Innovation

BIOINNOVATION

Empower the age of smart mRNA medicine

Programmable RNA sensor and molecular tools refine therapeutic payload production

By **Xiaojing Gao**

COVID-19 put a spotlight on mRNA vectors, which were programmed, manufactured, and distributed at an unprecedented speed. mRNA is safer than conventional DNA vectors because it cannot possibly insert into the human genome and cause mutations. It is also short-lived, which minimizes the risk of persistent side effects. mRNA has the potential to empower broad swaths of gene and cell therapies, such as encoding smart circuits that detect and remove cancer cells or senescent cells (for rejuvenation). Chimeric antigen receptor (CAR) T cells are a notable example that transformed the cancer therapy landscape. These cells are conventionally engineered ex vivo and therefore remain prohibitively expensive. The ability to engineer them in vivo using mRNA vectors lowers both logistical and financial barriers (*1*). Imagine a future where the treatment for a recalcitrant cancer is as straightforward as receiving a vaccine shot.

The COVID-19 vaccine produces the antigen whenever it enters a cell. How can mRNA vectors be made smarter—i.e., produce payloads in the right cells at the right time? For example, if mRNA-encoded payloads were used to activate a subtype of regulatory T cells to manage an autoimmune disease, it would be counterproductive—or even catastrophic—if the payloads were also produced in immunostimulatory cells. In contrast to the cornucopia of DNA-level controls that bestow cell type or state specificity, control methods compatible with mRNA delivery are underdeveloped. Similar specificity is partially achieved through engineered lipid nanoparticles, but that alone remains inadequate.

The advent of sequencing techniques allows us to now identify signatures of distinctly produced endogenous RNAs (referred to as markers hereafter) in virtually

Function and mechanism of RADAR

The left panel shows that RADAR (RNA sensing using ADAR) ensures the production of payloads only in cells that express specific RNA markers. The right panel shows the mechanism: dsRNA formation, ADAR recruitment, and editing-based alteration of the stop codon. The stop codon is intentionally placed again CCA with one mismatch in the middle, known to enhance editing. Self-cleaving 2A peptides are used to separate the variable peptide encoded by the sensing region from the constitutive marker and the payload.

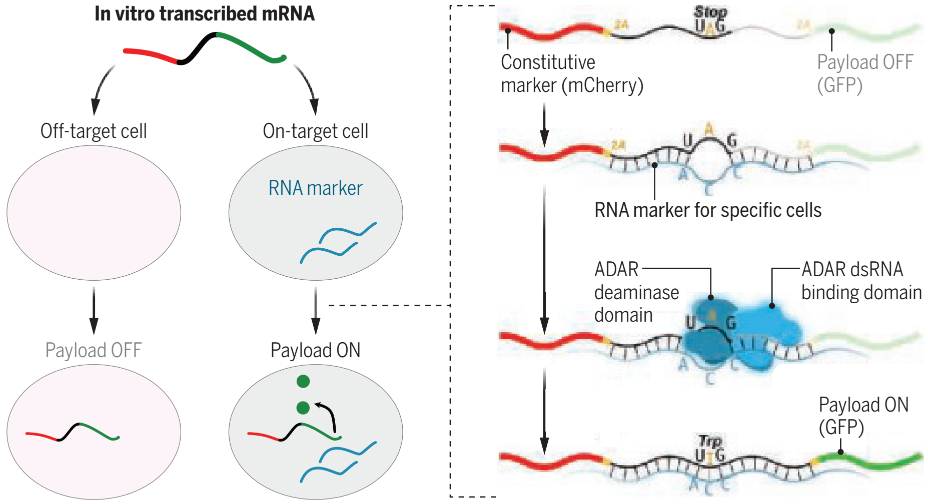

A, adenosine; ADAR, adenosine deaminase acting on RNA; C, cytosine; dsRNA, double-stranded RNA; G, guanine; GFP, green fluorescent protein; I, inosine; Trp, tryptophan; U, uracil.

CREDITS: (PHOTO) CHELSEA HU; (GRAPHIC) ADAPTED FROM N. KOLBER BY A. MASTIN/*SCIENCE*

any cell type or state. All that is needed is a design that produces payloads in response to such cell type– or state-specific marker RNAs (see the figure). For the past decade, researchers have designed RNA molecules on the basis of biophysical rules (*2*). These engineered RNA sensors change conformation upon base pairing with marker RNAs, which leads to payload production. Despite their success in vitro and in bacteria, it took considerable engineering to make them functional in mammalian cells (*3–5*). My colleagues and I hypothesized that one critical confounding factor is our immune pathways. Double-stranded RNA (dsRNA), inevitably formed during the operation of these sensors, signifies viral infection. Therefore, dsRNA is engaged by multiple endogenous housekeeping proteins in our cells. These proteins may affect sensor performance in unpredictable, cellular context–dependent ways, and it is unclear how one could engineer around them.

Not dismayed, we decided to turn this bug into a feature and investigated whether we could incorporate one of these housekeeping mechanisms into a new sensor design. We settled on enzymes called ADAR (adenosine deaminase acting on RNA) because of the specific reaction that they catalyze. ADAR binds to dsRNA and edits the adenosine (A) within to inosine (I), which is then treated as guanine (G) during translation (*6*). The key feature of our sensor, called RADAR (RNA sensing using ADAR) (see the figure), is a middle coding region that is reverse complementary to a segment of the marker RNA and that harbors an in-frame stop codon (*7*). In the absence of the marker, the stop codon prevents the production of the downstream payload. Marker-sensor hybridization induces ADAR-mediated editing, which alters the stop codon to a tryptophan codon and green-lights payload production (*8*). We have since validated RADAR functionality in human cancer cell lines, the mouse central nervous system, and even plants, which suggests the broad applicability of this programmable sensor.

As RADAR advanced inside our laboratory, the outside world took a sharp turn. In 2022, BioNTech and Moderna stocks tumbled. The Nasdaq Biotechnology Index dropped almost 30% in 6 months. Later that year, convinced that the entrepreneurial route would bring RADAR's impact to mRNA medicine sooner than what the typical academic pace would allow, I cofounded Radar Therapeutics with Eerik Kaseniit, Sophia Lugo, and James Collins. We optimistically set out to brave what some would later refer to as biotechnology's nuclear winter. Investors resonated with our vision. But 2023 saw the greatest peak in biotech bankruptcies since 2010. In the end, the founding team and our laboratory's resourcefulness prevailed. We built out the platform; identified the most compelling indications; and, most notably, established a distinct second-generation design (unpublished; provisional patent application filed). Our design overcomes key challenges that faced the first-generation designs in an exciting field (*7*, *9–11*) and opens doors to new engineering possibilities. It holds the promise to sense markers, such as splicing variants and highly structured RNAs, that pose challenges for the old designs and to outperform the old designs' signal-to-baseline ratios.

Radar Therapeutics closed an oversubscribed $13.5 million seed round earlier this year and counted Eli Lilly and Company among its investors. We garnered media attention, such as being featured in *Endpoints News* and the *Business of Biotech* podcast. We are recognized by multiple awards, often from major industrial players and potential partners, including J&J Innovation's Cell & Gene Therapy Award; AbbVie's Golden Ticket Award; Amgen's Diversity, Inclusion, and Belonging Award; and a California Life Sciences Wacker Biotech Discovery Award (providing another $100,000). Such resources and recognitions enabled us to assemble a stellar team of experienced and passionate scientists and engineers, who work tirelessly to optimize RADAR for its first indications.

Beyond RADAR [supported by a National Institutes of Health (NIH) Trailblazer Award], we are building a program of synthetic biology for human health, with an emphasis on mRNA compatibility. Although RADAR detects intracellular states, it is also important to respond to what happens outside the cells (e.g., CAR T cell production only in tumor microenvironments). We therefore developed a sister sensor for that (supported by an NIH New Innovator Award) (*12*). We also engineer protein-level circuits in parallel because they complement RNA-based sensors with specific benefits, such as direct interface with endogenous protein-level signaling pathways (*13*). Finally, we recognize the immunogenic risk of viral and bacterial components often used by synthetic biologists, and we are "humanizing" some of the commonly used ones (*14*, *15*). We expect such engineering efforts to contribute to a new age of smart mRNA medicine, both academically and through additional entrepreneurial endeavors. ■

Department of Chemical Engineering, Stanford University, Stanford, CA, USA. Email: xjgao@stanford.edu

REFERENCES AND NOTES

1. J. G. Rurik *et al.*, *Science* **375**, 91 (2022).
2. A. A. Green, P. A. Silver, J. J. Collins, P. Yin, *Cell* **159**, 925 (2014).
3. V. M. Hunt, W. Chen, *ACS Synth. Biol.* **11**, 397 (2022).
4. M. H. Hanewich-Hollatz, Z. Chen, L. M. Hochrein, J. Huang, N. A. Pierce, *ACS Cent. Sci.* **5**, 1241 (2019).
5. E. M. Zhao *et al.*, *Nat. Biotechnol.* **40**, 539 (2022).
6. K. Nishikura, *Annu. Rev. Biochem.* **79**, 321 (2010).
7. K. E. Kaseniit *et al.*, *Nat. Biotechnol.* **41**, 482 (2023).
8. L. Qu *et al.*, *Nat. Biotechnol.* **37**, 1059 (2019).
9. K. Jiang *et al.*, *Nat. Biotechnol.* **41**, 698 (2023).
10. R. V. Gayet *et al.*, *Nat. Commun.* **14**, 1339 (2023).
11. Y. Qian *et al.*, *Nature* **610**, 713 (2022).
12. X. Zhang *et al.*, *Nat. Chem. Biol.* 10.1038/s41589-025-01872-w (2025).
13. A. E. Vlahos *et al.*, *Nat. Commun.* **13**, 912 (2022).
14. E. Wolfsberg *et al.*, bioRxiv 10.1101/2025.02.24.639918 (2025).
15. C. A. Aldrete *et al.*, *Nat. Chem. Biol.* 10.1038/s41589-024-01831-x (2025).

ACKNOWLEDGMENTS

X.G. is a cofounder and on the scientific advisory board of Radar Therapeutics and is grateful for all the laboratory members, who strive together to realize our shared vision, and for the federal and foundation grants that support the works mentioned herein.

10.1126/science.adw0397

FINALIST

Luke Cox

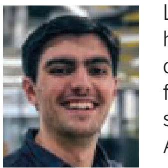

Luke Cox received his undergraduate degree and PhD from the University of Bristol. After completing postdoctoral work at the University of Bristol and working as a research engineer for start-up Ultraleap, Luke started his company, Impulsonics, in 2023. His research focuses on moving cells using acoustic waves for biotechnology automation. **www.science.org/doi/10.1126/science.adw0393**

FINALIST

Dounia Abbadi

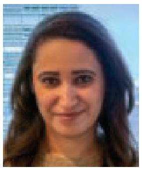

Dounia Abbadi received an undergraduate degree and PhD from University of Toulouse III - Paul Sabatier. She is currently completing her postdoctoral fellowship at NYU Grossman School of Medicine in the Department of Microbiology. She is also the chief scientific officer of Regerna Therapeutics, a start-up company of which she has been a cofounding scientist since June 2023. Her research aims to study the regulation of muscle development and apply this understanding to the treatment of muscle-wasting diseases through the first-in-class development and therapeutic use of mRNA binding proteins. **www.science.org/doi/10.1126/science.adw0395**

PHOTOS: (TOP TO BOTTOM) XIMENA VASTO; OLGA KATSARA

RESEARCH

IN *SCIENCE* JOURNALS

Edited by **Michael Funk**

ANIMAL COMMUNICATION

Closer than we thought

One hallmark of human language is the combination of elements into larger meaningful structures, a pattern referred to as compositionality. Compositionality can be trivial, in which the two parts are added together to give meaning, or nontrivial, in which the meaning in one part modifies the meaning in the other. Recent research has found the presence of trivial compositionality across a number of species, but it has been argued that nontrivial compositionality is unique to humans. Berthet *et al.* used a large dataset of bonobo vocalizations in conjunction with a distributional semantics approach and found that not only did they display compositionality, but three of the four types were nontrivial. —Sacha Vignieri *Science* p. 104, 10.1126/science.adv1170

Wild bonobos extensively use complex vocal utterances, not unlike how humans combine elements in speech.

NEURODEVELOPMENT

Cell-by-cell view of a developing cochlea

Sensory organs play a major role in how animals interact with the environment. de Haan *et al*. used in utero injection and lineage tracing to resolve cellular differentiation trajectories of the developing inner ear in mice. Lentiviral injection into the mouse amniotic cavity at embryonic day 7.5 allowed the authors to determine the various cell types within the cochlear epithelium, neural crest–derived glia, and intermediate cells in the cochlea. Their results led to the identification of cell types that were previously misclassified, and represent a comprehensive single-cell atlas of clonal relationships within the mouse cochlea. —Mattia Maroso

Science p. 60, 10.1126/science.adq9248

CHEMICAL BIOLOGY

A transposition system for proteins

There are many natural and engineered enzymatic systems for breaking apart and piecing back together DNA and RNA. With a few exceptions, proteins are not amenable to this kind of manipulation once they are produced and folded. Hua *et al*. developed a chemical transposition system for proteins in which an internal section can be entirely replaced by an exogenously supplied polypeptide. Matching the kinetics of the two splicing reactions is key to efficient transposition. This system functions on folded proteins in vitro, and the authors also demonstrated reactions in live cells. —Michael A. Funk

Science p. 68, 10.1126/science.adq8540

METALLURGY

Suppressed cyclic creep

A range of techniques are used to strengthen metal alloys to increase their duty life, but these approaches often reduce the ability of the alloys to resist asymmetric stress cycling, which can cause cumulative unidirectional plastic strain. Pan *et al*. showed that it is possible to achieve both high strength and superior resistance to cyclic creep by engineering the gradient hierarchy of dislocation cells in single-phase, face-centered cubic 304 stainless steel. Under asymmetrical cyclic stresses, continuous stacking fault formation and crystal structure transformation led to sustained structural refinement. This process resulted in enhanced strain hardening, reduced dynamic recovery, and mitigated strain localization, thus lowering

PHOTO: MARTIN SURBECK

cumulative ratcheting strain.
– Marc S. Lavine

Science p. 82, 10.1126/science.adt6666

SOLAR CELLS

Strain-incorporated rubidium

Cooperative lattice contraction created by small chlorine and rubidium ions allows the formation of a stable wide-bandgap perovskite for use in tandem solar cells. The small size of rubidium cations usually prevents the formation of the perovskite phase, but Zheng *et al*. showed that the strain induced with added chlorine prevents phase segregation of the rubidium and cesium cations in the perovskite and creates a phase with a wide band gap (1.67 electron volts). A perovskite solar cell had an open-circuit voltage of 1.3 volts, 93.5% of the radiative open-circuit voltage limit. —Phil Szuromi

Science p. 88, 10.1126/science.adt3417

HUMAN GENETICS

Transcription networks in erythropoiesis

Most genetic variants associated with phenotypes or diseases are located in noncoding regions of the genome that play a crucial role in regulating gene expression. However, the mechanisms through which these variants exert their effects remain largely unclear in most cases. Martin-Rufino *et al*. have developed “Perturb-multiome,” a technology that uses CRISPR to disrupt key regulatory proteins while simultaneously analyzing changes in DNA accessibility and gene activity in individual blood-forming cells. The authors identified critical regions of the human genome that regulate gene expression in response to perturbations, which are essential for shaping blood cell development despite comprising only a small fraction of the genome. This approach facilitates linking genetic variants to their functions across the genome, thereby advancing our understanding of gene regulation in both health and disease. —Di Jiang

Science p. 52, 10.1126/science.ads7951

PHOTO: MATTEO SANTON

CELL BIOLOGY

Signals for host defense or cell death

In contrast to proliferating cells, the activation of the RHIM domain–containing kinase RIPK3 in neurons does not induce necroptosis but rather an antiviral transcriptional response. Kofman *et al.* investigated the molecular mechanisms underlying this response. In cortical neurons, RIPK3-dependent transcriptional responses required other RHIM domain–containing proteins that are also critical for necroptosis in proliferating cells. Fibroblasts rendered resistant to necroptosis produced a RIPK3-dependent transcriptional signature upon viral infection similar to that of virally infected neurons. —Wei Wong

Sci. Signal. (2024) 10.1126/scisignal.ado9745

FIBROSIS

Immune aging aggravates lung fibrosis

During aging, the lungs become more susceptible to damage caused by respiratory pathogens and chronic diseases such as idiopathic pulmonary fibrosis, but the role of the aging immune system in this process remains incompletely understood. Using mouse models of bone marrow transplantation, Farhat *et al.* found that an aged hematopoietic system enhances susceptibility to lung fibrosis. Transplantation of aged bone marrow into young mice increased the influx of monocytes, which gave rise to profibrotic alveolar macrophages due to impaired induction of interleukin-10–producing regulatory T cells after lung injury. These findings provide insight into the age-associated changes to the immune system that contribute to lung fibrosis. —Claire Olingy

Sci. Immunol. (2025) 10.1126/sciimmunol.adk5041

IN OTHER JOURNALS

Edited by **Corinne Simonti** *and* **Jesse Smith**

CAMOUFLAGE

Hiding in plain sight

Cuttlefish are known for their amazing ability to produce color and texture patterns on their skin using muscularly controlled chromatophores and papillae. These animals have been shown to use this control flexibly across a wide array of conditions to hide or mimic. How *et al.* recorded approaching broadclub cuttlefish from the perspective of their crab prey and found that the predators used four different camouflage displays, or some mixture thereof, to hide themselves as they approached. Approaching cuttlefish took on the appearance of a floating mangrove leaf, a branching coral, a passing stripe, or a small fish depending on prey species and environmental conditions.
—Sacha Vignieri *Ecology* (2025) 10.1002/ecy.70021

Broadclub cuttlefish (*Sepia latimanus*) mimic the shapes and coloration of leaves and coral to sneak up on prey.

NEUROSCIENCE

Imaging the prosocial human brain

Despite the negative media headlines, humans are an incredibly prosocial species. Human prosociality includes altruism, fairness in resource distribution, cooperative behavior in collaboration, and reciprocity of favors. To identify brain functions and structures that support prosocial behavior, Ishihara *et al*. used data-driven analysis of multimodal magnetic resonance imaging (MRI) data. The higher the degree of prosocial behavior, the greater the functional connectivity between cerebral hemispheres. This was also higher in individuals with a better functional balance in the same brain region between the cerebral hemispheres.

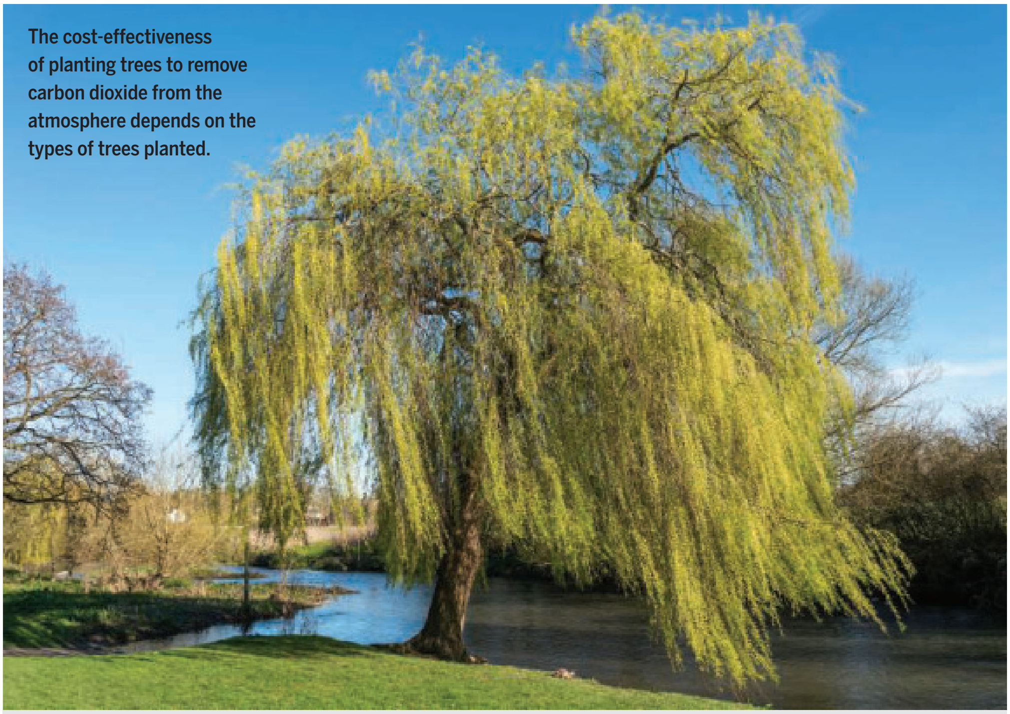

The cost-effectiveness of planting trees to remove carbon dioxide from the atmosphere depends on the types of trees planted.

CLIMATE

Arboreal decarbonization

One of the most popular strategies used to remove carbon dioxide from the air is planting trees. However, not all tree-planting strategies are equally beneficial; questions such as which species grow best in a given environment, which ones will thrive better in a higher–carbon dioxide world, and which ones are the most cost-effective all must be considered in decisions about which types of trees to plant. Cho *et al.* investigated these issues in the United Kingdom to quantify uncertainties related to climate and economic conditions and to examine how planting choices are affected by modern methods of decision-making. Despite the risks, tree planting can be one of the most cost-effective ways to remove carbon dioxide from the air. —Jesse Smith *Proc. Natl. Acad. Sci. U.S.A.* (2025) 10.1073/pnas.2320961122

Additionally, individuals with stronger structural connectivity between hemispheres and larger corpus callosum volumes exhibited higher degrees of prosocial behavior. —Peter Stern

eNeuro (2025) 10.1523/ENEURO.0304-24.2025

PROPAGANDA

Identifying propaganda

To amplify the ruling party's propaganda, autocratic governments use secretive techniques to influence the media. In China, inaccurate or misleading government-authored narratives in newspapers are challenging to identify because propaganda can be difficult to define, operationalize, and detect. Waight *et al.* defined scripted propaganda, news stories planted by the government, and then developed a method to identify it through leaked directives from the Chinese government's publicity and propaganda department. The authors analyzed a decade of news stories to find where newspapers copied phrases from directives. Propaganda was also detected without access to directives when similar messages across different news sources were printed on the same day. This new method allows scholars to monitor the Chinese president's tight control of the media. —Ekeoma Uzogara

Proc. Natl. Acad. Sci. U.S.A. (2025) 10.1073/pnas.2408260122

SCIENCE OF SCIENCE

Quality suffers when racing to publish

Harnessing metadata from the Protein Data Bank (PDB), Hill and Stein showed that proteins seen as being more important (and generating more citations) stoke more competition among researchers racing to publish structures first. However, although they are completed more quickly, the resulting structures are of poorer quality. This "race to the bottom" pattern is not observed among structures from structural genomics groups less focused on winning publication races. Since PDB's 1971 founding, efforts to improve the quality of these initially lower-quality structures are estimated to have cost $2.3 to $6.6 billion. —Brad Wible

Q. J. Econ. (2025) 10.1093/qje/qjaf010

BEHAVIOR

Danger neurons

The ability to recognize and respond to imminent threats is critical for survival in all animals. Cheung *et al.* investigated the brain circuits mediating innate fear responses in mice during naturalistic predator encountering. Focusing on the ventromedial hypothalamus (VMHdm), the authors identified a specific subpopulation of neurons encoding for threat and safety and a different subpopulation representing predator imminence. Their results indicate that multiple internal states associated with an unexpected threat, including threat recognition, anxiety, and fear, are represented simultaneously in the brain by different subsets of VMHdm neurons. Therefore, targeting specific subpopulations in the VMHdm could be an effective approach for treating psychiatric disorders associated with abnormal responses to stimuli. —Mattia Maroso

Neuron (2025) 10.1016/j.neuron.2025.02.003

PLASTIC UPCYCLING

Zinc in the microwave

Plastic waste accumulation remains a worldwide problem, and the most common plastics, polyethylene and polypropylene, are especially challenging to break down. One approach has been to heat the waste to high temperature, but without expensive catalysts, it can be difficult to achieve a valuable product distribution. Zhao *et al.* report a protocol in which the pulverized polyolefins are mixed with zinc oxide, which facilitates efficient microwave heating. The inexpensive zinc also catalyzes depolymerization to favor hydrocarbon products well suited to lubricant applications. —Jake S. Yeston

Nat. Commun. (2025) 10.1038/s41467-024-55584-1

PHOTO: GREG BALFOUR EVANS/ALAMY STOCK PHOTO

REVIEW SUMMARY

INSECT DECLINE

Integrating multiple evidence streams to understand insect biodiversity change

Rob Cooke†, Charlotte L. Outhwaite†, Andrew J. Bladon, Joseph Millard, James G. Rodger, Zhaoke Dong, Ellie E. Dyer, Siobhan Edney, John F. Murphy, Lynn V. Dicks, Cang Hui, J. Iwan Jones, Tim Newbold, Andy Purvis, Helen E. Roy, Ben A. Woodcock, Nick J. B. Isaac*

BACKGROUND: Insects are the dominant form of animal life on our planet in terms of species diversity, abundance, and biomass. They perform a plethora of functions that are essential to human health and well-being and occupy central positions in trophic networks. Insects are declining in many regions of the world in response to interacting drivers. Understanding the mechanisms behind these changes is essential if we are to prevent further declines and safeguard populations of insects in the future. Insects are a challenging group to study because they are hyperdiverse, have complex life cycles, are functionally complex, and experience substantial population fluctuations. In addition, the fragmented and unrepresentative available evidence base means that the global state of insect biodiversity remains unclear. In the face of these challenges, new approaches are required to determine the global status of insects and their responses to drivers of change.

ADVANCES: Time-series data provide the most direct evidence for biodiversity trends. However, insect time series are typically too short and too variable to show clear trends, and geographic coverage is too patchy for global inference. Increasingly, data from experiments, spatial comparisons, expert elicitation, and other sources are being used to make large-scale assessments of biodiversity change. These alternative evidence types have their own strengths, weaknesses, and gaps. In this Review, we address the grand challenge of understanding insect biodiversity change by using these fragmentary data. We propose an approach for combining multiple evidence types that would allow us to take advantage of the strengths of each while mitigating their weaknesses. This will enable informed assessments of insect responses to drivers of change, acknowledging uncertainty, resulting in better directed conservation action. Although conceived with the challenges of insects in mind, our approach is equally applicable to other taxonomic groups.

OUTLOOK: Evidence on the global state of insect biodiversity is incomplete. There is an urgent need to understand how, and crucially why, insect biodiversity is changing. We cannot wait decades for additional data and answers to emerge from new monitoring schemes before acting. We propose an approach to better understand how insects are changing in the context of multiple drivers of global change. To achieve this understanding, we must combine evidence from existing data from a range of sources to enable generalization across space, time, and taxonomy. This will facilitate more robust assessments of insect biodiversity change and improve our confidence in those assessments so that informed conservation and policy recommendations can be made to protect insect biodiversity. ■

The list of author affiliations is available in the full article online.
***Corresponding author. Email: njbi@ceh.ac.uk**
†These authors contributed equally to this work.

Cite this article as R. Cooke *et al.*, *Science* 388, eadq2110 (2025). DOI: 10.1126/science.adq2110

READ THE FULL ARTICLE AT
https://doi.org/10.1126/science.adq2110

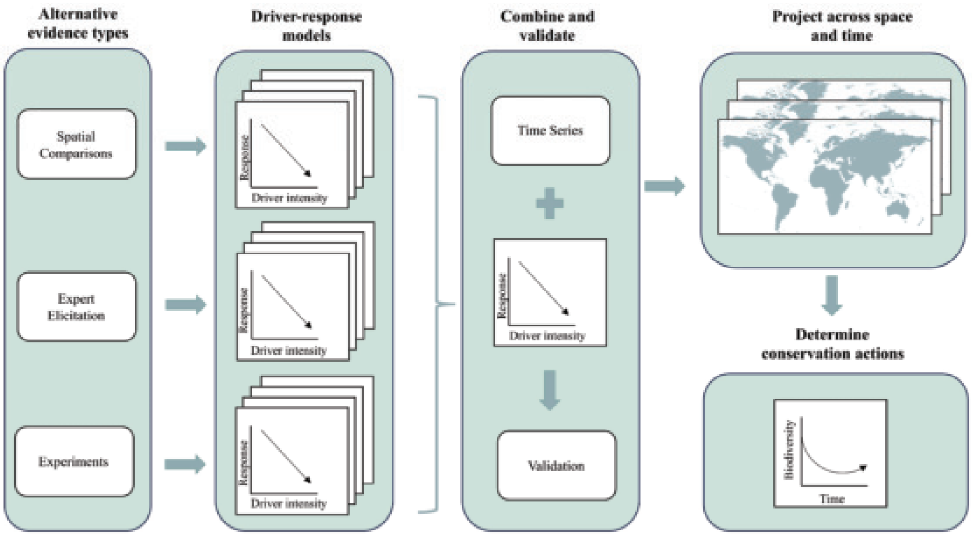

Harnessing the breadth of evidence on insect biodiversity change. By combining data from a range of sources—including from time series, spatial comparisons, expert elicitation, and experiments—we can gain a more complete picture of how insects respond to drivers of change while allowing transparency in uncertainty and data gaps.

RESEARCH ARTICLE SUMMARY

ULTRASOUND IMAGING

Nonlinear sound-sheet microscopy: Imaging opaque organs at the capillary and cellular scale

Baptiste Heiles, Flora Nelissen, Rick Waasdorp, Dion Terwiel, Byung Min Park, Eleonora Munoz Ibarra, Agisilaos Matalliotakis, Tarannum Ara, Pierina Barturen-Larrea, Mengtong Duan, Mikhail G. Shapiro, Valeria Gazzola, David Maresca*

INTRODUCTION: Enabling discoveries in the field of biology often requires new ways of visualization. One of the most informative methods for observing dynamic cellular processes in living organisms uses light-sheet microscopy to leverage genetically encoded fluorescent reporters. Unfortunately, optical microscopy is phototoxic to cells and remains restricted to the study of thin transparent specimens. The physics of high-frequency ultrasound is ideally suited to in vivo cellular imaging by providing a combination of deep penetration (~1 cm) and high spatiotemporal resolution (~100 µm, 1 ms). In addition, the recent introduction of genetically encoded gas vesicles (GVs) as the "green fluorescent protein for ultrasound" creates new opportunities for in vivo studies of cellular function. To equip ultrasound with capabilities analogous to those given to optical microscopy by fluorescent proteins, there is a need for fast high-resolution and volumetric ultrasound imaging methods capable of visualizing acoustic reporter genes and acoustic biosensors. If this can be achieved, the resulting capabilities will allow researchers to explore previously inaccessible cellular biology in vivo with unparalleled information content, resolution, coverage, and translatability to biological research and clinical development.

RATIONALE: We introduce the concept of nonlinear sound-sheet microscopy (NSSM), a method capable of detecting both genetically encoded GVs and synthetic lipid-shelled microbubbles (MBs) across thin living tissue sections. The fundamental idea behind this method is to modulate acoustic pressure along the main lobe of nondiffractive ultrasound beams to confine the nonlinear scattering of GVs and MBs to thin tissue sections. Because GVs and MBs respond to increasing acoustic pressure levels in a nonlinear way, they can be distinguished from surrounding tissues that respond to increasing pressure levels in a linear way. To maximize the volumetric field of view of NSSM, we developed our imaging method on a class of high-frequency ultrasound transducers called row-column–addressed (RCA) arrays. In our current implementation, the imaging field of view was approximately 1 cm^3.

RESULTS: Firstly, we assessed the capacity of NSSM to detect bacterial acoustic reporter genes in three dimensions. *Escherichia coli* engineered to constitutively express nonlinearly scattering GVs were successfully detected along the two orthogonal directions of a 15-MHz RCA array. By sweeping electronically the sound-sheet plane along the two orthogonal directions of the RCA array, we captured volumetric images of bacterial acoustic reporter genes spanning 8.8 × 8.8 × 10 mm^3. Secondly, we performed longitudinal NSSM of genetically labeled tumors and revealed three-dimensional (3D) patterns of GV expression over several days. We showed that NSSM can be used to track tumor growth but also to quantify both tumor and necrotic core volumes. Thirdly, we demonstrated that NSSM is capable of detecting synthetic lipid-shelled MBs, a class of resonant ultrasound contrast agents used as vascular reporters. Using NSSM at kilohertz frame rates in arbitrarily selected planes, we acquired nonlinear Doppler images of the rat brain vasculature across the entire brain. Lastly, the combination of NSSM with ultrasound localization microscopy allowed us to map cerebral blood flows below 3 mm/s, thereby revealing the capillary vasculature in living rat brains in 100-µm-thick tissue sections.

CONCLUSION: We demonstrated the ability of NSSM to confine nonlinear scattering of genetically encoded GVs and synthetic lipid-shelled MBs to wavelength-thin opaque tissue sections. NSSM is an imaging method that can either be tuned for speed or coverage. In two dimensions and at an ultrasound frequency of 15 MHz, NSSM can scan 1 cm deep with a theoretical frame rate of 25.6 kHz. In three dimensions, NSSM can acquire 8.8 × 8.8 × 10 mm^3 volumes of tissue with a theoretical volume rate of 233 Hz. To use NSSM to the fullest, new generations of brighter acoustic reporter genes and faster biosensors will have to be developed. Additionally, the sensitivity of NSSM should be improved further to enable single-cell detection. If we are successful, NSSM will carry a wave of opportunities for dynamic imaging studies of biological processes across scales. ■

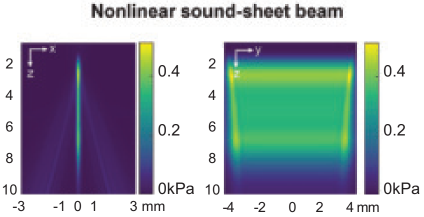

3D ultrasound imaging of gene expression in cancer

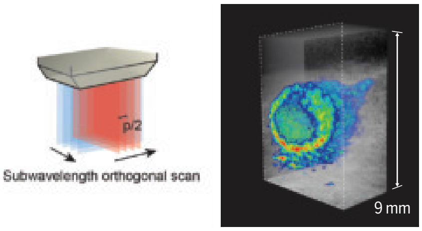

Selective-plane ultrasound imaging of brain capillaries

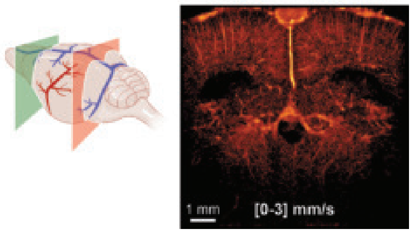

Nonlinear sound-sheet microscopy. The ability to excite acoustic reporters one plane at a time enables molecular ultrasound imaging at the cellular and capillary scales. (i) In NSSM, the nonlinear scattering of acoustic reporters is confined to thin sound sheets spanning 0.1 × 10 × 9 mm^3. (ii) Orthogonally swept sound-sheet imaging enables the 3D visualization of gene expression in opaque organs, whereas (iii) sound-sheet localization microscopy enables deep super-resolution imaging of brain capillaries. *p*, pitch of the RCA. *p*/2 was equal to 55 µm in this study.

The list of author affiliations is available in the full article online.
*Corresponding author. Email: d.maresca@tudelft.nl
Cite this article as B. Heiles *et al.*, *Science* **388**, eads1325 (2025). DOI: 10.1126/science.ads1325

READ THE FULL ARTICLE AT
https://doi.org/10.1126/science.ads1325

RESEARCH ARTICLE SUMMARY

MOLECULAR BIOLOGY

Exogenous RNA surveillance by proton-sensing TRIM25

Myeonghwan Kim, Youngjoon Pyo, Seong-In Hyun, Minseok Jeong, Yeon Choi, V. Narry Kim*

INTRODUCTION: Exogenous RNAs, including therapeutic mRNAs and viral RNAs, must navigate cellular barriers and defenses to enter cells and synthesize proteins. Current clinical mRNA technologies use ionizable lipid nanoparticles (LNPs) to deliver in vitro–transcribed (IVT) mRNA with a 5′ cap, poly(A) tail, and N^1-methylpseudouridine (m1Ψ) modification, which enhance protein production. The ionizable lipids in LNPs become positively charged upon endosome acidification, triggering endosomal rupture and releasing mRNA into the cytosol. These innovations have substantially improved transgene expression, establishing mRNA as a transformative therapeutic platform. Nevertheless, despite the broad applications of LNP-mRNA, the regulatory mechanisms remain poorly understood. A deeper understanding of the cellular processes governing the life cycle of exogenous RNAs is important for advancing mRNA therapeutics.

RATIONALE: To systematically identify cellular regulatory factors, we conducted a genome-wide CRISPR-Cas9 knockout screen. HCT116 cells were transduced with a single guide RNA (sgRNA) library and subsequently transfected with mRNAs encoding enhanced green fluorescent protein (EGFP). The IVT mRNAs were synthesized with or without m1Ψ to determine how this modification enhances protein output. We also performed a counterscreen using a cell line stably expressing EGFP to distinguish factors that regulate endogenous versus exogenous mRNAs. Fluorescence-activated cell sorting was used to isolate cells displaying the lowest and highest fluorescence, and the enriched sgRNAs were sequenced to identify positive and negative regulators, respectively.

RESULTS: From the screens using IVT mRNAs, we found positive regulators including genes involved in heparan sulfate proteoglycan (HSPG) synthesis, vesicular transport, and vacuolar adenosine triphosphatase (V-ATPase) subunits. HSPGs are cell surface glycoproteins with covalently attached heparan sulfate chains. Interfering with HSPGs reduced mRNA internalization, indicating their role in LNP uptake. V-ATPase is a proton pump that acidifies endosomes. Depletion or inhibition of V-ATPase blocks endosomal escape of LNP-mRNA.

Our screen also identified TRIM25—an RNA binding E3 ubiquitin ligase—as a key cytosolic suppressor. Knockout or knockdown of TRIM25 results in an increase of gene expression from LNP-mRNA. TRIM25 functions across multiple human and mouse cell types, indicating a widespread and conserved surveillance mechanism. TRIM25 acts by inducing RNA turnover without substantial impact on translation or deadenylation. TRIM25 downregulates circular RNAs as well as linear RNAs, suggesting an endoribonucleolytic mechanism. We identified two endoribonucleases, N4BP1 and KHNYN containing the NYN domain, serving as decay factors along with zinc-finger antiviral protein (ZAP) in a TRIM25-dependent manner. m1Ψ reduces TRIM25's RNA binding and ubiquitination activity, helping RNAs evade its suppressive effect. TRIM25 does not show specificity toward RNA sequence, cap structure, or poly(A) tail length. Instead, it specifically targets foreign RNAs delivered by acidified endosomes. TRIM25's RNA binding affinity increases even at mildly acidic pH, suggesting activation by protons released from ruptured endosomes.

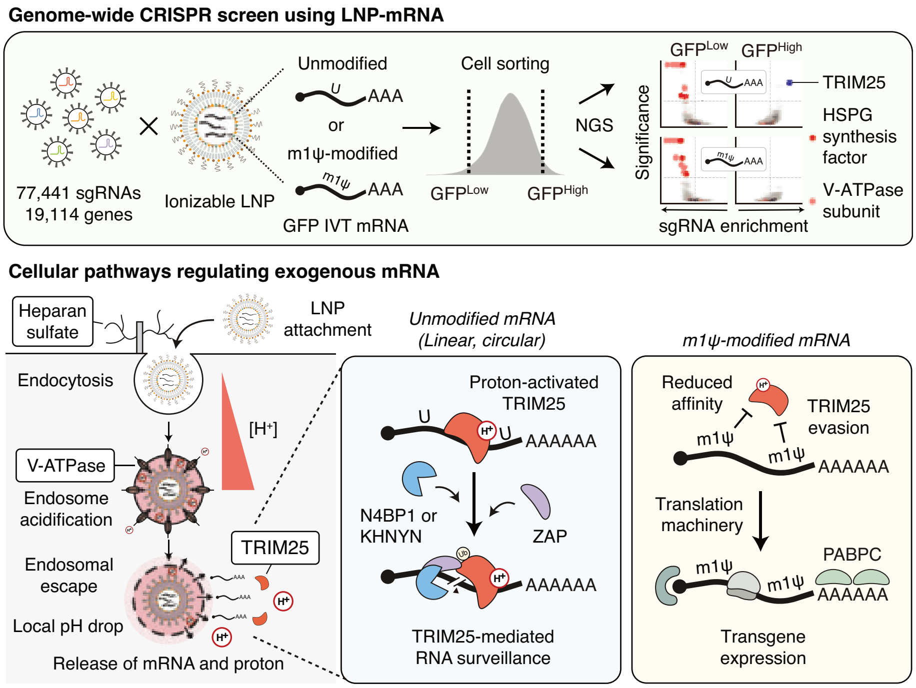

Genome-wide screen identifies cellular regulators of exogenous RNA delivered by LNP. Heparan sulfate facilitates cellular uptake. V-ATPase acidifies endosomal lumen, enabling endosomal escape. TRIM25, activated locally by protons from ruptured endosomes, captures RNA and induces RNA cleavage. Endoribonucleases N4BP1 and KHNYN, along with ZAP, redundantly mediate TRIM25-dependent RNA surveillance. m1Ψ modification helps RNA to evade TRIM25, increasing protein output.

CONCLUSION: This study elucidates the cellular mechanisms regulating the delivery and stability of LNP-mRNAs by identifying HSPGs, V-ATPase, and TRIM25 as key factors. Our comprehensive mapping of cellular pathways offers insights into RNA immunity and therapeutics. m1Ψ reduces TRIM25's RNA binding, mitigating TRIM25's suppressive effect, which explains why m1Ψ effectively improves IVT mRNAs. Notably, TRIM25 specifically targets exogenous RNAs entering the cytosol through the endocytic pathway, with its RNA binding affinity escalating with even subtle pH changes. Our findings propose a model where TRIM25 is locally activated by protons released from acidified endosomes, enabling TRIM25 to selectively recognize nonself RNAs. This posits TRIM25 as a proton-sensing defender responsive to endosomal damage and implicates the role of protons as signaling entities. ■

The list of author affiliations is available in the full article online.
*Corresponding author. Email: narrykim@snu.ac.kr

Cite this article as M. Kim *et al.*, *Science* **388**, eads4539 (2025). DOI: 10.1126/science.ads4539

READ THE FULL ARTICLE AT
https://doi.org/10.1126/science.ads4539

RESEARCH ARTICLE SUMMARY

OSTEOARTHRITIS

Osteoarthritis treatment via the GLP-1–mediated gut-joint axis targets intestinal FXR signaling

Yuanheng Yang†, Cong Hao†, Tingying Jiao†, Zidan Yang†, Hui Li†, Yuqing Zhang, Weiya Zhang, Michael Doherty, Chuying Sun, Tuo Yang, Jiatian Li, Jing Wu, Mengjiao Zhang, Yilun Wang, Dongxing Xie, Tingjian Wang, Ning Wang, Xi Huang, Changjun Li, Frank J. Gonzalez, Jie Wei*, Cen Xie*, Chao Zeng*, Guanghua Lei*

INTRODUCTION: Although previous research has demonstrated the functional roles of gut microbiota–derived metabolites in systematic immune and metabolic disorders, few studies have explored the possible actions of these metabolites in conditions with localized effects, such as joint diseases. Osteoarthritis, a prevalent localized joint disease often referred to as "wear and tear" arthritis, affects more than 595 million people worldwide. Nevertheless, its underlying mechanism is not fully understood, and no disease-modifying drugs are available. Understanding the disease mechanisms of osteoarthritis and developing mechanism-based therapeutic approaches is an urgent yet unmet clinical need. Gut microbiota dysbiosis and several microbial metabolites have been implicated in osteoarthritis; however, whether a functional gut-joint axis exists has yet to be established.

RATIONALE: Bile acids, an important and abundant class of microbial metabolites, act as signaling molecules through receptors, such as farnesoid X receptor (FXR). FXR inhibition in L cells stimulates glucagon-like peptide 1 (GLP-1) production and secretion, and GLP-1 receptor (GLP-1R) agonists show anti–cartilage degrading effects in osteoarthritis, which suggests that GLP-1 is a potential mediator linking the intestine and the joint. These findings raise the possibility of a functional and targetable gut-joint axis. Given that bile acid receptors are promising targets with several available US Food and Drug Administration (FDA)–approved drugs, understanding the importance of bile acid metabolism and signaling and its relevance to osteoarthritis may offer previously unrealized translational opportunities.

RESULTS: Through targeted metabolomics analysis of two independent cohorts totaling 1868 individuals, we identified alterations in bile acid metabolism with reduced levels of glycoursodeoxycholic acid (GUDCA) in osteoarthritis patients compared with controls. Similar patterns were observed when correlating reduced GUDCA with osteoarthritis severity indicators. GUDCA supplementation mitigated osteoarthritis progression in mice, primarily through FXR inhibition. Knockout of *Fxr* in intestinal stem cells increased the number of GLP-1–positive L cells through enhanced stem cell proliferation, resulting in elevated serum levels of GLP-1. GLP-1R–positive cells—but not GLP-1–positive cells—are present in joints. Intra-articular injection of a GLP-1R antagonist, exendin 9-39 amide, abolished the therapeutic effects of GUDCA on osteoarthritis, which indicates that L cell–derived GLP-1 entered the joint to ameliorate osteoarthritis progression. Additionally, intra-articular injection of liraglutide, an FDA-approved GLP-1R agonist, mitigated cartilage degradation in mice. Furthermore, metagenomic sequencing of stool samples from 981 individuals revealed gut microbiota dysbiosis and a lower relative abundance of *Clostridium bolteae* in osteoarthritis patients. Additionally, *C. bolteae* showed the strongest positive correlation with GUDCA within the same cohort. In mice, colonization with *C. bolteae* increased the levels of ursodeoxycholic acid (UDCA) (a precursor of GUDCA) and alleviated the progression of osteoarthritis. Notably, UDCA (an FDA-approved drug) supplementation mitigated osteoarthritis progression through this gut-joint axis in mice, and UDCA use was also associated with a lower risk of clinically relevant end point of osteoarthritis-related joint replacement in a cohort of 5972 individuals.

CONCLUSION: We elucidated a pathway through which gut microbial metabolites influence osteoarthritis progression and uncovered the existence of a functional and targetable gut-joint axis. We suggest that orchestrating the gut microbiota–GUDCA–intestinal FXR–GLP-1–joint pathway offers a potential strategy for osteoarthritis treatment. Because FXR is a known druggable target, these findings provide the foundation for developing disease-modifying drugs for osteoarthritis. ■

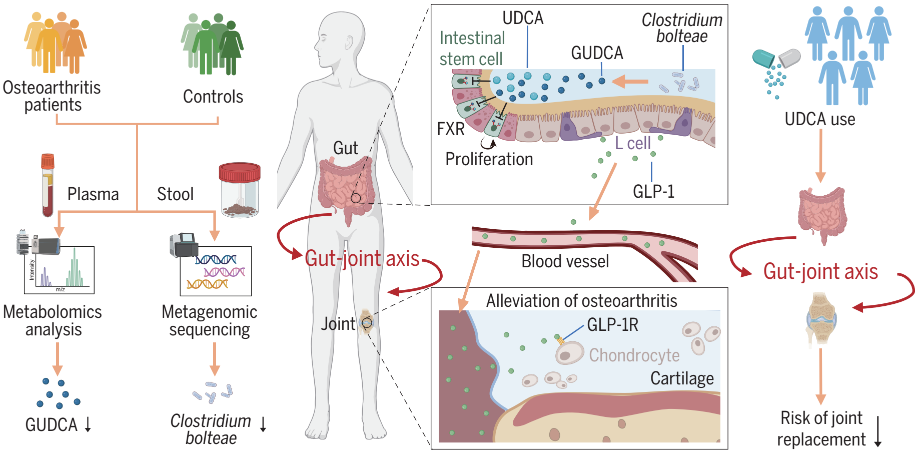

Gut microbiota–GUDCA–intestinal FXR–GLP-1–joint pathway offers a potential treatment for osteoarthritis. Osteoarthritis patients had lower GUDCA levels in the plasma and reduced *C. bolteae* abundance in the stool. Treatment with GUDCA, *C. bolteae,* and UDCA alleviated osteoarthritis in mice by suppressing FXR and enhancing intestinal L cell–derived GLP-1 production. UDCA use was associated with lower risk of joint replacement in humans. m/z, mass/charge ratio. [Figure created with BioRender.com]

The list of author affiliations is available in the full article online.
***Corresponding author. Email: zengchao@csu.edu.cn (C.Z.); weij1988@csu.edu.cn (J.W.); xiecen@simm.ac.cn (C.X.); lei_guanghua@csu.edu.cn (G.L.)**
†These authors contributed equally to this work.

Cite this article as Y. Yang *et al.*, *Science* 388, eadt0548 (2025). DOI: 10.1126/science.adt0548

READ THE FULL ARTICLE AT
https://doi.org/10.1126/science.adt0548

RESEARCH ARTICLE SUMMARY

CATALYSIS

Homogeneous-heterogeneous bifunctionality in Pd-catalyzed vinyl acetate synthesis

Deiaa M. Harraz†, Kunal M. Lodaya†, Bryan Y. Tang, Yogesh Surendranath*

INTRODUCTION: Although it has long been appreciated that heterogeneous catalyst materials can serve as precatalysts for homogeneous active species, and vice versa, seldom are both phases invoked in a single catalytic cycle. The assessment of catalyst phase encodes subsequent approaches for scientific study and rational catalyst design. The question of catalyst phase is particularly pertinent for palladium (Pd)–catalyzed vinyl acetate synthesis, a large-scale industrial process. In this reaction, heterogeneous Pd metal catalysts are used, and thin acetic acid wetting layers form on the catalyst surface that enable the formation of soluble Pd(II) species. The mechanism of vinyl acetate synthesis remains poorly understood, owing to uncertainty regarding the roles of both heterogeneous Pd(0) and homogeneous Pd(II). In this work, we used electrochemical probes to study vinyl acetate synthesis, revealing that interconversion of heterogeneous Pd(0) and homogeneous Pd(II) is required for catalysis, with each species playing a complementary role in the catalytic cycle.

RATIONALE: We envisioned that electrochemistry could provide a distinctive lens for elucidating the role of Pd(II) in this reaction, as the formation of Pd(II) proceeds via corrosion of metallic Pd, intrinsically an electrochemical process. Thus, the electrochemical potential of the catalyst, and how reaction rates scale with potential, illuminate the role of corrosion in the catalytic cycle. We conducted potentiometric and voltammetric experiments in an acetic acid–potassium acetate electrolyte as a model liquid-phase reaction medium and further extended our studies to more industrially relevant vapor-phase conditions using a solid electrolyte potentiometry technique that we developed.

RESULTS: In our model acetic acid–potassium acetate reaction medium, we found that Pd/C is subject to corrosion to form Pd(II) acetate, driven by O_2 or anodic electrolysis. In this same solution, Pd(II) acetate rapidly reacts with ethylene to selectively produce vinyl acetate with concomitant formation of Pd(0). Under thermochemical reaction conditions, variation in O_2 partial pressure changes both the rate of vinyl acetate production as well as the electrochemical potential of the Pd/C catalyst. From these findings, we hypothesized that vinyl acetate synthesis can proceed via either O_2 driven, or external polarization driven, corrosion of Pd(0) to Pd(II) followed by rapid Pd(II)-mediated ethylene acetoxylation. We compared the rate-potential scaling of thermochemical aerobic vinyl acetate synthesis (from measuring the open circuit potential and thermal reaction rate of Pd/C under ethylene and varying amounts of O_2), electrolytic vinyl acetate synthesis (from external polarization of Pd/C under ethylene in the absence of O_2), and electrolytic corrosion (from external polarization of Pd/C under inert atmosphere). All three of these processes display a common scaling of product formation rate versus catalyst potential, signifying that they share a common kinetically relevant charge transfer step, arising from the Pd corrosion half-reaction. These observations support a mechanistic model for thermochemical vinyl acetate synthesis in which heterogeneous nanoparticulate Pd(0) serves as an active oxygen reduction electrocatalyst to furnish the high potentials required for corrosion to form homogeneous Pd(II), which then mediates selective ethylene acetoxylation, and redeposits as heterogeneous Pd(0). To extend these mechanistic investigations to the vapor phase, we used solid electrolyte potentiometry with a sodium β″-alumina solid-state electrolyte to evaluate the catalyst potential in the absence of a bulk liquid phase. Under vapor-phase reaction conditions, we observed the same rate-potential scaling for vinyl acetate synthesis as was observed in the liquid-phase reaction, suggesting that a similar mechanism is operative under vapor-phase conditions. Additionally, inhibiting the corrosion of Pd(0) to Pd(II) by galvanic protection resulted in reversible poisoning of catalysis in both the liquid and vapor phases, highlighting the essential role of phase conversion in this catalytic cycle.

CONCLUSION: Our results point to a mechanism in which catalyst phase conversion is an on-pathway process, required to furnish a bifunctional catalyst system in which heterogeneous Pd(0) and homogeneous Pd(II) carry out complementary roles of oxygen reduction and olefin functionalization, respectively. This paradigm challenges the tacit assumption that catalysis proceeds via either homogeneous or heterogeneous modes and instead highlights how dynamic phase interconversion can serve to harness and couple complementary reactivity across molecular and material active sites. ■

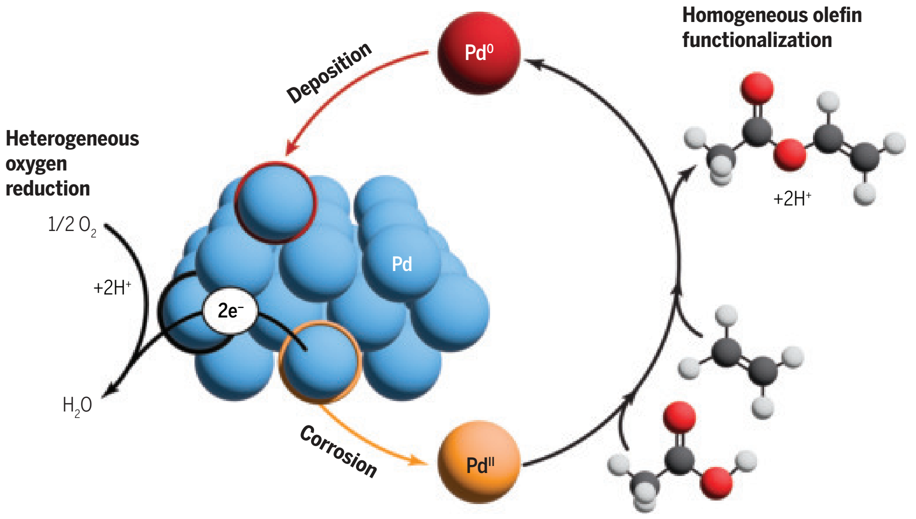

Mechanistic model for vinyl acetate synthesis, highlighting the complementary roles of metallic Pd(0) and soluble Pd(II). Efficient electrocatalysis of the oxygen reduction reaction by metallic Pd furnishes the high potential required for Pd(II) formation in an acetic acid–acetate medium. Pd(II) carries out the selective acetoxylation of ethylene to form vinyl acetate and also Pd(0), which redeposits onto the heterogeneous catalyst surface.

The list of author affiliations is available in the full article online.

*Corresponding author. Email: yogi@mit.edu

†These authors contributed equally to this work.

Cite this article as D. M. Harraz *et al.*, *Science* **388**, eads7913 (2025). DOI: 10.1126/science.ads7913

READ THE FULL ARTICLE AT
https://doi.org/10.1126/science.ads7913

RESEARCH ARTICLE SUMMARY

EVOLUTION

A geological timescale for bacterial evolution and oxygen adaptation

Adrián A. Davín*, Ben J. Woodcroft*, Rochelle M. Soo, Benoit Morel, Ranjani Murali, Dominik Schrempf , James W. Clark, Sandra Álvarez-Carretero, Bastien Boussau, Edmund R. R. Moody, Lénárd L. Szánthó, Etienne Richy, Davide Pisani, James Hemp, Woodward W. Fischer, Philip C. J. Donoghue, Anja Spang, Philip Hugenholtz*, Tom A. Williams*†, Gergely J. Szöllősi*†

INTRODUCTION: Microbial life dominates the biosphere, but a timescale of early microbial evolution has proven elusive as a result of an inadequate fossil record. The lack of maximum age calibrations—the earliest point in time at which a given group might have emerged—is particularly problematic. However, the geochemical record bears the imprint of microbial metabolism through time, providing a complementary source of information. A pivotal event in this history was the Great Oxidation Event (GOE) ~2.43 to 2.33 billion years ago (Ga), which marked a substantial increase in atmospheric oxygen. This transition, driven by the evolution of cyanobacterial oxygenic photosynthesis and carbon burial, transformed the biosphere from predominantly anoxic to oxic, causing widespread adaptation to oxygen. In this study, we used the temporal link between atmospheric oxygenation and the evolutionary spread of aerobic metabolism to calibrate the phylogeny of the bacterial domain.

RATIONALE: To date the bacterial tree, we introduced multiple new maximum age calibrations by linking the GOE to the age of aerobic lineages. We used a Bayesian approach that assumes that aerobic nodes are unlikely to be older than the GOE but can predate it given sufficient evidence from fossils or sequence divergence. To implement this approach, we integrated phylogenetic reconciliation with machine learning to map transitions from anaerobic to aerobic lifestyles onto the bacterial tree. By aggregating signals across the genome, we could robustly infer aerobic and anaerobic phenotypes from incomplete ancestral gene repertoires.

RESULTS: We identified 84 anaerobic to aerobic transitions on a species tree of 1007 bacteria. Most transitions occurred after the GOE and were driven by horizontal acquisition of respiratory and oxygen tolerance genes. However, despite the GOE calibration, at least three transitions predated this event, suggesting that aerobic respiration evolved before widespread atmospheric oxygenation and may have facilitated the evolution of oxygenic photosynthesis in cyanobacteria. Our molecular clock analyses estimated that the last bacterial common ancestor lived in the Hadean or earliest Archaean era (4.4 to 3.9 Ga), whereas bacterial phyla originated in the Archaean and Proterozoic eras (2.5 to 1.8 Ga); most bacterial families are as old as land plants and animal phyla, dating back to the late Proterozoic (0.6 to 0.75 Ga).

CONCLUSION: We infer that the earliest aerobic bacteria emerged in the Archaean, predating the GOE by 900 million years. After the GOE, aerobic lineages experienced faster diversification than their anaerobic counterparts, highlighting the impact of atmospheric oxygenation on bacterial evolution. The approach developed here provides a framework for linking microbial traits to Earth's geochemical history, offering a pathway for exploring the evolution of other phenotypes in the context of Earth's history. ■

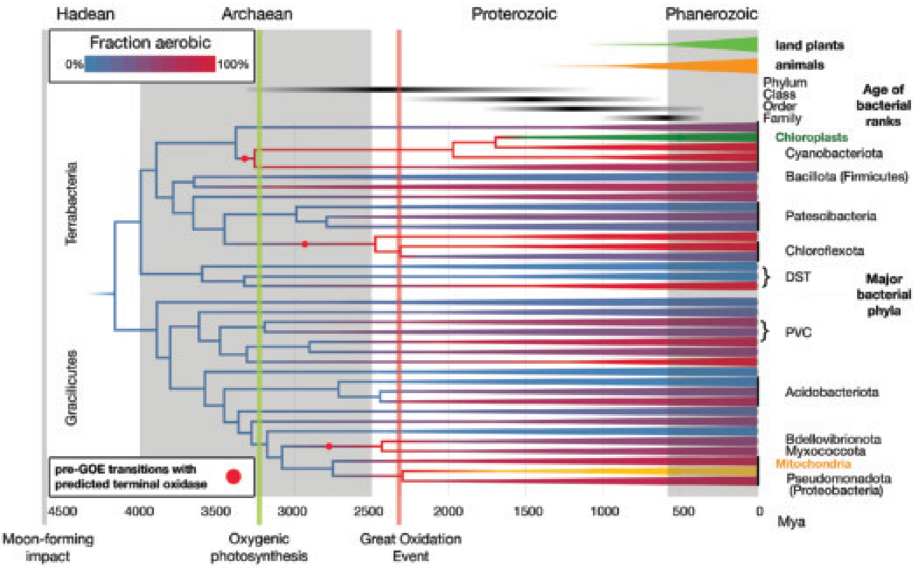

An integrated approach to date bacterial evolution and reconstruct the history of oxygen adaptation. We inferred a bacterial timetree by integrating genomic, fossil, and geochemical data and linking oxygen tolerance and aerobic metabolism to the GOE. Colors denote anaerobic (blue) and aerobic (red) states, whereas shades of purple show the fraction of aerobic lineages within extant bacterial phyla. Mitochondria and plastids were included to leverage the more extensive eukaryotic fossils. Land plants and animals are indicated for temporal comparison.

The list of author affiliations is available in the full article online.
*Corresponding author. Email: aaredav@gmail.com (A.A.D.); b.woodcroft@qut.edu.au (B.J.W.); p.hugenholtz@uq.edu.au (P.H.); thwillia@gmail.com (T.A.W.); gergely.szollosi@oist.jp (G.J.S.)
†These authors contributed equally to this work.

Cite this article as A. A. Davín *et al.*, *Science* **388**, eadp1853 (2025). DOI: 10.1126/science.adp1853

READ THE FULL ARTICLE AT
https://doi.org/10.1126/science.adp1853

RESEARCH ARTICLE SUMMARY

NEUROSCIENCE

Human high-order thalamic nuclei gate conscious perception through the thalamofrontal loop

Zepeng Fang[†], Yuanyuan Dang[†], An'an Ping[†], Chenyu Wang, Qianchuan Zhao, Hulin Zhao*, Xiaoli Li*, Mingsha Zhang*

INTRODUCTION: Exploring the neural substrates underlying human consciousness is one of the most exciting and challenging tasks in modern science. There are at least two distinct modes of consciousness: the conscious state (awake, asleep, and coma, etc.) and the conscious content (specific conscious experience). Human high-order thalamic nuclei activity is known to closely correlate with conscious states. However, it is not clear how those thalamic nuclei and thalamocortical interactions directly contribute to the transient process (which occurs on a millisecond scale) of human conscious perception. Whereas most studies have focused the search for the neural correlates of conscious perception on the cerebral cortex, relatively few studies have explored the functional role of subcortical structures, including high-order thalamic nuclei. Recently it has been hypothesized that the high-order thalamic nuclei act as gates to modulate cortical activity during conscious perception; however, there is a lack of direct empirical evidence from human studies to support such argument.

RATIONALE: The thalamus has been conventionally assumed to act as a prerequisite of sensory information for conscious perception rather than directly contributing to it. However, this assumption has been challenged by novel theoretical hypothesis and empirical evidence, mostly from anatomy and neuroimaging studies, which have shown the direct involvement of the human thalamus in various cognitive functions. Although several theories of consciousness have proposed that the thalamocortical loops might play a critical role in human conscious perception, it is largely unknown how consciousness-related information is processed and transferred within these loops. Moreover, because there is great functional heterogeneity across thalamic nuclei, it is necessary to identify the respective roles of different thalamic nucleus in conscious perception. However, precisely capturing neural activity with high spatial and temporal resolution in human thalamic nuclei and in thalamocortical loops is very difficult owing to technical restrictions. Simultaneous intracranial recordings from human thalamic nuclei and thalamocortical loops provide an excellent opportunity to elucidate the dynamic process of thalamocortical loops during the emergence of conscious perception.

RESULTS: We simultaneously recorded stereoelectroencephalography (sEEG) data from multiple thalamic nuclei and prefrontal cortex (PFC) while patients were performing a novel visual consciousness task. In this task, the matched saccadic response between the conscious and unconscious conditions largely minimized the confusion of report-related activity with consciousness-related activity. Compared with the ventral nuclei and PFC, the intralaminar and medial nuclei presented earlier and stronger consciousness-related activity, including both event-related potential (ERP) and event-related spectral perturbation (ERSP). Transient thalamofrontal neural synchrony and cross-frequency coupling were both driven by the θ phase (2 to 8 Hz) of the activity in intralaminar and medial nuclei during the emergence of conscious perception. The coupling between these two thalamic nuclei and lateral PFC (LPFC) was stronger than that between these nuclei and other PFC subregions during conscious perception. Further decoding analysis of the stimulus-evoked activity in the intralaminar and medial nuclei and LPFC showed that the accuracy was highest when decoding conscious perception (conscious versus unconscious) compared with decoding other task-related events (such as stimulus contrast, rule cues, saccade direction, and saccade reaction time).

CONCLUSION: We provide direct sEEG evidence in the human brain that supports the gate role of the intralaminar and medial nuclei in the rapid process of conscious perception. More specifically, the intralaminar and medial nuclei play a more important role than the ventral nuclei during the emergence of conscious perception. The interaction between the LPFC and intralaminar and medial nuclei, which originates from the intralaminar and medial nuclei, may play an essential role during conscious perception. Moreover, the stimulus-evoked activity in the thalamofrontal loop primarily encodes consciousness-related information rather than other task-relevant events. These results support the argument that the intralaminar and medial thalamic nuclei play a gate role to modulate the activity of PFC during the emergence of conscious perception. ■

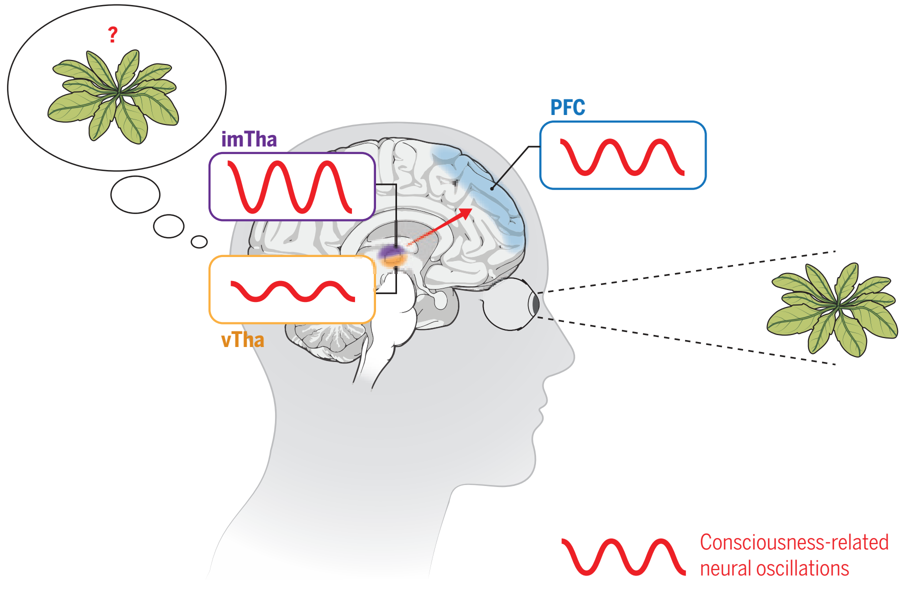

The intralaminar and medial thalamic nuclei (imTha) play a gate role in human conscious perception. The consciousness-related neural activity in imTha is earlier and stronger than that in ventral nuclei (vTha) and prefrontal cortex (PFC), and consciousness-related information originally flows from imTha to PFC during the emergence of human conscious perception.

The list of author affiliations is available in the full article online.
*Corresponding author. Email: zhaohulin_90@sohu.com (H.Z.); xiaoli@bnu.edu.cn (X.L.); mingsha.zhang@bnu.edu.cn (M.Z.)
†These authors contributed equally to this work.

Cite this article as Z. Fang *et al.*, *Science* **388**, eadr3675 (2025). DOI: 10.1126/science.adr3675

READ THE FULL ARTICLE AT
https://doi.org/10.1126/science.adr3675

RESEARCH ARTICLES

HUMAN GENETICS

Transcription factor networks disproportionately enrich for heritability of blood cell phenotypes

Jorge Diego Martin-Rufino[1,2,3]†, Alexis Caulier[1,2,3]†*, Seayoung Lee[3], Nicole Castano[1,2,3], Emily King[1,2,3], Samantha Joubran[1,2,3], Marcus Jones[4], Seth R. Goldman[4], Uma P. Arora[1,2,3], Lara Wahlster[1,2,3], Eric S. Lander[3,5,6], Vijay G. Sankaran[1,2,3,7]*

Most phenotype-associated genetic variants map to noncoding regulatory regions of the human genome, but their mechanisms remain elusive in most cases. We developed a highly efficient strategy, Perturb-multiome, to simultaneously profile chromatin accessibility and gene expression in single cells with CRISPR-mediated perturbation of master transcription factors (TFs). We examined the connection between TFs, accessible regions, and gene expression across the genome throughout hematopoietic differentiation. We discovered that variants within TF-sensitive accessible chromatin regions in erythroid differentiation, although representing <0.3% of the genome, show a ~100-fold enrichment for blood cell phenotype heritability, which is substantially higher than that for other accessible chromatin regions. Our approach facilitates large-scale mechanistic understanding of phenotype-associated genetic variants by connecting key cis-regulatory elements and their target genes within gene regulatory networks.

Human genetic studies have uncovered tens of thousands of genetic variants associated with complex diseases and phenotypes. With increasingly large sample sizes, the fraction of heritability explained is approaching saturation (*1*–*4*). However, genetic mapping fails to identify the mechanisms by which variants impact phenotypes, limiting biological understanding and the development of therapeutic strategies (*5*).

Base editing can assess the effect of variants and connect them with target genes and molecular pathways implicated in human disease. Although there has been recent progress in achieving high-throughput base editing (*6*–*10*), systematic analysis of all variants of interest is not currently feasible.

Another approach leverages the fact that most trait-associated variants are located in noncoding regulatory elements of the genome, where they alter transcription factor (TF) and related protein binding and thereby regulate gene expression (*11*–*13*). A powerful way to study the mechanisms influenced by genetic variation could thus be to modulate TFs and simultaneously read out the genome-wide consequences on chromatin accessibility of cis-regulatory elements and gene expression (Fig. 1A). To assess many TFs across diverse cell states involved in physiology and disease (*14*, *15*), such studies should be performed at single-cell resolution and in disease-relevant primary cells (*16*, *17*).

In this study, we developed Perturb-multiome to achieve this goal and apply it to study perturbations of key TFs in primary human hematopoietic stem and progenitor cells (HSPCs), which can then be differentiated to produce mature red and other blood cells. We found that the regulatory regions in erythroid differentiation whose chromatin accessibility is sensitive to perturbation of these TFs (i.e., TF-sensitive regulatory regions) comprise <0.3% of all regions in the genome but are enriched by nearly 100-fold for single-nucleotide polymorphisms (SNPs) associated with certain blood cell phenotypes. Our framework can be applied to human diseases and phenotypes beyond hematopoiesis to advance the understanding of genetic variants and the mechanisms underlying inherited risk for complex diseases.

Results

Pooled TF perturbation screens to uncover coordinated chromatin accessibility and RNA alterations

Perturb-multiome applies a library of CRISPR-based perturbations to a cell population and recovers three distinct readouts from each single cell: (i) the identity of the genetic perturbation [single-guide RNA (sgRNA)]; (ii) chromatin accessibility at cis-regulatory elements [single-cell sequencing assay for transposase-accessible chromatin (scATAC-seq)]; and (iii) gene expression [single-cell RNA sequencing (scRNA-seq)] (Fig. 1, A and B).

To apply Perturb-multiome in primary cells, we designed the method to overcome challenges in gene-editing efficiency and to effectively identify a specific perturbation. To achieve high editing efficiency with minimal toxicity, we delivered pooled sgRNAs through an optimized CRISPR droplet sequencing (CROP-seq) vector and electroporated recombinant Cas9 ribonucleoprotein (*6*, *18*) [Fig. 1B; fig. S1, A to C; and materials and methods]. To optimally identify perturbations, we developed a biotin-based enrichment strategy (fig. S11, materials and methods, and supplementary text). We achieved high specificity by amplifying CROP-seq transcripts containing the identity of the perturbation in each single cell by using biotinylated primers, which were then pulled down with streptavidin-coated magnetic beads and further amplified for sequencing.

We applied Perturb-multiome to primary human HSPCs, which can be differentiated to faithfully recapitulate hematopoietic differentiation in vitro (*6*, *19*, *20*). We perturbed 19 TFs, ranging from well-known master hematopoietic regulators to others with suggested roles in hematopoiesis (fig. S3A) (*21*). For each TF, we delivered three different sgRNAs targeting distinct positions in the coding sequences, along with six controls [three nontargeting sgRNAs and three sgRNAs targeting the "safe harbor locus" adeno-associated virus integration site 1 (AAVS1) in the genome to account for potential effects induced in cells by double-stranded DNA breaks and repair] (table S1 and materials and methods). We profiled cells across four time points. With modest sequencing depth, we detected (i) sgRNA identity in 91.1% of cells (137,604 cells); (ii) an average of 27,774 ATAC fragments and 10,803 distinct ATAC peaks per cell; and (iii) an average of 15,970 RNA molecules from 4,129 distinct genes per cell (fig. S2, A to H). Across the cell population, we detected 230,083 distinct ATAC peaks and 33,415 expressed transcripts.

We focused on the process of red blood cell production, or erythropoiesis, because nearly half of blood cell trait–associated variants have associations with the erythroid lineage, and genetic variation explains a substantial portion (between 7.19 and 26.95%) of the heritability of these phenotypes (fig. S8A and materials and methods) (*1*, *2*, *13*). After a brief initial stage of multilineage differentiation to enable some differentiation to non-erythroid fates, we promoted erythroid differentiation of HSPCs. Cells were assayed at days 7, 9, 11, and 14. We recovered a wide range of cell states, from early common progenitors and non-erythroid lineages (megakaryocyte, monocyte, dendritic cell, and granulocyte precursors)

---

[1]Division of Hematology/Oncology, Boston Children's Hospital and Department of Pediatric Oncology, Dana-Farber Cancer Institute, Harvard Medical School, Boston, MA, USA. [2]Howard Hughes Medical Institute, Boston, MA, USA. [3]Broad Institute of MIT and Harvard, Boston, MA, USA. [4]Nascent Transcriptomics Core, Department of Biological Chemistry and Molecular Pharmacology, Harvard Medical School, Boston, MA, USA. [5]Department of Biology, Massachusetts Institute of Technology, Cambridge, MA, USA. [6]Department of Systems Biology, Harvard Medical School, Boston, MA, USA. [7]Harvard Stem Cell Institute, Cambridge, MA, USA.

***Corresponding author. Email: acaulier@broadinstitute.org (A.C.); sankaran@broadinstitute.org (V.G.S.)**

†These authors contributed equally to this work.

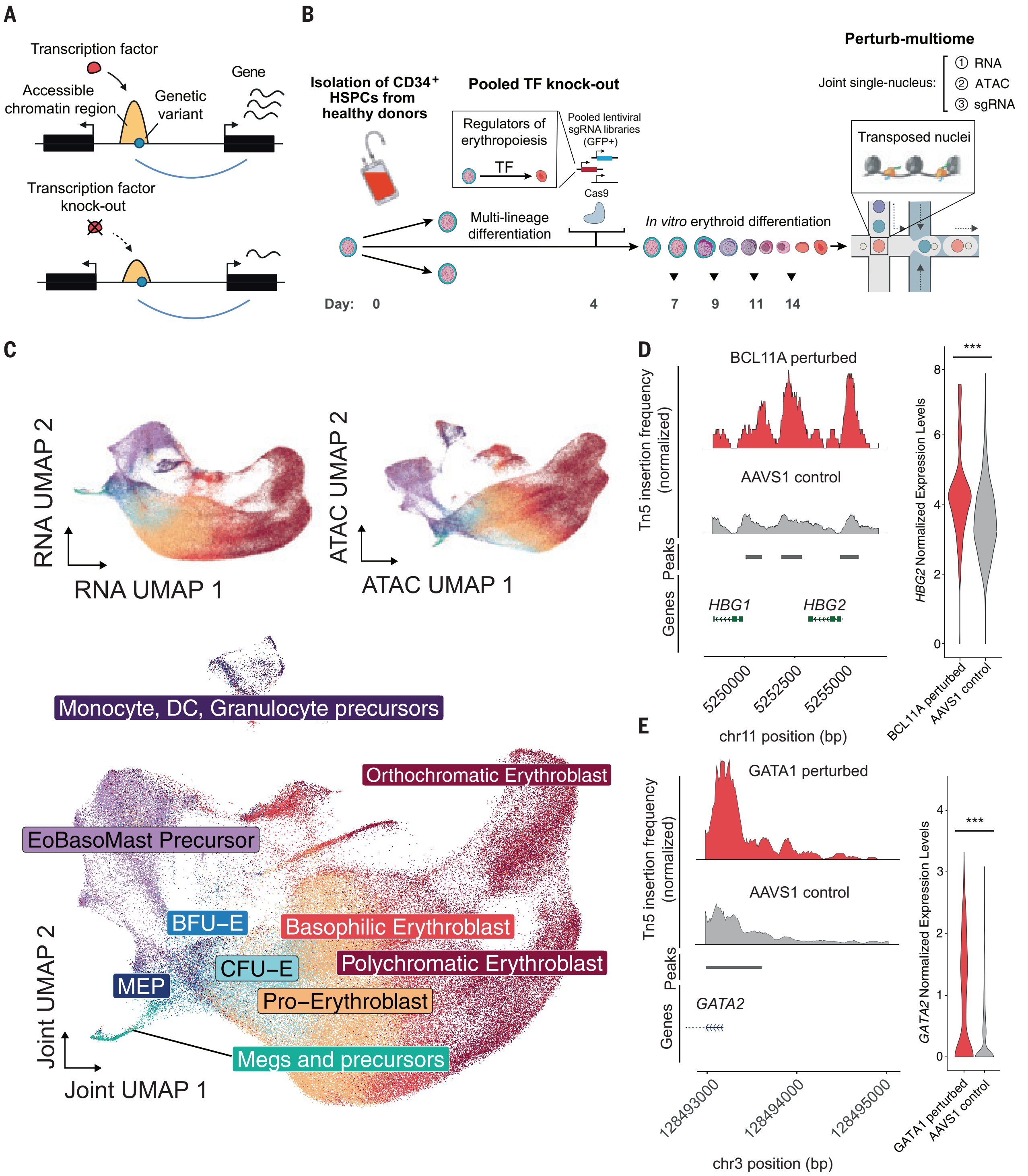

Fig. 1. Perturb-multiome: Pooled CRISPR screens with coupled single-cell RNA and chromatin accessibility readouts to profile primary human hematopoiesis. (**A**) (Top) Simplified representation of a basic gene regulatory network in which a transcription factor (TF) modulates chromatin accessibility of a cis-regulatory element (enriched in trait- or disease-associated genetic variation) and its linked gene. (Bottom) Changes in accessibility and expression after experimental TF knockout. (**B**) Schematic of the experimental setup for pooled TF knockout with multimodal single-cell readouts. Days spanned since thawing of hematopoietic stem and progenitor cells (HSPCs) are noted at the bottom. Between days 0 and 4, cells underwent in vitro multilineage differentiation, after which cells underwent in vitro erythroid differentiation. GFP, green fluorescent protein. (**C**) (Top left) Uniform manifold approximation and projection (UMAP) reduction using RNA measurements collected from all single cells in the experiment. (Top right) UMAP reduction using chromatin accessibility measurements collected from all single cells in the experiment. (Bottom) UMAP reduction using a weighted–nearest neighbor graph (*56*) to integrate RNA and chromatin accessibility peak information from the same single cells. Cell types were annotated using a human bone marrow dataset (*22*) (materials and methods). DC, dendritic cells; EoBasoMast Precursor, eosinophil-easophil-mastocyte precursor; MEP, megakaryocytic-erythroid progenitors;

Meg, megakaryocytes; BFU-E, burst-forming unit – erythroid; CFU-E, colony-forming unit – erythroid. (**D**) (Left) Normalized Tn5 insertion frequency in BCL11A perturbed cells (perturbation score > 2; see materials and methods) and control AAVS1 cells. Chromatin accessibility peaks are denoted below and were called using all cells in the experiment. (Right) *HBG2* gene expression levels in BCL11A-perturbed cells and AAVS1 control cells. *** represents an adjusted *P* value < 0.001 using a Wilcoxon rank sum test. (**E**) (Left) Normalized Tn5 insertion frequency in GATA1 perturbed cells (perturbation score > 2; see materials and methods) and control AAVS1 cells. Chromatin accessibility peaks are denoted below and were called using all cells in the experiment. (Right) *GATA2* gene expression levels in GATA1 perturbed cells and AAVS1 control cells. *** represents an adjusted *P* value < 0.001 using a Wilcoxon rank sum test.

to terminal erythroid precursors that closely mimic cell states present in human bone marrow (*22*) (Fig. 1C; fig. S1, D to J; and materials and methods).

Perturb-multiome faithfully identified various well-characterized gene regulatory mechanisms in hematopoiesis. For example, cells with perturbations in the BCL11A TF, a repressor of fetal hemoglobin and a regulator of the fetal-to-adult hemoglobin switch (*23*, *24*), displayed both increased chromatin accessibility at the fetal hemoglobin promoters and increased gene expression at the fetal hemoglobin genes (*HBG1* and *2*), compared with controls (Fig. 1D). Similarly, cells with perturbations in GATA1 TF showed significantly higher promoter accessibility and gene expression at *GATA2* (Fig. 1E), which is consistent with the negative feedback loop between GATA1 and GATA2 (*25*, *26*). These results illustrate the ability of Perturb-multiome to obtain fine-grained insights into physiologically relevant processes directly in primary human cells.

Assessment of perturbation effects and identification of TF-sensitive accessible chromatin regions and genes.

As a first step in our analysis, we sought to characterize (i) the gene-editing efficiency of each sgRNA and (ii) the perturbation level actually achieved in individual cells, which can vary among cells receiving the same sgRNA.

To characterize gene editing efficiency, we used pooled single-cell genotyping (fig. S3B and materials and methods) (*6*). We relied on genotyping rather than the mRNA level of the targeted gene, because some CRISPR-Cas9 edits that disrupt protein-coding regions do not alter mRNA levels. We analyzed 17,665 single cells in droplets, performing 55 multiplexed polymerase chain reactions (PCRs) in each cell to estimate editing efficiency. These PCRs corresponded to the human genomic sites targeted by sgRNAs, as well as 10 regions within the integrated lentiviral genome to identify the sgRNA in the cell (Fig. 2A, left, and fig. S3, C and D).

Given that a simple binary classification of cells either being perturbed or not has limitations during dynamic processes such as differentiation, we defined "perturbation scores" for both the ATAC and RNA data by comparing the chromatin accessibility and gene expression profiles of the cell with those from nearest-neighbor control cells, which represent a similar differentiation state (Fig. 2A, middle and right; fig. S3F; and materials and methods) (*27*). The perturbation scores were well correlated with sgRNA editing efficiency (fig. S3E). The exceptions included two TFs (GATA2 and SPI1) for which we achieved strong knockdown (confirmed by protein levels) but saw low perturbation scores in erythroid lineages; these TFs have their strongest effects in nonerythroid lineages (fig. S3G) (*28*, *29*). The accessible chromatin regions (ACRs) identified in Perturb-multiome were similar to the ACRs characterized in ex vivo bone marrow hematopoietic cells (*30*), suggesting that our findings are representative of gene regulation in human hematopoietic cells (fig. S3, H and I, and materials and methods).

We then defined TF-sensitive ACRs and TF-sensitive genes by using a linear model that incorporated the perturbation level achieved in each single cell (materials and methods). We found that roughly 21.8% of the ACRs (50,114/230,083) (table S2) and 26.0% of expressed genes (8,694/33,415) (table S3) were affected by at least one TF perturbation (fig. S5, A and B). Calibration analyses are included in the supplementary text. TF-sensitive and non–TF-sensitive ACRs were similarly distributed across genomic features and the genome (figs. S4B and S8B). Of these TF-sensitive results, 32% of ACRs and 22% of genes responded to only a single TF perturbation (fig. S4, C, D, and F). To assess data robustness, we examined an independent biological replicate (using HSPCs from a different donor and sgRNAs targeting different locations in the coding sequences of each TF, for a subset of eight TFs) and found that the results were highly correlated, both qualitatively and quantitatively, with average correlation of >0.9 for TFs targeted in both replicates (Fig. 2, B and C, and fig. S4A). GATA1-sensitive genes and ACRs were in agreement with independent GATA1 loss-of-function datasets (*31*, *32*) (fig. S7, C and D). In summary, a continuous perturbation score was used to identify TF-sensitive genes and ACRs in the heterogeneous cell populations that we studied (supplementary text).

Properties of TF-sensitive ACRs and genes

Having used Perturb-multiome to separately analyze changes in chromatin accessibility and gene expression, we next examined the correlation between these features in single cells carrying a given sgRNA to define ACR-gene linkages (Fig. 3A and materials and methods). If an ACR regulates a gene and TF perturbation modulates the ACR's accessibility, the regulated gene will change its expression. To assess ACR-gene linkages, for each cell we defined two scores: (i) the average expression of the TF-sensitive genes for a given TF and (ii) the average expression of the genes correlated with TF-sensitive ACRs. We found strong concordance between these scores (Fig. 2D; fig. S5, C and D; and materials and methods).

First, we examined the effect of TF perturbation on ACR-gene pairs lying within 50 kb of one another. For pairs in which the ACR and the gene were both TF-sensitive (hereafter TF-sensitive ACR-gene pairs), the correlation (at the single-cell level) was higher; this result was seen at all six erythroid TFs for which there was a substantial number of such pairs (fig. S6, A and B, and fig. S7, A and B). For example, pairs in which the ACR and gene were both GATA1-sensitive had higher correlations across single cells (Fig. 3B, top). We found that TF-sensitive pairs were 10.34 times more likely among pairs in which the gene responded to enhancer perturbation [by CRISPR interference (CRISPRi)] than among pairs where the gene did not show a response [odds ratio (OR) 10.34, $P < 0.001$, Fisher's exact test] (Fig. 3B, bottom, and materials and methods) (*33*). This suggests the possibility of using ACR-gene pair TF sensitivity in correlated pairs to reconstruct gene regulatory networks on a genome-wide scale.

Second, we considered ACR-gene pairs within 2 Mb that showed coordinated changes and examined their three-dimensional proximity, based on Hi-C data from human HSPCs (materials and methods) (*34*). We found that significant TF-sensitive ACR-gene pairs had higher odds of being found within topologically associated domains (TADs) in HSPCs (OR 1.53, $P < 0.001$) (Fig. 3C).

Third, we observed that TF-sensitive genes exhibited lower RNA polymerase II pausing compared with non–TF-sensitive genes with similar expression levels (fig. S4E and materials and methods) (*35*).

Fourth, we examined whether TF-sensitive ACRs occurred near binding sites for the perturbed TF. We analyzed published chromatin immunoprecipitation sequencing (ChIP-seq) datasets for two of our TFs, GATA1 and NFE2, in primary human proerythroblasts (materials and methods) (*36*). We found that TF-sensitive ACRs in the regions surrounding GATA1 and NFE2 ChIP-seq peaks showed

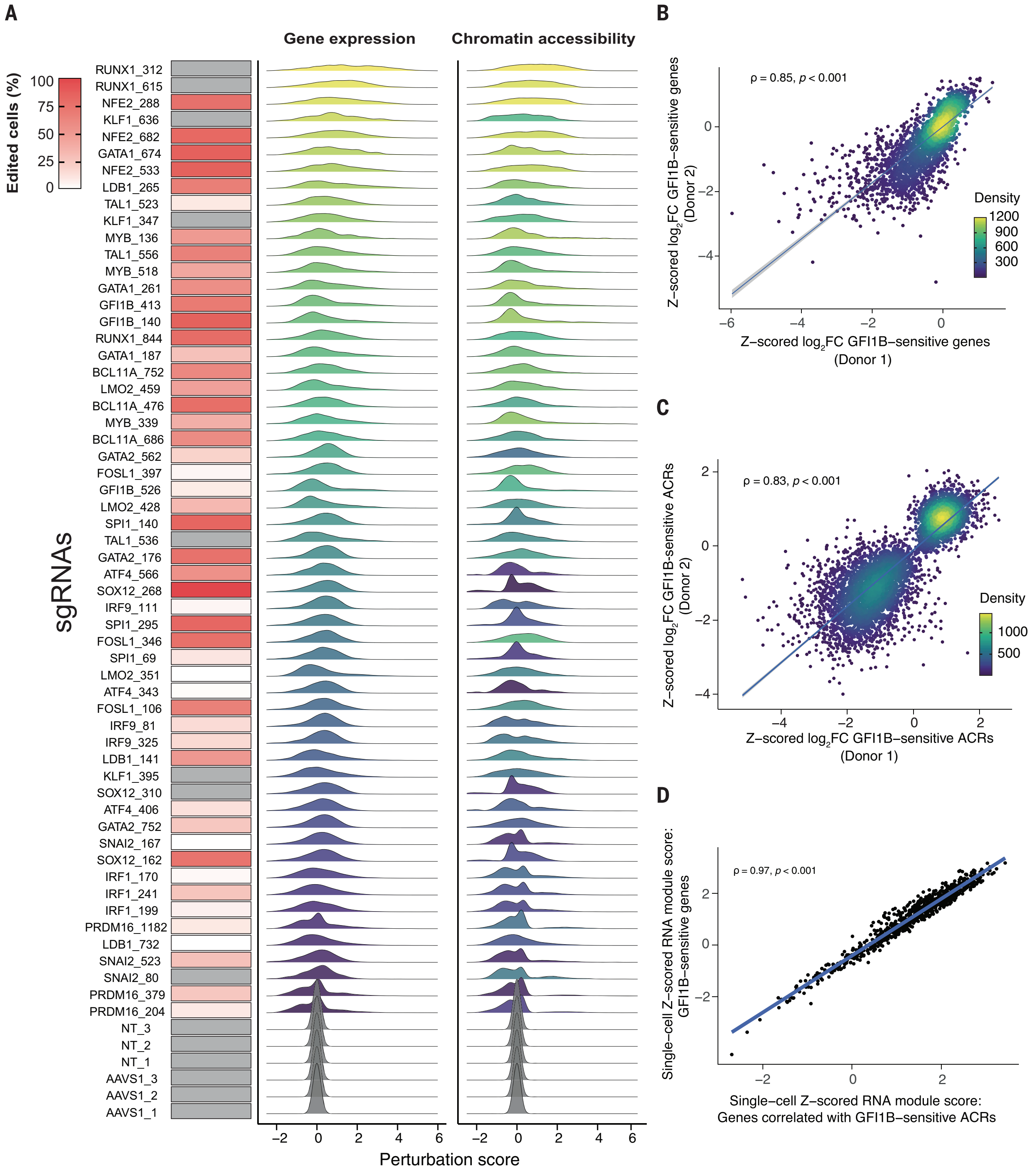

Fig. 2. Widespread gene expression and chromatin accessibility changes in response to transcription factor perturbations. (**A**) (Left column) Percent of edited cells from pooled single-cell genotyping experiments for each sgRNA (fig. S3, B to D, and materials and methods). Amplicons with missing data (not covered by single-cell multiplexed PCR) and nontargeting (NT) guides are shown in gray. (Middle column) Per-guide perturbation score distribution computed on single-cell RNA counts. (Right column) Per-guide perturbation score distribution computed on single-cell chromatin accessibility peak counts. Each sgRNA is ordered along the color gradient based on the median perturbation score across all cells with that guide, for the RNA or chromatin accessibility modalities. (**B**) Scatter plot of the *Z*-scored $\log_2$FC (FC, fold change) for RNA gene expression levels (shown are statistically significant genes after multiple hypothesis testing correction) between cells with one of the GFI1B-targeting sgRNAs and AAVS1-targeting control sgRNAs from two independent pooled TF Perturb-multiome screens in two different HSPC donors. The Spearman correlation coefficient ρ is shown, as well as a regression line with confidence intervals. (**C**) Scatter plot of the *Z*-scored $\log_2$FC for ATAC peak counts (shown are statistically significant genes after multiple hypothesis testing correction) between cells with one of the GFI1B-targeting sgRNAs and AAVS1-targeting control sgRNAs for two independent pooled TF Perturb-multiome screens in

two different HSPC donors. The Spearman correlation coefficient ρ is shown, as well as a regression line with confidence intervals. (**D**) Scatter plot of the single-cell *Z*-scored RNA module score computed using GFI1B-sensitive genes [defined as in (B)] and the single-cell *Z*-score RNA module score computed using genes correlated with GFI1B-sensitive ACRs [defined as in (C); see materials and methods], for cells with a *Z*-scored perturbation score >1. The Spearman correlation coefficient ρ is shown, as well as a regression line with confidence intervals.

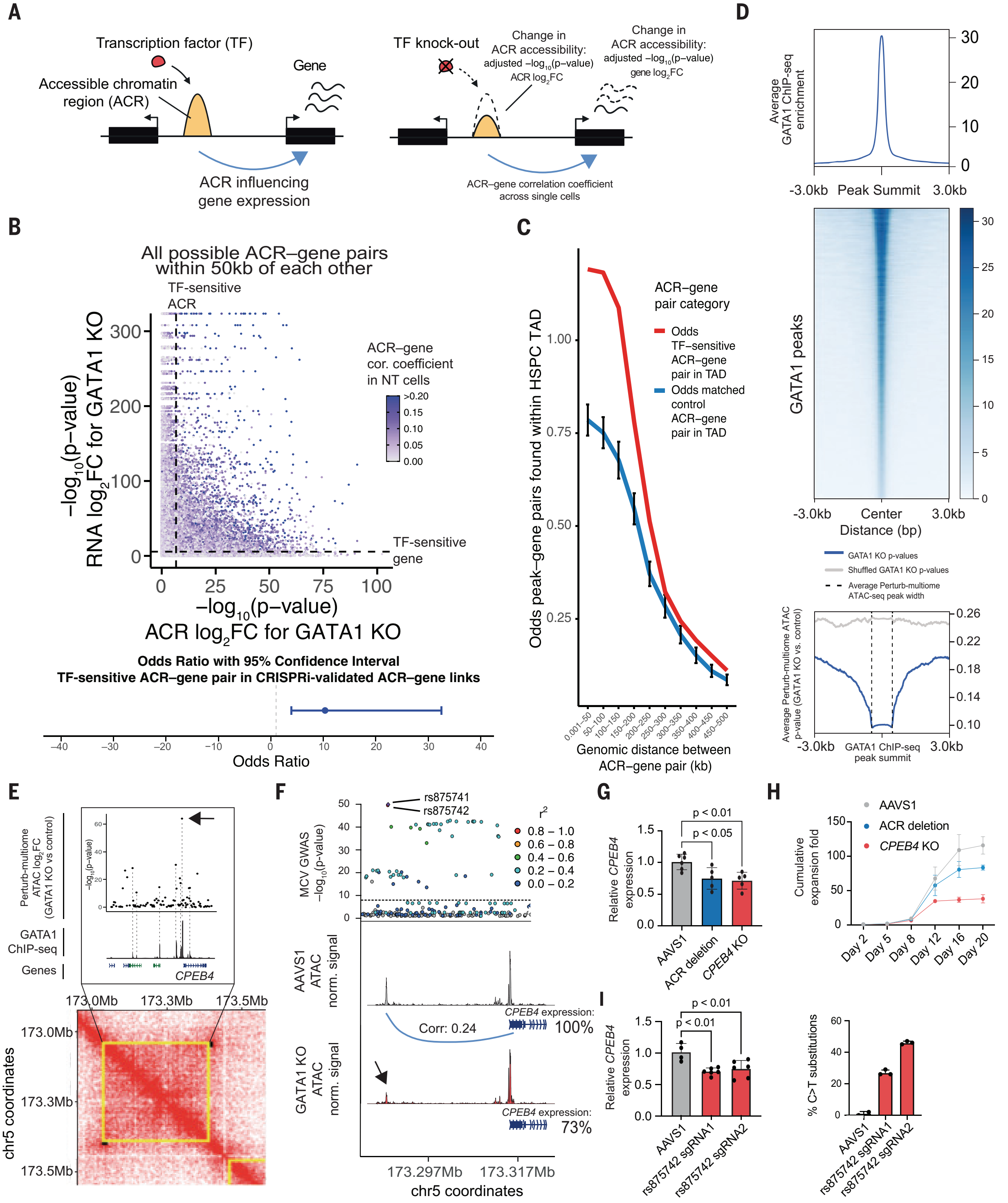

Fig. 3. Genome-wide characterization of TF-sensitive elements. (**A**) Simplified representation of the metrics analyzed in this figure for a basic TF-cis-regulatory element–target gene regulatory network. (**B**) (Top) Scatter plots of the ACR and gene $-\log_{10}$(P value) for GATA1-targeting sgRNAs, respectively, for all possible ACR-gene pairs within 50 kb of each other. Dots are colored by the ACR-gene correlation coefficient computed in cells with control NT sgRNAs (materials and methods). The vertical and horizontal dashed lines represent the *P* value cutoffs for TF sensitivity of ACRs and genes, respectively. (Bottom) OR with 95% confidence interval of a TF-sensitive ACR-gene pair to be found in CRISPRi-validated ACR-gene links (materials and methods). (**C**) Odds of ACR-gene pairs being found within

HSPC topologically-associated domains (TADs) (*34*), as a function of genomic distance and TF-sensitivity status. The odds for TF-sensitive ACR-gene pairs are shown in red. The odds for randomly sampled expression and accessibility matched control ACR-gene pairs (each non–TF-sensitive, each selected among a distribution of nonsensitive elements with similar expression and accessibility levels to their TF-sensitive counterparts) are shown in blue. Each genomic distance bin has the same number of pairs as the TF-sensitive pair, and sampling was repeated 100 times to build a distribution for each genomic bin (*34*) (materials and methods). The bars represent 1 SD. (**D**) (Top) Profile plot of independent GATA1 ChIP-seq enrichment surrounding called ChIP-seq peaks from day 12 erythroid progenitors (*36*). (Middle) Heatmap plot for GATA1 ChIP-seq reads surrounding GATA1 peaks. (Bottom) Profile plot of Perturb-multiome *P* values for the $\log_2$FC of accessibility for ACRs in cells with GATA1-targeting sgRNAs compared with control centered on GATA1 ChIP-seq peaks as defined in the top panel. (**E**) Analysis of Perturb-multiome differential accessibility results within an HSPC TAD in hg19 coordinates. Shown are the Perturb-multiome $-\log_{10}$(*P* values) for the $\log_2$FC of accessibility for ACRs in cells with GATA1-targeting sgRNAs compared with control, GATA1 ChIP-seq signal (*36*), gene annotations highlighting the GATA1-sensitive *CPEB4* gene, and chromosome loops from Hi-C data (*34*). TADs are shown in yellow and loop anchors in black (materials and methods). The TF-sensitive ACR with the most significant change compared with control (discussed in Fig. 3F) is highlighted with an arrow. (**F**) (Top) Locus zoom plot in hg19 coordinates showcasing $-\log_{10}$(*P* values) for variants associated with mean corpuscular volume (MCV) (*2*). The color scale represents the squared correlation (r^2) between rs875741 and other neighboring alleles. (Middle and bottom) Normalized (norm.) ATAC signal in cells with AAVS1-targeting and GATA1-targeting cells, respectively. The TF-sensitive ACR with the most significant change compared with control is highlighted with an arrow. The Spearman's rank correlation coefficient ($\rho = 0.24$) between this ACR and *CPEB4* is shown, as well as the mean *CPEB4* expression relative to control. (**G**) Bar plots of the relative *CPEB4* expression for HSPCs edited with a control dual cut in the AAVS1 locus, a deletion of the putative *CPEB4* enhancer on chromosome 5, or a *CPEB4* knockout (KO), and subsequently differentiated into the erythroid lineage. Data for day 14 of erythroid differentiation, for two distinct HSPC donors (deletion efficiencies for this experiment are shown in fig. S7G). (**H**) Cumulative expansion fold for HSPCs edited with a control dual cut in the AAVS1 locus, a deletion of the putative *CPEB4* enhancer on chromosome 5, or a *CPEB4* knockout, and subsequently differentiated into the erythroid lineage. (**I**) (Left) Bar plots of the relative *CPEB4* expression for HSPCs edited with the TadCBE cytosine base editor precomplexed with AAVS1-targeting control sgRNAs or two different sgRNAs targeting rs875742. Data for day 14 of erythroid differentiation, for two distinct HSPC donors. (Right) Gene editing efficiencies for one of the donors shown in the left panel.

stronger significance levels [i.e., higher $-\log_{10}$(*P* values)] (Fig. 3D and fig. S7, E and F).

We then focused on one of the ACR-gene pairs with the highest TF sensitivity upon GATA1 perturbation. This pair, located at 5q35.2, involves the *CPEB4* gene and an ACR 25 kb upstream of the gene's transcription start site and lies within a TAD in HSPCs. *Cpeb4* plays a role in mouse erythropoiesis but has not been studied in humans (*37*). The ACR has two variants in strong linkage disequilibrium with each other that are associated with multiple red blood cell traits (*1*, *2*). We found that the most significant TF-sensitive ACRs within the TAD were strongly correlated with GATA1 ChIP-seq peaks (Fig. 3E) (*2*). Besides having high gene-ACR correlation, independently, *CPEB4* and the ACR each also had the most significant changes in response to GATA1 perturbation within the TAD (Fig. 3F). These observations suggest that GATA1 binds at the ACR to modulate *CPEB4* expression.

To test this hypothesis, we used CRISPR-Cas9 to delete the ACR in primary cells. The deletion resulted in decreased *CPEB4* expression during erythroid differentiation (Fig. 3G and fig. S7G). Furthermore, perturbation of *CPEB4*—and to a lesser extent, deletion of the regulatory element—resulted in impaired terminal erythroid differentiation, which is consistent with the variant associations within the ACR with multiple erythroid traits and prior studies on the role of *Cpeb4* in mouse erythropoiesis (Fig. 3H) (*37*). We next examined the effect of editing one of the variants with base editor TadCBE (*38*) (materials and methods). This single-nucleotide change reduced the expression of *CPEB4* in primary erythroblasts (Fig. 3I). Together, these results illustrate how coupling readouts of TF perturbation, gene expression, and chromatin accessibility in the same single cells can identify TF-sensitive ACR-gene pairs with important roles in human erythropoiesis and can help systematically pinpoint associations between phenotypes and variants discovered by genome-wide association studies (GWASs).

TF-sensitive cis-regulatory elements are massively enriched in the heritability of blood cell phenotypes

Encouraged by the *CPEB4* example, we sought to examine more broadly how TF-sensitive regulatory regions were related to naturally occurring genetic variation underlying blood cell phenotypes and diseases. We began by noting that TF-sensitive ACRs are under greater constraint (lower rate of genetic variation) (*39*) compared with the nonaccessible genome (Fig. 4A and materials and methods). Furthermore, for several TFs, the average constraint for TF-sensitive ACRs was higher than for non–TF-sensitive ACRs. This suggested that the TF-sensitive ACRs may play key, conserved functional roles in hematopoiesis.

We explored whether genetic variants associated with blood cell phenotypes were enriched in the TF-sensitive ACRs by examining how credible sets for each trait overlapped with TF-sensitive ACRs, non–TF-sensitive ACRs, and random genomic regions. We found that, averaged across traits, the proportion of regions that contained a variant in a credible set for a trait was much higher for TF-sensitive ACRs (50.59%) than for non–TF-sensitive ACRs (39.25%) and random genomic regions (22%) (Fig. 4B). When we examined the results for individual TFs and traits, we found striking differences. The highest proportion was 65.75% for TF-sensitive ACRs containing variants in credible sets for basophil number (Fig. 4B, figs. S8F and S9, and materials and methods).

For each of the blood cell traits, we also examined the proportion of heritability explained by SNPs in various regions, using partitioned linkage disequilibrium score regression (LDSC) (materials and methods). We examined four types of ACRs: (i) TF-sensitive ACRs active during erythroid differentiation, (ii) all TF-sensitive ACRs, (iii) all ACRs active during erythroid differentiation, and (iv) all ACRs observed in both erythroid and non-erythroid cells (materials and methods and fig. S8C). Although TF-sensitive ACRs active during erythroid differentiation comprise <0.3% of the genome, heritability in these regions showed ~100-fold enrichment for several traits—that is, 22.25% of the heritability for erythroid traits lies in this small proportion of the genome (Fig. 4, C and D). By contrast, the ACRs active during erythroid differentiation and all TF-sensitive ACRs showed lower enrichment (up to ~46-fold and ~26-fold enrichment for certain traits, respectively) (Fig. 4, C and D). We observed similar trends for posterior probability distributions of fine-mapped variants (fig. S10). The set of all ACRs comprises much more of the genome (7.24%) and explains more of the heritability (~79%), but the enrichment is much lower (~11-fold) (Fig. 4, C and D). Notably, the TF-sensitive ACRs active during erythroid differentiation were also significantly enriched in TF binding motifs compared with all ACRs active during erythroid differentiation (fig. S8, D and E). Furthermore, we observed that credible sets of GWAS variants that lie within the TF-sensitive regions showed clear patterns of cell type–specific enrichments for their respective traits, unlike other variants (Fig. 4E and materials and methods). These results suggest a critical role for TF-sensitive ACRs and the associated variants lying within them in explaining the heritability of blood cell phenotypes.

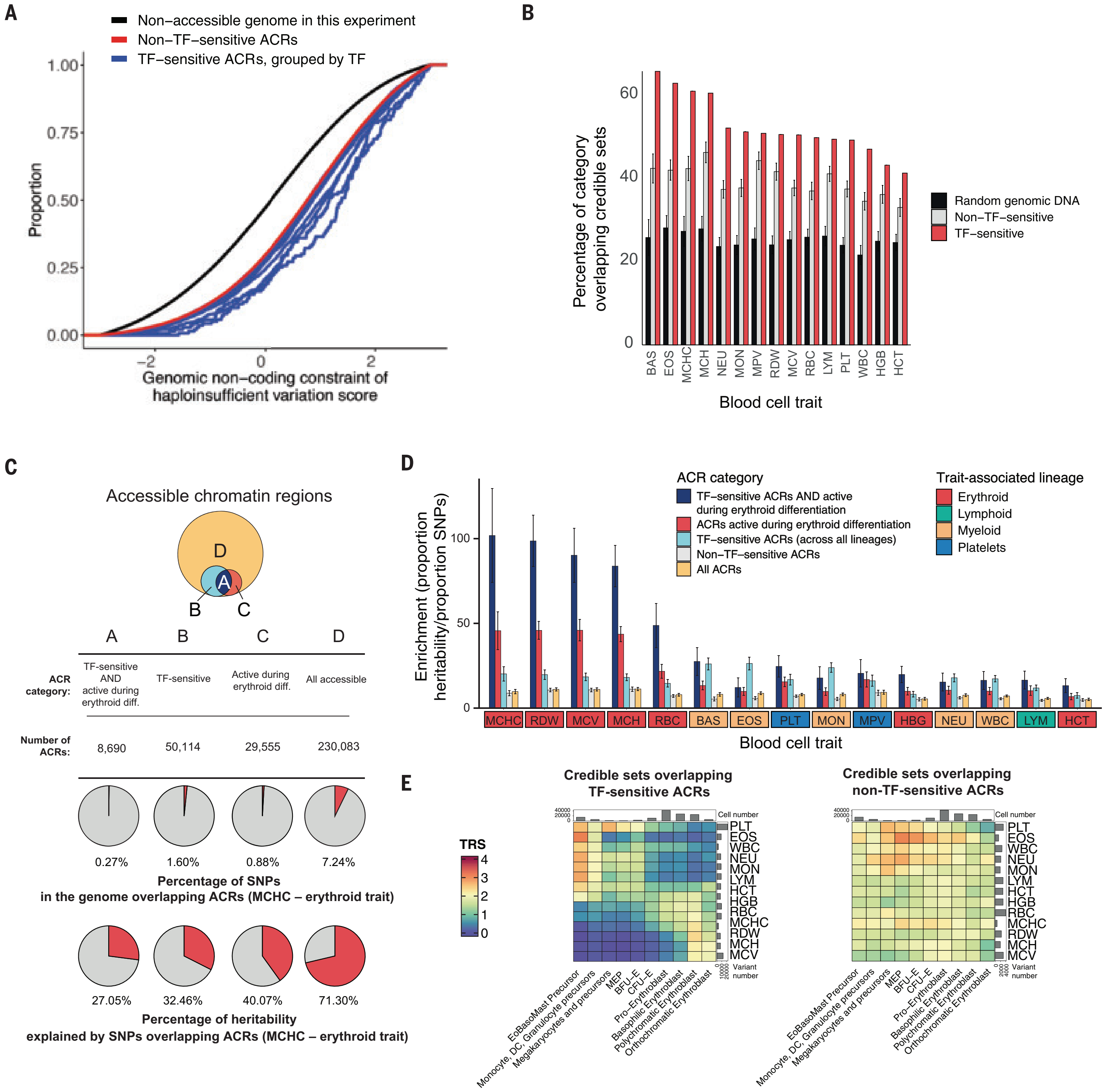

Fig. 4. Characterization of genetic variation within TF-sensitive cis-regulatory elements. (**A**) Cumulative distribution of the genomic noncoding constraint of haploinsufficient variation score (*39*), colored by functional category. Each blue line represents all TF-sensitive ACRs for a given TF. (**B**) Bar plots for the percentage of 95% credible sets overlapping TF-sensitive ACRs, for each blood cell trait. Error bars represent the standard deviation of 100 sampling events of non-TF-sensitive accessible ACRs ("Non–TF-sensitive") or of any genomic region ("Random genomic DNA") (materials and methods). (**C**) (Top) Area-proportional Venn diagrams representing the number of total ACRs. (Middle) Percentage of SNPs in the genome that overlap ACRs for mean corpuscular hemoglobin concentration (MCHC). (Bottom) Percentage of heritability explained by SNPs overlapping ACRs. (**D**) Bar plots of the enrichment (proportion of heritability divided by the proportion of SNPs) for the four functional categories defined in (C), as well as non–TF-sensitive ACRs. Traits are colored by the respective associated lineage. (**E**) Heatmaps of the trait relevant score (TRS) (materials and methods) for variants belonging to credible sets overlapping TF-sensitive ACRs (left) and not overlapping TF-sensitive ACRs (right). Similar enrichments were observed using only variants from the 95% credible sets directly overlapping with the aforementioned elements (data not shown). Blood cell traits indicated in the figure are as follows: BAS, basophil count; EOS, eosinophil count; HCT, hematocrit; HGB, hemoglobin; LYM, lymphocyte count; MCH, mean corpuscular hemoglobin; MCHC, mean corpuscular hemoglobin concentration; MCV, mean corpuscular volume; MON, monocyte count; NEU, neutrophil count; PLT, platelet count; RBC, red blood cell count; RDW, red cell distribution width; WBC, white blood cell counts. BAS, EOS, MON, NEU, and WBC are non-erythroid myeloid traits; LYM is a lymphoid trait; PLT is a megakaryocytic trait; and HCT, HGB, MCH, MCHC, MCV, RBC, and RDW are erythroid traits.

Collectively, we found that ACRs that change in response to TF perturbation are disproportionately enriched for phenotype-relevant genetic variation. More broadly, if this is true for other complex diseases and phenotypes, it suggests that systematic mapping of TF-mediated gene regulatory networks could accelerate variant-to-function mapping.

Discussion

Understanding the molecular and functional consequences of noncoding variation is essential to dissect the mechanisms underlying complex diseases and phenotypes. These insights have proven key for the development of new diagnostic and therapeutic interventions, as recently achieved in the hemoglobin disorders by emerging gene therapies (*11*, *20*, *36*, *37*, *39*). Scalable approaches to functionalize regulatory elements and link them to large sets of candidate phenotype-associated genetic variation are critical for making progress toward these goals, especially in human tissues with complex mixtures of cells.

Analysis of genome-wide TF-sensitive regions after perturbation of 19 TFs identified a tiny subset of the genome (<0.3%) highly enriched in heritability for blood cell phenotypes, relative to hematopoietic- or erythroid-specific accessible chromatin. Notably, these regions overlapped an average of 51% of credible sets for blood cell traits (ranging from 41.31 to 65.75%) and had up to a 100-fold heritability enrichment for certain cell traits. In the future, expanding perturbations to more TFs will likely uncover additional enrichments for genetic variation.

Several of the TFs studied are master regulators of hematopoietic differentiation, and their perturbation results in developmental blocks (*40*–*43*). We nonetheless obtained fine-grained observations of the effects of TFs at each stage by using analytical approaches that weigh comparisons by the perturbation scores of each single cell with respect to nearest-neighbor control cells, thereby leveraging the asynchronous nature of hematopoietic differentiation and overcoming the variable efficiencies and effects of perturbations.

The TF perturbation approach is modular and compatible with alternative strategies to modulate gene expression (*44*, *45*). Endogenous tagging of TFs with degrons or related approaches could explore the immediate consequences of TF degradation (*46*–*49*). However, this strategy is not currently applicable to large numbers of regulators and in HSPCs isolated from human donors (*50*). Although we focused on single perturbations per cell, future efforts using multiplexed perturbations could be used to discern the combinatorial logic of TF regulatory control (*51*, *52*). While this work was under review, additional studies reported distinct but related approaches to performing pooled perturbations with multiomic readouts in cell lines (*53*, *54*), illuminating the broad potential for these types of approaches and the possibility to expand them with additional genome perturbation tools.

We focused on the study of TF-sensitive regions and likely causal variants, which allowed us to study a larger fraction of phenotype-relevant variation beyond those that directly disrupt TF-binding motifs (*13*). These regions will be excellent candidates for saturation mutagenesis to identify functional base pairs and pinpoint causal variants. In addition, TF-sensitive networks are likely to harbor additional genes and associated regulatory elements with still-to-be-characterized critical hematopoietic functions.

We envision that the identification of TF-sensitive gene regulatory networks through perturbation approaches will help in prioritizing and understanding the mechanisms underlying a wide range of human diseases and phenotypes across many tissues and organs.

REFERENCES AND NOTES

1. D. Vuckovic *et al.*, *Cell* **182**, 1214–1231.e11 (2020).
2. M.-H. Chen *et al.*, *Cell* **182**, 1198–1213.e14 (2020).
3. B. V. Halldorsson *et al.*, *Nature* **607**, 732–740 (2022).
4. L. Yengo *et al.*, *Nature* **610**, 704–712 (2022).
5. US Food and Drug Administration, "FDA Approves First Gene Therapies to Treat Patients with Sickle Cell Disease" (2023); https://www.fda.gov/news-events/press-announcements/fda-approves-first-gene-therapies-treat-patients-sickle-cell-disease.
6. J. D. Martin-Rufino *et al.*, *Cell* **186**, 2456–2474.e24 (2023).
7. R. Cuella-Martin *et al.*, *Cell* **184**, 1081–1097.e19 (2021).
8. R. E. Hanna *et al.*, *Cell* **184**, 1064–1080.e20 (2021).
9. F. J. Sánchez-Rivera *et al.*, *Nat. Biotechnol.* **40**, 862–873 (2022).
10. S. I. Gould *et al.*, *Nat. Biotechnol.* (2024).
11. D. E. Bauer *et al.*, *Science* **342**, 253–257 (2013).
12. F. W. Albert, L. Kruglyak, *Nat. Rev. Genet.* **16**, 197–212 (2015).
13. J. C. Ulirsch *et al.*, *Nat. Genet.* **51**, 683–693 (2019).
14. A. Regev *et al.*, *eLife* **6**, e27041 (2017).
15. J. E. Rood, A. Maartens, A. Hupalowska, S. A. Teichmann, A. Regev, *Nat. Med.* **28**, 2486–2496 (2022).
16. J. A. Morris *et al.*, *Science* **380**, eadh7699 (2023).
17. G. R. Schnitzler *et al.*, *Nature* **626**, 799–807 (2024).
18. P. Y. Ting *et al.*, *Nat. Methods* **15**, 941–946 (2018).
19. R. A. Voit *et al.*, *Nat. Immunol.* **24**, 69–83 (2023).
20. S. K. Nandakumar *et al.*, *eLife* **8**, e44080 (2019).
21. L. S. Ludwig *et al.*, *Cell Rep.* **27**, 3228–3240.e7 (2019).
22. A. G. X. Zeng *et al.*, Single-cell transcriptional mapping reveals genetic and non-genetic determinants of aberrant differentiation in AML. bioRxiv 2023.12.26.573390 (2024). doi:10.1101/2023.12.26.573390
23. V. G. Sankaran *et al.*, *Science* **322**, 1839–1842 (2008).
24. A. Basak *et al.*, *J. Clin. Invest.* **125**, 2363–2368 (2015).
25. J. D. Martin-Rufino, V. G. Sankaran, *Curr. Opin. Hematol.* **28**, 269–276 (2021).
26. T. Moriguchi, M. Yamamoto, *Int. J. Hematol.* **100**, 417–424 (2014).
27. L. Jiang *et al.*, *Nat. Cell Biol.* **27**, 505–517 (2025).
28. S. Koschmieder, F. Rosenbauer, U. Steidl, B. M. Owens, D. G. Tenen, *Int. J. Hematol.* **81**, 368–377 (2005).
29. I. J. A. Peters, E. de Pater, W. Zhang, *Front. Cell Dev. Biol.* **11**, 1250827 (2023).
30. C. Weng *et al.*, *Nature* **627**, 389–398 (2024).
31. S. E. Pierce, J. M. Granja, W. J. Greenleaf, *Nat. Commun.* **12**, 2969 (2021).
32. L. S. Ludwig *et al.*, *Blood* **139**, 2534–2546 (2022).
33. A. R. Gschwind *et al.*, An encyclopedia of enhancer-gene regulatory interactions in the human genome, bioRxiv 2023.11.09.563812 [Preprint] (2023). doi:10.1101/2023.11.09.563812
34. X. Zhang *et al.*, *Mol. Cell* **78**, 506–521.e6 (2020).
35. K. Mukherjee, J. J. Bieker, *Cell Rep.* **41**, 111830 (2022).
36. Q. Qi *et al.*, *Blood* **137**, 1327–1339 (2021).
37. W. Hu, B. Yuan, H. F. Lodish, *Dev. Cell* **30**, 660–672 (2014).
38. M. E. Neugebauer *et al.*, *Nat. Biotechnol.* **41**, 673–685 (2023).
39. S. Chen *et al.*, *Nature* **625**, 92–100 (2024).
40. L. Gutiérrez *et al.*, *Blood* **111**, 4375–4385 (2008).
41. M. C. Simon *et al.*, *Nat. Genet.* **1**, 92–98 (1992).
42. D. L. Stachura, S. T. Chou, M. J. Weiss, *Blood* **107**, 87–97 (2006).
43. H. Zeng, R. Yücel, C. Kosan, L. Klein-Hitpass, T. Möröy, *EMBO J.* **23**, 4116–4125 (2004).
44. T. I. Jensen *et al.*, *Genome Res.* **31**, 2120–2130 (2021).
45. R. Schmidt *et al.*, *Science* **375**, eabj4008 (2021).
46. H. Yoon, J. C. Rutter, Y.-D. Li, B. L. Ebert, *J. Clin. Invest.* **134**, e175265 (2024).
47. Y.-D. Li *et al.*, *Nat. Chem. Biol.* **20**, 1640–1649 (2023).
48. M. Słabicki *et al.*, *Nature* **585**, 293–297 (2020).
49. A. S. Fedl *et al.*, *Nat. Immunol.* **25**, 1663–1677 (2024).
50. B. Lehnertz *et al.*, *Blood* **138**, 2642–2654 (2021).
51. R. T. Walton, Y. Qin, P. C. Blainey, CROPseq-multi: A versatile solution for multiplexed perturbation and decoding in pooled CRISPR screens. bioRxiv 2024.03.17.585235 [Preprint] (2024). doi: 10.1101/2024.03.17.585235
52. N. E. Anvar *et al.*, *Nat. Commun.* **15**, 3577 (2023).
53. E. Metzner, K. M. Southard, Y. M. Norman, *Cell Syst.* **16**, 101161 (2025).
54. R. E. Yan *et al.*, *Nat. Biotechnol.* (2024).
55. J. D. Martin-Rufino *et al.*, sankaranlab/perturb_multiome, Version v1, Zenodo (2025). doi: 10.5281/zenodo.14854259

ACKNOWLEDGMENTS

We are grateful to the members of the Sankaran and Lander Laboratories, as well as A. Guillaumet and A. Sule for valuable discussions regarding this work. **Funding:** J.D.M.-R. was supported by fellowships from La Caixa Foundation (ID 100010434), the Rafael del Pino Foundation, and the American Society of Hematology. This work was supported by the Broad Institute Gene Regulation Observatory (V.G.S.), the New York Stem Cell Foundation (V.G.S.), a gift from the Lodish Family to Boston Children's Hospital (V.G.S.), the Howard Hughes Medical Institute (V.G.S.), and NIH grants R01 DK103794, R01 CA265726, R01 CA292941, R33 CA278393, and R01 HL146500 (V.G.S.). V.G.S. is an Investigator of the Howard Hughes Medical Institute and is supported by the Jan Ellen Paradise, MD Professorship in Pediatrics from Harvard Medical School. **Author contributions:** Conceptualization, J.D.M.-R., A.C., V.G.S.; Formal analysis, J.D.M.-R., A.C., E.K., S.R.G., E.S.L., V.G.S.; Funding acquisition, J.D.M.-R, V.G.S; Investigation, J.D.M.-R., A.C., S.L., N.C., E.K., S.J., S.R.G., U.P.A., L.W., E.S.L., V.G.S.; Methodology, J.D.M.-R., A.C., E.S.L., V.G.S; Resources, S.R.G., E.S.L., V.G.S.; Software, J.D.M.-R., A.C., E.K.; Supervision, V.G.S.; Visualization, J.D.M.-R., A.C.; Writing – original draft, J.D.M.-R., A.C., V.G.S.; Writing – review & editing, J.D.M.-R., A.C., E.S.L., V.G.S., with input from all authors. **Competing interests:** V.G.S. is an advisor to Ensoma, unrelated to this work. **Data and materials availability:** Raw and processed data have been deposited at GEO (accession nos. GSE274110 and GSE274113), and the corresponding code is available in our GitHub repository (https://github.com/sankaranlab/perturb_multiome) and Zenodo (*55*).

SUPPLEMENTARY MATERIALS

science.org/doi/10.1126/science.ads7951
Materials and Methods
Supplementary Text
Figs. S1 to S14
Tables S1 to S6
References (*56*–*69*)
MDAR Reproducibility Checklist

Submitted 28 August 2024; accepted 12 February 2025
10.1126/science.ads7951

NEURODEVELOPMENT

Ectoderm barcoding reveals neural and cochlear compartmentalization

Sandra de Haan[1,2,3]†, Jingyan He[1]†, Agustin A. Corbat[1], Lenka Belicova[1], Michael Ratz[1], Elin Vinsland[4], Jonas Frisén[1], Matthew W. Kelley[2], Emma R. Andersson[1]*

Placodes and the neural crest are defining features of vertebrates. In this study, we investigate their lineages in mice using in utero approaches. We demonstrated that nanoinjection at embryonic day 7.5 targeted the ectoderm, including the future nervous system, placodes, and neural crest, allowing highly efficient manipulation of the future nervous system and inner ear. By using heritable DNA barcodes and high-throughput next-generation single-cell lineage tracing, we elucidated convergent differentiation pathways and identified distinct nervous system–, neural crest–, and otic placode–derived lineages. Clonal analyses identified early neural and cochlear compartmentalization, linking differentiated cell types to their progenitors or cellular siblings. This provides foundational insights for neuroscience and developmental biology.

The primary senses of touch, taste, sight, smell, and hearing allow us to interpret our world and communicate with one another. These senses develop from placodes and neural crest cells, pivotal vertebrate innovations that have enabled the complexity and diversity of vertebrate structures (*1*). Both are transient embryonic stem cell populations, wherein placodes are ectodermal thickenings that give rise to essential sensory organs, and neural crest cells are multipotent stem cells that contribute to a wide array of tissues including sensory organs. Understanding the lineages and differentiation of ectoderm, placodes, and neural crest cells could shed light on vertebrate evolution, inform regenerative medicine, and offer insights into the mechanisms underlying tissue development and repair. However, manipulation and study of such placodes and the neural crest in mammalian embryos has been hindered by their poor accessibility.

The mammalian cochlea is a sensory organ containing a mosaic of specialized sensory cells, the organ of Corti, which mediates hearing. The cochlea is derived from the neural crest and the otic placode, an ectodermal thickening that invaginates to form the otocyst (*2*, *3*). Loss of cochlear hair cells or associated supporting cells causes permanent hearing loss or deafness (*4*, *5*). Understanding cochlear development could guide regenerative efforts by identifying target cells for proliferation or transdifferentiation to restore hearing (*6*). Despite decades of research on cochlear cell type specification and extensive single-cell transcriptional profiling (*7*–*10*), definitive lineage tracing and mapping of relationships between individual cochlear cell types is limited (*11*, *12*) and can be confounded by convergent differentiation of similar cells such as inner and outer hair cells (*13*–*16*).

In utero barcode lineage tracing of ectoderm

To address these challenges and exhaustively lineage trace different stem cell compartments, we adapted neural plate targeting with in utero nanoinjection [NEPTUNE (*17*, *18*)] to map ectoderm, otic placode, and neural crest with next-generation single-cell lineage tracing (*19*–*21*). We injected a tdTomato-30N barcode lentiviral library into the mouse amniotic cavity at embryonic day 7.5 (E7.5) and collected whole embryos for single-cell RNA sequencing (scRNA-seq) at E9.5 and E10.5. The lentivirus integrates into the genome and each progenitor is thus labeled with a fluorophore and unique barcode that are inherited and expressed by daughter cells. scRNA-seq of tdTomato$^+$ cells enables simultaneous cell profiling, cell type assignment, and reconstruction of clonal relationships based on shared barcodes (*22*–*29*) (Fig. 1A).

We obtained 63,687 neural and epithelial cells in 31 clusters, which could be assigned to 4963 multicellular clones comprising 14,461 cells (Fig. 1, B and C). The dataset encompassed neural cell types from forebrain lineages to spinal cord domains (Fig. 1B, fig. S1, and tables S1 and S2). The most prevalent "single-cell–type" clones were composed of midbrain progenitors (346 clones, 954 cells; Fig. 1D and fig. S2A) and migrating neural crest cells (250 clones, 618 cells; Fig. 1D and fig. S2A). The most common "multiple-cell–type" clones comprised midbrain progenitor cells and the midbrain excitatory neuronal lineage (286 clones, 1005 cells; Fig. 1E and fig. S2A) or different hindbrain progenitors (166 clones, 439 cells; Fig. 1E and fig. S2A). To summarize the co-occurrence of cell-type pairs within clones, we calculated the frequencies of intersections between two cell types (Fig. 1F). Hindbrain populations contributed roughly half of retrieved clones and were strongly linked to one another, whereas midbrain and forebrain populations similarly displayed extensive internal linking (Fig. 1F and fig. S2A).

To correct for population size differences, we calculated clonal coupling scores for each cell type pair defined as the observed versus expected random sharing of barcodes (*14*, *30*). The clonal coupling *z*-score represents the deviation from random distribution in number of standard deviations. Positive values indicate higher-than-expected clone sharing, and negative values indicate lower-than-expected clone sharing (fig. S2B). The correlation between clonal coupling scores identified segregated forebrain, midbrain, hindbrain, and spinal cord lineages with coupling of progenitors and their putative fated mature cell types within each branch (Fig. 1G and table S3). Epithelial cells and neural crest cells occupied a separate branch of the tree together with three neural populations, including preoptic area progenitors and dorsal midbrain and hindbrain progenitor populations, which arise from anterior or lateral neural plate populations, respectively. These cells thus appear to arise from competence domains that are highly self-restricted already at E7.5 and that are more closely developmentally related to epithelia than to other brain regions.

In utero transduction labeled the otic vesicle (Fig. 2A), and subsetting and subclustering of 3161 *Epcam*$^+$ epithelial cells (Fig. 1B) revealed a *Tbx2*$^+$*Oc90*$^+$*Lmx1a*$^+$*Sox10*$^+$*Fbxo2*$^+$ population of presumptive otic placode or otic vesicle cells (178 cells; Fig. 2, B and C). Otic clones were rare and were predominantly otic-only clones (four clones; Fig. 2D), suggesting that the region fated to become otic placode is relatively self-restricted already at E7.5.

These results show that E7.5 in utero injection can target ectoderm contributing to neural plate, neural crest, and epithelial cells, including the otic placode. Barcode lineage tracing from E7.5 demonstrates compartmentalization of the fore-, mid-, and hindbrain and segregation of neural plate edge progenitors. To resolve otic and neural crest fates in the mature cochlea, we therefore next aimed to lineage trace the differentiated cochlea.

Cochlear targeting by E7.5 in utero injection of the mouse amniotic cavity

Otocyst formation occurs between E7.0 and E9.0 in mice (Fig. 3A) (*31*–*33*). The otic placode and neural crest are exposed to amniotic fluid and are targetable with in utero injection (Figs. 1 and 2), which should allow for labeling of their potential derivatives in the postnatal cochlea (Fig. 3, B to D). We injected lentivirus encoding fluorophores into the amniotic cavity at diferent

---

[1] Department of Cell and Molecular Biology, Karolinska Institutet, Solna, Sweden. [2] Laboratory of Cochlear Development, National Institute on Deafness and Other Communication Disorders, National Institutes of Health, Bethesda, MD, USA. [3] Department of Human Genetics, Leiden University Medical Center, Leiden, Netherlands [4] Department of Medical Biochemistry and Biophysics, Karolinska Institutet, Solna, Sweden.
*Corresponding author. Email: emma.andersson@ki.se
†These authors contributed equally to this work.

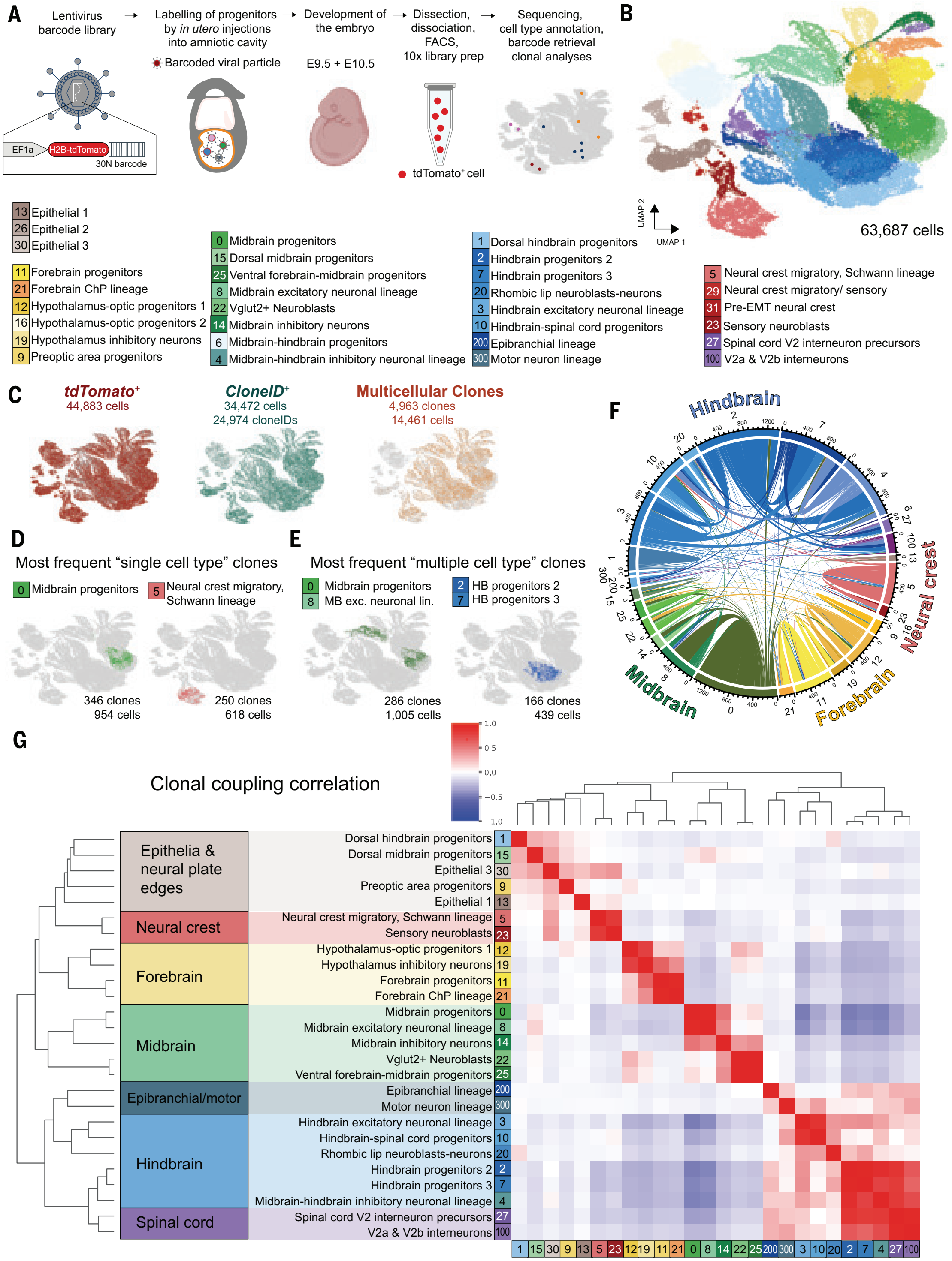

Fig. 1. Next-generation single-cell lineage tracing of mouse ectoderm with in utero barcode delivery resolves clonal coupling by neural compartment. (**A**) Workflow of in vivo barcode labeling of ectoderm by injection of a diverse barcode lentiviral library into the amniotic cavity at E7.5. Each targeted progenitor expresses a barcode coupled to tdTomato expression, which is inherited by daughter cells. Whole E9.5 and E10.5 embryos were collected and dissociated, and cells were sorted for tdTomato, followed by scRNA-seq with 10x Genomics to enable transcriptomic profiling and clonal retrieval to determine clonal relationships across ectoderm derivatives. (**B** and **C**) Uniform manifold projection (UMAP) of sorted and sequenced targeted neural and epithelial cells (B) with projected tdTomato RNA, identified barcodes assigned to CloneIDs, and identification of multicellular clones (C). (**D**) Examples of the most prevalent "private" clones, multicellular clones that contain only one cell type. (**E**) Examples of the most prevalent clones containing two or more cell types. (**F**) Circos plot depicting co-occurrences of cell pairs for all clones. Line thickness is proportional to the number of pairs. Populations with fewer than five clones total were excluded from analyses. (**G**) Hierarchically ordered heatmap of clonal coupling correlation scores. MB, midbrain; exc., excitatory; lin., lineage; HB, hindbrain.

stages and assessed labeling efficiency. Skin labeling served as a proxy for successful injections. For injections at E7.35 to E8.0, all mice with green fluorescent protein–positive (GFP$^+$) skin had GFP$^+$ cochleae (Fig. 3E). For injections between E8 and E8.5, 80% of skin-GFP$^+$ mice had GFP$^+$ cochlea (Fig. 3E), and after E8.5, only 70% of mice had GFP$^+$ cochleae, suggesting that the otic placode becomes less accessible for targeting from E8.0 onwards (Fig. 3E). High-titer lentivirus [1×10^{10} to 2×10^{10} infectious units (ifu)/mL] injected between E7.35 and E7.5 resulted in up to 93% targeting of hair cells (88.3 ± 3.7, mean ± SD; Fig. 3, F and G), and mosaic hair cell targeting was achieved with lower-titer lentivirus or with later–time point injections (Fig. 3, F and H). Supporting cells were targeted in a similar fashion (fig. S3).

We assessed cell type targeting using mosaic tdTomato–nuclear localization signal transduction (Fig. 3, I to Q). All expected cell types were labeled, including hair cells and supporting cells, such as inner and outer pillar cells, Deiters' cells, and inner phalangeal cells, whereas the tympanic border cells of the basilar membrane were negative (Fig. 3, I to K). Neurons and glia were also targeted (Fig. 3L). Furthermore, in utero

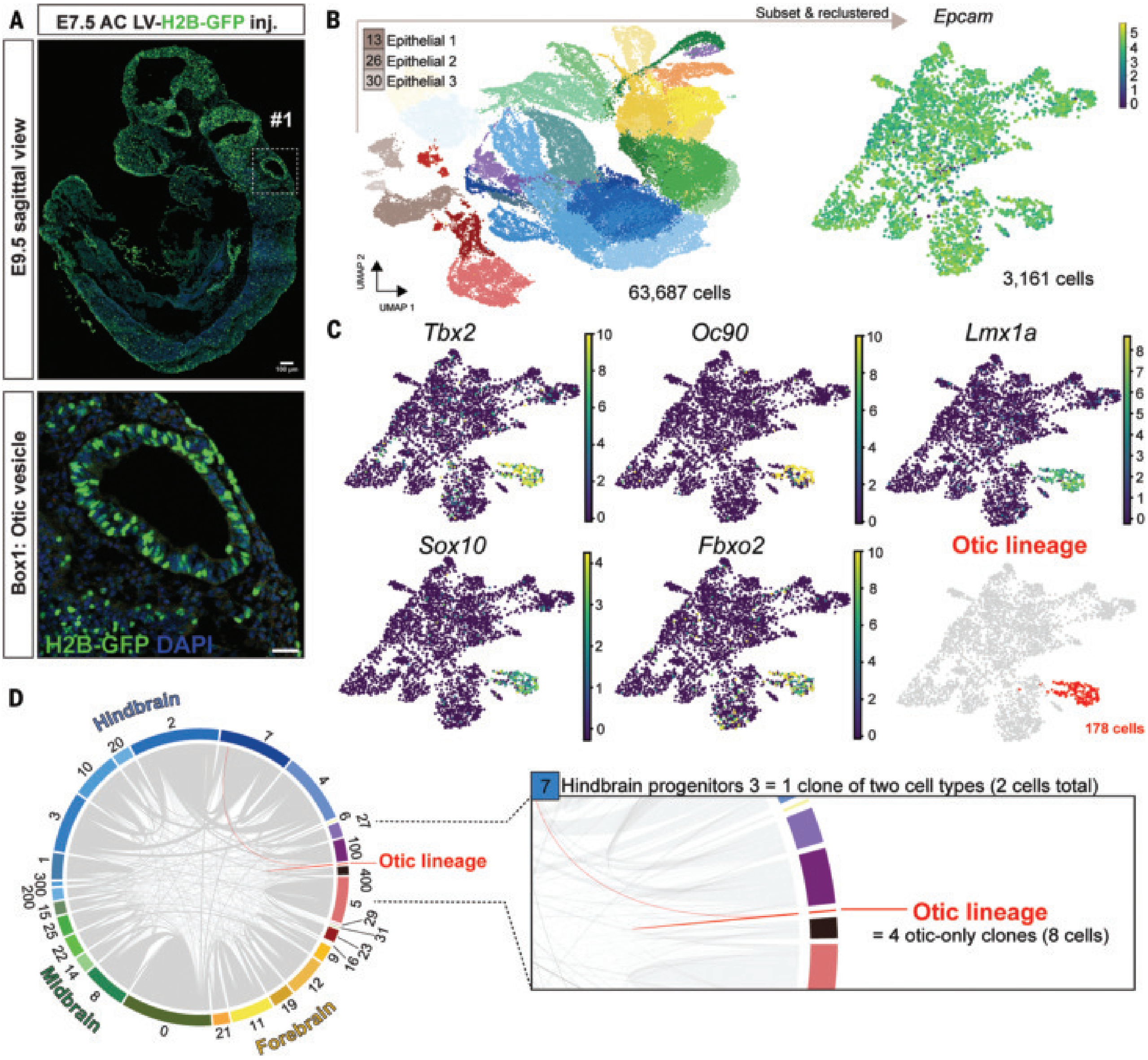

Fig. 2. Otic placode targeting with in utero transduction at E7.5. (**A**) Representative section of E9.5 whole embryo, transduced with histone 2B (H2B)–GFP lentivirus (LV) at E7.5 by in utero amniotic cavity (AC) injection (inj.). The boxed region, magnified, shows transduction of the otic vesicle. Scalebars, 100 (top) and 30 (bottom) μm. (**B**) The three epithelial clusters (clusters 13, 26, and 30) were subset and subclustered. To the right, *Epcam* amounts are shown in the subset. (**C**) Otic markers in the epithelial subset. The otic lineage subcluster is shown in red. (**D**) Circos plot depicting co-occurrences of cell pairs for all clones. Line thickness is proportional to the number of pairs. The otic population and clones are shown in the magnified portion of the circos plot.

transduction labeled Reissner's membrane epithelial cells and interdental cells but did not label spiral limbus cells derived from periotic mesenchyme (Fig. 3, M and N). Stria vascularis (SV) cells were positively labeled (Fig. 3O), as were root cells (Fig. 3P), but lateral wall (LW) mesenchymal cells were negative (Fig. 3P). The modiolus, a mesoderm-derived spongy bone structure containing spiral ganglion neurons, was negative (Fig. 3Q). Collectively, these data confirm that the otic placode and neural crest can be targeted with in utero injections into the amniotic cavity, presenting a valuable tool for investigation of their derivatives.

In utero barcode lineage tracing of the cochlea

To lineage trace otic placode and neural crest derivatives in the differentiated cochlea, we injected the tdTomato-30N barcode lentiviral library into the amniotic cavity at E7.5 and collected cochleae for analysis after birth, when differentiated cochlear cell types can be resolved with scRNA-seq (7) (Fig. 4A). Cochleae from eight pups were collected, dissociated into single cells, and processed for scRNA-seq, yielding 15,461 cells in 24 cell types or clusters, including hair cells and supporting cells of the organ of Corti, interdental cells, inner sulcus, Kölliker's organ, outer sulcus, Hensen's cells, SV cells, root cells, and Reisner's membrane epithelial cells. In addition, we recovered all subtypes of spiral ganglion neurons, periotic mesenchyme, various myelinating Schwann glia populations, satellite glia, and macrophages (Fig. 4B, fig S4, and table S4). Eighty-six percent (86.2%) of cells expressed tdTomato, spanning all cell populations, except periotic mesenchymal cells (Fig. 4C).

Clonal analysis across embryonic origins

To benchmark the clonal analyses, we assessed clonal architecture of cells with known embryonic

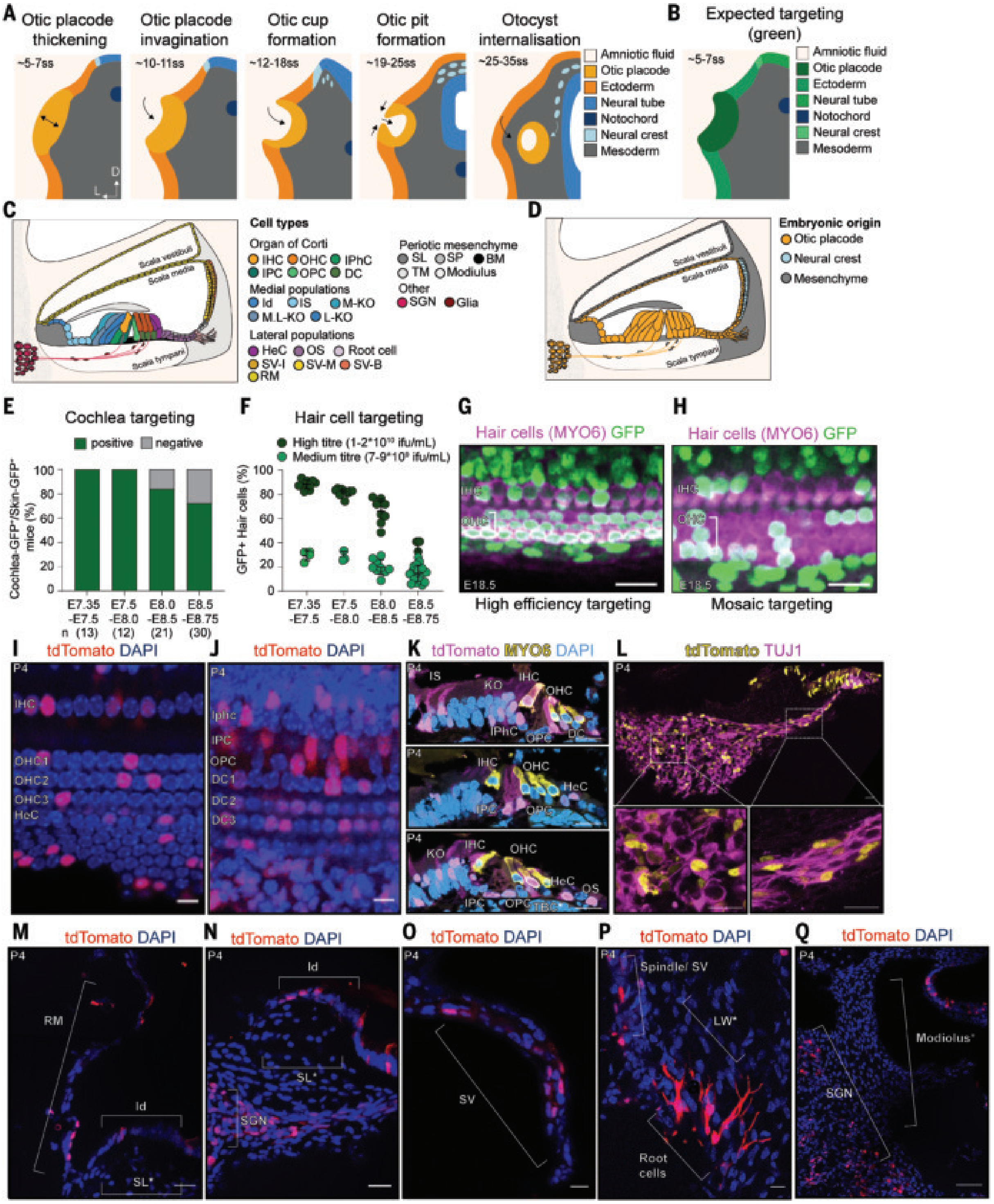

Fig. 3. Otic and neural crest derivatives in the inner ear are efficiently targeted with in utero nanoinjection at E7.5. (**A**) Otocyst formation begins with otic placode specification and subsequent thickening at the 5-7 somite stage (ss; corresponding to E7.5 to E8.75 depending on mouse strain, shown in pale orange), followed by otic vesicle invagination and internalization. In parallel, the neural crest (pale blue) delaminates from the dorsal neural tube and contributes to the developing spiral ganglion and cochlear LW. (**B**) Populations that should be accessible to H2B-GFP or H2B-tdTomato lentivirus injections at E7.5 (shades of green). (**C**) Schematic cross section of a mature cochlear duct, including the organ of Corti. (**D**) Expected embryonic origin of cell types in the cochlear duct. (**E**) Otic placode targeting efficiency, defined as the percentage of mice with GFP$^+$ cochlea or GFP$^+$ skin. *n* = number of mice analyzed in brackets under each stage. (**F**) Hair cell targeting efficiency for high and medium titer viruses, defined as percentage of GFP$^+$ hair cells per total hair cells. Each datapoint represents one transduced embryo or collected mice. (**G** and **H**) Representative examples of high-efficiency hair cell targeting after injection of high-titer virus (207 nl of 1.8 × 10^{10} ifu/mL at E7.5) (G) and mosaic targeting after injection of medium-high–titer virus (276 nl of 7.8 × 10^9 ifu/mL at E8.5) (H) in wholemount immunofluorescence (GFP, green) for hair cells (MYO6, magenta) at E18.5. (**I** and **J**) Optical slices from confocal stacks of

postnatal cochlear wholemounts from embryos transduced at E7.5 to E8.0 and collected at postnatal day 4 (P4), showing tdTomato$^+$ cells (red) and nuclei [4′,6-diamidino-2-phenylindole (DAPI), blue] in the hair cell layer (I) and underlying supporting cells (J). (**K**) Cross sections of the organ of Corti from embryos transduced with tdTomato lentivirus at E7.5 and collected at P4, showing tdTomato (magenta) expression in hair cells (MYO6, yellow), supporting cells, and in cells medial and lateral to the organ of Corti. (**L**) Cross sections of cochlea from embryos transduced with tdTomato lentivirus at E7.5 and collected at P4, showing tdTomato$^+$ (yellow) spiral ganglion neurons (Tuj1, magenta; left higher-magnification panel) as well as glia surrounding neuronal protrusions (right higher-magnification panel). (**M** to **Q**) Cross section of cochlea showing targeting of cell types outside of the organ of Corti. Scale bars, 20 μm. Data are means with SD. BM, basilar membrane; D, dorsal; DC, Deiters' cell; HeC, Hensen's cells; IHC, inner hair cells; Id, interdental cells; IPC, inner pillar cells; IPhC, inner phalangeal cells; IS, inner sulcus; L, left; L-KO, lateral Kölliker's organ; M-KO, medial Kölliker's organ; M.L-KO, mediolateral Kölliker's organ; OHC, outer hair cells; OPC, outer pillar cells; OS, outer sulcus; RM, Reissner's membrane epithelial cells; SC, supporting cell; SGN, spiral ganglion neurons; SL, spiral limbus; SP, spiral prominence; SV-I, stria vascularis intermediate cells; SV-M, stria vascularis marginal cells; SV-B, stria vascularis basal cells; TM, tectorial membrane.

origins (*2*). Cells derived from otic ectoderm, including lateral Kölliker's organ or Hensen's cells, displayed similar clonal architecture, encompassing cochlear floor populations, such as hair cells and supporting cells (Fig. 4D and fig S5). By contrast, Reissner's membrane epithelial cells, otic placode cochlear roof cells, contributed to clones containing adjacent lateral SV marginal cells (Fig. 4D). Neural crest–derived SV intermediate cells shared clones with glia, as expected (Fig. 4D).

We grouped cell types into groups on the basis of their reported embryonic origin and anatomical location. Most clones were shared exclusively between cells within these groups (fig. S6). Because macrophages can engulf and clear away cells, clone sharing with macrophages might not reflect a shared embryonic origin. Resolving such barcode sharing might instead reveal macrophage activity in cochlear remodeling, but too few macrophages were recovered to draw definitive conclusions, and such studies are outside the scope of the present work. Glial and otic cell types, which are not expected to share a progenitor using this lineage tracing approach, were found together in 16 clones (<1.7% of clones) containing a total of 128 glia cells and 178 otic cells out of a total of 4535 and 9643 cells, respectively, suggesting low error and/or contamination rate (<2.2%). This contamination was likely driven by glia–spiral ganglion neuron contamination, a common issue with inner ear scRNA-seq data due to these cells' proximity (*34*–*37*). Neuronal-glial clone sharing was restricted to neuronal cells with glial gene expression (*Mbp* and *Mpz*), which represents either a neuronal subtype or is a result of glial contamination (fig. S7). These data corroborate that in utero barcode lineage tracing accurately reports shared embryonic origins with high resolution and low contamination rates.

We next systematically assessed clonal composition (Fig. 4, E and F). Of the 945 multicellular clones, 765 encompassed different cell types (shared clones, 8279 cells), whereas 180 were composed of a single cell type (private clones, 547 cells). Clones were shared between different glial cell fates; different organ of Corti cell types, organ of Corti and medial cochlear floor cell fates; and between medial and lateral populations within the organ of Corti. There were no clones with both SV marginal and intermediate cells. Hensen's cells shared clones with both cells of the organ of Corti and lateral populations, including outer sulcus cells. Root cells, a rare and relatively understudied population of cells, had a similar sharing pattern to Hensen's cells. The most frequent cell pairings encompassed different glial populations or Kölliker's organ populations with interdental and inner sulcus cells, reflecting their proliferation and abundance in the dataset. The existence of clones containing various cell types of the organ of Corti, including medial and lateral cell populations, demonstrates that the progenitors at the time of labeling were multipotent and had the capacity to differentiate into any of the cell types present in the organ of Corti. Furthermore, the data indicate that otic placode–derived cells and neural crest–derived cells had strong clonal relations within but not across origins (Fig. 4G).

Clonal coupling analyses reveal early lineage specification

Clonal coupling analysis of the entire cochlear dataset demonstrated a clear separation of glial cells and all other cell types in the dataset, with coupling z-scores less than –4, except glia-macrophage coupling scores, which ranged from 0 to less than –4 (fig. S8). Although both glia and SV intermediate cells are thought to derive from neural crest, their negative clonal coupling (z-score < –4) suggests either distinct origins or an early fate restriction within the neural crest (fig. S8). To remove possible noise from the dataset, glia and macrophages were excluded, and the data were reanalyzed (Fig. 5A). Cells physically adjacent to each other in the pseudostratified epithelium had the highest coupling scores, including inner hair cells and inner phalangeal cells, inner and outer pillar cells, outer hair cells and Deiters' cells, and outer sulcus and Hensen's cells. Hensen's cells were most strongly coupled to outer sulcus cells (coupling score or z-score =12.34; table S5) and less strongly coupled to outer hair cells (coupling score or z-score = 5.47). By contrast, outer hair cells were most strongly coupled to other outer hair cells and to Deiters' cells (coupling score or z-score = 10.32 and 9.33, respectively), whereas inner hair cells were most strongly coupled to other inner hair cells and inner phalangeal cells (coupling score or z-score = 6.21 and 5.97, respectively).

To identify groups of cells with similar clonal coupling patterns, clonal coupling correlation scores (*14*) were computed (Fig. 5B). Clonal coupling correlation analysis revealed three main branches, including (i) a branch encompassing neurons, SV intermediate cells, and cochlear roof cells; (ii) a branch encompassing medial cochlear floor cells; and (iii) a branch constituted of the organ of Corti and lateral cochlear floor cells. The third branch segregates into different physical regions of the cochlear floor, including a medial domain consisting of Kölliker's organ, interdental and inner sulcus cells, the organ of Corti containing hair cells and supporting cells, and a lateral domain consisting of Hensen's cells, outer sulcus cells, and root cells (Fig. 5C). Inner and outer hair cells, whose convergent development risks being misinterpreted in pseudotime analyses, were found to be most strongly correlated with inner phalangeal cells and pillar cells or Deiters' cells, respectively. Hensen's cells, which are sometimes considered to belong to the organ of Corti or regarded as a supporting cell subtype, exhibited the highest correlation scores with outer sulcus cells, and clonal correlation analysis grouped Hensen's cells with outer sulcus and root cells, demonstrating instead that, developmentally, Hensen's cells belong to a domain lateral to the organ of Corti (Fig. 5, A to C).

Clonal coupling analysis reveals conserved coupling across the tonotopic axis

The apex-to-base architecture of the spiral cochlea enables the separation of sound frequencies. During cochlear development, cell cycle exit and differentiation are uncoupled: cell cycle exit occurs from apex to base, whereas differentiation occurs in the base-to-apex direction, prompting the question of whether clonal architecture is maintained along this axis. To assess clonality as a function of apex-to-base architecture, we designed a Gaussian mixture model (GMM) for single-cell tonotopic assignment based on tonotopic gene expression gradients (*38*). We assessed clone sharing along the tonotopic axis for cells in the lateral domain, for cells with the highest apex or base assignment accuracy (Fig. 5, D and E; fig. S9; and table S6), for cells with balanced apex-to-base representation

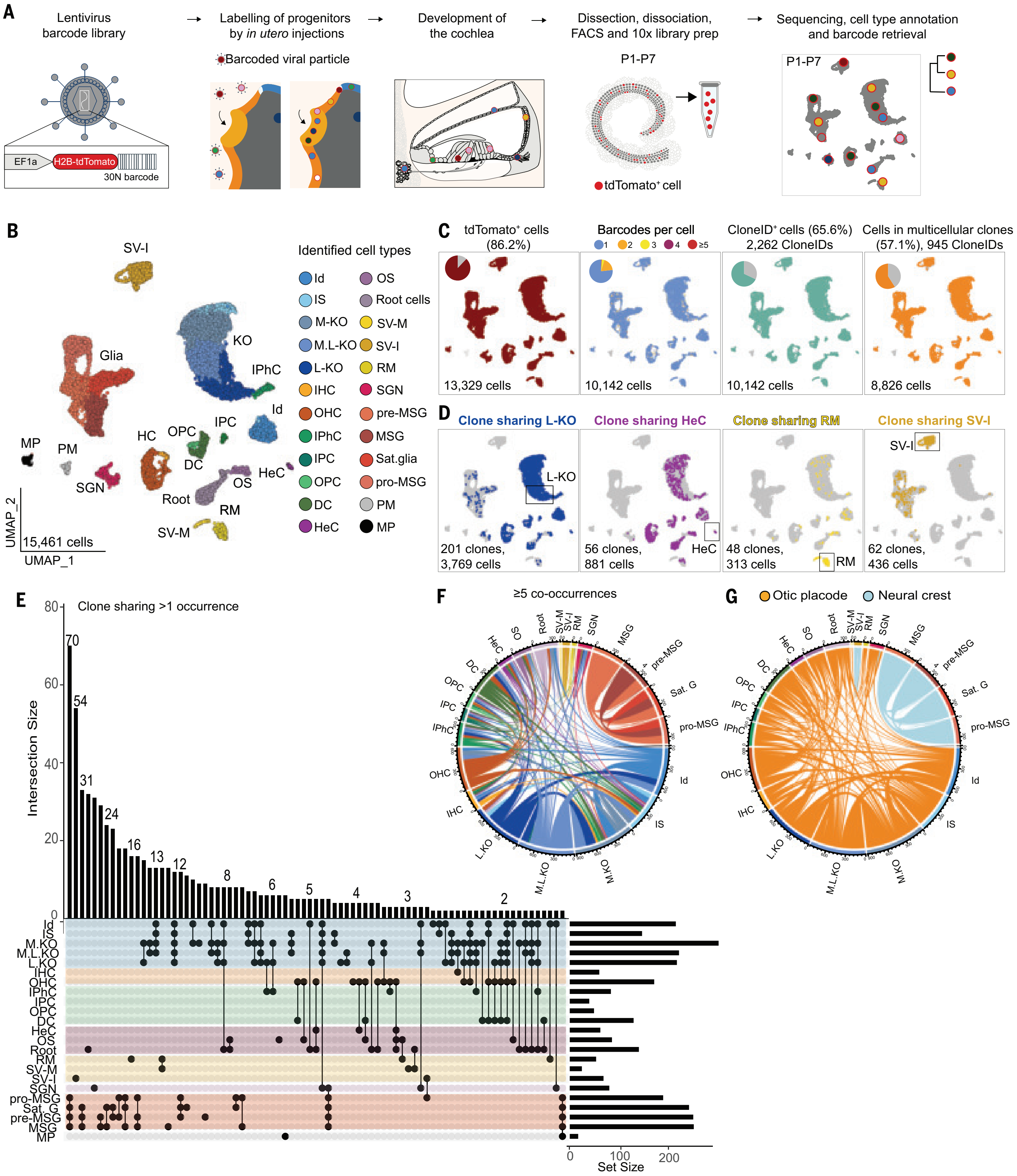

Fig. 4. Next-generation single-cell lineage tracing of cochlea with in utero transduction of otic placode and neural crest resolves segregation of embryonic origins. (**A**) Workflow of in vivo barcode labeling of cochlear progenitors by injection of a diverse barcode lentiviral library into amniotic fluid at E7.5 to E8.0. Each targeted progenitor expresses a barcode coupled to tdTomato expression, which is inherited by daughter cells that differentiate into cochlear cell types. Dissection and dissociation of cochleae from eight pups at P1 to P7 followed by scRNA-seq with 10x Genomics enables transcriptomic profiling and clonal retrieval to study clonal relationships in the postnatal cochlea. (**B**) UMAP of 15,461 cells originating from cochlea of eight transduced pups. (**C**) Barcode expression features,

including tdTomato$^+$ cells, number of barcodes per cell, cells with an assigned CloneID number, and number of cells in multicellular clones. (**D**) Clone sharing patterns for all clones, including the specified cell types. (**E**) Upset plot showing distribution for sharing patterns occurring >1 (the full set is in supplementary materials), ordered by cell type group (medial cells, blue; hair cells, orange; organ of Corti supporting cells, green; lateral cells, purple; wall populations, yellow; spiral ganglion neurons, light purple; glia, red; macrophages, gray). The set size is equivalent to the number of clones per cell type. (**F** and **G**) Circos plots depicting co-occurrences of cell pairs for clones with five or more co-occurrences (F) and colored by expected embryonic origin (G). Sat. G., satellite glia; MSG, myelinating Schwann glia.

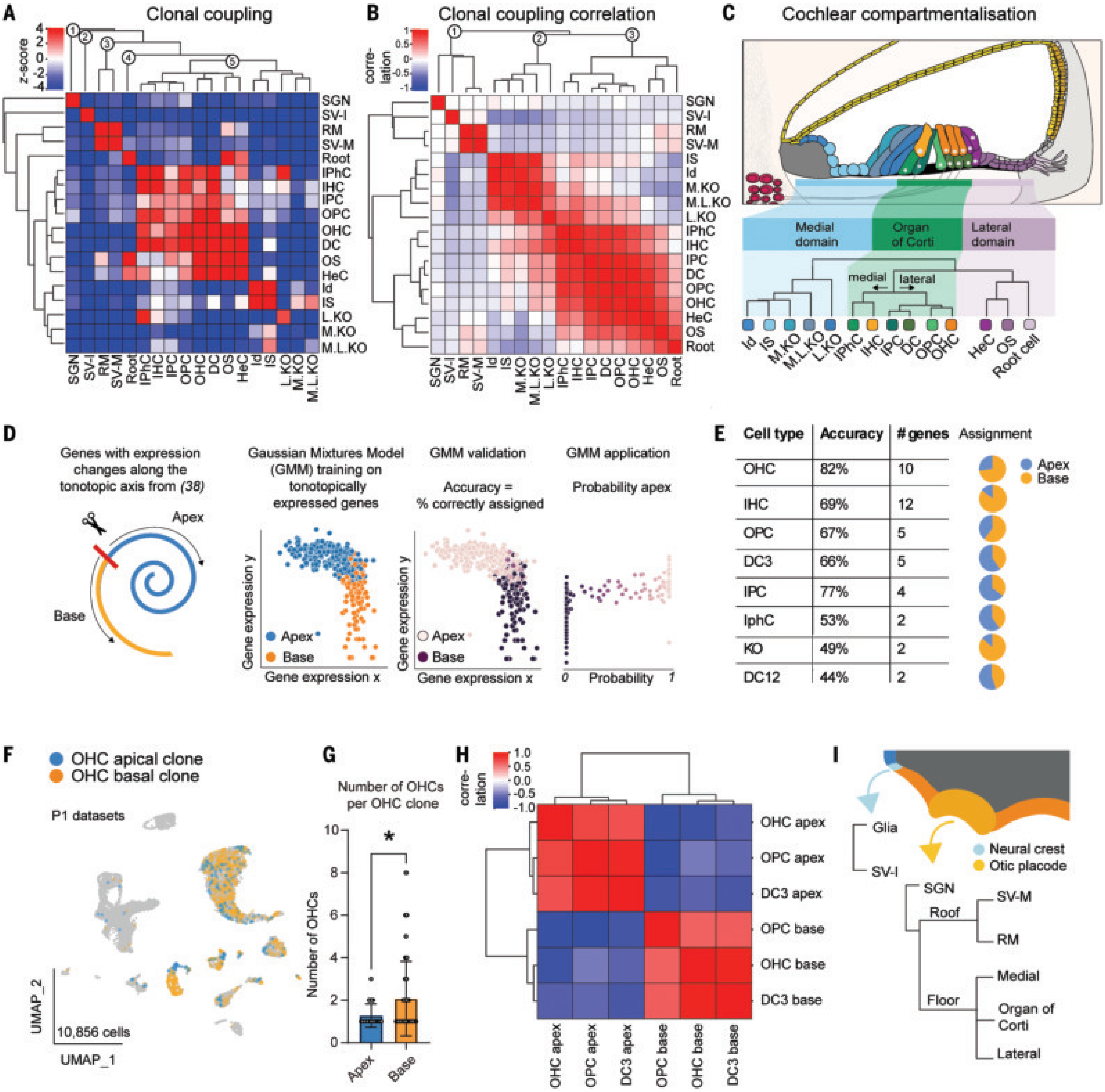

Cell type	Accuracy	# genes
OHC	82%	10
IHC	69%	12
OPC	67%	5
DC3	66%	5
IPC	77%	4
IphC	53%	2
KO	49%	2
DC12	44%	2

Fig. 5. Clonal coupling analyses reveal cochlear compartmentalization with base expansion and preserved lineage architecture. (**A**) Hierarchically ordered heatmap of *z*-scores between cell types and dendrogram depicting the coupling of cell types. *Z*-scores <–2 (blue) and >2 (red) are considered significant. (**B**) Hierarchically ordered heatmap of clonal coupling correlation scores. (**C**) Schematic representation of dendrogram tree Branch 3 in (B). (**D**) GMM workflow for tonotopy assignment of cells based on differentially expressed genes in (*38*). (**E**) GMM accuracy in predicting apex vs base cell assignment (*38*). (**F**) UMAP of P1 datasets used for tonotopy analysis, showing clones containing apex outer hair cells (blue) and base outer hair cells (orange). (**G**) Number of outer hair cells per apex and base clone. Unpaired *t* test, *$P < 0.05$. (**H**) Clonal coupling correlation scores between apex and base outer pillar cells, outer hair cells, and row three Deiters' cells. (**I**) Clonal analysis–based model of cochlear development.

(no more skewed than 1:3 or 3:1), and in which each cell type comprised at least 50 cells, allowing for analysis of outer hair, outer pillar, and Deiters' cells. Apex and base outer hair cells shared clones with all otic populations (Fig. 5F), and, in line with the later cell-cycle exit of the base, base outer hair cell clones contained more outer hair cells (Fig. 5G). There was a clear separation of apical and basal clones, demonstrating that clone dispersion along tonotopic regions is limited, and clonal architecture is preserved (Fig. 5H).

In utero barcode labeling and clonal analysis of the otic placode and neural crest revealed separate branches of development within these progenitor pools and a series of compartmentalizations within the otic placode, ultimately generating an organ of Corti flanked by a medial and a lateral clonally coupled domain (Fig. 5I).

Discussion

This study presents a solid method to target and manipulate the ectoderm, including the neural plate, placodes, and the neural crest, contributing to sensory organ formation in mice with in utero injection prior to otic placode invagination and neural crest delamination. This approach overcomes previous technical barriers and paves the way to manipulation of other embryonic cranial placodes and their derivatives, including sensory organs (inner ear, demonstrated here, olfactory organ, and eyes), cranial ganglia (including trigeminal, geniculate, petrosal, and nodose ganglia derived from various placodes), and the anterior pituitary (which derives from the adenohypophyseal placode). We demonstrate the broad nervous system coverage and versatility of this method with the first high-throughput next-generation lineage analyses of the entire embryonic mouse nervous system and developing inner ear. This study reveals lineages from neural plate, otic placode, and neural crest as well as cochlear compartmentalization and resolves separate developmental lineages despite convergent hair cell differentiation. On the basis of barcode lineage tracing, we propose an otic placode embryonic origin for root cells and reclassify Hensen's cells as lateral to the organ of Corti.

Inner ear lineages have been queried in mice with Cre-based lineage tracing (*12*, *39*), tetrachimeric blastocyst aggregation (*12*), and E11.5 otocyst retroviral labeling (*11*). These studies revealed that the cochlea originates from the neural crest and otic placode and provided valuable clonal insights. Retroviral otocyst labeling yielded four multicellular clones from the organ of Corti (*11*), suggesting clonal coupling of hair cells to supporting cells. By using lentiviral otic barcode labeling at E7.5 and next-generation single-cell lineage tracing, we identified 945 multicellular clones, comprising 8826 cells in the cochlea. Of these, 379 clones included 1093 organ of Corti cells, allowing for in-depth clonal analyses.

Categorization of cells as supporting cell subtypes in the organ of Corti was initially based on function and/or a shared prosensory origin with hair cells (*40*). Hensen's cells have been defined as supporting cells based on SOX2 expression (*41*). Clonal coupling analyses in this study identified a separate domain lateral to the organ of Corti, with stronger coupling of Hensen's cells to outer sulcus cells. The Hensen's cells lineage thus diverges from the organ of Corti; therefore, based on lineage-based classification, Hensen's cells should not be considered an organ of Corti supporting cell. The laterally coupled domain included root cells, the embryonic origin of which is unknown, despite extensive elegant characterization with scRNA-seq (*42*). The root cells' coupling to Hensen's cells and outer sulcus cells reveals an otic placode origin for root cells. The data support a model in which three major otic placode domains, fated as early as E7.5, develop into the cochlea, with a clonally coupled organ of Corti subdomain.

Barcode-based lineage tracing faces several limitations (*19*–*21*), including loss of barcoded cells during dissociation, fluorescence-activated cell sorting, droplet encapsulation, or library preparation. However, cell loss rates should be similar to conventional scRNA-seq, a current state-of-the-art method to infer lineages by using pseudotime approaches. Pseudotime analyses struggle with divergent and convergent cell fates (*13*–*16*), an issue that is circumvented by next-generation single-cell lineage tracing. Accordingly, inner and outer hair cells were not assigned a convergent lineage but demonstrated lineage segregation together with their flanking supporting cells. Another limitation is the lack of spatial information of cell types and their clonal information, which we instead inferred by using tonotopic gene expression. Future barcode labeling studies could preserve spatial information by indexing of cochlear regions or with spatial transcriptomics.

This study (i) establishes in utero injection as a tool to target ectoderm fated to become the nervous system, embryonic placodes, or neural crest; (ii) provides atlases of single-cell clonal relationships between cell types of the mouse embryonic nervous system and postnatal cochlea; and (iii) demonstrates compartmentalization of lineages within the nervous system and cochlea.

REFERENCES AND NOTES

1. B. M. Edens, M. E. Bronner, *Curr. Top. Dev. Biol.* **159**, 132–167 (2024).
2. E. C. Driver, M. W. Kelley, *Development* **147**, dev162263 (2020).
3. M. Montcouquiol, M. W. Kelley, *Cold Spring Harb. Perspect. Med.* **10**, a033266 (2020).
4. M. M. Mellado Lagarde *et al.*, *Proc. Natl. Acad. Sci. U.S.A.* **111**, 16919–16924 (2014).
5. A. Maraslioglu-Sperber, F. Blanc, S. Heller, *Hear. Res.* **447**, 109021 (2024).
6. F. Zheng, J. Zuo, *Hear. Res.* **349**, 182–196 (2017).
7. L. Kolla *et al.*, *Nat. Commun.* **11**, 2389 (2020).
8. S. Wang *et al.*, *Dev. Cell* **59**, 1538–1552.e6 (2024).
9. M. S. Matern *et al.*, *Cell Rep.* **42**, 112545 (2023).
10. P. Jean *et al.*, *Proc. Natl. Acad. Sci. U.S.A.* **120**, e2221744120 (2023).
11. H. Jiang *et al.*, *PLOS ONE* **8**, e69314 (2013).
12. J. Xu *et al.*, *Nat. Commun.* **8**, 15046 (2017).
13. J. C. Burns, M. C. Kelly, M. Hoa, R. J. Morell, M. W. Kelley, *Nat. Commun.* **6**, 8557 (2015).
14. D. E. Wagner *et al.*, *Science* **360**, 981–987 (2018).
15. M. M. Chan *et al.*, *Nature* **570**, 77–82 (2019).
16. A. McKenna, J. A. Gagnon, *Development* **146**, dev169730 (2019).
17. K. Mangold *et al.*, *Cell Rep. Methods* **1**, 100043 (2021).
18. K. Mangold, J. He, S. Stokman, E. R. Andersson, *J. Vis. Exp.* **180**, 63148 (2022).
19. S. VanHorn, S. A. Morris, *Dev. Cell* **56**, 7–21 (2021).
20. D. E. Wagner, A. M. Klein, *Nat. Rev. Genet.* **21**, 410–427 (2020).
21. L. Kester, A. van Oudenaarden, *Cell Stem Cell* **23**, 166–179 (2018).
22. M. Ratz *et al.*, *Nat. Neurosci.* **25**, 285–294 (2022).
23. S. Andrews, Babraham Bioinformatics - FastQC A Quality Control Tool for High Throughput Sequence Data (2019); https://www.bioinformatics.babraham.ac.uk/projects/fastqc/.
24. M. Martin, *EMBnet. J.* **17**, 10–12 (2011).
25. W. Kaisers, seqTools: Analysis of nucleotide, sequence and quality content on fastq files. R package version 1.34.0, SeqTools (2023); https://doi.org/10.18129/B9.bioc.seqTools.
26. L. Thielecke, K. Cornils, I. Glauche, *Bioinformatics* **36**, 2189–2194 (2020).
27. M. D. Young, S. Behjati, *Gigascience* **9**, giaa151 (2020).
28. C. S. McGinnis, L. M. Murrow, Z. J. Gartner, *Cell Syst.* **8**, 329–337.e4 (2019).
29. S. L. Wolock, R. Lopez, A. M. Klein, *Cell Syst.* **8**, 281–291.e9 (2019).
30. R. C. Bandler *et al.*, *Nature* **601**, 404–409 (2022).
31. M. Anniko, S. O. Wikström, *Am. J. Otolaryngol.* **5**, 373–381 (1984).
32. T. Ohyama, A. K. Groves, *Genesis* **38**, 195–199 (2004).
33. C. S. Jayasena, T. Ohyama, N. Segil, A. K. Groves, *Development* **135**, 2251–2261 (2008).
34. B. R. Shrestha *et al.*, *Cell* **174**, 1229–1246.e17 (2018).
35. C. Petitpré *et al.*, *Nat. Commun.* **9**, 3691 (2018).
36. T. R. Sanders, M. W. Kelley, *Proc. Natl. Acad. Sci. U.S.A.* **119**, e2203935119 (2022).
37. S. Sun, C. Siebald, U. Müller, *Curr. Opin. Otolaryngol. Head Neck Surg.* **29**, 391–399 (2021).
38. J. Waldhaus, R. Durruthy-Durruthy, S. Heller, *Cell Rep.* **11**, 1385–1399 (2015).
39. L. Freyer, V. Aggarwal, B. E. Morrow, *Development* **138**, 5403–5414 (2011).
40. G. Wan, G. Corfas, J. S. Stone, *Semin. Cell Dev. Biol.* **24**, 448–459 (2013).
41. E. Chrysostomou *et al.*, *J. Neurosci.* **40**, 9401–9413 (2020).
42. S. Gu *et al.*, *Sci. Rep.* **10**, 18100 (2020).
43. L. Belicova, J. He, P. Zydowicz-Machtel, E. Andersson, Barcode library sequencing from a plasmid amplicon - supplementary files, Zenodo (2024); https://doi.org/10.5281/zenodo.14223943.
44. L. Belicova, J. He, P. Zydowicz-Machtel, E. Andersson, Lentiviral barcode library sequencing - supplementary files, Zenodo (2024); https://doi.org/10.5281/zenodo.14223303.

ACKNOWLEDGMENTS

We thank members of the Andersson and Kelley labs for their constructive input, S. Linnarsson for cell type annotation support, B. Semsch and J. Sun for helping with colony maintenance and in utero injections, and P. Zydowicz-Machtel for assisting with barcode library characterization. The data handling and computations were performed on resources provided by the Swedish National Infrastructure for Computing (SNIC) or the National Academic Infrastructure for Supercomputing in Sweden (NAISS) at UPPMAX. We acknowledge NBIS/SciLifeLab for support through the Bioinformatics Peer Review Support track. **Funding:** Karolinska Institutet-NIH Doctoral Student funding 2017_7 (E.R.A., M.W.K.); Karolinska Institutet Starting Grant 2016-2019 2-560/2015-280 (E.R.A.); Karolinska Institutet Grant for Salary 2020-2021 2-2110/2019-7 (E.R.A.); Karolinska Institutet Consolidator Grant 2022-2026 2-195/2021 (E.R.A.); Karolinska Institutet StratNeuro Grants (E.R.A., E.V.); European Union (BRAINTIME) (E.V.); Erling-Persson Foundation (HDCA) (E.V.); Vetenskapsrådet 2014-02770, 2017-01054, 2021-03537 (E.R.A.); Knut & Alice Wallenbergs Stiftelse 2020,0109 (E.R.A., J.F.); The Hearing Research Foundation/Hörselforskningsfonden FA22-0015, FA24-0014 (E.R.A.); Horizon Europe, MSCA, grant agreement ID 101057846 (L.B.); Wallenberg Bioinformatics Support (E.R.A., L.B.). **Author contributions:**

Conceptualization: S.d.H., J.H., A.A.C., M.W.K., E.R.A.; Methodology: S.d.H., J.H., A.A.C., L.B., M.R., E.V., J.F., M.W.K., E.R.A.; Investigation: S.d.H., J.H., A.A.C., E.V., M.W.K., E.R.A.; Visualization: S.d.H., J.H., A.A.C., L.B., E.R.A.; Funding acquisition: M.W.K., E.R.A.; Project administration: M.W.K., E.R.A.; Supervision: M.W.K., E.R.A.; Writing – original draft: S.d.H., A.A.C., E.R.A.; Writing – review & editing: S.d.H., J.H., A.A.C., L.B., E.V., M.W.K., E.R.A. **Competing interests:** J.F. is a consultant to 10x Genomics. The remaining authors declare that they have no competing interests. **Data and materials availability:** All processed sequence files, derived data, and code are available in various online repositories. scRNA-seq data was deposited in Array Express (https://www.ebi.ac.uk/biostudies/arrayexpress). At Annotare/ArrayExpress, E9.5 and E10.5 embryo data can be found with accession number E-MTAB-14817, and cochlea data, with accession number E-MTAB-14691. Raw and processed barcode library sequencing files are accessible on Zenodo: barcode library sequencing from a plasmid amplicon (*43*) and lentiviral barcode library sequencing (*44*). The Trex workflow is available on Github (https://github.com/frisen-lab/TREX), as is the code to process the E9.5 and E10.5 data (https://github.com/Emma-R-Andersson-Lab/E9.5-and-E10.5-embryo-lineage-tracing), the code to process cochlea clonal data (https://github.com/Emma-R-Andersson-Lab/DeHaan-et-al-Trex_Cochlea), and the code for tonotopy analysis (https://github.com/Emma-R-Andersson-Lab/deHaan_Apex_vs_Base_2024). All data and associated analytical processes are thus either included in the manuscript or deposited as described above. **License information:**

SUPPLEMENTARY MATERIALS

science.org/doi/10.1126/science.adq9248
Materials and Methods
Figs. S1 to S10
Tables S1 to S7
MDAR Reproducibility Checklist

Submitted 10 July 2024; accepted 12 February 2025
10.1126/science.adq9248

CHEMICAL BIOLOGY

Protein editing using a coordinated transposition reaction

Yi Hua†, Nicholas E. S. Tay†, Xuanjia Ye, Jeremy A. Owen, Hengyuan Liu, Robert E. Thompson, Tom W. Muir*

Protein engineering through the ligation of polypeptide fragments has proven enormously powerful for studying biochemical processes. In general, this strategy necessitates a final protein-folding step, constraining the types of systems amenable to the approach. Here, we report a method that allows internal regions of target proteins to be replaced in a single operation. Conceptually, our system is analogous to a DNA transposition reaction but uses orthogonal pairs of engineered split inteins to mediate the editing process. This "protein transposition" reaction is applied to several systems, including folded protein complexes, allowing the efficient introduction of a variety of noncoded elements. By carrying out a molecular "cut and paste" under native protein-folding conditions, our approach substantially expands the scope of protein semisynthesis.

The ability to assemble proteins from synthetic and recombinant fragments, i.e., semisynthesis, has had a tremendous impact on the biomedical sciences. Through the introduction of unnatural amino acids, posttranslational modifications (PTMs), spectroscopic and biochemical probes, as well as combinations thereof, protein semisynthesis provides the means to tackle mechanistic problems that are difficult to address using other approaches (*1*). Despite these attributes, not every protein is a good candidate for in vitro semisynthesis using current strategies. Whereas the size of the protein of interest is usually not a deciding factor, the location of the desired modification site within the primary sequence often can be. Most studies have focused on the installation of modifications within the N- or C-terminal proximal regions of the protein because this requires a single ligation step using a short, synthetically accessible peptide fragment. By contrast, the introduction of modifications into the interior of a protein through semisynthesis is much more challenging, requiring multiple ligation steps using three or more fragments (Fig. 1A). As with any multistep process, the overall yield can be modest due to accumulated losses during each successive ligation and purification step. Moreover, generation of the necessary fragments can be nontrivial. This is especially true for the flanking recombinant protein segments, which, lacking the ability to adopt a native fold, can be difficult to isolate in useful amounts (*2*, *3*). Irrespective of the number of ligation steps used, the final protein product must be able to efficiently fold into its native state after assembly of the fragments. This can be challenging for many proteins and multisubunit protein complexes under in vitro conditions (*4*, *5*). Thus, there remain numerous systems in which in vitro semisynthesis could be used to address specific functional or structural questions, but where the above constraints preclude such an undertaking.

Motivated by the need for a streamlined and broadly applicable method, we report here a strategy that allows for protein semisynthesis without the need for a dedicated folding step. Our approach represents a conceptual departure from previous efforts (*1*, *6*–*8*), which have involved the stepwise assembly of individually prepared and purified protein fragments (Fig. 1A). Our method takes inspiration from DNA transposition, in which an exogenous transposon sequence is inserted into a recipient locus through the action of a transposase enzyme (*9*) (Fig. 1B). To adapt transposition to a protein context, we envisioned using orthogonal pairs of split inteins that undergo protein trans-splicing (PTS) reactions (*10*) (fig. S1). PTS has been widely applied in the protein semisynthesis area (*1*), but there are only scattered reports of using this process to modify internal regions of proteins (*8*, *11*, *12*). Our previous work used a combination of naturally split and artificially split inteins to perform a one-pot protein assembly from three purified building blocks (*8*). However, the yield of this tandem PTS process was modest, making it of limited practical value. More recently, Pless and coworkers have used pairs of split inteins to modify, through a microinjection process, ion channels in individual *Xenopus* oocyte cells (*12*, *13*). Again, the estimated yields of these tandem PTS reactions are low (<5%). Building on these earlier efforts, we wondered whether the efficiency of such insertion processes could be improved by using pairs of engineered split inteins with suitably tuned and balanced properties. This would allow for a more robust "protein transposition" reaction in which a recipient protein containing strategically embedded pairs of split inteins is reacted with a "transposon" construct containing the insert of interest flanked by the complementary split intein fragments (Fig. 1C). In principle, this in vitro reaction could be performed in the context of a natively folded host protein or protein complex.

Efficient protein transposition requires matched split intein splicing kinetics

Conceivably, the proposed transposition reaction could occur through one of two pathways: (i) a stepwise mechanism, in which one intein pair engages and splices before the other, or (ii) a coordinated-type process whereby the two splicing reactions occur concomitantly from a single intermediate where both intein pairs are actively associated (Fig. 2A). The latter scenario is more desirable because it would avoid the buildup of intermediates that by definition constitute fragments of the recipient protein that could proceed down a misfolding pathway. Because both binding and splicing kinetics can vary widely for different split inteins (*14*–*20*), the choice of which pair to use in the transposition reaction was likely to be critical for optimizing the system. Thus, our initial efforts were channeled toward identifying suitable split intein pairs.

We designed a test system in which two orthogonal intein fragments, separated by a short linker containing a tobacco etch virus (TEV) protease cut site, were inserted between the model proteins, maltose binding protein (MBP) and enhanced green fluorescent protein (eGFP) (Fig. 2B and fig. S2). MBP and eGFP have no affinity for one another, minimizing any bias

---

Department of Chemistry, Princeton University, Princeton, NJ, USA.
***Corresponding author. Email: muir@princeton.edu**
†These authors contributed equally to this work.

that an interaction between the flanking regions of the recipient protein might have on the reaction pathway. This modular system allowed us to vary the split inteins used in the transposition reaction with the goal of finding an optimal pair. To reduce the size of the embedded transposition apparatus within the recipient construct, we used an atypically split intein on the N-terminal side [either Cat (*17*) or VidaL (*18*)] and a canonically split intein on the C-terminal side [Cfa (*15*)]; the former have short Int^{N} sequences, whereas the opposite is true for the latter. A series of MBP-IntA^{N}-linker-IntB^{C}-eGFP proteins were generated, along with the corresponding transposon constructs, IntA^{C}-insert-IntB^{N}, containing the model insert (HA epitope tag) flanked by the complementary split inteins (Fig. 2B and fig. S3). The matching constructs were mixed in a 1:1 ratio, and the reactions were monitored over time by SDS–polyacrylamide gel electrophoresis (SDS-PAGE) and liquid chromatography–mass spectrometry (LC-MS) (Fig. 2C and figs. S4 and S5). In all cases, we observed generation of the expected transposition products; however, the efficiency of the reaction varied as a function of the split intein pairs used (table S1). For instance, in the reaction involving the VidaL and Cfa split inteins, we observed a buildup of hemispliced intermediates formed by single intein splicing (Fig. 2C); by contrast, these intermediates were less pronounced when we used Cat and Cfa (figs. S4 and S5).

We used an experiment based on isotopic labeling and mass spectrometry to investigate the possibility that the efficiency of the transposition reaction might reflect alternate reaction pathways (Fig. 2D). ^{14}N- or ^{15}N-labeled MBP-IntA^{N}-linker-IntB^{C}-eGFP recipient proteins (fig. S6) were co-mixed at a 1:1 ratio and then reacted with corresponding transposon construct. Assuming that a coordinated pathway is taken, the transposition product should retain either ^{14}N or ^{15}N labels in both MBP and eGFP and only two peaks should be observed in the mass spectrum at a 1:1 ratio (Fig. 2E). If a purely stepwise pathway is operational, then there will be two products with uniform isotopic labeling and two with mixed labeling (Fig. 2E). Control studies that invoked the TEV cleavage site within the linker region of the recipient protein indicated that the ratio of the four isotopic products in a purely stepwise process is 1:1:1:1 (fig. S7). In the case of the reaction involving the VidaL and Cfa inteins, we observed four distinct masses within the product fraction. The ratio of these MS peaks was ~2:1:1:2, suggesting that a combination of coordinated and stepwise pathways was operational (Fig. 2F and fig. S8). When pairing Cat and Cfa, we observed fewer products generated from the stepwise pathway (fig. S9). To improve the coordinated-to-stepwise ratio, we introduced a mutant into Cfa (mut-Cfa) predicted to have slower splicing kinetics (Cfa^{N} M75L, M81L, designated Cfa$^{N}_{m}$) compared with the wild type (*15*), which would better synchronize the splicing rates to that of both Cat and VidaL (fig. S10) (*17*, *18*). Transposition reactions involving mut-Cfa and either VidaL or Cat produced two major peaks in the mass spectrum corresponding to the uniformly labeled species (Fig. 2F and figs. S8 and S9). In the case of the mut-Cfa and Cat pairing, almost all reactions occurred by a coordinated-type pathway, indicated that this pairing is well matched in terms of binding and splicing kinetics (figs. S11 to S14). Kinetic studies using a partially inactivated transposition system in which one of the intein pairs is mutated so as to prevent splicing but not association (figs. S15 to S17) indicated that the splicing kinetics of mut-Cfa and Cat are the most closely matched of the inteins used (figs. S18 to S21). Varying the ratio of reactants had minimal effect on conversion efficiency when using mut-Cfa and Cat (fig. S22). On the basis of these results, we elected to use the Cat/mut-Cfa pairing in our subsequent studies.

Protein transposition occurs seamlessly on folded proteins

To test if the transposition reaction can proceed within folded proteins, we inserted the Cat/mut-Cfa apparatus into a surface exposed loop in eGFP, specifically at position 174–175 (Fig. 3A). This site has previously been used in split eGFP constructs (*21*), and we anticipated that it would be permissive to polypeptide insertions (fig. S23A). This recipient protein was treated with the HA-embedded transposon with flanking complementary split inteins. We observed efficient protein transposition, with the embedded splicing apparatus being cleanly removed and replaced by the exogenous insert (Fig. 3B and fig. S23B). The fluorescence

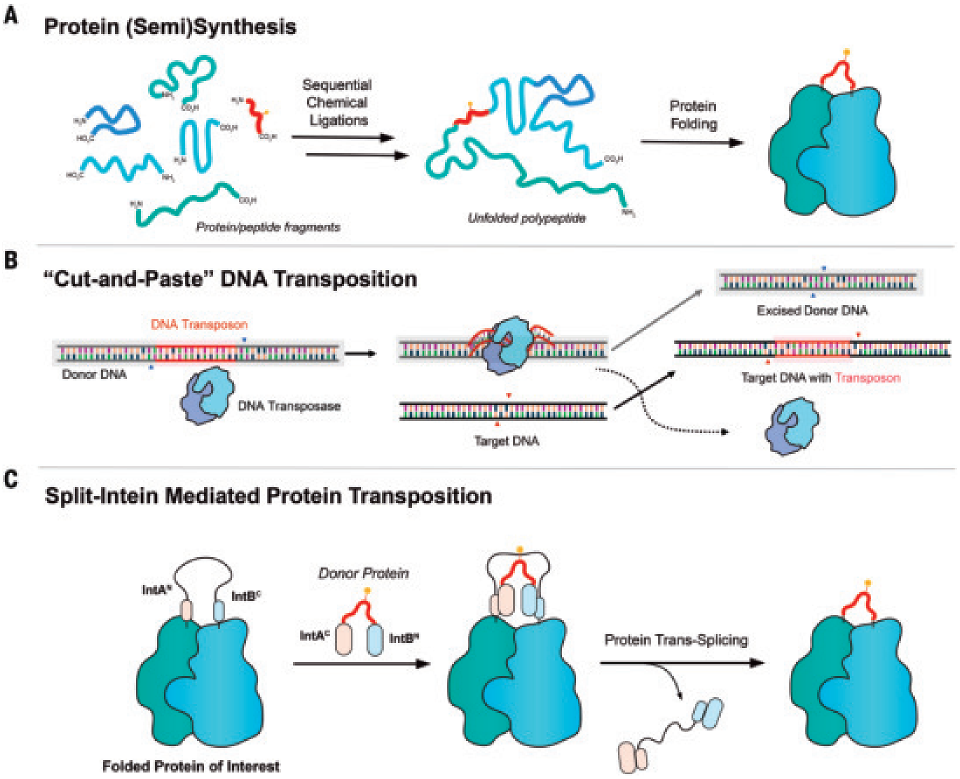

Fig. 1. Design of a split intein–mediated protein transposition reaction. (**A**) Traditional protein semi(synthesis) using the stepwise assembly of multiple peptide fragments. Accumulated losses during the multistep synthesis combined with an obligate final protein-folding step limit the scope of this approach. (**B**) Schematic showing the convenience of the "cut and paste" mechanism of DNA transposition. (**C**) A coordinated protein transposition reaction carried out by a pair of orthogonal split inteins flanking the modification site. The approach circumvents the need to generate and manipulate protein fragments and does not require a folding step.

properties of eGFP, which are highly sensitive to the native three-dimensional (3D) structure of the protein (*22*), provided a convenient means with which to monitor the folded state of the protein during the reaction. We observed no change in the eGFP emission spectrum during the reaction, which is consistent with the transposition occurring in a coordinated manner on the folded protein (Fig. 3C and fig. S23C). To explore the scope of the reaction, the embedded transposition apparatus was installed at two additional sites in eGFP, at a second surface exposed loop (position 158–159) and within a β-sheet region (position 124–125). The former was well tolerated and supported efficient protein transposition when treated with the transposon construct, whereas the latter led to misfolded protein and less-efficient transposition (fig. S24). This result suggests that our transposition reaction is best suited for polypeptide regions that are sterically accessible for intein-splicing. We also applied the transposition system to the euchromatic histone-lysine N-methyltransferase, G9a, a multidomain protein with a predicted highly disordered N-terminal region (residues 1 to 440) (*23*, *24*). We introduced the transposition apparatus into an intrinsically disordered region (IDR) of G9a (residues 161 to 208) and subsequently treated this recombinant recipient protein with the HA-embedded transposon (fig. S25). This led to efficient transposition for this system, thus highlighting the suitability of IDRs for our methodology.

To demonstrate transposition on a much larger protein, we chose the endonuclease-deficient version of *Streptococcus pyogenes* CRISPR associated protein 9 (dCas9), an ~160-kDa globular protein that has been extensively engineered for genomics applications (*25*–*27*). Specifically, we investigated whether an exogenous cassette could be transposed into a permissive site (residues 573–574 located within a loop) in the middle of the protein (Fig. 3D) (*28*). A chimeric version of the protein was generated in which the splicing apparatus, separated by a His tag, was embedded at this position (fig. S26A). We expected that this embedded His tag could be used to purify the transposition product from the recipient using a reverse nickel-affinity chromatography procedure (fig. S26B). This engineered version of dCas9 (recipient dCas9) retained its biological activity, as demonstrated by the ability to bind a target DNA sequence in the presence of a cognate guide RNA (Fig. 3F) compared with its unmodified counterpart. In initial studies, we showed that this recipient dCas9 is capable of undergoing a successful transposition reaction using the transposon containing an HA tag (fig. S27).

In principle, our approach provides the means to alter both the side chains and amide backbone of a target protein. To illustrate this point, we set about introducing a completely abiotic polymer into the dCas9 protein. The dCas9 recipient was reacted with a transposon construct in which a polyethylene glycol (PEG) chain was nested between the $\mathrm{Cat}^{\mathrm{C}}$ and $\mathrm{Cfa}^{\mathrm{N}}{}_{\mathrm{m}}$ fragments (Fig. 3D and figs. S28 and S29). This experiment necessitated the development of an efficient modular strategy for the generation of transposon constructs containing synthetic inserts of choice (fig. S28). We first validated the incorporation of the PEG chain into our model MBP-eGFP fusion protein by SDS-PAGE and electrospray ionization mass spectrometry (ESI-MS) (fig. S30), which gave us confidence that this abiotic polymer could be inserted into protein backbones. As in the previous examples, the transposition reaction proceeded smoothly, affording a backbone engineered version of dCas9 that retained its DNA-binding activity in the presence of complementary guide RNA (Fig. 3, E and F). The success of this example underscores the substantial synthetic flexibility granted by our transposition approach.

Protein transposition enables insertion of functional probes for the biochemical study of protein complexes

Next, we investigated whether our system could be used to directly engineer a protein complex. As noted earlier, proteins that reside within multisubunit complexes represent a blind spot for in vitro semisynthesis (*1*). Our strategy should help to alleviate this limitation by allowing direct manipulation of a suitable engineered preformed recipient complex. To test this, we inserted the transposition apparatus into a key regulatory region of SMARCA5, the core ATPase subunit of the ATP-dependent chromatin remodeling complex ACF (*29*–*31*). Previous studies from our group identified a central basic domain with the sequence KRERK, called the acidic patch binding (APB) motif, in this ~120-kDa protein required for chromatin-remodeling activity (*32*). The SMARCA5 recipient protein used in our studies contained the pretransposition apparatus in place of this basic domain, which ablates the APB-dependent functions of SMARCA5 (Fig. 4A). Thus, we predicted that successful reaction with a transposon construct containing this missing regulatory domain would restore the chromatin remodeling activity of the multisubunit ACF complex, i.e., transposition should act as an "on" switch. Coincubation of the transposon constructs (figs. S31 to S33) with the preformed ACF complex harboring the transposition apparatus within the SMARCA5 subunit led to the efficient generation of the expected products, which were confirmed by SDS-PAGE and Western blotting (Fig. 4B and figs. S34 and S35). Coimmunoprecipitation studies indicated that the ACF complex remained intact after the transposition reaction (fig. S35A). We then conducted chromatin-remodeling studies using a restriction enzyme accessibility assay (REAA) (*33*). Consistent with the reaction acting as an on switch, we observed that transposition restored chromatin-remodeling activity to the ACF complex (Fig. 4C).

We next used our transposition technology to study the effect of dynamic PTMs within SMARCA5. Phosphoproteomics analyses of cancer cell lines have identified a phosphorylated tyrosine residue (pTyr^{742}) that is adjacent to the SMARCA5 basic APB motif (*34*, *35*). This tyrosine residue is highly conserved in SMARCA5 homologs (fig. S36). Although the function of this PTM is not known, its location proximal to this critical domain led us to speculate that it might alter ACF-remodeling activity. Indeed, structural modeling using an available cryo–electron microscopy (cryo-EM) structure of SMARCA5 homolog ISW1 bound to the nucleosome (*36*) suggests that this phosphotyrosine is positioned to interact with basic sidechains in the APB motif, thereby affecting its function (fig. S37). To explore the functional impact of this PTM, we used our transposition system to successfully install a peptide transposon containing pTyr^{742} within the ACF complex (Fig. 4B and fig. S32). Consistent with our hypothesis, we observed a phosphorylation-dependent decrease in ACF-remodeling activity as readout by electrophoretic mobility shift assays (Fig. 4D and figs. S38 and S47).

To demonstrate that our technology could install biochemical probes into the interior of recipient proteins, we incorporated a diazirine-containing photo-methionine (photo-Met) residue adjacent to the basic domain of SMARCA5 (Fig. 4A). A transposon construct containing this cross-linker was generated and then reacted with the ACF recipient to give the expected semisynthetic ACF complex (Fig. 4B), which retains remodeling activity (fig. S39). This cross-linker probe was then exploited to gain insight into how the basic domain in SMARCA5 regulates ACF activity. Semisynthetic SMARCA5 was irradiated with ultraviolet (UV) light in the presence of a nucleosomal substrate. Immunoblotting of this reaction mixture revealed robust cross-linking to histone H2A (Fig. 4E and fig. S40), which corroborates our earlier finding of an anchoring effect of the basic region of SMARCA5 to the nucleosome acidic patch (*32*). Cross-linking between SMARCA5 and histone H2A was ablated when the photo-Met was replaced by the native Ala (fig. S40) or in the presence of an excess of the latency-associated nuclear antigen (LANA) peptide (Fig. 4E and fig. S41), which binds to the acidic patch of the nucleosome (*37*).

Because split inteins do not cross-react with mammalian proteins (*38*), we wondered whether the transposition reaction would work in a more complex cellular environment. To investigate this, the SMARCA5 recipient protein bearing an internal HA tag was expressed in human embryonic kidney (HEK) 293T cells, and the isolated nuclei from these cells were treated with the transposon construct containing a recombinant FLAG tag (fig. S42). As in

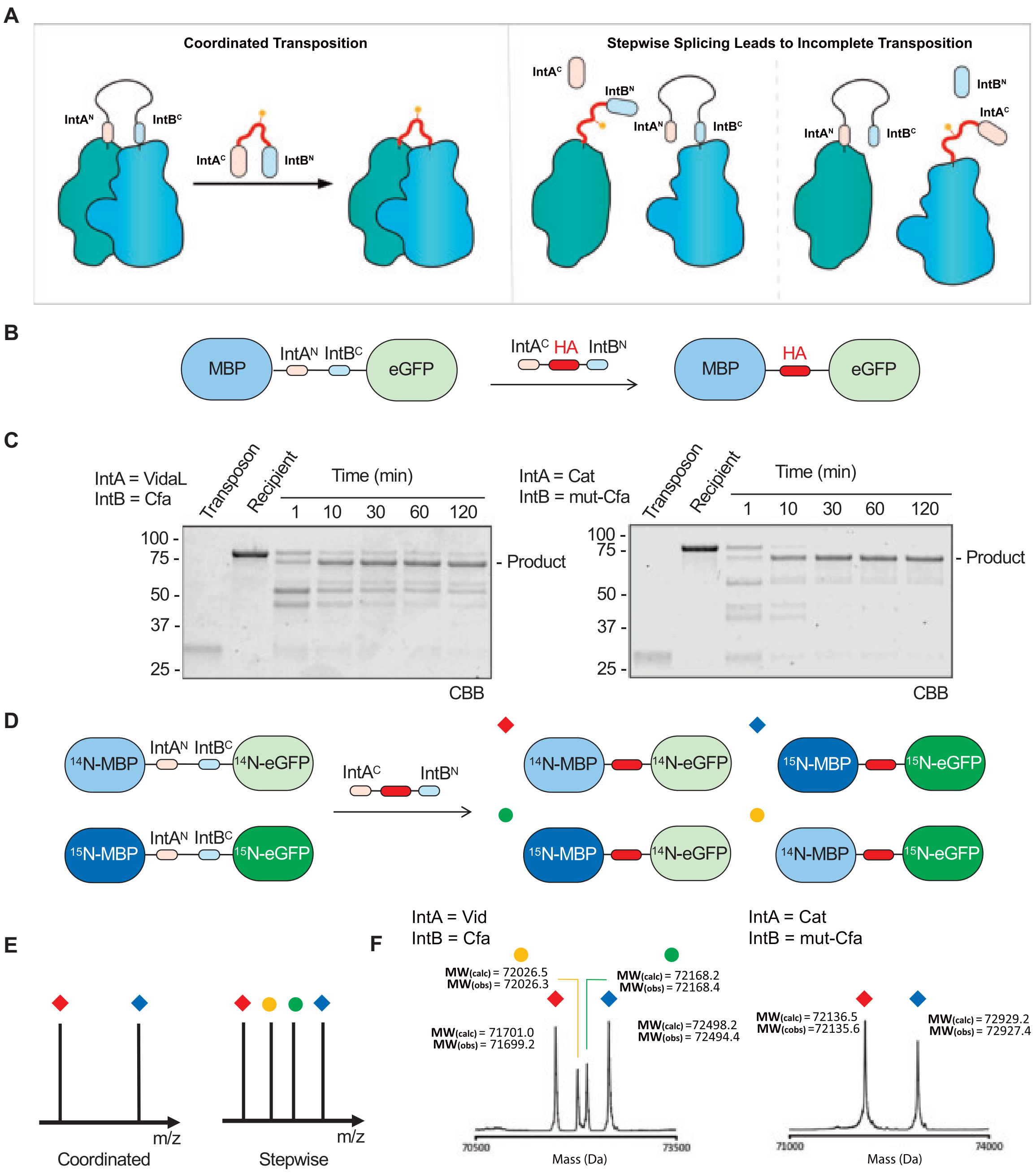

Fig. 2. Efficient protein transposition requires matched split-intein splicing kinetics. (**A**) Product outcomes for protein transposition depend on split-intein splicing kinetics. Mismatched splicing kinetics for the two split inteins can lead to a buildup of unwanted reaction intermediates. (**B**) Design of an MBP-eGFP model system for optimizing the protein transposition reaction. (**C**) Characterization of transposition reactions using the VidaL/Cfa split intein pair (left) and Cat/mut-Cfa pair (right). MBP-eGFP recipient and transposon donor constructs (2 μM of each) were reacted for the indicated times in 100 mM phosphate, 150 mM NaCl, 1 mM EDTA, and 1 mM tris(2-carboxyethyl)phosphine (TCEP), pH 7.2. Reactions mixtures were analyzed by SDS-PAGE with Coomassie blue staining (CBB). The expected transposition product is indicated. Lower bands correspond to incomplete splicing intermediates. For estimated transposition yields, see table S1. (**D**) Design of an isotopic labeling experiment to differentiate between stepwise and coordinated processes. A 1:1 mixture of uniformly ^{14}N- or ^{15}N-labeled MBP-eGFP recipient proteins are reacted with the transposon construct. Up to four different isotopic compositions in the transposition product are possible depending on the reaction pathway. These kinetic outcomes are denoted by colored balls. (**E**) Anticipated product mass spectrometry readout distinguishing the coordinated versus stepwise transposition pathways. (**F**) Mass spectrometry characterization of transposition products in an isotopic labeling experiment for different intein pairs. Each isotopically labeled recipient (2 μM total) is reacted with an equimolar amount of HA tag transposon (2 μM) for 2 hours in 100 mM phosphate, 150 mM NaCl, 1 mM EDTA, and 1 mM TCEP, pH 7.2. After the transposition, the products were isolated by reversed-phase high-performance liquid chromatography (RP-HPLC), and the isotopic compositions were detected by ESI-MS and deconvoluted. These experiments reveal that the VidaL/Cfa split intein pair proceeds through a stepwise process, whereas the Cat/mut-Cfa pair enables almost fully coordinated transposition.

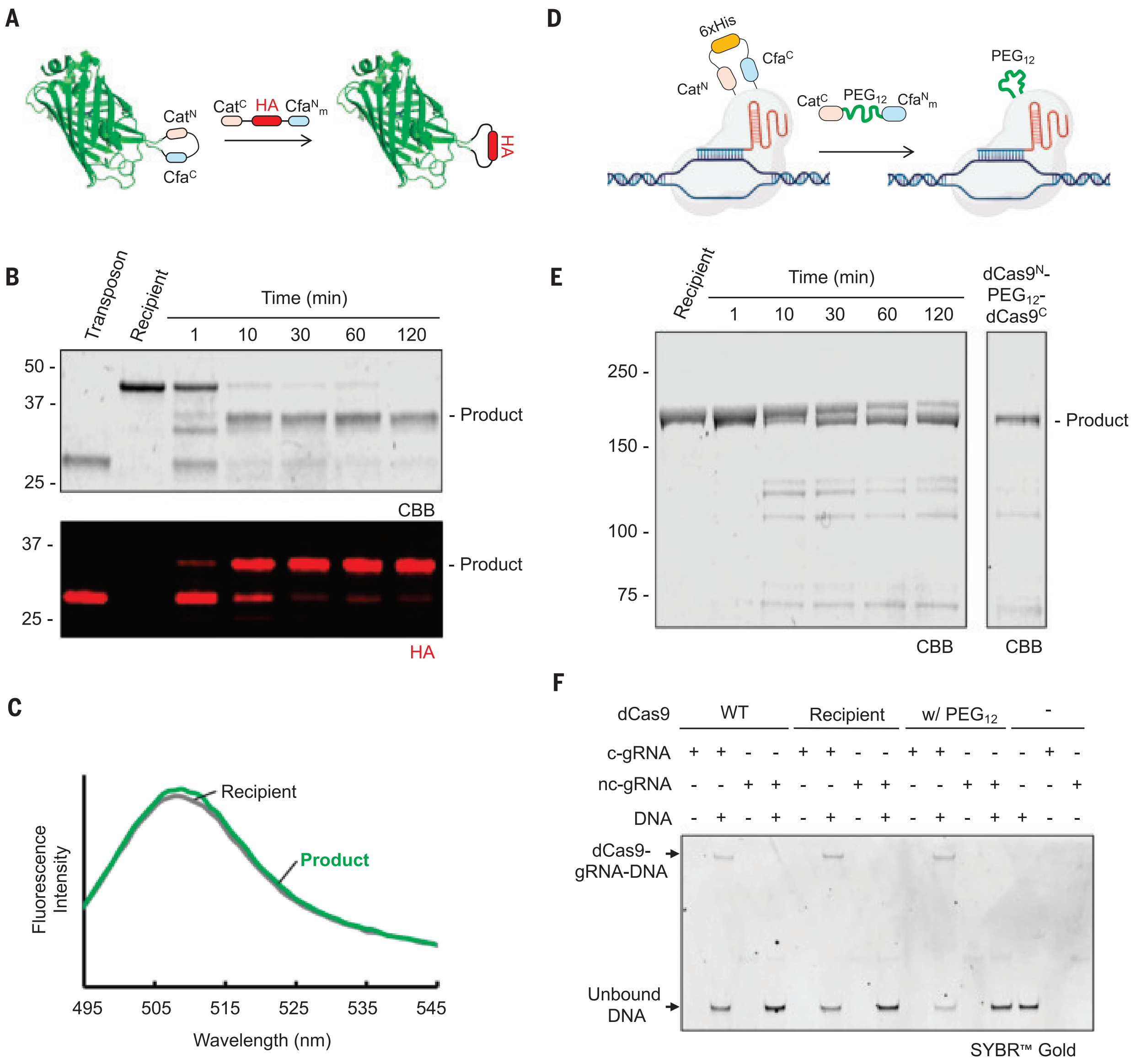

Fig. 3. Protein transposition enables traceless installation of protein tags and chimeric cargo on folded proteins. (**A**) Scheme illustrating the transposition reaction on an internal loop of eGFP. (**B**) eGFP recipient and HA tag transposon constructs (2 μM each) were reacted for the indicated times in 100 mM phosphate, 150 mM NaCl, 1 mM EDTA, and 1 mM TCEP, pH 7.2. Reactions mixtures were analyzed by SDS-PAGE with CBB staining and Western blotting with the anti-HA antibody. The expected transposition product is noted in both analyses. For estimated transposition yields, see table S1. (**C**) Fluorescence emission spectra (λ_{ex} = 488 nm) of the recipient eGFP protein before and after the transposition reaction. (**D**) Schematic of the transposition reaction within the dCas9 fold using Cat/mut-Cfa orthogonal split intein pair. In the example shown, the 6x His tag inside the recipient dCas9 gets replaced by a PEG_{12} abiotic polymer, enabling purification of the product from the unreacted recipient. (**E**) Analysis of the dCas9 transposition reaction involving a PEG_{12}-containing transposon construct. Recipient dCas9 and PEG_{12} transposon constructs (1.5 μM each) were reacted for the indicated times in 50 mM Tris, 250 mM NaCl, 1 mM TCEP, and 10% v/v glycerol, pH 7.5. Reaction mixtures were further purified by reverse nickel-affinity chromatography. Both the reaction progress (left) and the purified product (right) were analyzed by SDS-PAGE with CBB staining, and the expected product is indicated (see also table S1). (**F**) DNA-binding activity of dCas9 constructs. A wild-type dCas9 without any transposition construct, the recipient dCas9, and the purified dCas9 containing PEG_{12} after transposition were mixed with DNA in the presence of the complementary guide RNA (c-gRNA) or noncomplementary guide RNA (nc-gRNA), and their DNA-binding capability was characterized by 5% native Tris-borate EDTA (TBE) gel electrophoresis with SYBR gold staining.

the in vitro examples, we observed highly efficient transposition (Fig. 4F). Encouraged by this result, we sought to reproduce this system in live cells. Coexpression of the SMARCA5 recipient protein and the FLAG-tag–containing protein transposon resulted in the successful transposition of the polypeptide cassette into the recipient protein (fig. S43). These experiments with SMARCA5 and the ACF complex highlight the broad applicability of protein transposition from in vitro biochemical studies to experiments in more complex settings.

A key consideration for the successful deployment of protein transposition will be the identification of permissive sites within the recipient in which to embed the split inteins. Clearly, not every location in a target protein will tolerate the insertion of the necessary transposition apparatus. The current protein transposition system necessitates the presence of a small number (two to four residues) of favorable

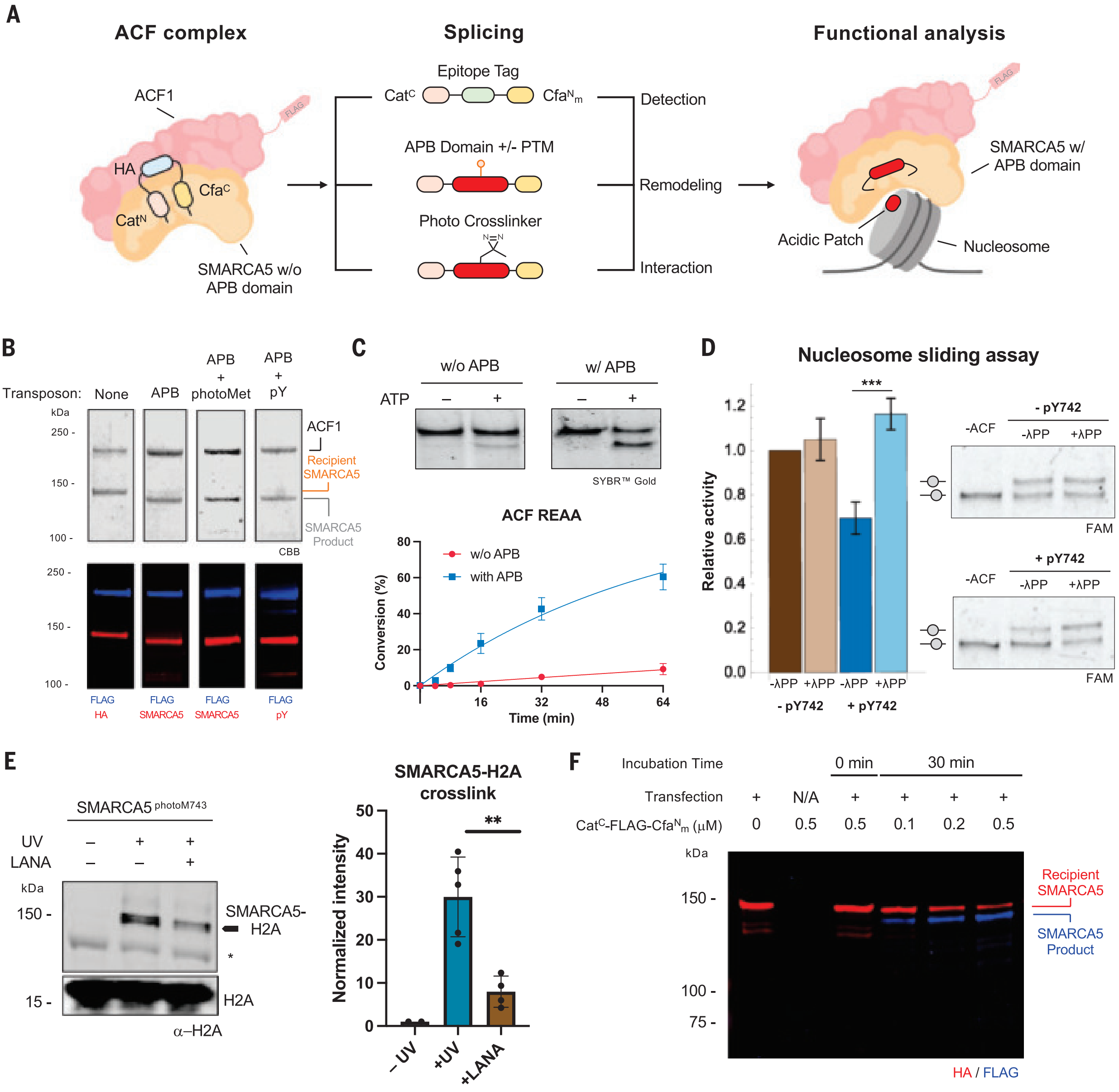

Fig. 4. Protein transposition on SMARCA5 and ACF complex enables functional evaluation of remodeling activity and binding preferences. (**A**) Scheme illustrating protein transposition using the Cat/mut-Cfa orthogonal split intein pair on the SMARCA5 subunit of ACF complex. Various chemical modifications can be installed through the transposon to enable different biochemical experiments. (**B**) Premade ACF complex containing the recipient SMARCA5 (500 nM) was mixed with a designated transposon construct (500 nM) in 25 mM HEPES, 60 mM KCl, 10 mM $MgCl_2$, 1 mM TCEP, 10% v/v glycerol, and 0.02% v/v IGEPAL CA630, pH 7.75. After overnight reaction at 4°C, the products were characterized by SDS-PAGE with CBB staining and Western blotting with indicated antibodies, as denoted by red or blue fluorescence. The APB transposons used in this experiment were as follows: SMARCA5 APB1 (APB), SMARCA5 APB +photoMet (APB w/photoMet), and SMARCA5 APB+pY (APB + pY) (see fig. S35 and table S1 for further details). (**C**) Top: remodeling activity of modified ACF complexes on mononucleosomes (MNs) as assayed by REAA (10 nM ACF, 10 nM MNs). Reintroducing the APB domain into a catalytically inactive ACF complex through protein transposition rescues its activity. Bottom: kinetics of remodeling for the indicated ACF complexes as measured by REAA. Error bars indicate the SEM of $n = 3$ independent experiments. Representative native gel analyses of the remodeling reactions are shown in fig. S46. (**D**) Introducing a phosphotyrosine modification into SMARCA5 ($pTyr^{742}$) markedly slows nucleosome sliding, as observed by electrophoretic mobility shift assay after repositioning (8.33 nM ACF, 10 nM MNs, 4 min). Upon λ protein phosphatase (λPP) treatment, ACF activity is fully restored. Off-center bead-on-a-string represents the non-remodeled MN, whereas the on-center bead-on-a-string represents the remodeled MN. Quantification is by gel densitometry. Error bars indicate the SEM from $n = 5$ replicates. Data were analyzed using two-tailed Student's t test. $^{***}P \leq 0.001$. See fig. S47 for more details. (**E**) A photo-methionine residue ($photoM^{743}$) installed within SMARCA5 through protein transposition enables photo–cross-linking between SMARCA5 (10 pmol) and a mononucleosome (5 pmol) upon UV irradiation (20 min). Left: immunostaining with an H2A antibody shows a positive cross-link between SMARCA5 and histone, which is ablated upon the addition of excess LANA peptide (10 μM), a competitive binder to the nucleosome acidic patch. The asterisk denotes nonspecific binding of histone antibody to SMARCA5. Right: densitometry analysis of the cross-linking signal in the immunoblot normalized to total H2A signal. Error bars indicate the SEM from $n = 5$ independent biological replicates (+UV) or $n = 4$ independent biological replicates (+LANA). Data were analyzed using two-tailed Student's t test. $^{**}P \leq 0.01$. (**F**) Immunoblot analysis of in nucleo protein transposition reaction between endogenously expressed recipient SMARCA5 in HEK 293T cells containing an embedded HA tag (red signal) and exogenously added transposon construct (0.1 to 0.5 μM) containing a FLAG tag (blue signal) over 30 min. Successful in nucleo transposition is denoted by the decrease in the HA signal with a concomitant increase in the FLAG signal.

extein residues (i.e., those residues immediately flanking the splicing junctions) to facilitate the transformation. Ideally, some or all of these residues would be naturally present in the recipient protein, thereby minimizing any mutations in the final product (as in the dCas9 example). The discovery and engineering of split inteins with minimal extein dependency should further reduce any scars present in transposition products (*1*, *10*). Surface exposed loops, linker domains, and intrinsically disordered regions [the prevalence and functional importance of which continues to grow (*39*)] are likely to be optimal sites. Given the wealth of protein structure information now available, including recent advances in computational methods (*40*–*42*), we anticipate that many potential target systems will be identified that fulfill these design criteria. Thus, the current approach is expected to greatly expand the range of proteins accessible to in vitro semisynthesis.

REFERENCES AND NOTES

1. R. E. Thompson, T. W. Muir, *Chem. Rev.* **120**, 3051–3126 (2020).
2. J. A. Gramespacher, A. J. Stevens, R. E. Thompson, T. W. Muir, *Protein Sci.* **27**, 614–619 (2018).
3. A. C. Conibear, E. E. Watson, R. J. Payne, C. F. W. Becker, *Chem. Soc. Rev.* **47**, 9046–9068 (2018).
4. N. P. Cowieson *et al*., *Proteomics* **6**, 1750–1757 (2006).
5. M. S. Willis *et al*., *Protein Sci.* **14**, 1818–1826 (2005).
6. G. J. Cotton, B. Ayers, R. Xu, T. W. Muir, *J. Am. Chem. Soc.* **121**, 1100–1101 (1999).
7. U. K. Blaschke, G. J. Cotton, T. W. Muir, *Tetrahedron* **56**, 9461–9470 (2000).
8. J. Shi, T. W. Muir, *J. Am. Chem. Soc.* **127**, 6198–6206 (2005).
9. C. Feschotte, E. J. Pritham, *Annu. Rev. Genet.* **41**, 331–368 (2007).
10. N. H. Shah, T. W. Muir, *Chem. Sci.* **5**, 446–461 (2014).
11. T. Otomo, N. Ito, Y. Kyogoku, T. Yamazaki, *Biochemistry* **38**, 16040–16044 (1999).
12. K. K. Khoo *et al*., *Nat. Commun.* **11**, 2284 (2020).
13. D. Sarkar *et al*., *Cell Chem. Biol.* **31**, 1000–1010.e6 (2024).
14. N. H. Shah, G. P. Dann, M. Vila-Perelló, Z. Liu, T. W. Muir, *J. Am. Chem. Soc.* **134**, 11338–11341 (2012).
15. A. J. Stevens *et al*., *J. Am. Chem. Soc.* **138**, 2162–2165 (2016).
16. A. J. Stevens *et al*., *Proc. Natl. Acad. Sci. U.S.A.* **114**, 8538–8543 (2017).
17. A. J. Stevens, G. Sekar, J. A. Gramespacher, D. Cowburn, T. W. Muir, *J. Am. Chem. Soc.* **140**, 11791–11799 (2018).
18. A. J. Burton, M. Haugbro, E. Parisi, T. W. Muir, *Proc. Natl. Acad. Sci. U.S.A.* **117**, 12041–12049 (2020).
19. I. V. Thiel, G. Volkmann, S. Pietrokovski, H. D. Mootz, *Angew. Chem. Int. Ed.* **53**, 1306–1310 (2014).
20. T. Pasch *et al*., *Chem. Sci.* **14**, 5204–5213 (2023).
21. T. Kobayashi *et al*., *PLOS ONE* **3**, e3822 (2008).
22. W. W. Ward, S. H. Bokman, *Biochemistry* **21**, 4535–4540 (1982).
23. G. Erdős, Z. Dosztányi, *Nucleic Acids Res.* **52** (W1), W176–W181 (2024).
24. A. Fiszbein *et al*., *Cell Rep.* **14**, 2797–2808 (2016).
25. L. S. Qi *et al*., *Cell* **152**, 1173–1183 (2013).
26. L. A. Gilbert *et al*., *Cell* **154**, 442–451 (2013).
27. P. D. Hsu, E. S. Lander, F. Zhang, *Cell* **157**, 1262–1278 (2014).
28. B. Zetsche, S. E. Volz, F. Zhang, *Nat. Biotechnol.* **33**, 139–142 (2015).
29. R. Deuring *et al*., *Mol. Cell* **5**, 355–365 (2000).
30. T. Tsukiyama, P. B. Becker, C. Wu, *Nature* **367**, 525–532 (1994).
31. M. J. Pazin, R. T. Kamakaka, J. T. Kadonaga, *Science* **266**, 2007–2011 (1994).
32. H. T. Dao, B. E. Dul, G. P. Dann, G. P. Liszczak, T. W. Muir, *Nat. Chem. Biol.* **16**, 134–142 (2020).
33. X. He, H.-Y. Fan, G. J. Narlikar, R. E. Kingston, *J. Biol. Chem.* **281**, 28636–28647 (2006).
34. K. Sharma *et al*., *Cell Rep.* **8**, 1583–1594 (2014).
35. P. V. Hornbeck *et al*., *Nucleic Acids Res.* **43** (D1), D512–D520 (2015).
36. L. Li *et al*., *Nat. Struct. Mol. Biol.* **31**, 266–274 (2024).
37. A. J. Barbera *et al*., *Science* **311**, 856–861 (2006).
38. I. Giriat, T. W. Muir, *J. Am. Chem. Soc.* **125**, 7180–7181 (2003).
39. A. S. Holehouse, B. B. Kragelund, *Nat. Rev. Mol. Cell Biol.* **25**, 187–211 (2024).
40. A. W. Senior *et al*., *Nature* **577**, 706–710 (2020).
41. R. Krishna *et al*., *Science* **384**, eadl2528 (2024).
42. J. Abramson *et al*., *Nature* **630**, 493–500 (2024).

ACKNOWLEDGMENTS

We thank members of the Muir lab for many helpful discussions during the course of this work. We also thank S. Kyin and H. H. Shwe at the Princeton Proteomics Facility. **Funding:** This work was supported by the National Institutes of Health (NIH-GMS grant R01 GM086868 and NIH-NCI grant R01 CA240768). N.E.S.T. is supported by an NIH postdoctoral fellowship (GM149123). J.A.O. is supported by a Damon Runyon Quantitative Biology Fellowship (DRQ-19-24). **Author contributions:** Y.H., N.E.S.T., R.E.T., and T.W.M. conceived the project. All authors contributed to the experimental design and execution. Y.H., N.E.S.T., and T.W.M. wrote the manuscript. **Competing interests:** T.W.M. is a scientific founder, scientific advisory board member, and shareholder for SpliceBio (Barcelona, Spain) and is a consultant for Merck. The remaining authors declare no competing interests. The Cfa intein used in this study has been patented by Princeton University (US patent 11,142,550). **Data and materials availability:** All data needed to evaluate the conclusions in the study are available in the main manuscript or the supplementary materials.

SUPPLEMENTARY MATERIALS

science.org/doi/10.1126/science.adq8540
Materials and Methods
Figs. S1 to S49
References (*43*–*55*)
MDAR Reproducibility Checklist

Submitted 3 June 2024; accepted 30 January 2025
10.1126/science.adq8540

VACCINATION

Vaccine-enhanced competition permits rational bacterial strain replacement in the gut

Verena Lentsch[1,2], Aurore Woller[3,4], Andrea Rocker[5], Selma Aslani[1], Claudia Moresi[1], Niina Ruoho[1], Louise Larsson[1], Stefan A. Fattinger[6,7], Nicolas Wenner[5], Elisa Cappio Barazzone[1], Wolf-Dietrich Hardt[6], Claude Loverdo[3], Médéric Diard[5,8]*, Emma Slack[1,8,9]*

Colonization of the intestinal lumen precedes invasive infection for a wide range of enteropathogenic and opportunistic pathogenic bacteria. We show that combining oral vaccination with engineered or selected niche-competitor strains permits pathogen exclusion and strain replacement in the mouse gut lumen. This approach can be applied either prophylactically to prevent invasion of nontyphoidal *Salmonella* strains, or therapeutically to displace an established *Escherichia coli*. Both intact adaptive immunity and metabolic niche competition are necessary for efficient vaccine-enhanced competition. Our findings imply that mucosal antibodies have evolved to work in the context of gut microbial ecology by influencing the outcome of competition. This has broad implications for the elimination of pathogenic and antibiotic-resistant bacterial reservoirs and for rational microbiota engineering.

Drug-resistant infections with *Escherichia coli* and *Salmonella* spp. are increasing (*1*). Both species typically colonize the gut before initiating disease and can be carried asymptomatically in the gut lumen. There is a pressing need for control and prevention strategies that are independent of antibiotics and that target not only disease but also gut pathogen reservoirs.

Most current vaccines focus on clearing infection from tissues, relying on serum antibodies and cellular immunity. However, protection from colonization of the gut lumen, topologically outside of the body, is fundamentally different. Invasion into this densely populated microbial ecosystem is a crucial step in enteropathogenic bacterial infections (*2*, *3*). Correspondingly, the microbiota plays a role in recovering homeostasis and excluding colonizing opportunistic pathogens (*4*, *5*). For example, fecal microbiota transplantation (FMT) can be curative in recurrent *Clostridioides difficile* infections (*6*) and dietary shifts or antibiotic treatment break colonization resistance, permitting *Salmonella* infection (*3*). Consequently, protective intestinal immune mechanisms have evolved to work in the context of gut microbial ecology.

Whole-cell inactivated oral vaccines induce high-affinity T cell–dependent immunoglobulin A (IgA) responses against the *Salmonella enterica* subspecies *enterica* serovar Typhimurium (*S*.Tm) and *E. coli* surface, including the O antigens of lipopolysaccharide (*7*, *8*). This IgA response aggregates *S*.Tm in the gut lumen via enchained growth, increasing bacterial clearance due to rapid flushing of aggregates

---

[1]Institute for Food, Nutrition and Health, ETH Zurich, Zurich, Switzerland. [2]Medical Research Council (MRC) Translational Immunology Discovery Unit, MRC Weatherall Institute of Molecular Medicine (WIMM), John Radcliffe Hospital, University of Oxford, Oxford, UK. [3]Sorbonne Université, CNRS, Institut de Biologie Paris-Seine (IBPS), Laboratoire Jean Perrin (LJP), Paris, France. [4]Unité de Chronobiologie théorique, Faculté des Sciences, Université Libre de Bruxelles (ULB), Brussels, Belgium. [5]Biozentrum, University of Basel, Basel, Switzerland. [6]Institute for Microbiology, Department of Biology, ETH Zurich, Zurich, Switzerland. [7]Science for Life Laboratory, Department of Medical Biochemistry and Microbiology, Uppsala University, Uppsala, Sweden. [8]Basel Research Centre for Child Health, Basel, Switzerland. [9]Sir William Dunn School of Pathology, University of Oxford, Oxford, UK.

***Corresponding author. Email: emma.slack@hest.ethz.ch (E.S.); mederic.diard@unibas.ch (M.D.)**

and exerting a selective pressure (*7*, *9*). Consequently, oral vaccination can alter the outcome of competition between O-antigen variants of *Salmonella* (*10*). Generalizing this concept, we expect high-affinity IgA to generate a fitness disadvantage for any targeted strain. Combining oral vaccination with oral supplementation of a live bacterial niche competitor could therefore drive competitive exclusion of the pathogen. An ideal niche competitor would be a nonpathogenic strain with complete metabolic niche overlap, a faster growth rate, and an absence of surface antigen cross-reactivity to the pathogen of interest. We here define the combination of a whole-cell inactivated oral vaccine with a live niche competitor as "vaccine-enhanced competition."

To explore the quantitative limits of vaccine-enhanced competition, we generated a mathematical model. This is based on exponential growth of wild-type *Salmonella*, a competitor strain, and the microbiota (modeled as a single entity) in the presence of finite shared and private niches, and clearance due to flow and death. Kinetic parameters were estimated from in vivo competition assays, combined with direct quantification of bacterial generation numbers using the unstable plasmid pAM34 (supplementary modeling text) (*11*). Finite niches were defined to be (i) available to the microbiota only, (ii) available to *Salmonella* and its competitor only, or (iii) competitively used by both *Salmonella* and the microbiota (supplementary modeling text). The rate of elimination of the target is expected to be related to (i) the magnitude of IgA-driven increase in clearance rate of the target and (ii) the extent of metabolic competition between the competitor and target strains, which suppresses the available niche for the pathogen (supplementary modeling text). The model predicts clearance of virulent *Salmonella* within a few days if a typical IgA response is combined with a fast-replicating competitor. Neither IgA alone nor competitor alone led to complete clearance. The model predicts complete robustness to the timing of competitor introduction, if some competitor bacterium is present at the time of challenge.

Using these timings as a guide, we explored vaccine-enhanced competition in the context of two in vivo models. First, we applied vaccine-enhanced competition to prevent disease and eliminate colonization in the mouse model of nontyphoidal salmonellosis in resistant (Nramp1$^{+/+}$) mice (*12*, *13*). Second, we demonstrated that vaccine-enhanced competition can be applied therapeutically to eliminate *E. coli* from the gut lumen of C57BL/6 mice. Vaccine-enhanced competition has broad potential to manipulate enterobacteriaceal colonization and disease.

Salmonella-based niche competitors enhance vaccine protection

As a proof of concept, a niche competitor with complete metabolic niche overlap was constructed by engineering the pathogen itself—i.e., *S.*Tm SL1344. To improve competitive fitness and abolish virulence, we deleted the master regulator of *Salmonella* pathogenicity island 1 (SPI-1) genes, *hilD*, and the *Salmonella* pathogenicity island 2 (SPI-2) component *ssaV* (*14*, *15*). Antibody cross-reactivity was reduced by inactivating the abequose O-acetylase *oafA* (*16*), converting the wild-type serovar O:4[5],12 to O:4,12 serovar *S.*Tm$^{\mathrm{Comp}}$ (fig. S1). It should be noted that the O antigen densely carpets the surface of *Salmonella*, and O-antigen modification alone is therefore sufficient to substantially decrease live-cell recognition by antibodies specific for the unmodified O antigen (*10*).

We first tested vaccine-enhanced competition on the basis of oral vaccination against the wild-type *S.*Tm (*S.*Tm$^{\mathrm{WT}}$), combined with precolonization with *S.*Tm$^{\mathrm{Comp}}$ at 3 or 19 days before challenge in the streptomycin nontyphoidal salmonellosis model (Fig. 1A and fig. S2) (*12*). Antibody titers at the end point were not altered by the presence of *S.*Tm$^{\mathrm{Comp}}$ (Fig. 1B). In control mice, *S.*Tm$^{\mathrm{WT}}$ robustly colonized the gut lumen to day 10 after infection (Fig. 1, C and D, and fig. S2). Niche competitor (*S.*Tm$^{\mathrm{Comp}}$) or oral vaccination alone mildly suppressed colonization (Fig. 1, C and D, and fig. S2). In mice that were both vaccinated and colonized with *S.*Tm$^{\mathrm{Comp}}$, *S.*Tm$^{\mathrm{WT}}$ initially colonized poorly (Fig. 1D and fig. S2) and was rapidly cleared. *S.*Tm$^{\mathrm{WT}}$ was undetectable in the cecum content in 7 of 13 mice in this group at day 10 of infection (Fig. 1, C and D, and fig. S2) and was suppressed by >100,000-fold in the remaining animals. Because *S.*Tm$^{\mathrm{Comp}}$ persists at low levels for several weeks in our specific pathogen–free (SPF) mouse colony (fig. S1), the time of precolonization with *S.*Tm$^{\mathrm{Comp}}$ did not significantly influence clearance efficacy (figs. S2 and S3). This is practically important because it indicates that a niche competitor can be fed considerably before an infection occurs. This highlights the need for rigorous safety testing, as these organisms need to colonize the gut long-term or to be delivered frequently.

Wherever *S.*Tm$^{\mathrm{WT}}$ was rapidly eliminated from the gut lumen, systemic sites were also sterile (Fig. 1, E and F, and fig. S2). Pathology, as measured longitudinally by fecal lipocalin-2 (LCN2) and at the end point by histopathology (Fig. 1, G to I), mirrored intestinal colonization. Pathology was prevented by the vaccine-enhanced competition regimen but only partially prevented by each intervention alone.

To further corroborate our findings of sterilizing immunity, we performed FMT from infected vaccine-enhanced competition–treated mice at day 9 into naïve streptomycin-pretreated mice (Fig. 1A). Transfer of 1 to 10 colony-forming units (CFUs) is sufficient to cause full-blown disease in this model (*15*, *17*). Despite the high-dose fecal transfer, only one animal of eight showed transmission of *S.*Tm$^{\mathrm{WT}}$ (Fig. 1, J and K). This donor did not have the highest fecal *S.*Tm$^{\mathrm{WT}}$ counts at the time of transfer but had the lowest ratio of competitor to wild type of all donors (40-fold excess, compared with >1000-fold excess). This suggests an additional benefit of the approach: A competitor can prevent transmission even in cases in which sterilizing immunity in the gut lumen is incomplete. By contrast, all mice receiving feces from the untreated control group of *S.*Tm-infected mice became infected (Fig. 1, J and K). Therefore, vaccine-enhanced competition permitted clearance of high-dose *S.*Tm$^{\mathrm{WT}}$ challenge from the gut and prevention of invasion into all examined sites. This also largely prevented transmission to naïve hosts, providing herd immunity.

Metabolic niche overlap is necessary for vaccine-enhanced competition

To investigate whether vaccine-mediated clearance from the gut lumen required complete metabolic niche overlap, we compared the functionality of *S.*Tm$^{\mathrm{Comp}}$ with that of a galactitol-utilization mutant *S.*Tm$^{\mathrm{Comp}\ \Delta gatABC}$ (Fig. 2A) (*18*, *19*). Lack of overlap for a single sugar (galactitol) in the competitor resulted in significantly slower competitive exclusion of *S.*Tm$^{\mathrm{WT}}$ in vaccinated mice, as compared with a full niche overlap (Fig. 2B). The mechanism therefore requires metabolic niche overlap.

We next investigated the ability of a more distantly related mouse commensal B2 *E. coli* 8178 (*Ec*^{8178}) to act as a niche competitor against *S.*Tm. This strain has a partial niche overlap with *S.*Tm in vivo (*20*, *21*). A benefit of using a more distantly related probiotic is that this *E. coli* produces a completely unrelated O-antigen structure, allowing us to use the "evolutionary trap" version of our *S.*Tm vaccine (Fig. 3A) (*10*)—a version of the vaccine covering all common *S.*Tm O-antigen variations. Colonization with *Ec*^{8178} did not induce detectable *Ec*^{8178}-binding intestinal IgA or serum IgG (fig. S4). Vaccine-enhanced competition based on combining the *S.*Tm$^{\mathrm{WT}}$ vaccination with *Ec*^{8178} could decrease initial *S.*Tm$^{\mathrm{WT}}$ expansion by ~1000-fold and completely prevented gut inflammation (Fig. 3, B to H) (*7*, *22*).

These experiments were then repeated with a completely unrelated probiotic strain (*Lactobacillus casei*) that has minimal niche overlap with *Salmonella* (*23*). Despite robust colonization, *L. casei* had no significant effect on vaccine-mediated protection (fig. S5).

A final aspect of niche competition tested is whether a more intact microbiome may contribute to niche competition. High-fat diet feeding induces mild and transient microbiota disruption (*21*). In this model, oral vaccination alone and niche competitor alone were effective in preventing *Salmonella* colonization. However, vaccine-enhanced competition performed

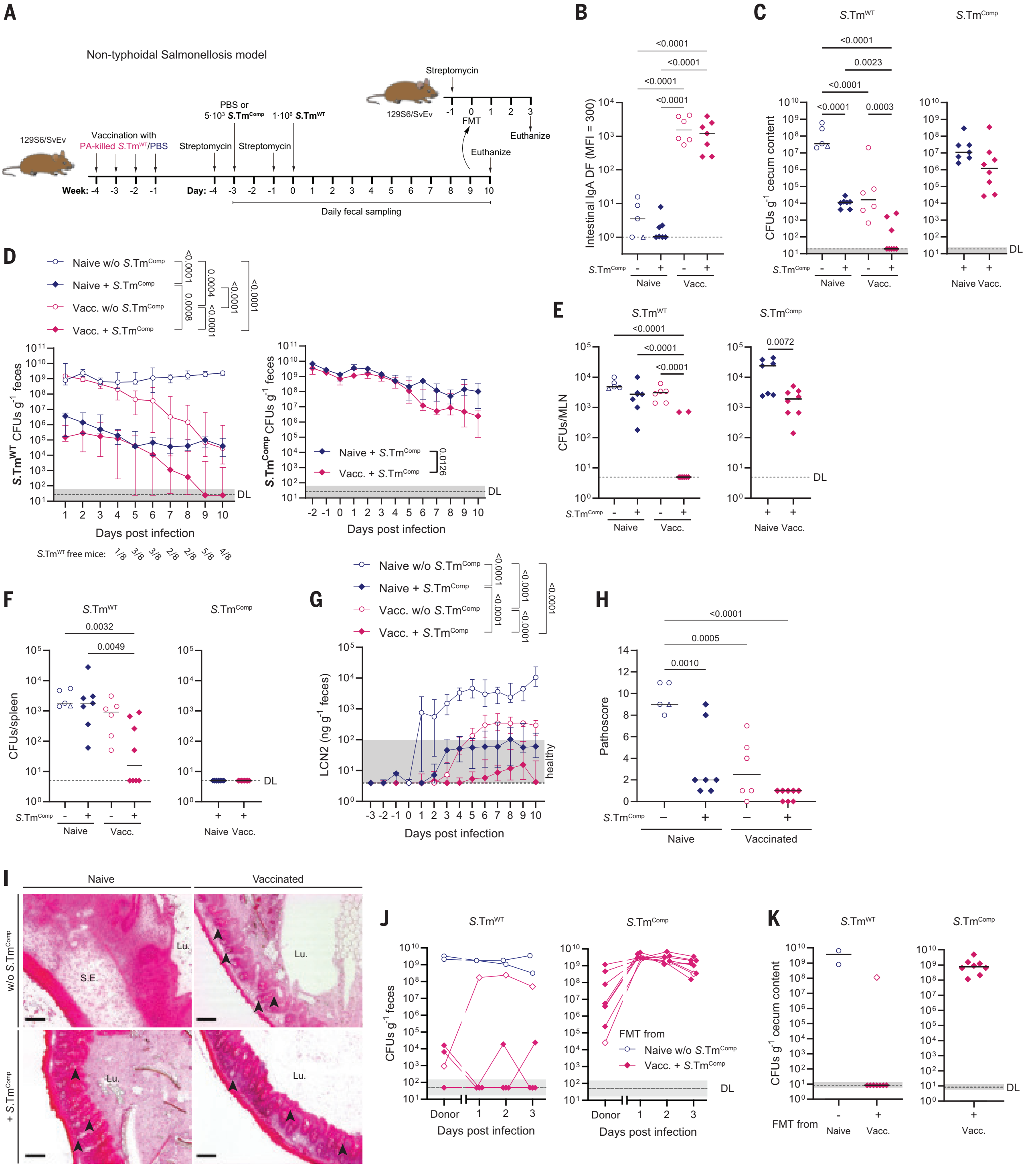

Fig. 1. Vaccine-enhanced competition based on an inactivated whole-cell oral vaccination and S.Tm$^{\text{Comp}}$ can eliminate S.Tm$^{\text{WT}}$ from the gut and prevent S.Tm$^{\text{WT}}$ transmission. (**A**) Experimental procedure. (**B**) Phosphate-buffered saline (PBS, blue) or peracetic acid–inactivated (PA)-S.Tm–vaccinated (pink) 129S6/SvEv mice were pretreated with streptomycin and infected with 1 × 10^{6} S.Tm$^{\text{WT}}$. Indicated groups were precolonized with 5 × 10^{3} S.Tm$^{\text{Comp}}$ at day −3 (filled symbols). S.Tm$^{\text{WT}}$-specific intestinal IgA titers at the end point. (**C** to **F**) S.Tm CFUs in cecum content (C), feces (D), MLN (E), and spleen (F). S.Tm$^{\text{WT}}$-free mice in (D) refers to Vacc.+S.Tm$^{\text{Comp}}$ group. (**G** to **I**) Intestinal inflammation determined by fecal LCN2 (G) and cecum histopathological scoring (H). Representative images of cecum stained with hematoxylin and eosin (H&E) (I). Arrowheads indicate goblet cells. Scale, 100 μm. (**J** and **K**) Streptomycin-pretreated naïve 129S6/SvEv mice received a FMT with feces collected on day 9 from (A) to (K). S.Tm$^{\text{WT}}$ and S.Tm$^{\text{Comp}}$ CFUs in feces (J) and cecum content (K). The pink open triangle depicts a donor from the Vacc.+S.Tm$^{\text{Comp}}$ group in which S.Tm$^{\text{WT}}$ transmission occurred. Pooled data from two independent experiments with switched antibiotic resistances [n = 5 to 8 mice per group in (A) to (I) or n = 8 mice per group in (J) and (K)]. Solid lines, median. Error bars, interquartile range. Dotted lines, DL. Shaded area, DL range. Open triangles, mouse (n = 1) euthanized prematurely because of severe disease. One-way analysis of variance (ANOVA) (H) performed on log-normalized data [(B), (C), (E), and (F)] or area under the curve (AUC) [(D) and (G)]. Unpaired two-tailed t test performed on log-normalized data [(B), (C), (E), and (F)]. DF, dilution factor; DL, detection limit; Lu., lumen; MFI, median fluorescence intensity; MLN, mesenteric lymph node; S.E., submucosal edema.

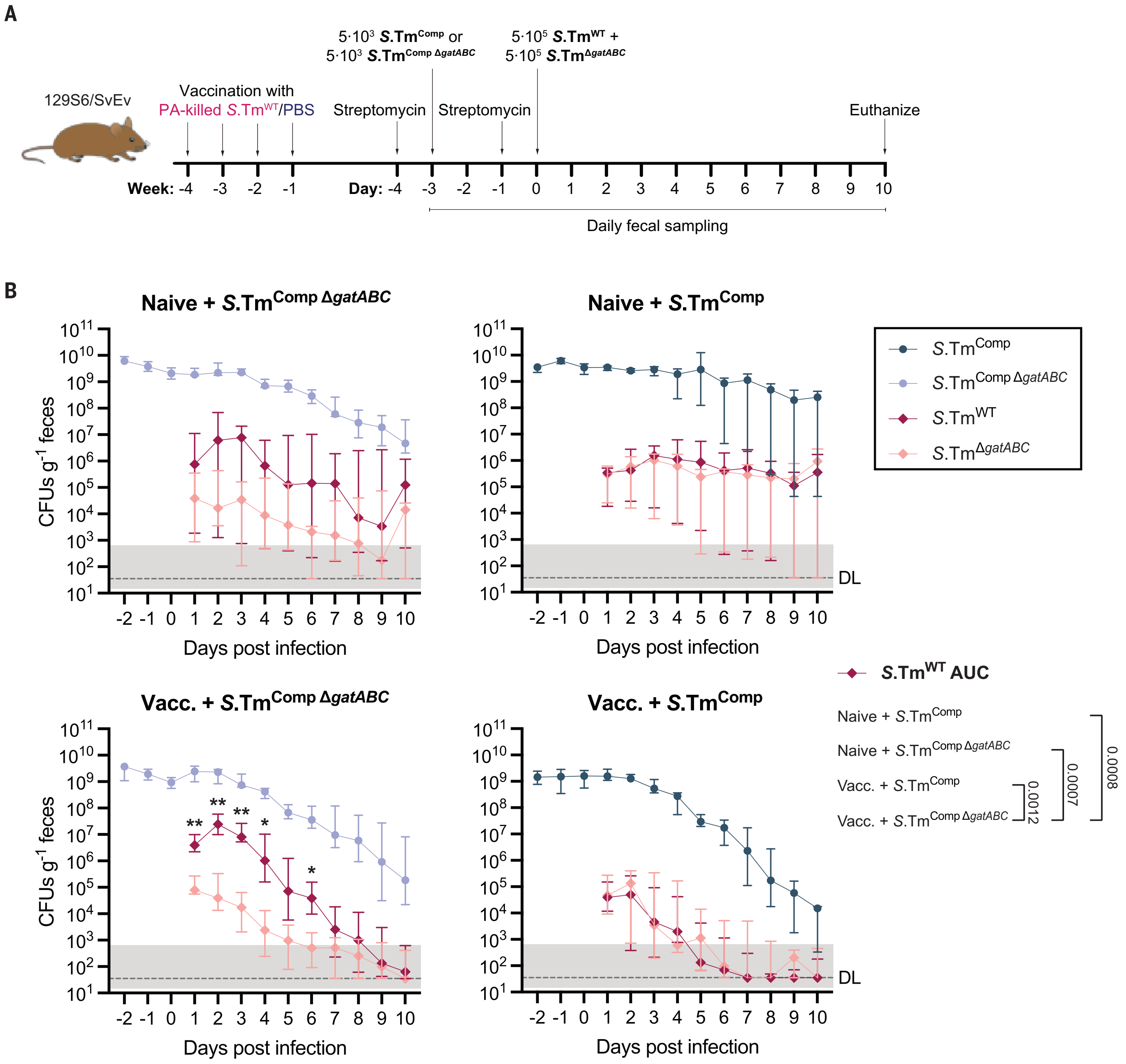

Fig. 2. Metabolic niche overlap of *S.*Tm^{WT} and *S.*Tm^{Comp} favors vaccine-enhanced competition. (**A**) Experimental procedure. PBS or PA-*S.*Tm–vaccinated 129S6/SvEv mice were precolonized with 5 × 10^{3} *S.*Tm^{Comp} or *S.*Tm$^{Comp\Delta gatABC}$ 3 days before infection and infected with a 1:1 ratio of 1 × 10^{6} *S.*Tm^{WT} and *S.*Tm$^{\Delta gatABC}$. (**B**) *S.*Tm CFUs in feces (*n* = 5 mice per group). Solid lines, median. Error bars, interquartile range. Dotted lines and shading, DL and range. Two-way ANOVA on log-normalized data between *S.*Tm^{WT} and *S.*Tm$^{\Delta gatABC}$ and one-way ANOVA on AUC comparing *S.*Tm^{WT} between treatment groups were performed.

slightly better in preventing disease, which suggests that combining oral vaccination and niche competition has benefits also in the presence of natural competitors (fig. S6). In the mouse typhoid model, mice are orally infected with a high dose of *Salmonella* without pretreatment or preexisting damage to the microbiota (*13*). Vaccine-enhanced competition also provides robust protection from colonization and gut inflammation in this model. Of note, because the high infection dose permits immediate invasion of *Salmonella* into Peyer's patches, protection of systemic sites was weak in this model (fig. S7) (*7*, *24*–*26*).

Vaccine-enhanced competition can displace an *E. coli* strain from the gut microbiota

To discover whether vaccine-enhanced competition can eliminate a strain already present in the microbiota, we used the nonencapsulated commensal *E. coli* strain HS as a target (*27*). These experiments were performed in C57BL/6 mice carrying a low-complexity microbiota that permits continuous *E. coli* colonization up to 10^{8} CFUs/g feces without antibiotic pretreatment (*28*). After precolonization with *E. coli* HS, mice were fed oral vaccine on days 3, 13, and 20 and the niche-competitor cocktail on days 10 and 17. *E. coli* HS and niche-competitor levels were monitored in feces until day 23 (Fig. 4A). Whole-cell inactivated oral vaccines for *E. coli* HS induced an IgA response against the surface of live *E. coli* HS but not

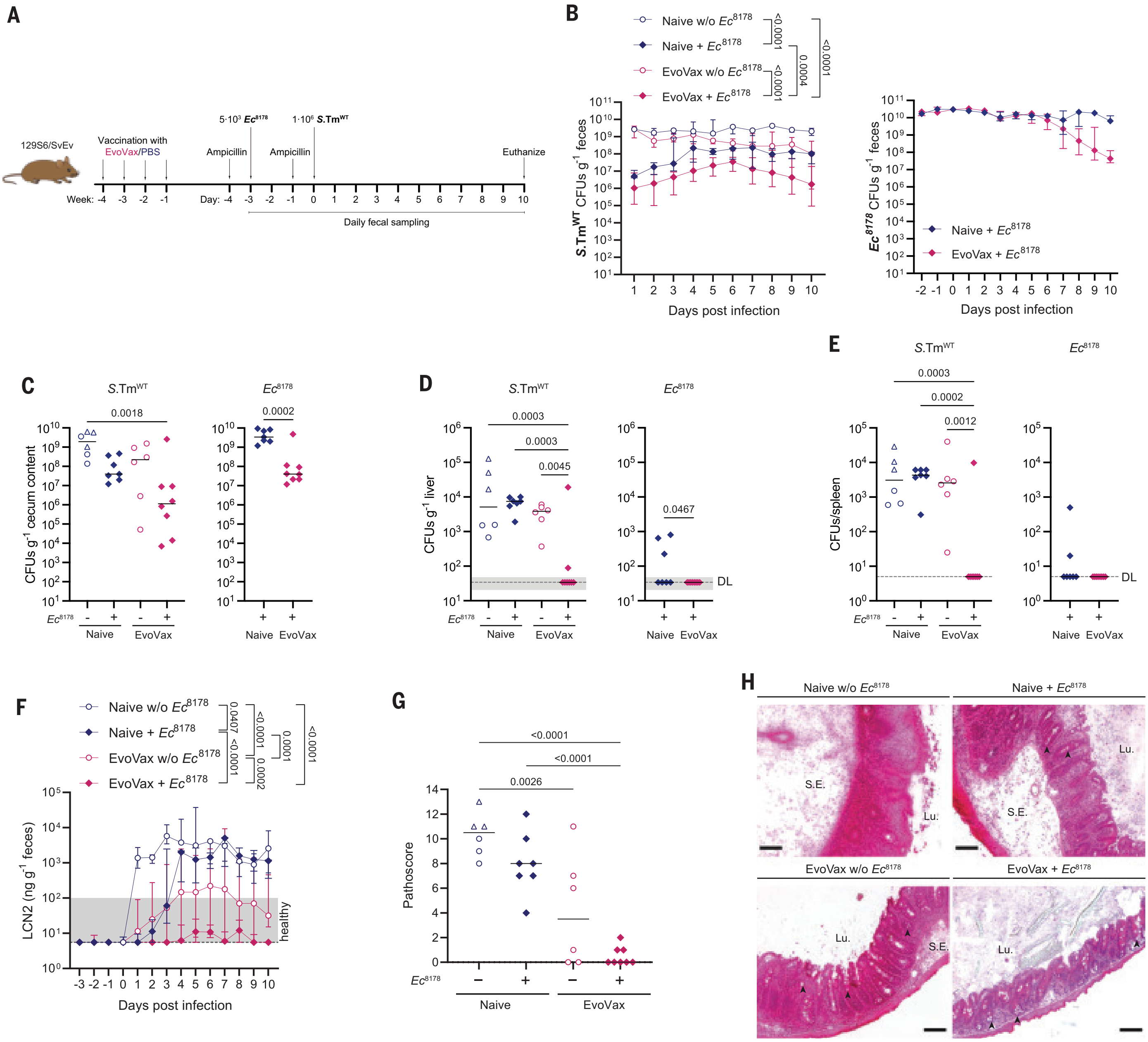

Fig. 3. Vaccine-enhanced competition with an imperfect niche competitor limits *S.*Tm$^{\text{WT}}$ colonization and prevents inflammation. (**A**) Experimental procedure. PBS (blue) or EvoVax-vaccinated (pink) 129S6/SvEv mice were pretreated with ampicillin and infected with 1×10^6 *S.*Tm$^{\text{WT}}$. Two groups were precolonized with 5×10^3 *Ec*^{8178} at 3 days before infection. (**B** to **E**) CFUs in feces (B), cecum content (C), liver (D), and spleen (E). (**F** and **G**) Intestinal inflammation determined by fecal LCN2 (F) and histopathological scoring of cecum (G). (**H**) Representative images of HE-stained cecum. Arrowheads show goblet cells. Scale bars, 100 μm. Pooled data from two independent experiments (n = 6 to 8 mice per group). Solid lines, median. Error bars, interquartile range. Dotted lines and shading, DL and range (when DL depends on sample weight). Open triangles, mice (n = 3) euthanized because of excessive pathology. One-way ANOVA (E) on log-normalized data (C) or AUC [(B) to (D)]. Unpaired two-tailed t test on log-normalized data for comparing two groups (C).

against the three *E. coli* strains making up the niche-competitor probiotic (Fig. 4B). Vaccine-enhanced competition resulted in complete displacement of the targeted *E. coli* strain in 50% of the treated animals, with strongly suppressed colonization seen in the remaining animals (Fig. 4, C and D). Each treatment alone had only a very mild effect on *E. coli* HS colonization levels (Fig. 4, C and D).

Therefore, the concept of oral vaccine-driven strain replacement is generalizable to nonencapsulated *E. coli* and can eradicate a bacterium already present in the gut microbiota.

Vaccine-enhanced competition requires intact adaptive immune system

Because immune stimulation could potentially induce antibody-independent effects contributing to pathogen clearance (*29*), we tested the role of adaptive immunity in vaccine-enhanced competition. Genetically immunodeficient lines with a low-complexity microbiota were not easily available, so we used antibodies to deplete CD4$^+$ T cells and B cells. Flow cytometry confirmed >90% depletion of T and B cells from the spleen, mesenteric lymph nodes, and blood of treated mice (Fig. 5, A and B, and fig. S8).

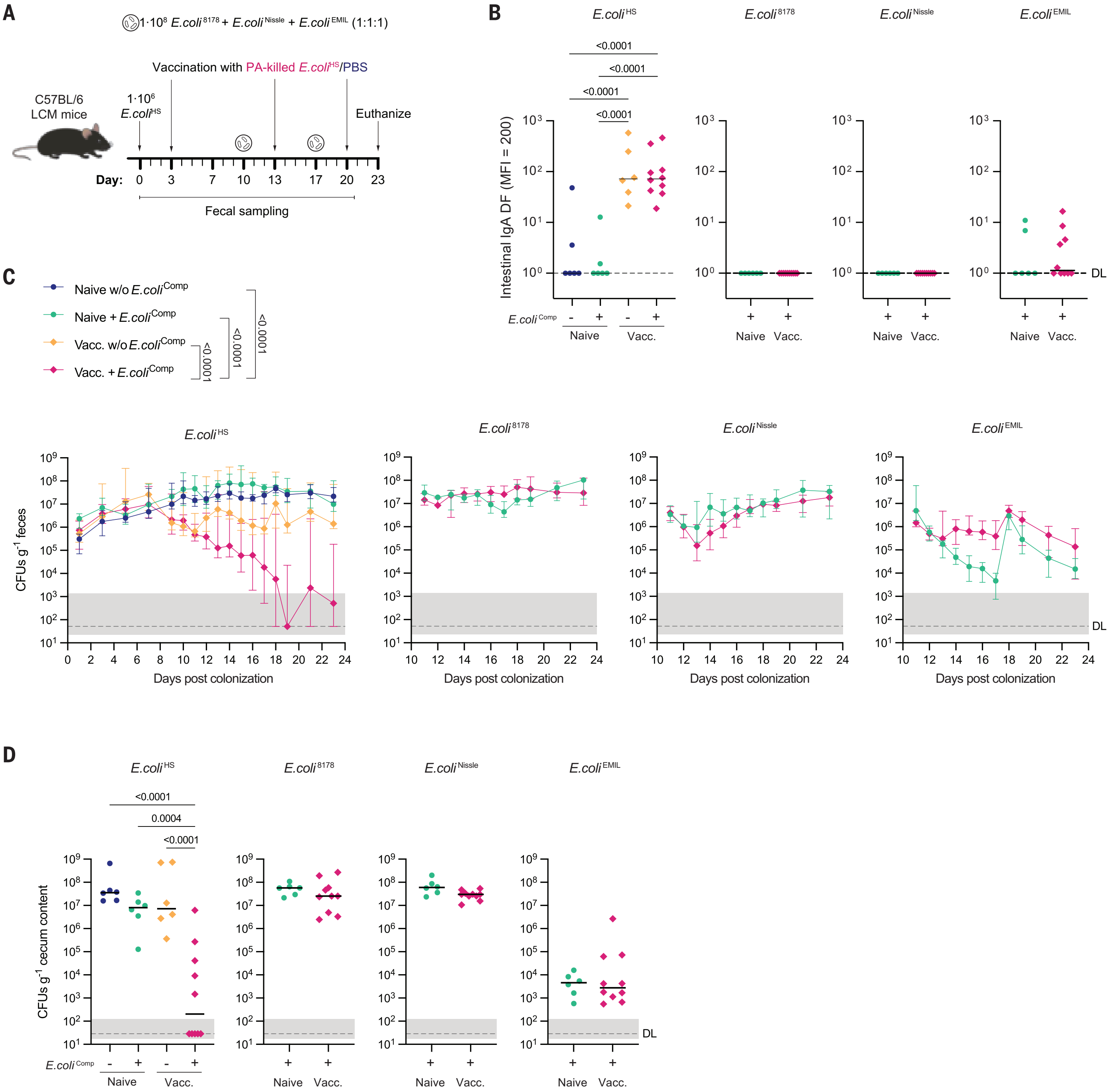

Fig. 4. Vaccine-enhanced competition can be used to therapeutically replace a gut *E. coli* strain. (**A**) Experimental procedure. C57BL/6 LCM mice were colonized with the commensal *E. coli* HS strain. Three days later, vaccination with either vehicle alone or PA–*E. coli* HS was started, and a cocktail of competitor *E. coli* was introduced orally on days 10 and 17. (**B**) Intestinal IgA titers specific for *E. coli* HS and the competitor strains at the end point. (**C** and **D**) Fecal (C) and cecal (D) CFUs. Pooled data from two independent experiments (n = 6 to 10 mice per group). Solid lines, median. Error bars, interquartile range. Dotted lines and shading, DL and range. One-way ANOVA on log-normalized data [(B) and (D)] or AUC (C). LCM, low-complexity microbiota.

$CD4^+$ T cell and B cell depletion during the vaccination period strongly suppressed induction of vaccine-specific IgA in both SPF 129SJL mice and gnotobiotic C57BL/6 mice (Fig. 5C and fig. S8). In the therapeutic clearance of *E. coli*, suppression of T-dependent antibody responses completely prevented *E. coli* HS elimination, whereas isotype-treated mice robustly cleared *E. coli* HS. This is consistent with a major contribution of vaccine-induced adaptive immunity (Fig. 5, D and E). In the prevention of *Salmonella* by using Ec^{8178} as a competitor, only the isotype control–treated mice receiving the vaccination-enhanced protection treatment remained healthy throughout the experiment, with no bloom of *Salmonella* and effective prevention of systemic spread (fig. S8), which again confirms the role of vaccine-induced adaptive immunity. Conversely, depleting $CD4^+$ and $CD8^+$ T cells only after vaccination (i.e., after induction of a T cell–dependent antibody

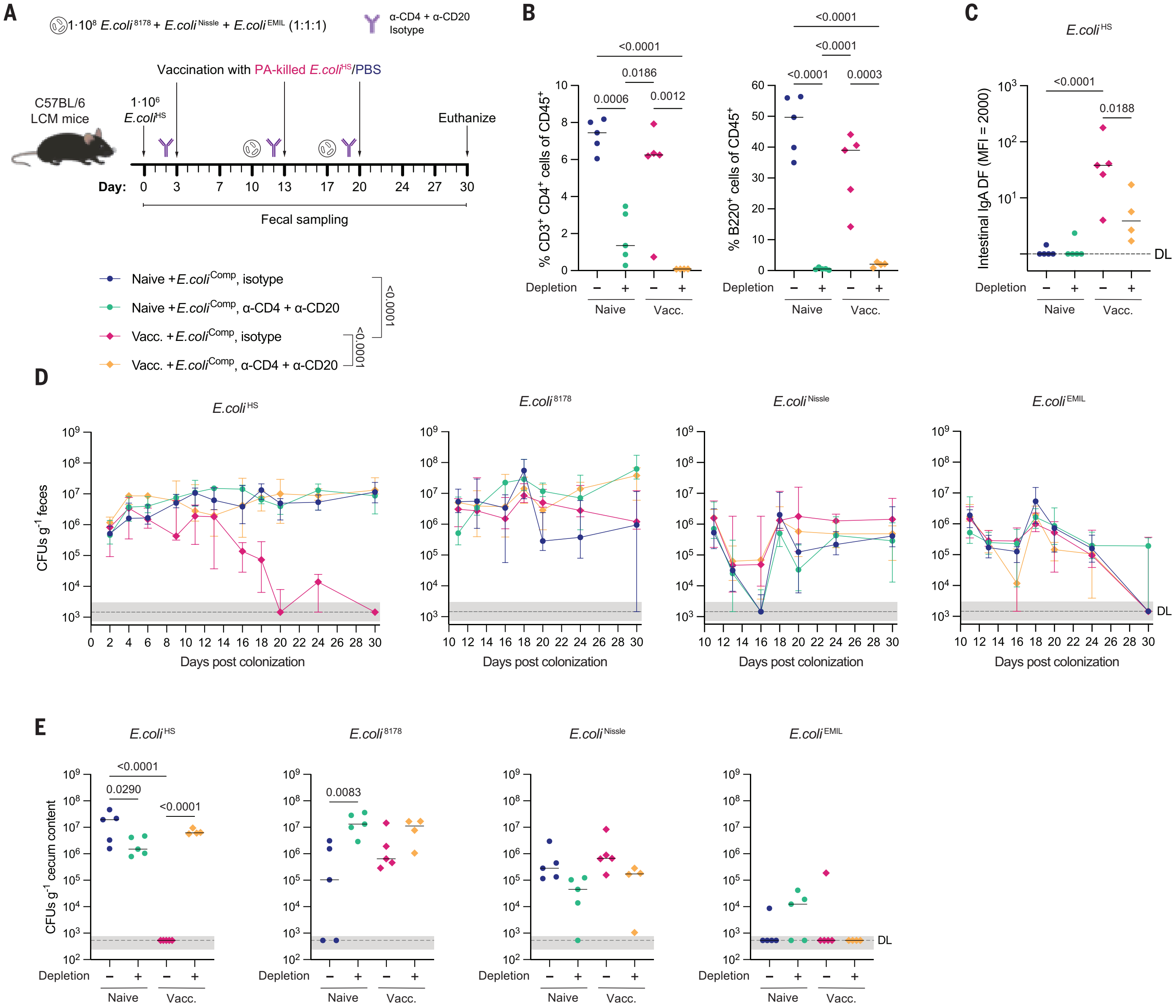

Fig. 5. Therapeutic clearance of *E. coli* is antibody dependent. (**A**) Experimental procedure. C57BL/6 LCM mice were colonized with *E. coli* HS. Three days later, vaccination with either vehicle alone or PA–*E. coli* HS was started, and a cocktail of competitor *E. coli* was introduced orally on days 10 and 17. Mice were treated with anti-CD4 and anti-CD20 or isotype controls 1 day before vaccination. (**B**) CD4$^+$ T cells and B cells in blood at the end point. (**C**) *E. coli* HS–specific intestinal IgA titers at the end point. (**D** and **E**) Fecal (D) and cecal (E) CFUs. Pooled data from two independent experiments (n = 4 or 5 mice per group). Solid lines, median. Error bars, interquartile range. Dotted lines and shading, DL and range. One-way ANOVA (B) on log-normalized data [(C) and (E)] or AUC (D).

response) had no impact on vaccine-enhanced competition (fig. S9). As the only adaptive immune component present in noninflamed gut are secretory antibodies, these findings are consistent with a role of T-dependent IgA in vaccine-enhanced competition.

Our high-dose inactivated oral vaccines are not potent inducers of effector T-cell responses, in contrast to live-attenuated vaccines (*24*). Correspondingly, live-attenuated vaccines are poor at preventing gut colonization but do generate T cell–dependent protection of deep tissues (fig. S9). This highlights a dichotomy in protective mechanisms between the gut lumen and systemic sites and between vaccine-enhanced competition and live-attenuated *Salmonella* vaccines.

Discussion

The concept that gut microbes contribute to prevention of pathogen colonization is well accepted (*2*, *3*, *30*, *31*). Secretory IgA increases the clearance rate of intestinal *Salmonella* and *E. coli* through enchained growth (*7*), and this exerts selective pressure on IgA-targeted bacteria (*10*). Here, we show that these processes work best together. This represents a fundamental shift in approach to designing vaccines for enteric bacteria. Published nutrient blocking and rationally designed microbiome engineering approaches can suppress *Salmonella* loads to ~10^5 CFUs/g feces (*32*, *33*), whereas our combined approach can generate a >10^9-fold reduction in colonization, down to undetectable levels.

Vaccine-enhanced competition requires both rational oral vaccine design and optimal niche-competitor selection. Earlier work on evolutionary trap vaccines provided a starting point for oral vaccine design targeting the O antigen of nonencapsulated Enterobacteriaceae (*10*). We explored two ends of the spectrum for niche-competitor selection and design, first by rationally modifying the target strain itself to generate a "perfect" competitor and second by testing commensal *E. coli* strains and a distantly related *Lactobacillus* strain (*21*, *27*). There has been considerable progress in the genomic prediction of community function and metabolic niche overlap (*34*), recently defined as nutrient blocking (*32*), indicating improved approaches are likely to involve designed niche-competitor consortia.

We can imagine several scenarios in which this type of prophylaxis could be relevant. Prevention of enteropathogenic bacterial infections during travel could be achieved by vaccine-enhanced competition given shortly before and potentially during travel. Orally administered vaccines and probiotics are ideal for self-administration. Additionally, we have shown that we can replace a strain already present in the gut, which allows elimination of opportunistic pathogen reservoirs, such as in patients scheduled for high-risk interventions (*35*, *36*). This could be game-changing in preventing invasive and increasingly multidrug-resistant disease in vulnerable human patients. Another interesting hypothesis is that IgA-mediated strain replacement may occur frequently without our intervention—i.e., is an evolved function of secretory IgA. This is consistent with observations of instability of *E. coli* at the strain level, but not the species level, over time in healthy volunteers (*37*).

Our observations may also explain some controversies in the existing *Salmonella* literature. For example, the extent of protection from nontyphoidal salmonellosis obtained with different types of oral vaccines in different laboratories varies extensively (*38*). Our data indicate that the variable efficacy of *Salmonella* niche competitors in the microbiota of mice is a critical determinant of protective efficacy. Microbiota composition also varies extensively between humans and over time (*39*). The vaccine-enhanced competition approach should remove the lottery of natural niche-competitor abundance and allow robust protection or therapy in most treated individuals. A limitation is that, because of practical and ethical restrictions, we have worked over relatively short time scales. We have not addressed the longevity of vaccine-induced responses or the potential within-host evolution of competitor strains that might be observed over months or years. In this context, we cannot exclude that very small reservoirs of infection below the detection limit may reemerge at very late time points after treatment, even in this very robust prophylaxis system.

Currently, we have focused on one strain of pathogenic *Salmonella* and one commensal *E. coli* strain. Given the extensive strain-level variation in antigenicity, pathogenicity, and metabolism between gut bacterial pathogens (*40*), the identification of the most relevant vaccine compositions and niche competitors may not be a case of simple extrapolation. Beyond nonencapsulated Enterobacteriaceae, there are open challenges in determining what the most relevant bacterial surface antigens are for IgA targeting and/or for designing oral vaccine strategies that optimally induce such responses. For example, *C. difficile* produces an S-layer with highly polymorphic exposed epitopes, which is challenging for vaccine design (*41*). *Klebsiella* species that have been implicated in exacerbating inflammatory bowel disease symptoms (*42*) are heavily encapsulated and likely require glycoconjugate vaccines for induction of relevant antibody responses (*43*). Further important future directions therefore include (i) improving the breadth and affinity of IgA responses induced and (ii) optimizing the design of niche competitors and competitor consortia.

We have identified a mechanism to prevent *Salmonella* colonization and achieve *E. coli* strain replacement in the gut. These results lay the foundation for targeted treatments for bacterial infections in mammals, promising advancements in medical science.

REFERENCES AND NOTES

1. C. J. L. Murray *et al.*, *Lancet* **399**, 629–655 (2022).
2. B. Stecher, *Int. J. Med. Microbiol.* **311**, 151484 (2021).
3. M. K. Herzog *et al.*, *Gut Microbes* **15**, 2172667 (2023).
4. M. Sassone-Corsi, M. Raffatellu, *J. Immunol.* **194**, 4081–4087 (2015).
5. K. Ilg *et al.*, *Infect. Immun.* **77**, 2568–2575 (2009).
6. S. Khanna, E. Voth, *Expert Rev. Gastroenterol. Hepatol.* **17**, 903–911 (2023).
7. K. Moor *et al.*, *Nature* **544**, 498–502 (2017).
8. K. Moor *et al.*, *Front. Immunol.* **7**, 34 (2016).
9. F. Bansept *et al.*, *PLOS Comput. Biol.* **15**, e1006986 (2019).
10. M. Diard *et al.*, *Nat. Microbiol.* **6**, 830–841 (2021).
11. D. Gil, J. P. Bouché, *Gene* **105**, 17–22 (1991).
12. B. Stecher *et al.*, *Infect. Immun.* **74**, 5047–5057 (2006).
13. D. M. Monack, D. M. Bouley, S. Falkow, *J. Exp. Med.* **199**, 231–241 (2004).
14. M. Diard *et al.*, *Nature* **494**, 353–356 (2013).
15. M. Diard *et al.*, *Curr. Biol.* **24**, 2000–2005 (2014).
16. J. M. Slauch, A. A. Lee, M. J. Mahan, J. J. Mekalanos, *J. Bacteriol.* **178**, 5904–5909 (1996).
17. L. Maier *et al.*, *PLOS Pathog.* **10**, e1004557 (2014).
18. C. Eberl *et al.*, *Cell Host Microbe* **29**, 1680–1692.e7 (2021).
19. E. Gül *et al.*, *Cell Host Microbe* **31**, 1140–1153.e3 (2023).
20. B. Stecher *et al.*, *PLOS Pathog.* **6**, e1000711 (2010).
21. S. Y. Wotzka *et al.*, *Nat. Microbiol.* **4**, 2164–2174 (2019).
22. P. Kaiser, E. Slack, A. J. Grant, W.-D. Hardt, R. R. Regoes, *PLOS Pathog.* **9**, e1003532 (2013).
23. V. Liévin-Le Moal, A. L. Servin, *Clin. Microbiol. Rev.* **27**, 167–199 (2014).
24. R. Ravindran, J. Foley, T. Stoklasek, L. H. Glimcher, S. J. McSorley, *J. Immunol.* **175**, 4603–4610 (2005).
25. S. K. Hoiseth, B. A. Stocker, *Nature* **291**, 238–239 (1981).
26. P. Kaiser *et al.*, *PLOS Biol.* **12**, e1001793 (2014).
27. K. Endt *et al.*, *PLOS Pathog.* **6**, e1001097 (2010).
28. L. Maier *et al.*, *Cell Host Microbe* **14**, 641–651 (2013).
29. M. G. Netea *et al.*, *Science* **352**, aaf1098 (2016).
30. J. M. Pickard, G. Núñez, *Am. J. Pathol.* **189**, 1300–1310 (2019).
31. M. T. Sorbara, E. G. Pamer, *Mucosal Immunol.* **12**, 1–9 (2019).
32. F. Spragge *et al.*, *Science* **382**, eadj3502 (2023).
33. S. Brugiroux *et al.*, *Nat. Microbiol.* **2**, 16215 (2016).
34. N. Kumar, T. C. A. Hitch, D. Haller, I. Lagkouvardos, T. Clavel, *Microb. Biotechnol.* **14**, 1757–1770 (2021).
35. V. Melkebeek, B. M. Goddeeris, E. Cox, *Vet. Immunol. Immunopathol.* **152**, 37–42 (2013).
36. S. D. Isidean, M. S. Riddle, S. J. Savarino, C. K. Porter, *Vaccine* **29**, 6167–6178 (2011).
37. J. N. V. Martinson *et al.*, *ISME J.* **13**, 2306–2318 (2019).
38. F. Fransen *et al.*, *Immunity* **43**, 527–540 (2015).
39. G. McCallum, C. Tropini, *Nat. Rev. Microbiol.* **22**, 105–118 (2024).
40. D. Yu, G. Banting, N. F. Neumann, *Can. J. Microbiol.* **67**, 553–571 (2021).
41. K. E. Dingle *et al.*, *J. Infect. Dis.* **207**, 675–686 (2013).
42. S. Federici *et al.*, *Cell* **185**, 2879–2898.e24 (2022).
43. L. Assoni, R. Girardello, T. R. Converso, M. Darrieux, *Infect. Dis. Ther.* **10**, 2157–2175 (2021).
44. V. Lentsch, Vaccine-enhanced competition permits rational bacterial strain replacement in the gut, ETH Zurich (2025); https://doi.org/10.3929/ethz-b-000717590.

ACKNOWLEDGMENTS

We thank B. Pugin for providing the *Lactobacillus casei* strains used in this work. We thank K. Foster, D. Hoces, M. Arnoldini, and members of the Slack lab for helpful discussions and comments; Y. Cherrak and E. Gül for technical advice; R. Rappold, A. de Wouters d'Oplinter, K. Vershynina, S. Ganguillet, and L. Rocha for their support in experiments; and the staff at the RCHCI, EPIC, and Biozentrum animal facilities for their excellent support. **Funding:** Funding for this work was provided by the Gebert Rüf Microbials (GR073_17). V.L., A.W., C.L., and E.S. are supported by the Gebert Rüf Microbials (GR073_17). E.S. acknowledges the support of the Swiss National Science Foundation (40B2-0_180953, 310030_185128) and European Research Council Consolidator Grant (865730). This work was supported as a part of NCCR Microbiomes, a National Centre of Competence in Research, funded by the Swiss National Science Foundation (grant no. 180575). Funding was provided by the Botnar Research Centre for Child Health as part of the Multi-Investigator Project: Microbiota Engineering for Child Health. E.S. is supported by the LOOP Zurich mTORUS project. M.D. is supported by an SNF professorship (PP00P_176954) and Gebert Rüf Microbials (PhagoVax GRS-093/20). W.-D.H. acknowledges funding by grants from the Swiss National Science Foundation (310030_192567, NCCR Microbiomes). C.L. is supported by Agence Nationale de la Recherche (ANR-21-CE45-0015, 376 ANR-20-CE30-0001) and MITI CNRS AAP adaptation du vivant à son environnement. **Author contributions:** Conceptualization: V.L., M.D., and E.S.; Investigation: V.L., A.W., A.R., S.A., C.M., S.A.F., N.R., N.W., L.L., E.C.B., and M.D.; Methodology: V.L., A.W., and C.L.; Software: A.W. and C.L.; Validation: V.L., A.W., and C.M.; Data curation: V.L., A.W., and C.M.; Formal analysis: V.L., A.W., and C.L.; Project administration, V.L. and E.S.; Funding acquisition: M.D. and E.S.; Resources: W.-D.H., C.L., and E.S.; Supervision: V.L., W.-D.H., C.L., M.D., and E.S.; Visualization: V.L. and A.W.; Writing – original draft: V.L. and E.S.; Writing – review and editing: V.L., A.W., A.R., C.M., S.A., N.R., S.A.F., N.W., L.L., E.C.B., D.H., C.L., M.D., and E.S. **Competing interests:** V. Lentsch, M. Diard, and E. Slack are inventors on a patent (application no. EP22186078.6) submitted by the University of Basel and ETH Zurich that covers combining a genetically engineered probiotic niche competitor and vaccination related to this work. V. Lentsch, M. Diard, and E. Slack are inventors on a patent (application no. EP24208390) submitted jointly by the University of Basel and ETH Zurich that covers combining probiotic niche competitors, vaccination, and bacteriophage treatment related to this work. No commercial development is currently associated with these patents, and no financial conflict of interest exists. **Data and materials availability:** Original code and raw data have been deposited at ETH Zurich Research Collection (*44*). Newly generated bacterial strains and all other materials are available from E.S. and M.D. **License information:** Copyright © 2025 the authors, some rights reserved; exclusive licensee American Association for the Advancement of Science. No claim to original US government works. https://www.sciencemag.org/about/science-licenses-journal-article-reuse. This research was funded in whole or in part by the Swiss National Science Foundation (40B2-0_180953, 310030_185128; grant no. 180575; 310030_192567), a cOAlition S organization. The author will make the Author Accepted Manuscript (AAM) version available under a CC BY public copyright license.

SUPPLEMENTARY MATERIALS

science.org/doi/10.1126/science.adp5011
Materials and Methods
Supplementary Modeling Text
Figs. S1 to S12
Tables S1 to S8
References (*45*–*57*)

Submitted 27 March 2024; accepted 6 February 2025
10.1126/science.adp5011

METALLURGY

Superior resistance to cyclic creep in a gradient structured steel

Qingsong Pan[1]†, Kunqing Ding[2]†, Song Guo[1,3]†, Ning Lu[4], Nairong Tao[1], Ting Zhu[2]*, Lei Lu[1]*

Cyclic creep, or ratcheting, is a severe form of fatigue deformation caused by cumulative unidirectional plastic strain under asymmetrical stress cycling with a nonzero mean stress. It often causes premature failure of structural materials, and enhancing ratcheting resistance is a challenge in materials engineering. We demonstrate superior ratcheting resistance in high-strength austenitic stainless steel with a gradient hierarchy of dislocation cells. The ratcheting rate is two to four orders of magnitude lower than for coarse-grained counterparts. Its resistance results from sustained microstructural refinement through deformation-induced coherent martensitic transformations to hexagonal close-packed nanolayers within stable dislocation cells. The progressively refined microstructure mitigates cyclic softening and suppresses strain localization during stress cycling, thus reducing ratcheting strain. The gradient dislocation architecture represents a promising design for high-strength, ratcheting-resistant materials.

Service failures in structural components such as turbine blades, pressure vessels, nuclear pipes, and offshore structures can lead to substantial financial costs and even loss of life (*1*–*3*). When metallic materials are subjected to asymmetrical stress cycling with nonzero mean stresses, a continuously increasing unidirectional strain commonly takes place, a phenomenon known as cyclic creep, or ratcheting (*2*–*8*). Ratcheting accelerates due to cyclic softening and strain localization, particularly when the applied stress exceeds the material's yield strength under prolonged conditions (*9*–*13*).

Various material design strategies, whether through tuning chemical composition, microstructure, or both, struggle to balance strengthening with ratcheting resistance (*1*–*3*, *9*, *11*). The ratcheting response worsens as the strength increases in most conventional single-principal-element alloys (*3*, *9*, *14*, *15*) and multi-principal-element alloys (*16*). For example, prestraining typically increases strength and improves short-term ratcheting resistance in materials with coarse grains (CGs) during early stress cycles (*17*). However, it reduces hardening capacity and promotes strain localization, weakening long-term ratcheting resistance (*3*, *9*). Nanostructured and heavily deformed materials, with abundant high-angle grain boundaries (GBs) and dense dislocations, also fail to achieve this balance. Although these materials resist ratcheting initially, they soften and coarsen under repeated cycles due to limited work hardenability and severe strain localization. These effects accelerate ratcheting, leading to early cracking and failure under prolonged asymmetrical stress cycling (*11*, *18*–*21*). A similar trend of weakened ratcheting resistance has been observed in high-strength dual-phase steels, primarily attributed to cyclic softening resulting from limited strain hardening and rapid dynamic recovery (*3*, *22*).

To improve the ratcheting resistance of high-strength materials, it is essential to mitigate cyclic softening and suppress strain localization under asymmetrical cyclic loading. Achieving this requires tailoring the microstructure to enhance strain-hardening capability, minimize dynamic recovery to mitigate cyclic softening, and prevent structural coarsening to control strain localization during asymmetrical cycling. Recently, a single-phase multi-principal-element alloy exhibited strong strengthening and hardening performance under monotonic tensile deformation, resulting in exceptional strength and ductility (*23*, *24*). This alloy features a hierarchical microstructure composed of stable, sample-level, gradient dislocation structure (GDS) confined within CGs. Therefore, exploiting the gradient dislocation architecture to enhance ratcheting resistance under asymmetrical cyclic stresses is of interest. In this study, we choose cost-effective austenitic 304 stainless steel (SS), which is widely used in diverse safety-critical applications (*25*). However, like most single-phase CG metals and alloys, conventional 304 SS not only has a low yield strength but also suffers from limited ratcheting resistance (*2*).

GDS steel

We produced a GDS material using a single-phase face-centered cubic (FCC) AISI 304 SS (Fe–18%Cr–8%Ni by weight percent). The initial sample consisted of randomly oriented, equiaxed CGs with an average size of ~37 μm (fig. S1, A to C). Dog-bone–shaped bar specimens with a gauge diameter of 6 mm and a gauge length of 13 mm were processed through cyclic torsion at ambient temperature (fig. S1D). After this treatment, equiaxed CGs from the surface to the core of the sample were homogeneously distributed, similar to those before cyclic torsion, as indicated by electron backscatter diffraction (EBSD) with scanning electron microscopy (SEM) (Fig. 1A). A prominent feature of GDS SS is the profuse dislocation cells with low-angle boundaries having misorientations of <15° distributed in most grains in the topmost layer (within ~100 μm from the surface) (Fig. 1, B to E). The low-angle boundary density (or cell size) gradually decreases (or increases) with depth from the top surface (Fig. 1B) due to the applied torsion, which generates radially gradient plastic strains in the sample cross section (fig. S1, E to G). At the core, the prevailing dislocation patterns in grains are individual planar dislocations and loose tangles (fig. S1, I and J). Thus, a sample-level GDS microstructure extending from the surface to the core was achieved in 304 SS after cyclic torsion. This GDS 304 SS retains a single-phase FCC structure, as confirmed by EBSD and transmission electron microscopy (TEM) (Fig. 1).

SEM and TEM observations revealed that the abundant equiaxed dislocation cells in the topmost grains are ~290 nm in size (Fig. 1, C to E). The cell walls, ~50 nm thick, contain a high density of dislocations (0.8×10^{15} m^{-2}) and exhibit small misorientations of ~0.6°, as estimated by orientation mapping (Fig. 1E). By contrast, the cell interiors contain fewer dislocations (Fig. 1F). The surface of GDS SS exhibits relatively low residual stress, ~70 MPa (fig. S1H), attributed to the nearly pure shear plastic strain imposed without any surface tooling. This contrasts with conventional processing methods such as shot peening (*26*). The GDS sample showed a pronounced gradient distribution of microhardness ranging from 2.0 GPa in the central region to 3.2 GPa at the topmost surface, which is higher than ~1.9 GPa of dislocation-free CGs (fig. S2).

Ratcheting resistance under asymmetrical stress cycling

We characterized both the uniaxial tensile and cyclic ratcheting performance of GDS SS at ambient temperature. Quasistatic uniaxial tensile tests showed an elevated yield strength (σ_y at 0.2% offset) of 489 ± 2 MPa, ~130% higher than that of CG counterparts (210 ± 5 MPa) (fig. S3A). A high uniform elongation (ε_u) of up to 52 ± 1% was measured for GDS SS, lower than that of CG counterparts (71 ± 1%). This combination of yield strength and uniform elongation in GDS 304 SS surpasses that of high-performance SS strengthened by nanotwin

---

[1] Shenyang National Laboratory for Materials Science, Institute of Metal Research, Chinese Academy of Sciences, Shenyang, P.R. China. [2] Woodruff School of Mechanical Engineering, Georgia Institute of Technology, Atlanta, GA, USA. [3] School of Materials Science and Engineering, University of Science and Technology of China, Shenyang, P.R. China. [4] School of Chemistry and Chemical Engineering, Shandong University, Jinan, P.R. China.
***Corresponding author. Email: llu@imr.ac.cn (L.L.); ting.zhu@me.gatech.edu (T.Z.)**

†These authors contributed equally to this work.

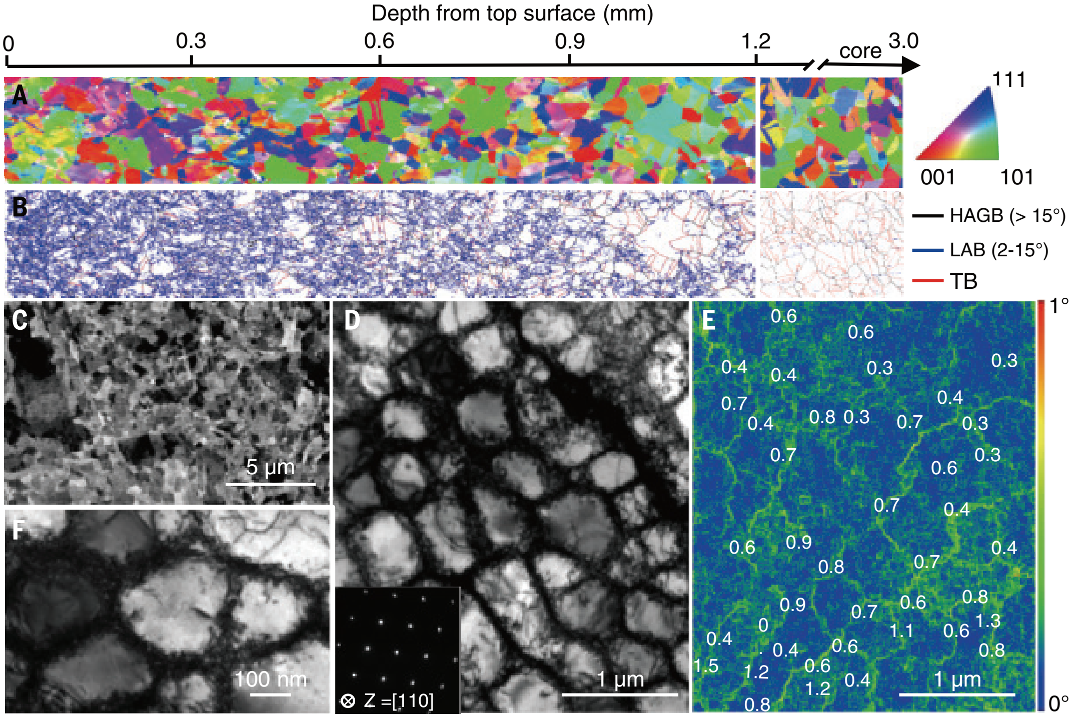

Fig. 1. Typical microstructure with gradient dislocation cells. (**A** and **B**) Cross-sectional EBSD images of GDS 304 SS processed by cyclic torsion showing the distributions of grain morphology and orientations (A) and internal boundaries [i.e., high-angle GBs (HAGBs), low-angle GBs (LABs), and TBs] with different misorientations (B) within an ~1.2 mm depth from the surface compared with those in the core. (**C** and **D**) Corresponding SEM and bright-field TEM images revealing dislocation cell structures at the topmost surface of the treated samples. The lower left inset in (D) shows the corresponding SAED patterns. (**E**) Misorientation angle of each cell wall measured using an electron precession diffraction technique in TEM. (**F**) Closer view of typical dislocation cells.

bundles and is comparable to additively manufactured hierarchical 316 SS (fig. S3B) (*27*).

We measured the ratcheting response of GDS 304 SS through asymmetrical tension-tension cyclic loading (stress control). Various combinations of maximum stress (σ_{max}) and minimum stress (σ_{min}) were applied while maintaining a stress ratio ($\sigma_{min}/\sigma_{max}$) of 0.1 and a frequency of 5 Hz (see table S1 for detailed loading parameters). Figure 2A shows a typical cyclic stress-strain curve of GDS SS tested at a σ_{max} of 510 MPa, which exhibits a substantially reduced progressive shift of the hysteresis loop along the tensile strain axis compared with CG SS (Fig. 2B). The GDS sample endured 10 million cycles without failure (~556 hours), reaching a cumulative ratcheting strain of ~2.1%. By contrast, the CG sample had a ratcheting-to-failure life (N_f) of 1.0×10^5 cycles (~5.6 hours) with a cumulative ratcheting strain of ~25.9%. The reduced cumulative ratcheting strain in the GDS sample results from its narrower hysteresis loop cycle by cycle (Fig. 2C), producing a much smaller ratcheting strain per cycle $\Delta\varepsilon_r$ than the CG counterpart at the same cycle number (Fig. 2D).

Improved ratcheting performance was also observed in bulk GDS 304 SS subjected to various σ_{max} ranging from 480 to 570 MPa (table S1). As shown in Fig. 2E, the cumulative ratcheting strain of GDS SS increased more slowly with increasing σ_{max} while exhibiting a longer ratcheting-to-failure life compared with the CG counterpart under the same σ_{max}. The cumulative ratcheting strain (8.7%) of the GDS sample cycled to failure at a σ_{max} of 570 MPa was smaller than that of the CG sample (~42%) at a lower σ_{max} of 420 MPa. By removing the inner core containing few dislocation cells, we obtained GDS tubular specimens (~0.75 mm thick), hereafter referred to as surface GDS. When tested at a high σ_{max} of 570 MPa, the surface GDS exhibited a lower cumulative ratcheting strain of 0.7% at a longer ratcheting life of 3.5×10^6 to 1.0×10^7 cycles (without failure) than the bulk GDS (fig. S3C). The instantaneous ratcheting rate of the surface GDS sample at a σ_{max} of 570 MPa was the smallest throughout the entire deformation stage compared with both CG and bulk GDS counterparts (fig. S3D). Using the equation $(\varepsilon_{max} - \varepsilon_{min})/2 - (\sigma_{max} - \sigma_{min})/2E$, where E is Young's modulus, the estimated plastic strain amplitude of surface GDS samples was found to gradually decrease under asymmetrical tension-tension cyclic loading but increased with higher σ_{max}, remaining smaller than that of bulk GDS and the CG counterpart under the same σ_{max} (fig. S3E).

We conducted additional cyclic experiments on bulk GDS samples under asymmetrical axial tension-compression and proportional axial-torsion stress-controlled cycling (multiaxial conditions; table S1). Figure S4, A and B, shows that GDS SS samples exhibit enhanced ratcheting resistance, with ratcheting strain rates two to three orders of magnitude lower than CG counterparts under negative stress ratios of –0.1 and –0.3. Similarly, exceptional ratcheting resistance was observed under combined axial and torsional fatigue conditions (fig. S4C), consistent with the results shown in Fig. 2. These findings confirm that the superior ratcheting resistance of GDS samples is an inherent property regardless of the stress ratio (positive or negative) or multiaxial mechanical loading.

Figure 2F presents the combinations of average ratcheting rate and maximum stress for a variety of metallic materials with different compositions and structures. The average ratcheting rate is defined as the cumulative ratcheting strain at failure, normalized by the fatigue life (cycles to failure), and the maximum stress is normalized by Young's modulus of the corresponding material. For the metals and alloys compared in Fig. 2F, the average ratcheting strain rate ranges from 10^{-6} to 10^{-3} and increases with applied maximum stress. By contrast, bulk GDS and surface GDS 304 SS exhibit average ratcheting strain rates as low as 10^{-10} to 10^{-6}, which are two to four orders of magnitude lower than those of their CG counterparts and high-strength steels with comparable strength (*2*, *3*, *20*, *22*). The low ratcheting rates of bulk GDS and surface GDS under high maximum stresses contrast with the accelerated ratcheting response in conventional transformation-induced plasticity (TRIP) steels (*15*), dual-phase steel (*3*), high-strength low alloy steel (*28*), additively manufactured SS (*20*), and deformed and nanostructured metallic materials (*3*, *18*, *19*, *21*).

Dynamic, coherently nanolayered martensitic transformation mechanism

To elucidate the underlying mechanisms responsible for the superior ratcheting resistance of GDS SS, we examined the deformation

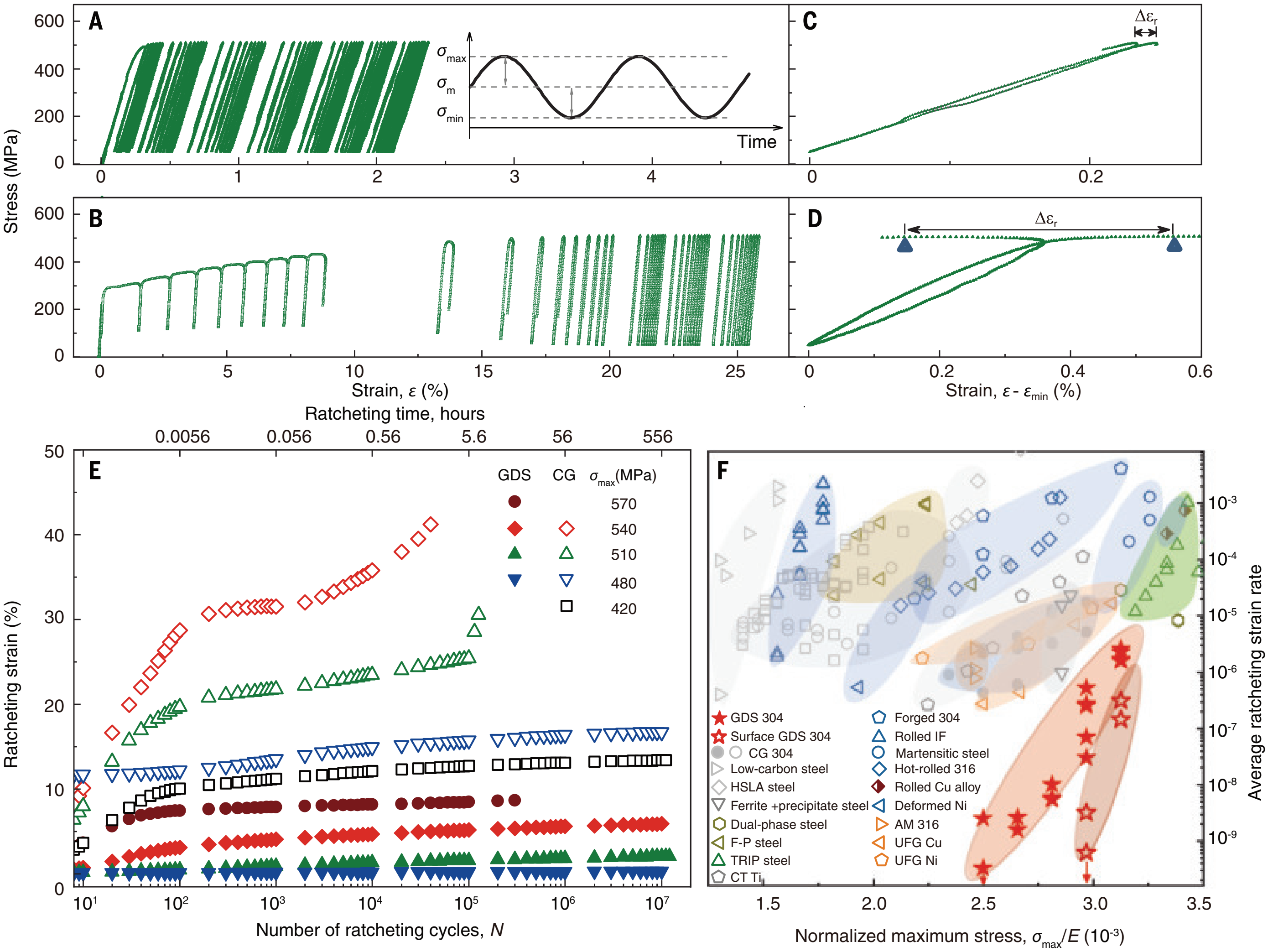

Fig. 2. Ratcheting response of GDS 304 SS at different maximum stresses. (**A** and **B**) Typical cyclic stress-strain evolution of GDS (A) and CG (B) samples subjected to asymmetrical tension-tension fatigue loading with a constant cyclic stress ratio ($\sigma_{min}/\sigma_{max}$) of 0.1 at a σ_{max} of 510 MPa. The upper right inset in (A) shows the sinusoidal loading curve under stress control. (**C** and **D**) Representative hysteresis loops for GDS (C) and CG (D) samples, with the origin of the strain axis in (C) and (D) shifted to allow comparison between the hysteresis loop. The ratcheting strain per cycle $\Delta\varepsilon_r$ is indicated by a double-headed arrow between two consecutive σ_{max} values in an individual hysteresis loop. (**E**) Ratcheting strain measured as a function of the number of cycles *N* for GDS and CG samples at various σ_{max} values. (**F**) Combinations of the average ratcheting strain rate and σ_{max} normalized by Young's modulus *E* for bulk and surface GDS samples compared with SS having homogeneous and heterogeneous microstructures (*3*, *14*), as well as representative structural materials, including martensitic steel (*2*), low-carbon steel (*3*), ferrite-pearlite (F-P) steel (*3*), TRIP steel (*15*), precipitate-strengthened steel (*22*), dual-phase steels (*3*), high-strength low-alloy (HSLA) steel (*28*), additively manufactured SS (*20*), and deformed and ultrafine-grained metals and alloys (*2*, *3*, *18*, *19*, *21*).

microstructure through interrupted testing of GDS samples cycled at a σ_{max} of 570 MPa. During the early stage of stress cycling (10% N_f), no significant structural changes were observed in the grains and dislocation cells (Fig. 3, A and B). However, numerous long, parallel microscale deformation bands with an average thickness of ~180 nm and spacing of ~3.5 μm began to form, with each band penetrating multiple cell walls in the topmost grains. The density of these bands decreased with depth from the top surface. Aberration-corrected high-angle annular dark-field scanning transmission electron microscopy (HAADF-STEM) revealed that these microscale deformation bands primarily consist of short stacking faults (SFs) (Fig. 3B), with an average length of ~25 nm and spacing of ~5.2 nm. As stress cycling progressed to 90% N_f, long, parallel microscale deformation bands continued to proliferate, resulting in an increased average thickness of ~320 nm and a decreased average band spacing of ~0.7 μm in the topmost grains (Fig. 3, C and D). Compared with the as-prepared GDS sample (Fig. 1), the size of the dislocation cells decreased slightly to ~217 nm, whereas the misorientation of the cell walls increased to ~1.1° (Fig. 3, D and E), accompanied by a higher density of dislocations (~1.3×10^{15} m^{-2}) at these cell walls.

The microscale deformation bands in GDS samples at 90% N_f were further characterized by selected area electron diffraction (SAED), bright-field TEM, and phase mapping (Fig. 3, D and E). These bands comprised newly formed hexagonal close-packed (HCP) nanolayers embedded in the FCC matrix, resulting in an HCP-FCC nanolaminate structure within each band. Atomic-resolution HAADF-STEM confirmed that each micrometer-long deformation band consisted of numerous multiple thin yet long HCP nanolayers, along with plenty of SFs and limited twin boundary (TB) segments within the FCC matrix (Fig. 3, F and G). The average length of the HCP nanolayers was ~160 nm,

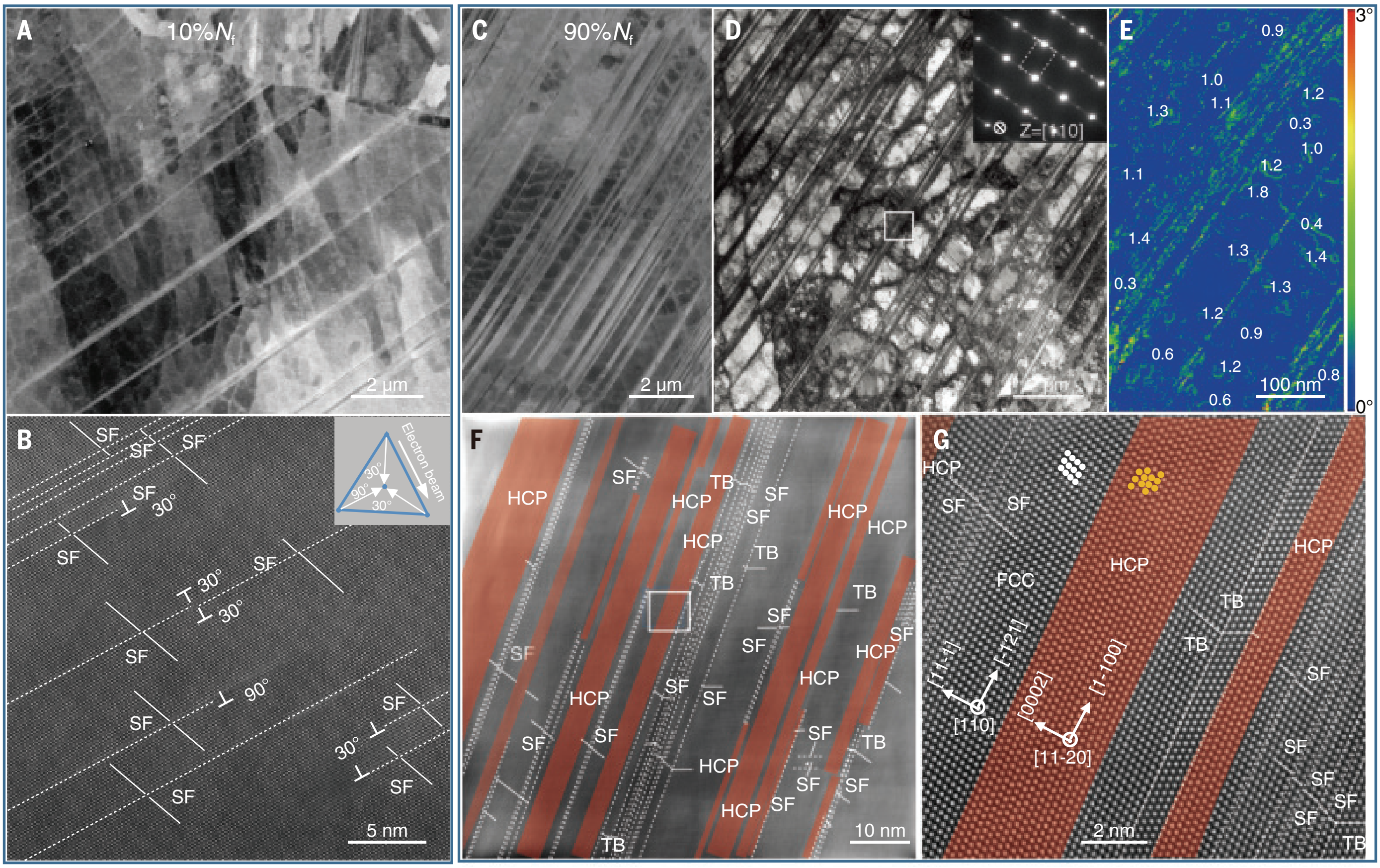

Fig. 3. Deformation microstructures of GDS 304 SS cycled under a σ_{max} of 570 MPa at 10% N_f [(A) and (B)] and 90% N_f [(C) to (G)] before failure. (**A** and **B**) SEM and HAADF-STEM images of the top surface layer of GDS SS at 10% N_f showing numerous microscale deformation bands spanning multiple dislocation cells consisting of nanosized SF segments. The inset shows a schematic diagram of the 90°and 30° Shockley partials (relative to the TEM beam direction) on FCC (111) slip planes. (**C** and **D**) SEM and bright-field TEM images at 90% N_f revealing widespread, dense, parallel microscale deformation bands intersecting multiple dislocation cells. The SAED pattern inset of these deformation bands shows parallel streaks along the [111] direction (indicated by the white arrow) due to SFs, alongside diffraction patterns of HCP martensite. (**E**) Orientation angle map revealing parallel HCP nanolayers at the topmost GDS surface measured using electron precession diffraction in TEM. (**F**) HAADF-STEM image of an individual deformation band revealing the ultrahigh density of HCP-FCC nanolaminates, along with numerous SFs. (**G**) Magnified HAADF-STEM image corresponding to the white-boxed region in (F) showing HCP nanolayers (highlighted in orange), SFs, and twin segments. In (B), (F), and (G), the dashed lines indicate (111) planes of SFs and TBs.

comparable to the spacing between opposite cell walls, whereas the average thicknesses of the HCP and FCC layers were ~5.2 nm and 7.8 nm, respectively. Therefore, a high volume fraction (~40%) of the nanolayered HCP phase formed within the microscale deformation bands. Both the SAED and HAADF-STEM results (Fig. 3, D, G, and H) indicated coherent HCP-FCC phase boundaries, with a typical orientation relationship of <0002>HCP//{111}FCC and <11$\bar{2}$0>HCP//<110>FCC. Energy-dispersive x-ray spectroscopy mapping showed uniform element distributions of all elements in both phases. These results suggest that a deformation-induced displacive transformation occurred from the austenitic FCC phase to the nanolayered martensitic HCP phase during ratcheting.

The FCC-to-HCP phase transformation, along with the formation of numerous SFs and limited TBs, introduces additional deformation mechanisms in GDS 304 SS beyond ordinary dislocation plasticity. As a result, ratcheting deformation in GDS samples involved extensive SFs and HCP activities, within fully developed dislocation cells as small as ~290 nm, leading to sustained nanoscale structural refinement. HAADF-STEM revealed numerous interlocked deformation bands in the top-layer grains, evidenced by intersecting HCP nanolayers corresponding to two HCP variants (Fig. 4, A and B). Moreover, extensive SFs formed in the FCC space between the interlocked HCP nanolayers, and these SFs frequently intersected each other or were obstructed by HCP-FCC phase boundaries (Fig. 4, B and C). By contrast, ratcheting deformation of most grains in the core of GDS samples was still dominated by extensive planar slip of full dislocations along {111} planes and loose dislocation tangles (fig. S5D). This ordinary full dislocation plasticity is similar to that observed in CG 304 SS, predominated by large dislocation cells (~500 nm) (figs. S5, A to C), as reported in most metals and alloys during ratcheting deformation (*2*, *14*, *18*, *29*).

By engineering a gradient hierarchy of dislocation cells, an unusual combination of deformation mechanisms involving SF formation and coherent FCC-to-HCP martensitic transformation can be activated, leading to significantly enhanced ratcheting resistance in GDS 304 SS along with high strength. The formation of ratcheting-regulated FCC and HCP nanolaminates is attributed to the combined effects of the following factors: the reduced characteristic length scale inherent in the GDS structure, the low SF energy of 304 SS, and the substantial cumulative plastic strain under asymmetrical cyclic stresses.

Unlike conventional plastic deformation involving full dislocation glide (*30*–*34*), the primary plastic carriers in GDS SS are Shockley partials and associated SFs. This response is mainly due to the reduced length scale of the

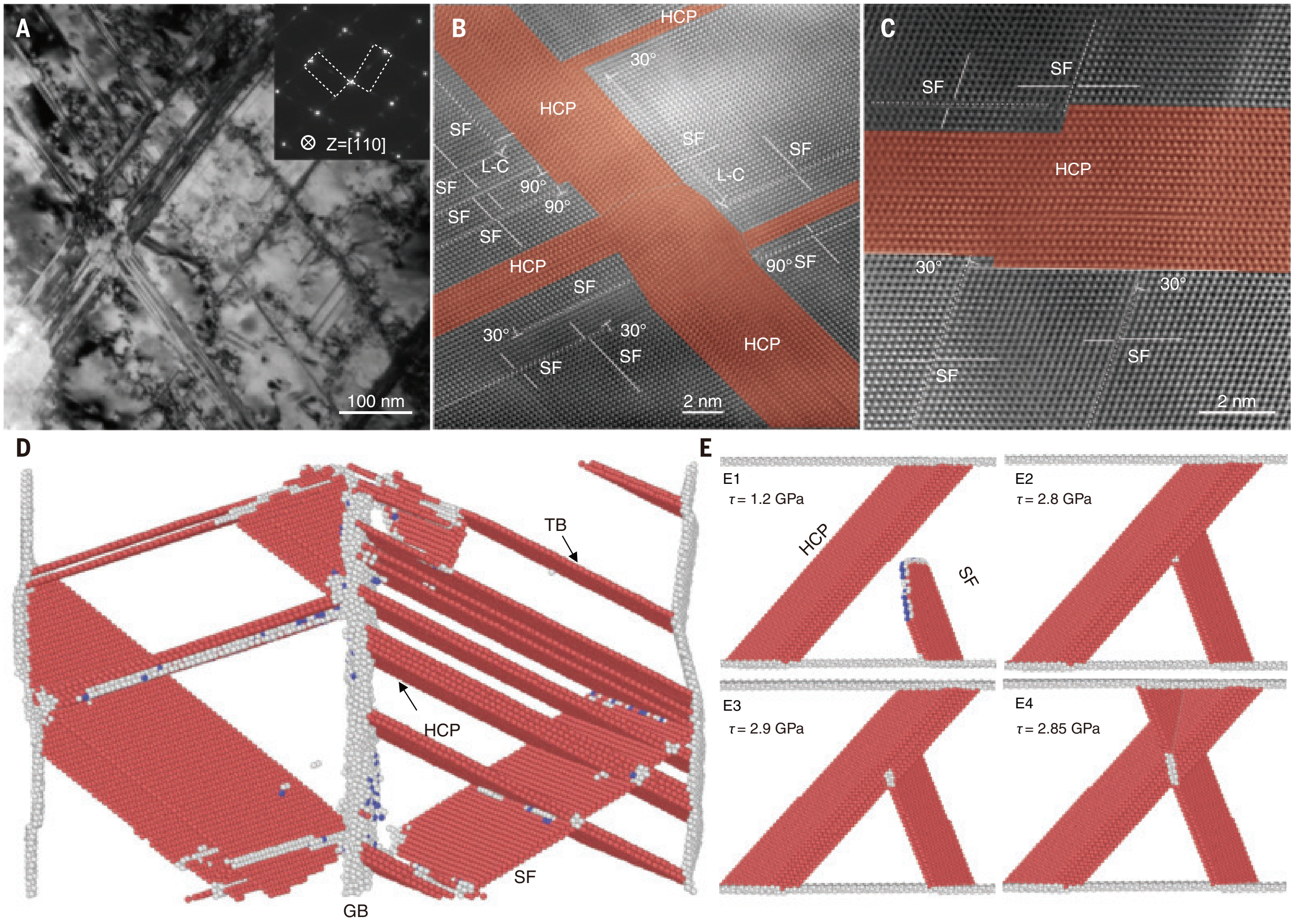

Fig. 4. Strengthening mechanisms of HCP nanolayers and SFs. (**A**) Bright-field TEM image of the topmost surface layer of GDS SS under a σ_{max} of 570 MPa at 90% N_f showing two variants of nanolayered HCP martensite intersecting each other. The inset shows SAED patterns from the intersecting HCP nanolayers. (**B**) HAADF-STEM image of a network of intersecting HCP nanolayers, SFs, and Lomer-Cottrell (L-C) locks. (**C**) Magnified HAADF-STEM image showing the interactions between an HCP nanolayer and intersecting SFs. (**D**) Atomic configurations from molecular dynamics simulation showing the formation of a network of HCP nanolayers, SFs, and TBs. Atoms in the FCC structure are omitted for clarity, and those in the HCP structure and at GBs and surfaces are colored red and white, respectively. (**E**) Atomic configurations from molecular dynamics simulation during the progressive slip transmission of an SF across an HCP nanolayer under increasing resolved shear stress τ acting on the SF (E1 to E4).

GDS structure formed through cyclic torsion. During ratcheting, significant long-range internal stresses develop to accommodate the strong structural heterogeneity introduced by the GDS structure (*26*, *35*, *36*), resulting in elevated local flow stresses, as evidenced by high microhardness values throughout GDS samples (fig. S2). To assess the effect of pretorsion on internal stresses, we estimated the internal stress level (X) of GDS samples using the yield stress difference between the prestrain and reference states: $X = \sigma_y$ (GDS) − σ_y (CG), based on tensile results (fig. S3A). By applying $(\sigma_{max} - X)/E$, the data for bulk GDS and surface GDS in Fig. 2F shift toward ratchet regime I corresponding to stage I hardening (*37*), as shown in fig. S6. According to (*37*), this stage involves low amplitudes of plastic deformation, favoring planar slip mechanisms, such as dislocation pile-up and SF formation.

High flow stresses in GDS samples provide large driving forces for the nucleation and migration of Shockley partials within highly stable dislocation cells. Additionally, the dense dislocations at cell walls serve as abundant sources for partial nucleation. Moreover, the low SF energy (~16.8 mJ/m^2) of 304 SS favors partial dislocation activity (*30*, *31*). Correspondingly, the critical size for the transition from full to partial dislocations with SFs is estimated to be ~240 nm, which closely matches the cell size (~290 nm) in the topmost GDS layer. The cumulative plastic strain of the GDS sample after a long ratcheting life of 3×10^5 cycles at a σ_{max} of 570 MPa reaches an enormous magnitude (~300), approximately three orders of magnitude greater than the net ratcheting strain (Fig. 2). The large cumulative plastic strain and associated plastic irreversibility under many cycles of asymmetrical stressing necessitate widespread SF activation. All of these factors promoting SF activity in GDS SS rarely coexist simultaneously in conventional coarse-grained or high-strength nanostructured metallic materials (*1*, *26*, *31*, *38*, *39*).

The extensive operation of partial dislocations during ratcheting deformation leads to the gradual accumulation of highly dense SFs, promoting the deformation-induced FCC-to-HCP martensitic transformation (Fig. 3 and fig. S7). The mechanism of this phase transformation differs under cyclic loading compared with monotonic loading. Under monotonic loading, the FCC-to-HCP transformation and deformation twinning occur through the glide of Shockley partials with parallel 1/6<112> Burgers vectors of the same sense on {111} planes (*40–43*). By contrast, under cyclic loading, FCC-to-HCP transformation is achieved through the glide of Shockley partials with coplanar 1/6<112> Burgers vectors along different directions (Fig. 3 and fig. S7). Partial glide through alternative Burgers vectors not only effectively accommodates applied shear strains with alternating signs during cyclic stressing, but also reduces the net local plastic shear strain at the ends of each slender HCP nanolayer. Consequently, the facile partial glide reduces local deformation incompatibility between the HCP nanolayers and the FCC matrix, lowering the likelihood of damage initiation.

The nanolayered HCP martensite plays a crucial role in the strengthening and hardening responses of GDS SS during ratcheting deformation. Unlike high-angle GBs or incoherent phase boundaries (*31*, *40*), the HCP nanolayers form coherent interfaces with the FCC matrix. These coherent boundaries act as strong barriers that effectively impede the glide of dislocations and SFs on slip planes inclined to the phase boundaries (Fig. 4, A to C). Molecular dynamics simulations revealed the strong obstruction of SFs by HCP nanolayers (Fig. 4, D and E). For example, a SF on an inclined {111} slip plane in the FCC matrix was hindered by a coherent phase boundary (Fig. 4, E1 and E2). Raising the resolved shear stress barely initiated the transmission of this SF across the phase boundary (Fig. 4E3). Further increases in shear stress allowed the dislocation to glide on an inclined $\{10\bar{1}1\}$ pyramidal plane inside the HCP nanolayer (Fig. 4, E3 and E4). Evidently, the high resistance to slip transmission stems from the strong coherent phase boundary and the high slip resistance on pyramidal planes within the HCP nanolayers (*11*, *39*).

The sustained structural refinement, from initial dislocation cells to finer networks of FCC-HCP nanolaminates and dislocation cells (Figs. 3 and 4), continuously enhanced the ability to obstruct the glide of full dislocations and partials by reducing mean free paths and segment lengths while providing abundant sources for defect nucleation and accumulation (Figs. 3 and 4). These results indicate that the increasing formation of FCC-HCP nanolaminates can sustainably enhance strain hardening and reduce dynamic recovery during asymmetrical stress cycling, thus significantly lowering ratcheting strain under prolonged cycling.

The nanolayered HCP martensite also plays a significant role in suppressing strain localization and damage accumulation in GDS SS during stress cycling, particularly compared with the mechanically induced body-centered cubic (BCC) martensite in the CG counterparts (*38*, *44–48*). The coherent FCC-HCP interfaces reduce local geometrical incompatibility and interfacial energy, stabilizing the HCP nanolayers by preventing heterogeneous coarsening (*11*, *39*), even at the nanoscale. These coherent interfaces, along with the aforementioned FCC-to-HCP phase transformation mediated by Shockley partials with different Burgers vector directions (Fig. 3 and fig. S7), effectively suppress fatigue damage nucleation. By contrast, uncontrolled transformation into a hard, incoherent BCC-based phase, accompanied by a large lattice dilatation (*40*), is known to be detrimental to ratcheting resistance, even for conventional TRIP steels that exhibit accelerated ratcheting and damage initiation due to phase transformation (*2*, *15*, *49*).

Three-dimensional x-ray tomography revealed the minimal cross-section contraction of GDS specimens after asymmetrical stress cycling (fig. S8, A and B), indicating their exceptional ratcheting resistance (Fig. 2). x-ray tomography further showed no discernable microcracks in GDS samples cycled to 90% N_f (fig. S8A); even after failure, cracks or dimples were only confined to regions near the fracture surface (fig. S8B). By contrast, CG samples exhibited macrocracks measuring hundreds of micrometers long on the topmost surface and numerous microcracks (tens of micrometers long) in the interior after 90% N_f (fig. S8C) resulting from widespread strain concentration and fatigue cracking. These damages were correlated with a high density of ultrafine, elongated BCC martensitic blocks (average transversal size of ~150 nm and longitudinal size ~800 nm) frequently detected near the cracks (fig. S8, D to F), similar to those found in fatigued metals with low SF energies (*1*, *29*).

The built-in gradient distribution of dislocation cells and the associated strength gradient also enhance the ratcheting resistance to GDS samples under asymmetrical stress cycling. During testing, this strength gradient leads to progressive yielding behavior and a corresponding plastic strain gradient from the soft core to the strong topmost surface (*26*, *36*). Accommodating this plastic strain gradient results in the accumulation of geometrically necessary defects, including dislocations, SFs, and martensitic HCP nanolayers (*26*, *36*). These defects contribute to sustained nonlinear kinematic and isotropic hardening for enhancing ratcheting resistance (fig. S9) (*50*). This effect is demonstrated by combining experimental measurements with a cyclic plasticity model to characterize the evolution of back stress and effective stress under asymmetric cyclic stressing. The back stress typically arises from geometrically necessary dislocations that generate long-range, directional internal stresses, whereas the effective stress originates from statistically stored dislocations that induce short-range, nondirectional internal stresses (*26*, *31*, *37*). Both impede plastic flow (*31*, *37*). Our cyclic plasticity modeling results of GDS samples (fig. S9A and table S2) closely match the measured cumulative ratcheting strain with cycles. They show a steeper hardening rate in back stress for GDS compared with CG samples under the same $\sigma_{\max}$. This is evidenced by a more rapid evolution of back stress during forward and reverse loading (fig. S9, B and C) caused by enhanced hardening and reduced recovery. Consequently, the net plastic strain per cycle is smaller and thus the ratcheting rate is lower in GDS than in CG samples. This sustained nonlinear kinematic and isotropic hardening with increasing cycles in GDS samples (fig. S9, D and E) underscores the benefit of progressive microstructural refinement through the continued accumulation of SFs and FCC-HCP nanolaminates during the ratcheting deformation of GDS 304 SS.

In summary, we have achieved a combination of high strength and superior resistance to cyclic creep (ratcheting) by engineering the gradient hierarchy of dislocation cells in single-phase FCC 304 SS. Under asymmetrical cyclic stresses, continuous SF formation and FCC-to-HCP coherent martensitic transformation lead to sustained structural refinement evolving from submicrometer dislocation cells to finer networks of FCC-HCP nanolaminates within stable dislocation cells. This progressively refined microstructure enhances strain hardening, reduces dynamic recovery, and mitigates strain localization, significantly lowering cumulative ratcheting strain even after long-term cycles. The principle of sustained microstructural refinement through a gradient dislocation architecture and deformation-induced FCC-to-HCP martensitic transformations can be applied to other alloy systems by adjusting the composition or deformation conditions.

REFERENCES AND NOTES

1. S. Suresh, *Fatigue of Materials* (Cambridge Univ. Press, ed. 2, 1998).
2. G. Z. Kang, *Int. J. Fatigue* **30**, 1448–1472 (2008).
3. S. K. Paul, *J. Mater. Res. Technol.* **8**, 4894–4914 (2019).
4. H. Hübel, *Nucl. Eng. Des.* **162**, 55–65 (1996).
5. J. L. Chaboche, *Int. J. Plast.* **5**, 247–302 (1989).
6. T. Hassan, E. Corona, S. Kyriakides, *Int. J. Plast.* **8**, 117–146 (1992).
7. Y. Y. Jiang, H. Sehitoglu, *Int. J. Plast.* **10**, 849–870 (1994).
8. D. L. McDowell, *Int. J. Plast.* **11**, 397–421 (1995).
9. T. Hassan, S. Kyriakides, *Int. J. Plast.* **10**, 149–184 (1994).
10. G. Z. Kang, Y. Li, Q. Gao, Q. H. Kan, J. Zhang, *Fatigue Fract. Eng. Mater. Struct.* **29**, 93–103 (2006).
11. K. Zhang, J. R. Weertman, *Metall. Mater. Trans., A Phys. Metall. Mater. Sci.* **40**, 2255–2263 (2009).
12. C. Holste, W. Kleinert, R. Gürth, K. Mecke, *Mater. Sci. Eng. A* **187**, 113–123 (1994).
13. F. Lorenzo, C. Laird, *Acta Metall.* **32**, 681–692 (1984).
14. K. Dutta, S. Sivaprasad, S. Tarafder, K. K. Ray, *Mater. Sci. Eng. A* **527**, 7571–7579 (2010).
15. S. Chang, Z. Zhu, X. Huang, J. Zhang, G. Kang, *Int. J. Fatigue* **181**, 108118 (2024).
16. X. C. Lu *et al.*, *J. Mech. Phys. Solids* **142**, 103971 (2020).
17. G. Z. Kang, Q. Gao, L. Cai, X. Yang, Y. Sun, *J. Mater. Sci. Technol.* **17**, 219–223 (2001).
18. P. Lukáš, L. Kunz, *Mater. Sci. Eng. A* **322**, 217–227 (2002).
19. S. Cheng *et al.*, *Acta Mater.* **57**, 1272–1280 (2009).
20. M. Zhang *et al.*, *Int. J. Fatigue* **121**, 252–264 (2019).
21. Y. Wu, J. Yang, X. Shen, R. Zhu, *J. Mater. Eng. Perform.* **26**, 837–842 (2017).

22. C. Backes, M. Smaga, T. Beck, *Int. J. Fatigue* **186**, 108410 (2024).
23. Q. Pan *et al.*, *Science* **374**, 984–989 (2021).
24. Q. Pan *et al.*, *Science* **382**, 185–190 (2023).
25. K. H. Lo, C. H. Shek, J. K. L. Lai, *Mater. Sci. Eng. Rep.* **65**, 39–104 (2009).
26. X. Y. Li, L. Lu, J. Li, X. Zhang, H. Gao, *Nat. Rev. Mater.* **5**, 706–723 (2020).
27. Y. M. Wang *et al.*, *Nat. Mater.* **17**, 63–71 (2018).
28. S. Sinha, S. Ghosh, *Int. J. Fatigue* **28**, 1690–1704 (2006).
29. P. Peralta, C. Laird, in *Physical Metallurgy*, D. E. Laughlin, K. Hono, Eds. (Elsevier, ed. 5, 2014), pp. 1765–1880.
30. J. P. Hirth, J. Lothe, *Theory of Dislocations* (Cambridge Univ. Press, 2017).
31. A. S. Argon, *Strengthening Mechanisms in Crystal Plasticity* (Oxford Univ. Press, 2008).
32. J. C. Stinville *et al.*, *Science* **377**, 1065–1071 (2022).
33. S. Lavenstein, Y. Gu, D. Madisetti, J. A. El-Awady, *Science* **370**, eabb2690 (2020).
34. Q. Pan, H. Zhou, Q. Lu, H. Gao, L. Lu, *Nature* **551**, 214–217 (2017).
35. H. Mughrabi, *Acta Metall.* **31**, 1367–1379 (1983).
36. Y. T. Zhu *et al.*, *Mater. Res. Lett.* **9**, 1–31 (2020).
37. X. Feaugas, C. Gaudin, *Int. J. Plast.* **20**, 643–662 (2004).
38. X. S. Yang, S. Sun, T.-Y. Zhang, *Acta Mater.* **95**, 264–273 (2015).
39. A. Pineau, A. Amine Benzerga, T. Pardoen, *Acta Mater.* **107**, 508–544 (2016).
40. J. W. Christian, *The Theory of Transformations in Metals and Alloys* (Elsevier, ed. 3, 2002).
41. H. He *et al.*, *Nano Lett.* **21**, 1419–1426 (2021).
42. H. Fujita, S. Ueda, *Acta Metall.* **20**, 759–767 (1972).
43. G. B. Olson, M. Cohen, *Metall. Trans., A* **7**, 1897–1904 (1976).
44. G. B. Olson, M. Cohen, *J. Less Common Met.* **28**, 107–118 (1972).
45. T. Suzuki, H. Kojima, K. Suzuki, T. Hashimoto, M. Ichihara, *Acta Metall.* **25**, 1151–1162 (1977).
46. K. P. Staudhammer, L. E. Murr, S. S. Hecker, *Acta Metall.* **31**, 267–274 (1983).
47. J. A. Venables, *Philos. Mag.* **7**, 35–44 (1962).
48. Y. Li *et al.*, *Science* **379**, 168–173 (2023).
49. M. Soleimani, A. Kalhor, H. Mirzadeh, *Mater. Sci. Eng. A* **795**, 140023 (2020).
50. N. Ohno, J. D. Wang, *Int. J. Plast.* **9**, 375–390 (1993).

ACKNOWLEDGMENTS

We thank J. P. Cui for performing HAADF-STEM experiments; S. G. Wang, C. J. Li, and L. Zhang for performing x-ray experiments and analyzing the results; and C. H. Li for performing the EBSD experiments. **Funding:** Q.P. and L.L. acknowledge financial support from the National Science Foundation of China (NSFC, grants 92463302, 92163202, 52122104, 52471151, and 52071321) and from the international partnership program of the Chinese Academy of Sciences (CAS grant 172GJHZ2023075GC). Q.P. is supported by the Excellent Youth Innovation Promotion Association and Strategic Priority Research Program, CAS. N.L. is supported by the Shandong Excellent Young Scientists Fund Program (Overseas) (grant 2023HWYQ-041). **Author contributions:** L.L. and T.Z. initiated and supervised the project. Q.P. and S.G. prepared the sample and performed the experiments. Q.P. and N.L. guided and analyzed TEM results. K.D. and T.Z. performed atomistic and cyclic plasticity simulations. Q.P., L.L., and T.Z. designed the experiments and drafted the manuscript. All coauthors contributed to the discussions and revised the manuscript. **Competing interests:** The authors declare no competing interests. **Data and materials availability:** All data are available in the main manuscript or the supplementary materials.

SUPPLEMENTARY MATERIALS

science.org/doi/10.1126/science.adt6666
Materials and Methods
Supplementary Text
Figs. S1 to S9
Tables S1 and S2
References (*51*–*66*)

Submitted 7 October 2024; accepted 20 February 2025
10.1126/science.adt6666

SOLAR CELLS

Strain-induced rubidium incorporation into wide-bandgap perovskites reduces photovoltage loss

Likai Zheng[1]†, Mingyang Wei[2]†, Felix T. Eickemeyer[1]†, Jing Gao[1]†, Bin Huang[3], Ummugulsum Gunes[4], Pascal Schouwink[5], David Wenhua Bi[6], Virginia Carnevali[7], Mounir Mensi[5], Francesco Biasoni[7,8], Yuxuan Zhang[4], Lorenzo Agosta[7], Vladislav Slama[7], Nikolaos Lempesis[7], Michael A. Hope[4]‡, Shaik M. Zakeeruddin[1], Lyndon Emsley[4], Ursula Rothlisberger[7], Lukas Pfeifer[1]*, Yimin Xuan[3]*, Michael Grätzel[1]*

A-site cation mixing can enhance the photovoltaic performance of a wide-bandgap (WBG) perovskite, but rubidium (Rb) cation mixing generally forms a nonperovskite phase. We report that lattice strain locks Rb ions into the α-phase of the lattice of a triple-halide WBG perovskite, preventing phase segregation into a nonperovskite Rb-cesium–rich phase. This process cooperates with chloride accommodation and promotes halide homogenization across the entire film volume. The resulting 1.67–electron volt WBG perovskite exhibits photoluminescence quantum yields exceeding 14% under 1-sun-equivalent irradiation, corresponding to a quasi–Fermi level splitting of ~1.34 electron volts. A WBG perovskite solar cell with an open-circuit voltage (V_{OC}) of 1.30 volts was prepared, corresponding to 93.5% of the radiative V_{OC} limit and representing the lowest photovoltage loss relative to the theoretical limit observed in WBG perovskites.

Perovskite solar cells (PSCs) represent the fastest-developing photovoltaic (PV) technology, having attained a certified power conversion efficiency (PCE) of 26.7% (*1*). To surpass the Shockley-Queisser limit for single-junction solar cells, tandem architectures have been developed that combine a wide-bandgap (WBG) perovskite top cell with a narrow-bandgap (NBG) bottom cell (*2*). In tandem cells, the WBG perovskites contribute to a higher open-circuit voltage (V_{OC}). Additionally, the bandgap tunability of WBG perovskites is of great interest for the development of light-emitting diodes (LEDs) and for indoor or semitransparent building-integrated PVs (*3*).

To date, WBG perovskites have been composed of mixed halides at the X-site and a combination of formamidinium (FA), methylammonium (MA), and cesium (Cs) at the A-site to achieve the desired bandgap, phase stability, and low defect density (*4*, *5*). Despite advances in compositional engineering, the PCE of WBG PSCs remains considerably lower than their theoretical limit, primarily because nonradiative recombination creates a V_{OC} deficit (*6*, *7*). Recent studies have identified that an inhomogeneous halide distribution already present in as-fabricated films could account for the limited optoelectronic performance (*8*–*10*). This inhomogeneity also compromises long-term stability, as the nonuniform energy landscape accelerates halide segregation through photogenerated hole trapping by iodide-rich, low-bandgap domains (*11*).

Homogenizing film composition remains a promising strategy to suppress bulk recombination in WBG PSCs. In 1.5-eV PSCs suitable for single-junction applications, introducing rubidium (Rb) additives is an effective approach to homogenize perovskite growth (*12*), eliminate detrimental impurities (*13*), and stabilize photoactive α-phases (*14*). However, solid-state nuclear magnetic resonance (NMR) studies have revealed that Rb ions are not accommodated into perovskite lattices but instead form secondary, nonperovskite phases with lead iodide (PbI_2) (*15*).

Here, we report the strain-induced incorporation of Rb ions into the lattice of triple-halide WBG perovskites, in stark contrast to the structures formed in normal-bandgap perovskites. X-ray diffraction (XRD) techniques, solid-state NMR, and computational studies indicate that Rb and Cl anions, when applied together, compensate for each other's ionic radii by exerting lattice contractions to better accommodate small ions at both A- and X-sites. This stabilization mechanism leads to a uniform distribution of Rb and Cs and induces halide homogenization, resulting in a flat electronic structure within the film. The Rb-incorporated WBG perovskite films exhibit

---

[1]Laboratory of Photonics and Interfaces, Institute of Chemical Sciences and Engineering, École Polytechnique Fédérale de Lausanne (EPFL), Lausanne, Switzerland. [2]Department of Materials Science and Engineering, National University of Singapore, Singapore. [3]School of Energy and Power Engineering, Nanjing University of Aeronautics and Astronautics, Nanjing, PR China. [4]Laboratory of Magnetic Resonance, Institute of Chemical Sciences and Engineering, EPFL, Lausanne, Switzerland. [5]X-Ray Diffraction and Surface Analytics Platform, Institute of Chemical Sciences and Engineering, EPFL, Sion, Switzerland. [6]Crystal Growth Facility, Institute of Physics, EPFL, Lausanne, Switzerland. [7]Laboratory of Computational Chemistry and Biochemistry, Institute of Chemical Sciences and Engineering, EPFL, Lausanne, Switzerland. [8]Department of Energy, Politecnico di Milano, Milano, Italy.
***Corresponding author: lukas.pfeifer@epfl.ch (L.P.); ymxuan@nuaa.edu.cn (Y.X.); michael.graetzel@epfl.ch (M.G.)**
†These authors contributed equally to this work.
‡Present address: Department of Chemistry, University of Warwick, Coventry, UK.

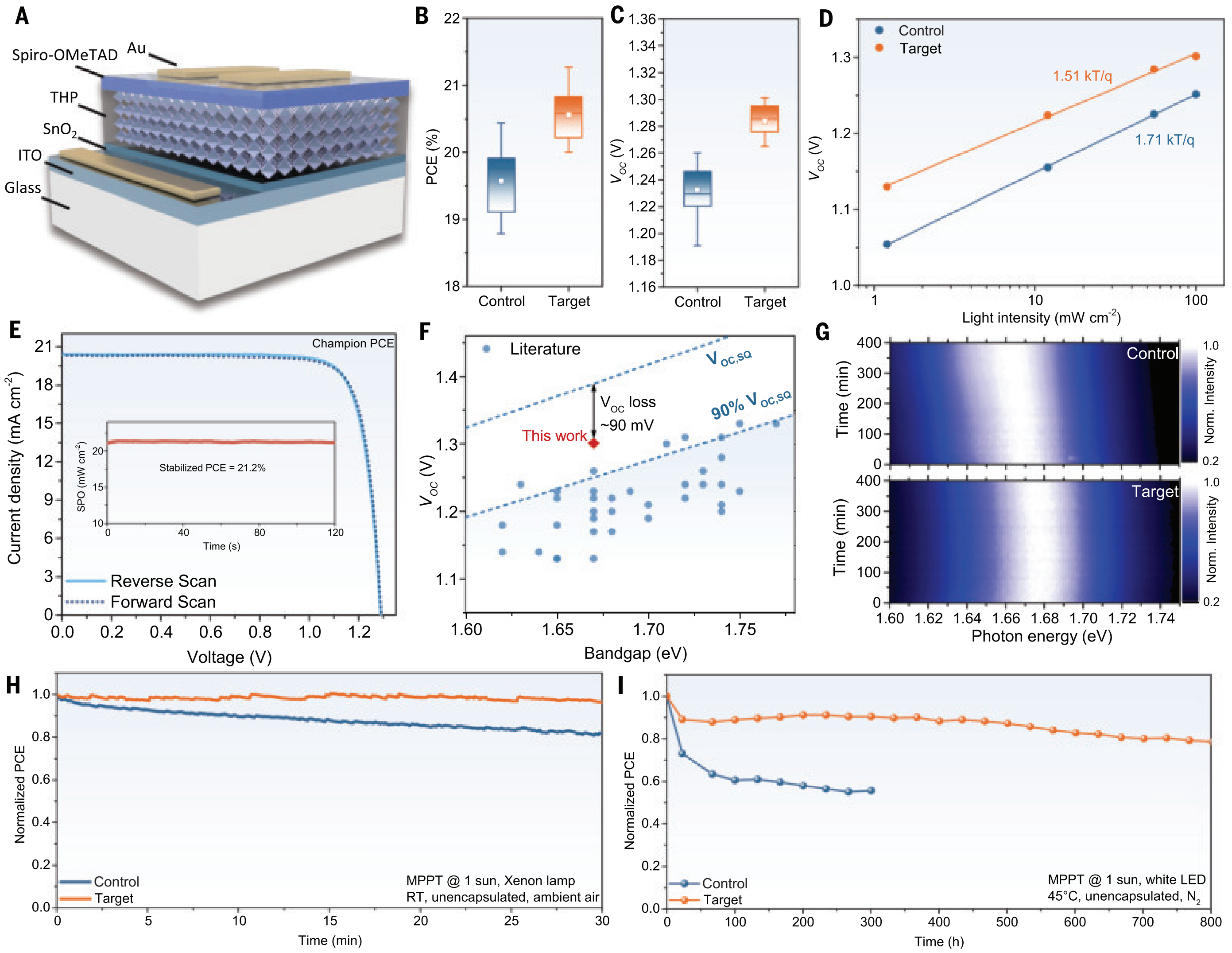

Fig. 1. Power-conversion performance of triple-halide WBG PSCs. (**A**) Schematic diagram of the devices. (**B** and **C**) Box plots of (B) PCE and (C) V_{OC} for control and target PSCs (16 devices for each condition). The horizontal lines of the box plots represent the 75th percentile, median value, and 25th percentile, going from top to bottom. The top and bottom whiskers are determined by the 95th and 5th percentile, respectively. (**D**) Light intensity plotted against V_{OC} for control and target PSCs. (**E**) *J-V* curves of the device with champion PCE under AM1.5G 1-sun illumination. The inset shows the stabilized power conversion efficiency. SPO, stabilized power output. (**F**) Summary of the reported V_{OC} values for representative PSCs with different bandgaps. SQ, Shockley-Queisser limit. (**G**) Time-dependent PL of pristine and Rb-doped THP films under 1-sun equivalent LED illumination. (**H**) MPP tracking (MPPT) of unencapsulated PSCs under simulated AM1.5G illumination (1 sun, xenon lamp) in ambient air without temperature control. The initial PCEs of the control and target PSCs were 19.65 and 20.45%, respectively. (**I**) MPP tracking of unencapsulated PSCs under 1-sun illumination (white LED) in an N_2 atmosphere at 45°C (ISOS-L-1I). The initial PCEs of the control and target PSCs were 18.83 and 19.75%, respectively.

photoluminescence quantum yields (PLQYs) exceeding 14%, corresponding to an internal V_{OC} of 1.34 V that approaches the radiative theoretical limit.

Device performance and stability of triple-halide WBG PSCs

Encouraged by recent reports on Rb additives used in efficient and stable single- or double-halide PSCs (*16*, *17*), we used Rb^+ to prepare triple-halide perovskite solar cells (THPSCs) with a perovskite composition of $Cs_{0.22}MA_{0.03}FA_{0.75}Pb(I_{0.82}Br_{0.15}Cl_{0.03})_3$ and featuring a layered architecture of glass/ITO/SnO_2/perovskite/spiro-OMeTAD/Au (Fig. 1A), where spiro-OMeTAD stands for 2,2′,7,7′-tetrakis(*N*,*N*-di-*p*-methoxyphenylamino)-9,9′-spirobifluorene. We varied the ratio of Rb added to the perovskite precursor and identified an amount of 3 mol % Rb to give optimal results (fig. S1). The introduction of Rb substantially improved the PCE of the PSCs compared with the Rb-free control samples, stemming chiefly from a substantial improvement in V_{OC} (Fig. 1, B and C; fig. S2; and table S1).

An ideality factor of 1.51 was observed for the target device, whereas the value of the control device was 1.71, indicating suppressed nonradiative recombination in the target device (Fig. 1D). Notably, the target device reached a very high V_{OC} of 1.22 V under only 11% of the AM1.5G 1-sun intensity. The optimized target device achieved a champion PCE of 21.4% with negligible hysteresis and values for short-circuit current density (J_{SC}), V_{OC}, and fill factor (FF) of 20.4 mA cm^{-2}, 1.29 V, and 81.3%, respectively. A steady-state PCE of 21.2% after 120 s maximum power point (MPP) tracking (Fig. 1E) was found for the same device.

The bandgap of the target device was determined to be 1.67 eV by analyzing its external quantum efficiency (EQE) spectrum, which

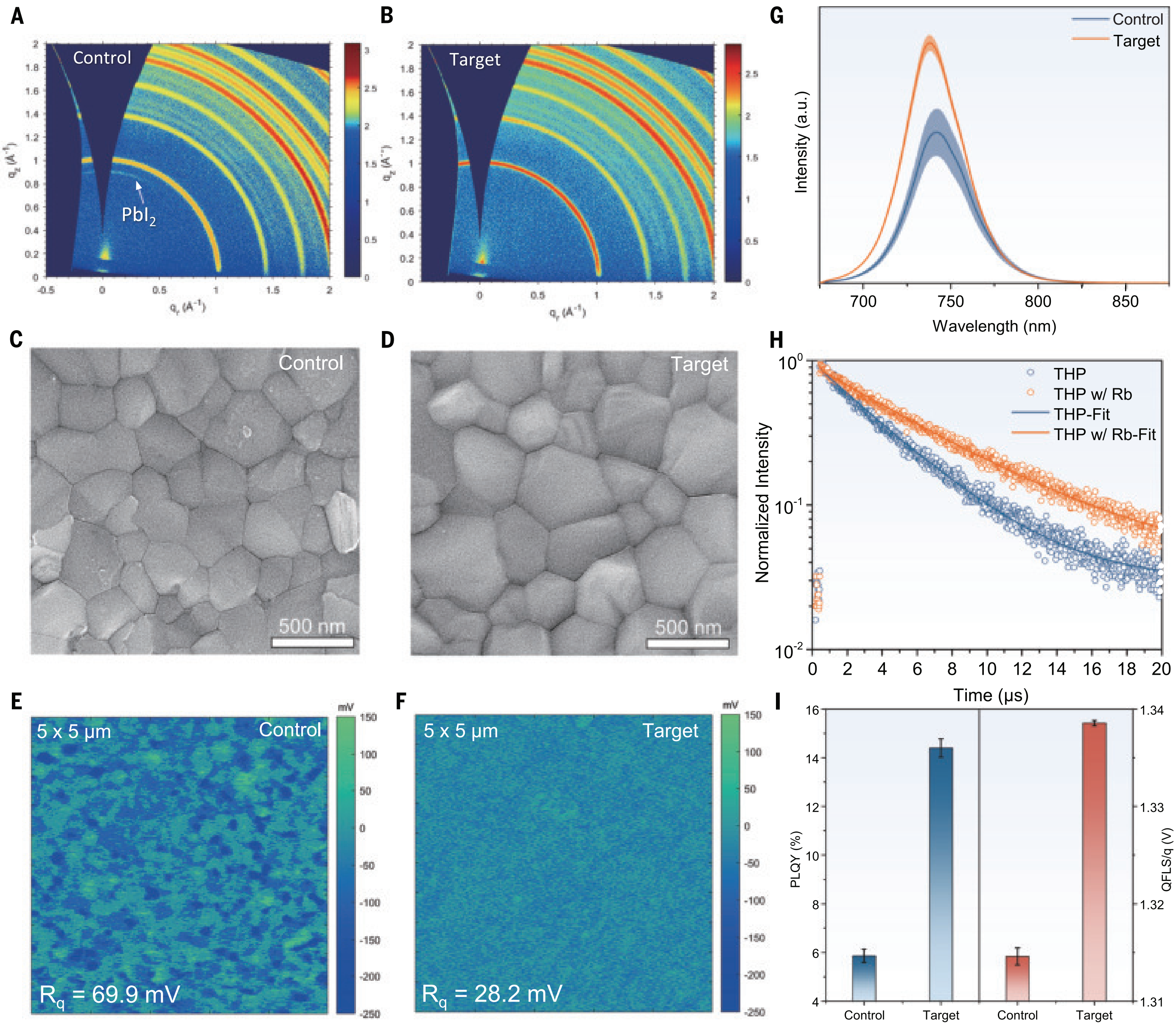

Fig. 2. Spectral and morphological characteristics of perovskite films. (**A** and **B**) GIWAXS patterns of (A) pristine and (B) 3% Rb-doped THP films. (**C** and **D**) Top view SEM images of (C) pristine and (D) 3% Rb-doped THP films. (**E** and **F**) Surface potential difference obtained by KPFM of (E) pristine and (F) 3% Rb-doped THP films. R_q represents the root mean square value. (**G**) Steady-state PL results of perovskite films with and without 3% Rb^+ measured in three different positions for each condition. a.u., arbitrary units. (**H**) TRPL results of perovskite films with and without 3% Rb^+. (**I**) PLQY and QFLS results of perovskite films with and without 3% Rb^+ (four individual samples for each condition).

exhibited an inflection point (*18*) at ~743 nm (fig. S3). The integrated J_{SC} from the EQE measurement was 20.4 mA cm^{-2}, matching well with the value extracted from the *J-V* curve. Notably, a champion V_{OC} of 1.30 V was obtained from a device with a high PCE of 20.65%, and a stabilized V_{OC} of 1.30 V was obtained after 60 s of continuous illumination (fig. S4). This value corresponded to 93.4% of the Shockley-Queisser limit of V_{OC}, equivalent to a loss of only 90 mV. This value is the lowest reported for PSCs with a bandgap ≥ 1.62 eV (Fig. 1F, fig. S5, and table S2).

Exploration of the role of Rb^+ in mitigating photoinduced phase segregation in triple-halide perovskite (THP) films involved a series of time-dependent photoluminescence (PL) measurements under 1-sun continuous illumination in a moisture-free atmosphere (Fig. 1G). The appearance of a red shift in the PL spectrum typically signifies the emergence of light-induced phase segregation. We used the spectral centroid (*19*) method for a comprehensive depiction of the PL spectrum's evolution over time (fig. S6). After 400 min, the unmodified THP film demonstrated the formation of a lower-energy PL peak, with the spectral centroid displaying a red shift exceeding 3.5 nm. Conversely, the Rb-doped THP film exhibited exceptional photostability, maintaining its original PL spectral characteristic without the emergence of lower-energy peaks. This improvement in phase stability allowed an unencapsulated target cell to maintain 96.4% of its initial PCE after operating in ambient air under 1-sun illumination (xenon lamp) at its MPP for 30 min (Fig. 1H), whereas the PCE of a control cell degraded to 81.7% of its initial PCE within the same time. Additionally, an unencapsulated

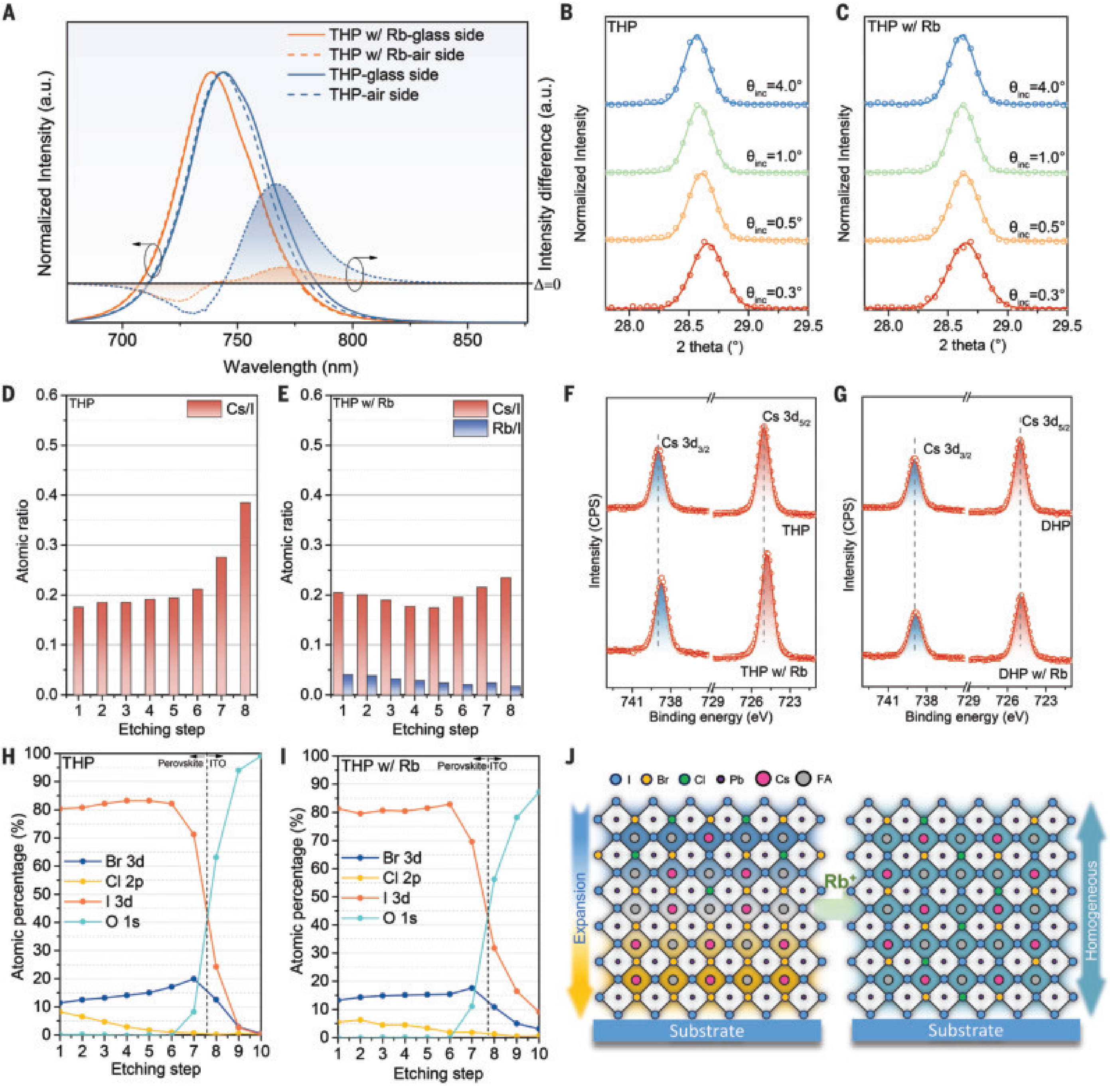

Fig. 3. Composition depth profiles of perovskite films. (**A**) Steady-state PL results (normalized) from glass and air sides of THP films without and with 3% Rb. The dashed curves represent the difference in intensity between the normalized PL spectra of glass and air sides for each condition. (**B** and **C**) Angle-dependent GIXRD results of perovskite films (B) without and (C) with 3% Rb. (**D** and **E**) Depth profile XPS results of Cs/I and Rb/I ratios in THP perovskite films (D) without and (E) with 3% Rb. (**F** and **G**) XPS results of (F) Cs and (G) Cl of triple halide perovskites without and with 3% Rb. CPS, counts per second. (**H** and **I**) Depth profile XPS results of halides and oxygen in perovskite films (H) without and (I) with 3% Rb. (**J**) Schematic diagram of trends in the distribution of the studied A- and X-site ions in THP films before and after Rb-doping and their effect on the observed lattice constants.

target device retained 80% of its initial PCE after 750 hours of continuously operating at MPP under 1-sun illumination (white LED) at 45°C in N_2 (ISOS-L-1I), whereas the PCE of a control device had decreased to 55% of its initial value after 300 hours (Fig. 1I).

Spectral and morphological characteristics of perovskite films

To explore the impact of Rb on the crystallization properties of THP films, we initiated our investigation with grazing-incidence wide-angle x-ray scattering (GIWAXS) measurements on THP films without and with 3% Rb^+ (Fig. 2, A and B). The reference perovskite displayed characteristic diffraction rings at scatter vector (**q**) values of ≈1, 1.37, 1.65, and 1.85 nm^{-1}, related to the (100), (110), (111), and (200) crystal planes of THP films, respectively. With the addition of 3% Rb^+, the previously observed PbI_2 signal disappeared, and stronger reflections of the (100) and (200) facets were observed.

This change in crystallization behavior of the perovskite films was accompanied by a considerable increase of the grain domain size, from an average of 336 nm to 393 nm, as observed by scanning electron microscopy (SEM) (Fig. 2, C and D). These results were also consistent with those obtained from atomic force microscopy (AFM) measurements on a scanned area of 5 μm by 5 μm (fig. S7), indicating fewer domain boundaries and thus fewer lattice defects. Furthermore, Rb-doped THP films showed a more homogeneous surface potential distribution, with an R_q (root mean square of deviation) value of 28.2 mV, whereas the pristine THP film exhibited an R_q of ~69.9 mV, as determined from Kelvin probe force microscopy (KPFM) measurements (Fig. 2, E and F). This result suggested a more homogeneous surface layer structure that would lead to a lower fluctuation of the optoelectronic properties, as was indeed seen in the PL statistics (Fig. 2G).

The PL data derived from measurements at three distinct regions of the films not only revealed an improvement in uniformity upon Rb doping but they also showed that the Rb-doped THP films exhibited markedly higher PL intensity, clearly suggesting a decrease in nonradiative recombination. Furthermore, we observed a slight blue shift in the PL peak, from 743 nm in the pristine films to 739 nm in the Rb-doped THP films, which was likely attributable to a change in octahedral tilting angles and simultaneous lattice contraction.

We then performed time-resolved photoluminescence (TRPL) analyses of both control and target THP films fabricated on glass with an octylammonium bromide top passivation layer. The results revealed that both sets of THP films adhered closely to a monoexponential decay model (Fig. 2H), highlighting changes in nonradiative recombination rates in the film bulk. The decay time was drastically increased from ~3.90 μs (control) to ~6.05 μs (target), indicating a suppression of nonradiative recombination in the Rb-doped THP film (table S3). This result was in good agreement with the measured PLQY, increasing from 5.8 ± 0.3% for pristine THP films to 14.4 ± 0.4% for target samples, accompanied by an increase in quasi–Fermi level splitting (QFLS) of ~24 meV (Fig. 2I).

Compositional depth profiles of perovskite films

The in-plane homogenization of THP films by Rb^+ doping motivated us to also probe the out-of-plane direction by evaluating the PL collected from both the front side (glass-THP interface) and back side (THP-air interface) of the sample. We plotted the normalized PL spectra for each sample, comparing measurements taken from the glass and air sides, and calculated the respective difference spectra (Fig. 3A). The transition of these spectra from negative to positive when transitioning from short to long wavelengths signified a red shift in the PL of the glass side relative to the air side. Notably, a substantial disparity in PL intensity between the two sides, particularly around 767 nm, hinted at a shoulder in the PL spectrum taken from the glass side of the pristine THP sample. We could tentatively attribute this feature to reabsorption stemming from an uneven bandgap distribution along the out-of-plane axis (see supplementary text 1 in the supplementary materials).

Further evidence of a bandgap widening in the absence of Rb was attained by grazing incidence x-ray diffraction (GIXRD) measurement with varying incidence angle, which was conducted to obtain the diffraction patterns at different film depths from the surface through the bulk and to the glass interface (Fig. 3, B and C, and fig. S8). With the incident angle increasing from 0.3° to 4.0°, we could observe changing XRD patterns with an increasing contribution of reflections related to indium tin oxide (ITO) as we probed deeper regions of the films (fig. S9). Focusing on the (200) facet, we observed a diffraction peak at a 2θ angle of 28.66° on the top surface of the pristine THP film with an incident angle of 0.3°, followed by a gradual shift to 28.61°, 28.58°, and 28.56° with the incident angle increasing to 0.5°, 1.0°, and 4.0°, respectively (Fig. 3B). This result was indicative of a more contracted lattice on the surface compared with the bulk region of the pristine THP film. After introducing Rb into the THP composition, the peak positions shifted to 28.65°, 28.63°, 28.62°, and 28.62° under incident angles of 0.3°, 0.5°, 1.0°, and 4.0°, respectively (Fig. 3C). Thus, Rb almost eliminated this gradual shift of the lattice constants along the out-of-plane direction of the THP films.

To delve deeper into the underlying mechanism affecting the change in lattice parameters, we performed depth-dependent x-ray photoelectron spectroscopy (XPS) analysis to explore the depth profiles of Cs and Rb for pristine and Rb-doped THP films (Fig. 3, D and E). The cross-sectional SEM images of the studied films showed a similar thickness of around 460 nm (fig. S10). The XPS measurements confirmed the presence of Cl in these films as well as the presence of Rb in the Rb-doped ones (figs. S11 and S12). Furthermore, they indicated that in the absence of Rb, Cs tended to accumulate at the bottom of the perovskite film, likely because of the faster crystallization of Cs-rich perovskites (*20*). However, with the introduction of Rb^+, there was a noticeable decrease in the concentration of Cs at the bottom of THP films, resulting in a more uniform distribution. Notably, these XPS measurements also revealed a strong shift in the Cs 3d signal to a lower binding energy (~300 meV) in Rb-doped THP samples compared with that of pristine THP, whereas no such difference was observed in the double-halide perovskite (DHP) case (Fig. 3, F and G). This shift indicates an increase in the electron density around the Cs ions after adding Rb.

As was observed for the distribution of Cs, the distributions of the halides were affected substantially by the presence of Rb^+ in THP films (Fig. 3, H and I). Although both the pristine and Rb-doped THP films displayed a relatively uniform iodide concentration of 82 atomic % of the halide content across the film, in line with its nominal composition, this uniformity was not seen for bromide (Br) and chloride (Cl). The former showed a distinct gradient increasing progressively from 11% at the top surface to 20% at the bottom interface, whereas the latter exhibited an inverse trend with a content of 8% at the top surface and <1% at the bottom interface. This variation in the distribution of Br and Cl could be expected to substantially contribute to the observed lattice inhomogeneity, especially given the substantial role of Cl in lattice contraction (*19*).

The introduction of Rb^+ into the film resulted in a more homogeneous distribution of both Br and Cl throughout the perovskite layer. Br maintained a consistent concentration of ~15%, across the entire thickness of the film, and Cl also showed a homogeneous distribution across the film. Therefore, we posited that the marked shift observed in the Cs signal in the XPS measurements could be attributed to a lower concentration of Cl ions at the surface, which were supplanted by iodine (I) and Br ions. Given that Cl ions have a higher electronegativity than do I and Br ions, this substitution resulted in a lower average electronegativity of surface anions, consequently enhancing the electron density surrounding Cs ions at the surface. Finally, the observed redistribution of Cs and halide elements could be expected to be a crucial factor affecting the lattice parameters along the out-of-plane direction of the THP films (Fig. 3J). This smoothing effect on the distribution of ions across the thickness of perovskite films was not observed in our double-halide-composition $[Cs_{0.22}FA_{0.78}Pb(I_{0.85}Br_{0.15})_3]$ films (fig. S13). Consequently, the difference in Cs 3d binding energy between DHP and Rb-doped DHP was also negligible (Fig. 3G), in line with our previous findings (*21*).

Strain-induced incorporation of Rb in THP

Although we had identified the mechanisms through which Rb enhances the efficiency of perovskite devices, the mode of incorporation of Rb^+ within the perovskite film remained to be ascertained. To this end, we conducted XRD measurements of THP films with different concentrations of Rb (0, 1, 3, 5, 10, 15, and 20%). As indicated by the results depicted in Fig. 4, A and B, the addition of Rb ions caused a shift

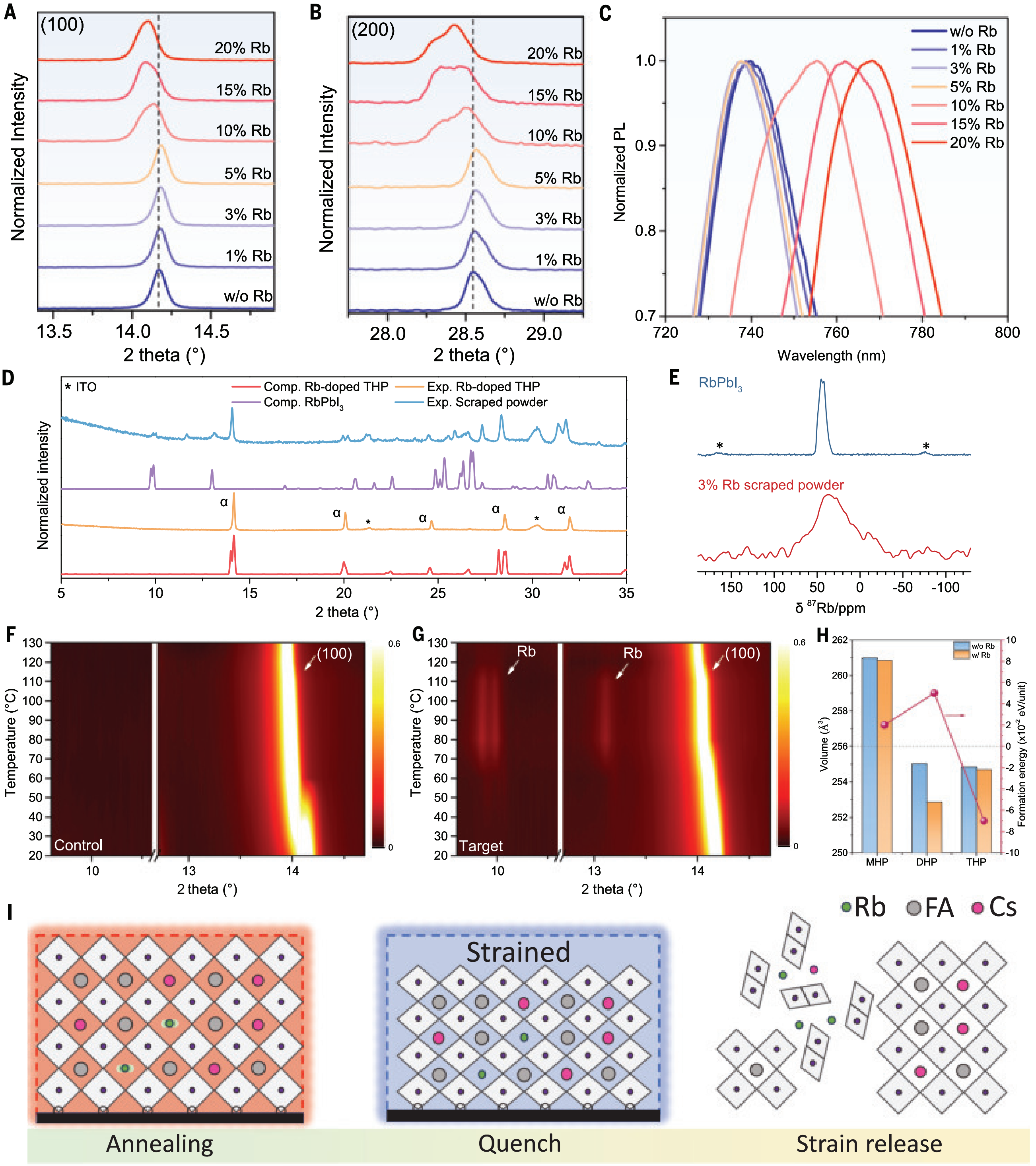

Fig. 4. Structural characterization of Rb-doped perovskites. (**A** and **B**) XRD reflections of the (A) (100) and (B) (200) facets of THP films containing different amounts of Rb^+. (**C**) Normalized PL spectra of THP films with different amounts of added Rb^+. (**D**) Powder XRD spectra of the film and scraped powder of THP doped with 3% Rb, along with computational XRD pattern for δ-$RbPbI_3$ phase and Rb-doped THP. (**E**) MAS solid-state ^{87}Rb NMR spectra of the scraped powder of a 3% Rb-doped THP film and δ-$RbPbI_3$ powder. Sidebands are denoted by asterisks. (**F** and **G**) Temperature-dependent XRD patterns for (F) control and (G) target THP films. (**H**) Bar chart: computational lattice volume for MHP, DHP, and THP with and without Rb^+. Dot/line plot: formation energies of Rb-doped MHP, DHP, and THP. With respect to acetylene solvent. (**I**) Schematic diagram of the strain-stabilized Rb-THP phase.

in the XRD peaks toward higher angles, a trend that continued until the Rb concentration reached 5%. Beyond this concentration, a further increase in the Rb concentration to 10% reversed the trend, with peaks even shifting to lower angles compared with the sample without Rb, followed by the appearance of peaks at 2θ = 10°, which can tentatively be assigned to a Rb-containing inorganic nonperovskite phase (fig. S14).

We observed a similar trend in a series of PL measurements, in which the PL peak shifted to shorter wavelengths upon increasing the concentration of Rb from 0 to 3%, followed by a gradual shift to longer wavelengths between 5% and 20% (Fig. 4C). This was confirmed by ultraviolet-visible (UV-vis) measurements (fig. S15), indicating an initial increase of the bandgap when increasing the amount of Rb additive altering the octahedral titling angle, followed by a decrease of the bandgap upon further addition of Rb. This result was consistent with a lattice contraction for up to 5% added Rb. Similar results were observed from adding rubidium bromide (RbBr) instead of RbI into the THP films (fig. S16), indicating the general effect of Rb cation incorporation. The smaller extent of lattice collapse observed with RbBr at concentrations above 10% indicates that the increase in lattice contraction allows for incorporating larger amounts of Rb^+ cations. These results on THP films were different from the response of DHP toward Rb^+ addition, where XRD analysis revealed a continuous shift of signals to lower 2θ angles upon increasing the Rb content up to 5% (fig. S17), indicating the absence of Rb^+ incorporation on A-cation sites in the lattice. Having conclusively demonstrated Rb incorporation into THP films, we also studied the feasibility of K incorporation following our approach. Addition of increasing amounts of potassium iodide (KI) to the THP films entailed a continuous lattice expansion and bandgap decrease, inferred from XRD and PL measurements (fig. S18), in contrast to the behavior observed with Rb-incorporated samples. This suggested that K^+ ions are unlikely to occupy A-sites of the perovskite lattice. This suggests that K^+ ions are not able to occupy the A-site of the perovskite lattice. This highlights the critical role of alkali cation size in A-site incorporation in THP materials.

Previous research has demonstrated that the incorporation of Cl into mixed I/Br perovskites depends on the Cl source used in the precursor solution (*19*). To determine whether the different behaviors of DHP and THP were caused simply by the presence of a Cl additive or indeed incorporation of Cl into the lattice, we compared the XRD patterns of three kinds of perovskites, each using a distinct Cl source [9% methylammonium chloride (MACl), 3% methylammonium lead chloride ($MAPbCl_3$), and 4.5% lead chloride ($PbCl_2$)], which were added to the same DHP precursor, while maintaining the same relative amount of Cl. Sets of samples with and without 3% of Rb^+ were prepared and analyzed by XRD (fig. S19). Notably, the $PbCl_2$ and $MAPbCl_3$ samples without Rb^+ exhibited peak shifts to higher diffraction angles, indicative of lattice contraction. However, when MACl was used as a chloride source, it did not produce any noticeable lattice contraction. Our observation aligned well with previous findings attributing the contraction to Cl incorporation into the perovskite lattice (*19*). Upon adding Rb^+ to the precursors of these perovskites, only the films prepared from samples containing $PbCl_2$ and $MAPbCl_3$ exhibited an additional peak shift to higher diffraction angles attributable to the Rb additive, whereas in the case of the MACl precursor, the Rb additive caused a peak shift in the opposite direction.

To investigate whether there is an increased strain caused by Rb addition leading to lattice contraction, we subsequently performed both out-of-plane and in-plane GIXRD measurements with an incident x-ray angle of 2° on films with and without Rb. Both the out-of-plane and in-plane GIXRD results were consistent with the θ-2θ measurements, indicating a shift of the diffraction peak corresponding to the (220) facet toward higher angles in response to Rb doping (fig. S20). This conclusion was further supported by the residual stress measurements presented in fig. S21, which even showed a slight reduction of residual stress in the Rb-doped film compared with the pristine film, as the linear fit of $2\theta\text{-}\sin^2\varphi$ (φ represents the tilt angle of the diffractometer about the sample surface normal) for the pristine THP films exhibit larger slope than the Rb-doped THP films.

These results were consistent with the possibility that Rb was incorporated into the THP lattice. However, because previous studies have not found any proof for Rb incorporation into organic-inorganic mixed halide perovskite powders (*15*), the mechanism behind this incorporation remained to be assessed. To address this question, we scraped a Rb-doped THP film off its substrate and measured its XRD pattern after placing the powder on an identical substrate. Notably, a Rb-containing nonperovskite phase was observed that was absent in the films that adhered to an ITO glass support accompanied by lattice expansion of the parent perovskite phase (Fig. 4D). However, no new phase was observed in the XRD pattern of the powder of an undoped THP film (fig. S22).

To confirm the presence of a Rb-based nonperovskite phase in the powder sample, we performed magic angle spinning (MAS) solid-state NMR experiments (supplementary text 2). Figure 4E shows the ^{87}Rb NMR spectra of the scraped powder from THP films prepared with 3% Rb^+. The signal was broader than pure nonperovskite $RbPbI_3$ and shifted to a lower frequency (table S4). To test whether this signal corresponded to Rb doped into the FA-rich parent perovskite phase, we performed $^{87}Rb\{^1H\}$ rotational echo double resonance (REDOR) experiments (*22*). In these experiments, two ^{87}Rb spectra were recorded, one with ^1H recoupling and one without. The signal intensities in these spectra are denoted S_1 and S_0, respectively. Any ^{87}Rb nuclei near ^1H diphase due to ^1H–^{87}Rb coupling, resulting in a loss of signal intensity in S_1. Figure S23 shows that there was no discernible dephasing with 2 ms of recoupling, indicating that there were no ^1H nuclei within ~5 Å of the Rb ions. This finding ruled out any appreciable incorporation of Rb^+ into the THP phase in the powder sample.

To identify the effect of Rb on Cs speciation in the powder sample, we acquired ^{133}Cs NMR spectra for scraped THP thin-film samples with and without Rb (fig. S24). Without Rb in the precursor solution, a single broad ^{133}Cs signal was observed at 47.4 parts per million (ppm), consistent with Cs in an FA- and iodide-rich perovskite phase. In contrast, when Rb^+ was included, the ^{133}Cs spectrum showed two broad signals: one arising from Cs in the perovskite phase, and another signal at ~230 ppm, which is associated with an inorganic nonperovskite phase. The signal was broader than for pure $\delta\text{-}CsPbI_3$, indicating cation mixing, halide mixing, or both. In combination with the broad ^{87}Rb signal, we concluded that the $Rb_{1-w}Cs_wPb(I_xBr_yCl_z)_3$ nonperovskite phase formed upon removing Rb-containing THP films from their substrate (*15*).

To study a possible contribution of strain on the incorporation of Rb, we conducted variable-temperature in situ XRD measurements on control and target THP thin films ranging from 20° to 130°C. Upon increasing the temperature, the lattice expanded as indicated by the continuous shift of the (100) peak position of the respective initial α-phase to lower 2θ angles (Fig. 4, F and G). During this lattice expansion, the appearance of a nonperovskite phase was observed in the target film when the temperature reached 80°C. In contrast, no such change was seen in the control sample, indicating that the nonperovskite phase only formed in the presence of Rb. The in situ formation of the Rb-based nonperovskite phase above 80°C is strong evidence that Rb^+ was incorporated in the perovskite phase at lower temperatures. Upon further increasing the temperature, the Rb nonperovskite phase started to fade and completely disappeared at 130°C. Furthermore, in situ XRD measurements were performed on powder scraped from the Rb-doped THP films (fig. S25). Diffraction peaks corresponding to the Rb-based nonperovskite phase were present from the start of the experiment and remained unchanged as the temperature increased. This confirms that Rb cannot be incorporated into the perovskite lattice for strain-released powder samples.

To further confirm the strain effect, we fabricated THP and Rb-doped THP films under varying annealing temperatures. As the annealing temperature increased, the pristine THP perovskite XRD peaks showed a progressively noticeable shift to higher 2θ angles, indicating increased lattice strain within the films (fig. S26) (*23*). Notably, the incorporation of rubidium caused a more pronounced shift in the XRD peaks at higher annealing temperatures, confirming that Rb incorporation is strain-assisted (fig. S27). This phenomenon was further corroborated by PL spectra (fig. S28), which revealed an increased bandgap at higher annealing temperatures with the addition of 3% Rb^+. Additionally, Rb incorporation was also observed in THP films deposited on fluoride tin oxide (FTO) substrates (fig. S29) and in THP films with a higher bandgap of 1.77 eV (fig. S30), confirming the general nature of strain-induced Rb^+ incorporation.

To elucidate the atomistic origins behind Rb incorporation in pure iodide perovskites [monohalide perovskite (MHP)], DHP, and THP, we performed density functional theory (DFT) and ab initio molecular dynamics (AIMD) calculations to verify the stability of these phases also at finite temperature. The α-phase perovskite structure of the three mixed FA/Cs perovskites $FA_{0.78}Cs_{0.22}PbI_3$, $FA_{0.78}Cs_{0.22}Pb(I_{0.85}Br_{0.15})_3$, and $FA_{0.73}Cs_{0.22}Pb(I_{0.82}Br_{0.15}Cl_{0.03})_3$ was examined without and with 4% Rb (fig. S31). The inclusion of Cl and Rb induced a shrinkage of the lattice of 3%. Rb incorporation in the DHP led to an overall stronger (volume) contraction than in THP, where the lattice was already contracted upon Cl addition, demonstrating that Rb and Cl addition have indeed some synergistic effects by reducing the overall lattice strain (Fig. 4H and table S5). For direct comparison with the experimental measurements, we also simulated the XRD pattern of the calculated Rb-substituted THP $FA_{0.74}Cs_{0.22}Rb_{0.04}Pb(I_{0.82}Br_{0.15}Cl_{0.03})_3$, which agrees well with the experimental XRD of the thin film (Fig. 4D), confirming the important role of chloride in enabling Rb incorporation into the lattice. By computing the stabilization or destabilization energy associated with Rb incorporation, we concluded that the MHP was destabilized upon 4% Rb incorporation by 0.04 eV per stoichiometric unit, whereas THP was stabilized by 0.01 eV per stoichiometric unit. The formation energies for MHP, DHP, and THP with 4% Rb incorporation were also computed. The ions (FA^+, Cs^+, Rb^+, Pb^{2+}, I^-, Br^-, Cl^-) dissolved in explicit ethyl acetate as the antisolvent (dielectric constant $\epsilon = 6.02$) used in the experiments were considered as reference states. It was determined that Rb incorporation is disfavored by 0.02 and 0.05 eV per stoichiometric unit in the case of MHP and DHP, respectively, whereas it is favored by 0.07 eV per stoichiometric unit for THP (Fig. 4H). Both the calculated stabilization or destabilization and formation energies contradict the simple stability estimate given by the Goldschmidt tolerance factor (*24*) and even its machine-learned extension (*25*), which predicted that all of these compositions should be stable (table S5), meaning that a pure geometrical consideration is not enough to explain stability in these cases.

Conclusions

Integrating our findings from XRD, GIXRD, PL, XPS, NMR, and DFT calculations, we propose that small amounts of Rb^+ can be incorporated into the lattice of THP films stabilized by strain. As illustrated in Fig. 4I, during the annealing of THP films at high temperatures, the lattice becomes more flexible, allowing the Rb cation to occupy the A-site. After thermal quenching, a black phase is obtained at room temperature by kinetically trapping the Rb-containing lattice, confirming the bottom interface's role in suppressing the α-to-δ phase transformation (*26*). However, the scraped powder experienced strain release after detachment from the substrate (*26*) that led to phase segregation of the Rb-containing δ phase, as detected by XRD and NMR measurements.

The incorporation of Rb resulted in a shift of the XRD diffraction peaks toward higher angles (*20*, *27*), whereas the PL spectrum became more symmetric and shifted toward shorter wavelengths along with a higher PLQY. These results are consistent with a reduction in phase segregation and nonradiative recombination resulting from strain-induced Rb incorporation (supplementary text 3). However, addition of Rb levels of >5% led to the formation of a new Rb-containing nonperovskite phase containing a mixture of A- and X-site ions, thus altering the composition of the remaining THP phase, akin to the DHP scenario (*28*, *29*). By using an optimal amount of Rb, a prepared WBG device achieved a V_{OC} of 1.3 V on the basis of a perovskite with a bandgap of 1.67 eV, representing the lowest V_{OC} deficit reported. This discovery opens new avenues for enhancing the performance of THP-based devices and provides fresh fundamental insights into the complex processes of cation and anion incorporation in WBG perovskite compositions.

REFERENCES AND NOTES

1. National Renewable Energy Laboratory, Best research-cell efficiency chart (2024); https://www.nrel.gov/pv/cell-efficiency.html.
2. L. Duan *et al.*, *Nat. Rev. Mater.* **8**, 261–281 (2023).
3. F. Xu, M. Zhang, Z. Li, X. Yang, R. Zhu, *Adv. Energy Mater.* **13**, 2203911 (2023).
4. T. Nie, Z. Fang, X. Ren, Y. Duan, S. F. Liu, *Nano-Micro Lett.* **15**, 70 (2023).
5. A. J. Ramadan, R. D. J. Oliver, M. B. Johnston, H. J. Snaith, *Nat. Rev. Mater.* **8**, 822–838 (2023).
6. E. T. Hoke *et al.*, *Chem. Sci.* **6**, 613–617 (2015).
7. D. J. Slotcavage, H. I. Karunadasa, M. D. McGehee, *ACS Energy Lett.* **1**, 1199–1205 (2016).
8. J.-P. Correa-Baena *et al.*, *Science* **363**, 627–631 (2019).
9. T. Huang *et al.*, *Sci. Adv.* **7**, eabj1799 (2021).
10. J. Wang *et al.*, *Nat. Energy* **9**, 70–80 (2023).
11. A. J. Barker *et al.*, *ACS Energy Lett.* **2**, 1416–1424 (2017).
12. Q. Jiang *et al.*, *Nature* **623**, 313–318 (2023).
13. Y. Zhao *et al.*, *Science* **377**, 531–534 (2022).
14. M. Saliba *et al.*, *Science* **354**, 206–209 (2016).
15. D. J. Kubicki *et al.*, *J. Am. Chem. Soc.* **139**, 14173–14180 (2017).
16. Q. Jiang *et al.*, *Nature* **611**, 278–283 (2022).
17. Z. Wang *et al.*, *Nature* **618**, 74–79 (2023).
18. L. Krückemeier, U. Rau, M. Stolterfoht, T. Kirchartz, *Adv. Energy Mater.* **10**, 1902573 (2020).
19. J. Xu *et al.*, *Science* **367**, 1097–1104 (2020).
20. Z. Liang *et al.*, *Nature* **624**, 557–563 (2023).
21. P. Yadav *et al.*, *Adv. Mater.* **29**, 1701077 (2017).
22. B. Reif, S. E. Ashbrook, L. Emsley, M. Hong, *Nat. Rev. Methods Primers* **1**, 2 (2021).
23. D.-J. Xue *et al.*, *Nat. Commun.* **11**, 1514 (2020).
24. Z. Li *et al.*, *Chem. Mater.* **28**, 284–292 (2016).
25. C. J. Bartel *et al.*, *Sci. Adv.* **5**, eaav0693 (2019).
26. J. A. Steele *et al.*, *Science* **365**, 679–684 (2019).
27. W. Yang *et al.*, *Adv. Funct. Mater.* **32**, 2110698 (2022).
28. Y. Hu, M. F. Aygüler, M. L. Petrus, T. Bein, P. Docampo, *ACS Energy Lett.* **2**, 2212–2218 (2017).
29. R. E. Beal *et al.*, *Matter* **2**, 207–219 (2020).

ACKNOWLEDGMENTS

Funding: L.Z., S.M.Z., and M.G. acknowledge financial support from the Güneş Perovskite Solar Cell A.S. Company, Adana, Turkey. Y.X. acknowledges financial support from the Basic Science Center Program for Ordered Energy Conversion of the National Natural Science Foundation of China (52488201). L.E. acknowledges support from the Swiss National Science Foundation (grant 200020_212046). M.W. acknowledges the support of the National University of Singapore Presidential Young Professorship (A-0010046-00-00, A-0010046-01-00). U.R. acknowledges the Swiss National Foundation (grant 200020_219440) and computational resources from the Swiss National Computing Centre CSCS. V.C. acknowledges computational resources from the Swiss National Computing Centre CSCS. **Author contributions:** L.Z. conceived of the idea, fabricated all the devices and samples, and conducted all the characterizations except those described below. L.Z., M.W., F.T.E., L.P., Y.X., and M.G. designed the project. U.G., Y.Z., M.A.H., and L.E. conducted the powder synthesis and solid-state NMR measurements. P.S. and D.W.B. conducted the x-ray diffraction measurements. J.G. conducted the SEM measurements. B.H. conducted the KPFM and AFM measurements. M.M. conducted the XPS measurements. V.C., F.B., L.A., V.S., N.L., and U.R. conducted the DFT calculations. J.G. and S.M.Z. provided valuable advice. L.P., Y.X., and M.G. supervised the project. L.Z., M.W., and J.G. co-wrote the manuscript. All authors contributed to data analysis and read and commented on the manuscript. **Competing interests:** The authors declare that they have no competing interests and they have not submitted patent applications related to this work. **Data and materials availability:** All data are available in the main text or the supplementary materials.

SUPPLEMENTARY MATERIALS

science.org/doi/10.1126/science.adt3417
Materials and Methods
Supplementary Text
Figs. S1 to S31
Tables S1 to S5
References (*30*–*71*)

Submitted 23 September 2024; accepted 20 February 2025
10.1126/science.adt3417

NEUROIMMUNOLOGY

Meningeal regulatory T cells inhibit nociception in female mice

Élora Midavaine[1], Beatriz C. Moraes[1], Jorge Benitez[1], Sian R. Rodriguez[1], Joao M. Braz[1], Nathan P. Kochhar[1], Walter L. Eckalbar[1], Lin Tian[2], Ana I. Domingos[3], John E. Pintar[4], Allan I. Basbaum[1]*†, Sakeen W. Kashem[5,6]*†

T cells have emerged as orchestrators of pain amplification, but the mechanism by which T cells control pain processing is unresolved. We found that regulatory T cells (T_{reg} cells) could inhibit nociception through a mechanism that was not dependent on their ability to regulate immune activation and tissue repair. Site-specific depletion or expansion of meningeal T_{reg} cells (mT_{reg} cells) in mice led to female-specific and sex hormone–dependent modulation of mechanical sensitivity. Specifically, mT_{reg} cells produced the endogenous opioid enkephalin that exerted an antinociceptive action through the delta opioid receptor expressed by MrgprD$^+$ sensory neurons. Although enkephalin restrains nociceptive processing, it was dispensable for T_{reg} cell–mediated immunosuppression. Thus, our findings uncovered a sexually dimorphic immunological circuit that restrains nociception, establishing T_{reg} cells as sentinels of pain homeostasis.

Pain prevalence is higher in women across multiple conditions, and chronic pain severity is frequently altered during gender affirming hormonal therapy (*1*). Although there is evidence that T cells contribute to sexually dimorphic pain processing, the exact mechanisms remain unclear (*2*). Regulatory T cells (T_{reg} cells) are a subset of CD4$^+$ T cells defined by the expression of the master transcriptional regulator FOXP3, which is encoded by a gene found on the X chromosome. In addition to their critical function in restraining inflammation, T_{reg} cells are major contributors of tissue reparative and supportive functions (*3*, *4*). However, it is not known whether and how T_{reg} cells directly alter neuronal activity to modulate nociception, independently of their immunomodulatory functions (*5*, *6*). In this study, we examined the role of T_{reg} cells in regulating pain sensing in mice.

Sex-specific suppression of nociceptive thresholds by meningeal T_{reg} cells

We focused on T_{reg} cells within nervous system tissue, localized to the meninges of the central nervous system (CNS) and to the leptomeninges of dorsal root ganglia (DRGs). As previously reported, we observed a more pronounced localization of T_{reg} cells in the lumbar and sacral segments of the spinal cord (SC) meninges, and T_{reg} cells were observed along meningeal nerve fibers, including fibers expressing the protein isolectin B4$^+$ (IB4$^+$) that marks nonpeptidergic sensory neurons (Fig. 1A and fig. S1A) (*7*). In the DRGs, T_{reg} cells predominated in the leptomeninges, with sparse presence within the DRG parenchyma (Fig. 1B and fig. S1B). We quantified the numbers of nonvascular-tissue T_{reg} cells in various organs within the nervous and lymphoid systems (Fig. 1C). We further refer to the SC meningeal and DRG leptomeningeal T_{reg} cells as meningeal T_{reg} cells (mT_{reg} cells) (Fig. 1C). We observed minimal localization of T_{reg} cells in peripheral nerves or CNS parenchyma, as previously noted (*8*), and observed nearly equivalent numbers of tissue T_{reg} cells in male and female mice across tissues (Fig. 1D and fig. S1, C and D).

To assess the feasibility of site-specific depletion of mT_{reg} cells, we performed intrathecal (IT) injections of pegylated diphtheria toxin (pegDT) in *Foxp3*-DTR mice expressing the diphtheria toxin receptor (DTR) under the control of the *Foxp3* promoter, leading to T_{reg} cell–specific cell death on toxin administration (*9*). Although an IT injection of Evans blue rapidly spreads through the meninges, DRGs, brain, and into the draining lymph nodes, pegylated fluorescently labeled molecules remain restricted to the SC meninges and to the DRGs (fig. S2, A and B). Consistently, a single dose of pegDT IT selectively depleted >90% of SC and DRG mT_{reg} cells in both male and female mice but spared T_{reg} cells located in all other organs (Fig. 1, E and F, and fig. S2C). *Foxp3*-DTR mice subjected to repeated pegDT IT did not exhibit weight loss, splenomegaly, or mortality that developed after systemic autoimmunity in *Foxp3*-DTR mice that received repeated intraperitoneal (IP) injections of diphtheria toxin (DT) (fig. S2, D to G). Thus, IT injections of pegDT allow for site-selective depletion of mT_{reg} cells while avoiding systemic inflammation.

We evaluated behavioral outcomes in mice after mT_{reg} cell depletion in response to pain mediated by mechanosensitive unmyelinated and myelinated primary afferent nerve fibers. A single dose of pegDT IT decreased mechanical nociceptive thresholds in naïve female, but not male, *Foxp3*-DTR mice (Fig. 1, G and H). Mechanical pain thresholds in C57BL/6 mice treated with pegDT IT and in *Foxp3*-DTR mice treated with vehicle IT did not differ (fig. S3A), which indicates that neither pegDT nor IT injections alone caused increased pain hypersensitivity. In addition, we assessed mice for noxious heat sensitivity (mediated by Trpv1$^+$ nociceptors), cold sensitivity (Trpm8$^+$ nociceptors), pinprick (Aδ fibers), and brush responses (Aβ fibers). Depletion of mT_{reg} cells selectively induced mechanical hypersensitivity in female mice, but in neither sex did it affect other sensory modalities or motor function (Fig. 1I and fig. S3, A to H). We concluded that mT_{reg} cells suppress mechanical nociceptive thresholds in a sex-dependent manner in uninjured mice.

mT_{reg} cells alleviate injury-induced mechanical hypersensitivity independently of tissue repair

We investigated whether mT_{reg} cells could suppress nociception after nerve injury. We used a well-established spared nerve injury (SNI) model of neuropathic pain, in which transection and ligation of two branches of the sciatic nerve induces permanent and unremitting mechanical hypersensitivity (Fig. 2, A and B). SNI also produces a nonhealing neuroma 4 weeks after the injury (*10*). Additionally, meninges are physically segregated from peripheral nerves through tight junctions. Thus, because tissue injury cannot be repaired to resolve pain, this model allows of assessment of mT_{reg} cell function in nociception specifically. After SNI, we observed no changes in meningeal T_{reg} cell numbers (fig. S4A). Because mice with SNI respond to mechanical stimuli at the limit of detection with von Frey filaments, we used the percent response method with the lightest available filament (*11*). This approach assesses pain sensitivity by measuring how often mice react to the most innocuous available mechanical stimuli. Nociceptive responses were increased in female mice with mT_{reg} cell depletion after SNI, but this was not observed in males (Fig. 2, C and D).

Our data indicated that mT_{reg} cells may decrease pain sensing; therefore, we investigated whether expanding mT_{reg} cells could alleviate mechanical hypersensitivity after SNI. T_{reg} cells express the high-affinity interleukin-2 (IL-2) receptor, and administrations of low doses of IL-2 can effectively expand T_{reg} cells in mice—a therapeutic approach used to treat autoimmune diseases in humans (*12*). IT injections of low-dose IL-2 selectively expanded mT_{reg} cells

---

[1]Department of Anatomy, University of California San Francisco, San Francisco, CA, USA. [2]Max Planck Florida Institute for Neuroscience, Jupiter, FL, USA. [3]Department of Physiology, Anatomy and Genetics, University of Oxford, Oxford, UK. [4]Department of Neuroscience and Cell Biology, Rutgers Robert Wood Johnson Medical School, Piscataway, NJ, USA. [5]Department of Dermatology, University of California San Francisco, San Francisco, CA, USA. [6]Dermatology, Veterans Affairs Medical Center, San Francisco, CA, USA.
***Corresponding author. Email: sakeen.kashem@ucsf.edu (S.W.K.); allan.basbaum@ucsf.edu (A.I.B.)**

†These authors contributed equally to this work

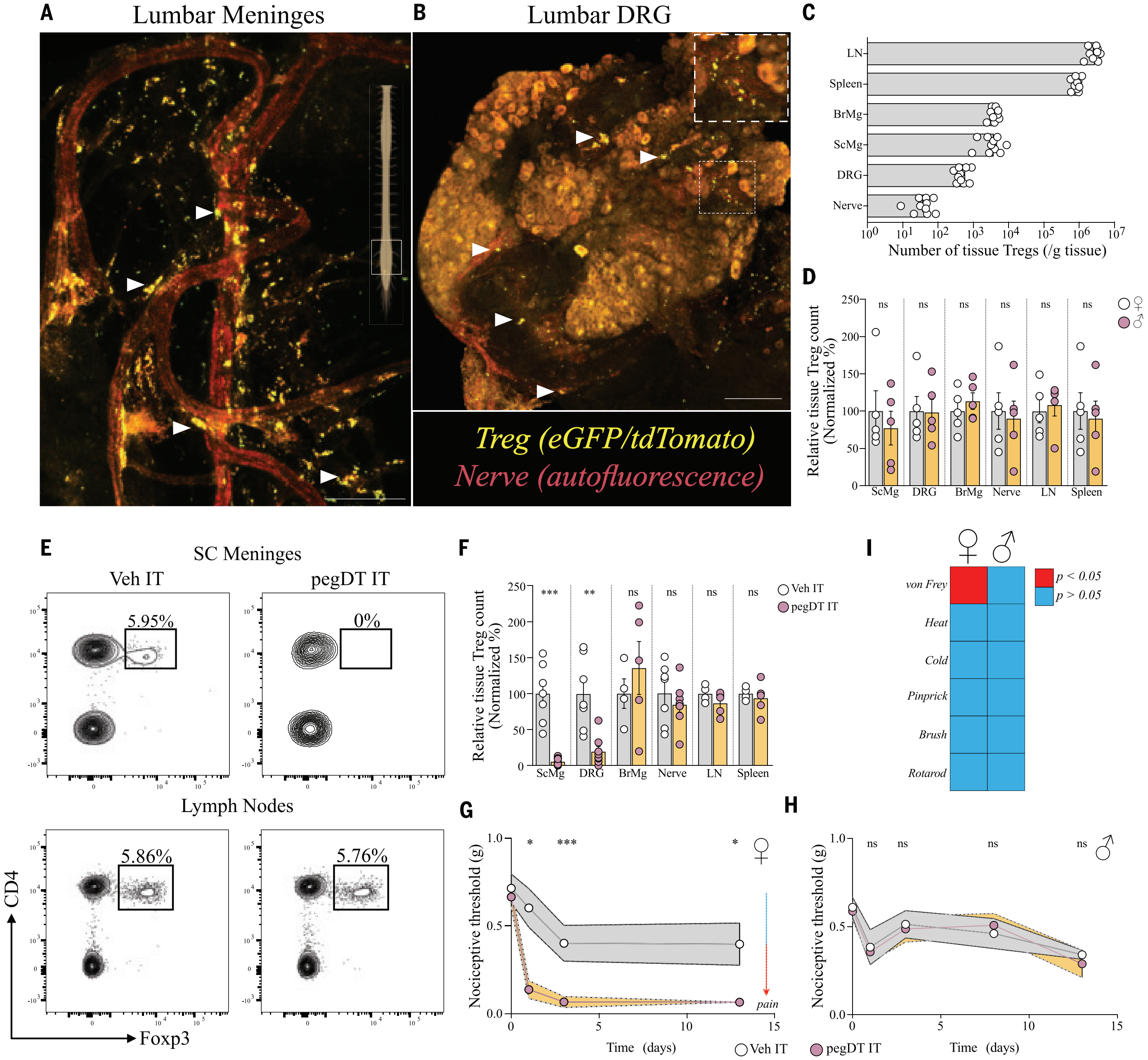

Fig. 1. Sex-selective suppression of mechanical pain hypersensitivity by mT_{reg} cells. (**A** and **B**) Representative (n = 5) whole-mount maximum projection confocal microscopy image of the lumbar SC meninges (A) and DRGs (B) showing T_{reg} cells (green-red: yellow) and nerves (autofluorescence, red) in *Foxp3*$^{eGFP\text{-}Cre\text{-}ERT2}$;*Rosa26*^{tdTomato} reporter mice. Inset in (B) shows DRG magnification. Scale bars, 100 μm (A) and 150 μm (B). Arrowheads indicate T_{reg} cells. (**C**) Total number of weight-adjusted tissue T_{reg} cells across organs in both sexes combined; n = 9 to 10 mice per organ. (**D**) Relative number of tissue T_{reg} cells from male (white; n = 5) mice and female (black; n = 5) mice per organ. 100% represents mean number of female T_{reg} cells per organ. Comparison is made between the sexes in each individual organ. (**E**) Representative concatenated flow cytometry (n = 5) plots of tissue T_{reg} cells after a single IT injection of 20 ng of pegDT. Gating strategy is provided in fig. S1. (**F**) Relative quantifications of tissue T_{reg} cell depletion 2 days after a single IT pegDT injection across organs; n = 4 to 8 mice per organ. 100% represents mean number of tissue T_{reg} cells in IT vehicle-injected mice per organ. (**G** and **H**) Nociceptive thresholds measured in *Foxp3*-DTR mice using von Frey filaments before (day 0) and after a single dose of 20 ng of IT pegDT or vehicle in female (n = 9 mice per group) (G) or male (n = 13 to 15 mice per group) mice (H). Downward-pointing arrow represents increased pain sensitivity. (**I**) Summary of behavioral differences comparing IT pegDT- and control-injected female and male mice. In graphs (C), (D), and (F), individual data points show data for one mouse, and bars show means ± SEMs. In graphs (G) and (H), individual data points show means ± SEMs. Statistics were calculated by unpaired two-tailed Mann-Whitney test [(D) and (F)] or two-way analysis of variance (ANOVA) with Sidak's test for multiple comparisons [(G) and (H)]. ScMg, spinal cord meninges; BrMg, brain meninges; LN, lymph nodes; Veh, vehicle. ns, not significant; *$P < 0.05$; **$P < 0.01$; ***$P < 0.001$.

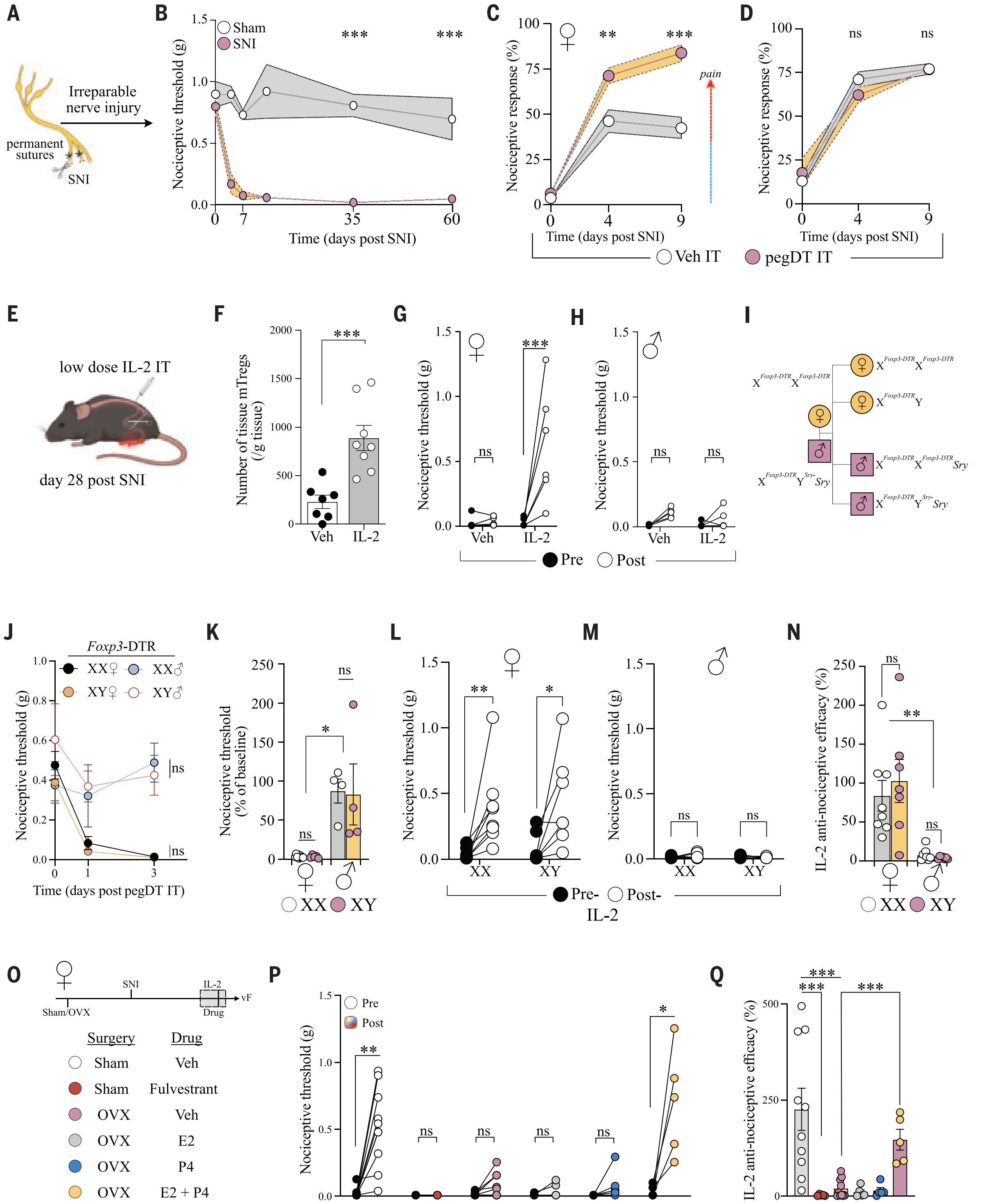

Fig. 2. mT$_{reg}$ cells control nociception dependent on sex hormones and independent of tissue repair. (**A**) Schematic representation of the SNI surgery. (**B**) Long-term assessment of mechanical pain thresholds in mice after SNI surgery (both sexes combined, no difference between the sexes); *n* = 7 to 8 mice per group. (**C** and **D**) Percent response to 0.008 g of von Frey filament in mice with SNI (day 0) and treated with IT pegDT or vehicle every 4 days. *n* = 8 per group for females and 9 to 10 per group for males. Upward-pointing arrow represents increased pain responsiveness. (**E**) Schematic representation of mT$_{reg}$ cell expansion in mice 4 weeks after SNI by three IT injections of low-dose IL-2 (0.1 μg). (**F**) Total mT$_{reg}$ cell number in meninges after low-dose IL-2 or vehicle IT injections (both sexes combined, no significant differences between the sexes); *n* = 7 to 8 mice per group. (**G** and **H**) Nociceptive thresholds of female (*n* = 7 to 12 mice per group) (G) and male (*n* = 5 mice per group) (H) mice given low-dose IL-2 or vehicle IT 4 weeks after SNI. (**I**) Schematic representation of the mating strategy of FCG *Foxp3*-DTR mice, demonstrating resulting XX and XY females and XX and XY male mice. (**J**) Nociceptive thresholds of FCG *Foxp3*-DTR female and male mice after a single IT pegDT injection. *n* = 5 to 9 per group for females and 4 per group for males. (**K**) Percent baseline nociceptive thresholds is determined as post–pegDT injection threshold divided by preinjection, basal mechanical threshold in male and female mice

with XX (white) or XY (pink) chromosomes. N = 4 to 9 mice per group. (**L** and **M**) Nociceptive thresholds of WT FCG female (n = 7 to 8 mice per group) (L) and male (n = 7 to 8 mice per group) (M) mice after low-dose IL-2 injections 4 weeks after SNI. (**N**) Antinociceptive efficacy determined as post–IL-2 injection threshold divided by preinjury, basal mechanical threshold in male and female mice with XX (white) or XY (pink) chromosomes. (**O**) Outline of experiment. (**P**) Nociceptive thresholds of sham or ovariectomized (OVX) female mice after low-dose IL-2 injections 4 weeks after SNI, and injected with either vehicle, fulvestrant, estrogen (E2), progesterone (P4), or both estrogen and progesterone; 5 to 10 mice per group. (**Q**) Antinociceptive efficacy determined as post–IL-2 injection threshold divided by preinjury mechanical threshold in female mice with hormone manipulation. In graphs (F), (G), (H), (K), (L), (M), (N), (P), and (Q), individual data points show data for one mouse, and bars show means ± SEMs. In graphs (B), (C), (D), and (J), individual data points show means ± SEMs. Statistics were calculated by two-way ANOVA with Sidak's test for multiple comparisons [(B), (C), (D), and (J)], unpaired two-tailed Mann-Whitney test (F), Wilcoxon matched-pairs signed rank test [(G), (H), (L), (M), and (O)], or Kruskal-Wallis with Dunn's multiple comparisons test [(K), (N), and (P)]. ns, not significant; $^{*}P < 0.05$; $^{**}P < 0.01$; $^{***}P < 0.001$.

in both male and female mice (Fig. 2, E and F, and fig. S4B). Although mT$_{\text{reg}}$ cell expansion promoted antinociception in female mice post-SNI, it did not exhibit a similar effect in males (Fig. 2, G and H). IT injections of IL-2 in uninjured mice did not increase nociceptive thresholds (fig. S4, C and D). In addition, mT$_{\text{reg}}$ cell expansion did not alter noxious heat and cold sensitivity in mice with SNI and did not induce motor impairment (fig. S4, E to J). Thus, the expansion of mT$_{\text{reg}}$ cells selectively alleviated mechanical hypersensitivity independently of their ability to repair tissue injury.

Gonadal hormones control the antinociceptive function of mT$_{\text{reg}}$ cells

There are reports of altered X chromosome inactivation during inflammatory state in females (*13*, *14*), which suggests that differences in *Foxp3* through sex chromosome dosage may contribute to female-specific function mT$_{\text{reg}}$ cells in nociceptive regulation. We used the four core genotypes (FCG) mouse model in which gonadal sex is independent of sex chromosomes (*15*). FCG mice harbor a deletion in the sex-determining region Y gene (*Sry*) on the Y chromosome and instead feature an autosomal transgenic insertion of *Sry*. This genetic configuration makes it possible to distinguish sex chromosome dose influence from the contribution of gonadal hormones (Fig. 2I). mT$_{\text{reg}}$ cell depletion in *Foxp3*-DTR mice crossed with FCG mice demonstrated that both XX and XY gonadal females, but not males, exhibited increased sensitivity after mT$_{\text{reg}}$ cell depletion. This revealed that gonadal hormones, but not sex chromosomes, mediated the mT$_{\text{reg}}$ cell suppression of mechanical nociceptive thresholds in the absence of nerve injury (Fig. 2, J and K). XX and XY chromosome gonadal female mice, but not male mice, displayed intact mT$_{\text{reg}}$ cell expansion–mediated alleviation of SNI-induced mechanical hypersensitivity (Fig. 2, L to N). Blocking the function of female sex hormones through ovariectomy or by antagonizing estrogen receptor signaling using fulvestrant abolished mT$_{\text{reg}}$ cell expansion–mediated antinociceptive efficacy (Fig. 2, O to Q). Mice that had undergone ovariectomy and received both estrogen and progesterone supplements—but not either hormone individually—reinstated nociception thresholds comparable to the thresholds of those mice that had not undergone ovariectomy (Fig. 2, O to Q). On the basis of our findings, we concluded that there was a consistent sex hormone–dependent contribution of mT$_{\text{reg}}$ cells to the modulation of mechanical hypersensitivity.

T$_{\text{reg}}$ cells express *Penk*, which encodes the endogenous opioid peptide enkephalin

T$_{\text{reg}}$ cells have increased expression of the *Penk* transcript, which encodes for proenkephalin—a peptide precursor of the analgesic Met- and Leu-enkephalin peptides (*16*, *17*). Although *Penk* is expressed in T$_{\text{reg}}$ cells found in the nervous system (*18*), whether T$_{\text{reg}}$ cell–derived enkephalin is required for controlling nociception is unknown. We reanalyzed public RNA sequencing data of activated T$_{\text{reg}}$ cells, resting T$_{\text{reg}}$ cells, as well as activated and resting CD4^{+} Foxp3^{-} conventional T cells (T$_{\text{conv}}$ cells) (*19*). We observed that *Penk* was higher in activated versus resting T$_{\text{reg}}$ cells (Fig. 3A). We also examined other opioid ligand and receptor genes but only recorded a very sparse expression of other opioid-related genes among CD4^{+} T cell subsets (Fig. 3B).

Enkephalin signals predominantly through the delta opioid receptor (δOR), encoded by the *Oprd1* gene, and with lesser affinity through the mu opioid receptor (μOR) (*20*). On the basis of our prior experience defining mechanical hypersensitivity through enkephalin-δOR circuits in the nervous system, we focused on T$_{\text{reg}}$ cell expression of *Penk* (*21*). Using published assay for transposase-accessible chromatin with sequencing (ATAC-seq) data (*19*), we observed more accessible chromatin regions in the *Penk* locus in activated T$_{\text{reg}}$ cells but not in other CD4+ T cell subsets. Moreover, this was similar to accessible chromatin within the promoter and enhancer regions in the *Penk* locus from cells of the developing forebrain, an established enkephalinergic area of the murine CNS (Fig. 3C). We found that a proportion of mT$_{\text{reg}}$ cells were positively stained for Met-enkephalin after cytokine stimulation, but meningeal CD4^{+} T$_{\text{conv}}$ cells and lymphoid T$_{\text{reg}}$ cells were not (Fig. 3D). We validated this observation by generating *Penk*$^{\text{Cre}}$;*Rosa26*$^{\text{tdTomato}}$ mice, which fate-labeled cells where *Penk* has been expressed. The frequency of mT$_{\text{reg}}$ cells that had expressed *Penk* in naïve mice (Fig. 3E) was similar to the frequency of Met-enkephalin–expressing cells determined by intracellular antibody staining by flow cytometry. Furthermore, very few lymphoid or intravascular T$_{\text{reg}}$ cells were labeled by the fate reporter, confirming the tissue-predominant expression of *Penk* by T$_{\text{reg}}$ cells (fig. S5, A and B). This suggested that enkephalin may have a role in tissue mT$_{\text{reg}}$ cells specifically. Compared with male mice, female mice had greater numbers of fate-labeled enkephalin-positive T$_{\text{reg}}$ cells in the meninges but not in the lymphoid organs (Fig. 3F and fig. S5C). Ovariectomy decreased the overall number of mT$_{\text{reg}}$ cells as well as the number of *Penk* fate-labeled mT$_{\text{reg}}$ cells in female mice (fig. S5, D and E). This distinction suggested that differences in T$_{\text{reg}}$ cells between the sexes may be tissue specific.

mT$_{\text{reg}}$ cell–derived enkephalin is required for restraining nociception

Enkephalin is rapidly degraded in the blood but persists in the cerebrospinal fluid (CSF) and nervous system tissues (*22*, *23*). Recent evidence has suggested that meningeal immune cell–derived factors regulate behavior through secreted factors in the CSF (*24*, *25*). Furthermore, factors in the CSF can modulate neuronal activity to promote pain (*22*). In mice where mT$_{\text{reg}}$ cells were depleted, enkephalin protein was not detected in the CSF; however, treating mice with IL-2 IT increased its protein level in the CSF (Fig. 3G). After SNI, there was an increase in *Penk* transcripts by mT$_{\text{reg}}$ cells and also in the proportion of *Penk* fate labeling among mT$_{\text{reg}}$ cells (fig. S5, F and G) Analyzing data from the Immunological Genome project (*26*), we found that in vitro T$_{\text{reg}}$ cells were the most prominent immune expressors of *Penk* (fig. S5H), and we validated that they could secrete enkephalin upon stimulation (fig. S5I).

To manipulate the enkephalin lineage of immune cells, we generated bone marrow chimeric mice by transplanting *Penk*$^{\text{Cre}}$;*Rosa26*$^{\text{DTR}}$ bone marrow into irradiated, congenically marked wild-type (WT) mice (*Penk*DTR$^{\Delta\text{heme}}$). This strategy enabled a selective DT-induced depletion of hematopoietic enkephalinergic cells and spares nonhematopoietic enkephalinergic cells of the nervous system and the stroma.

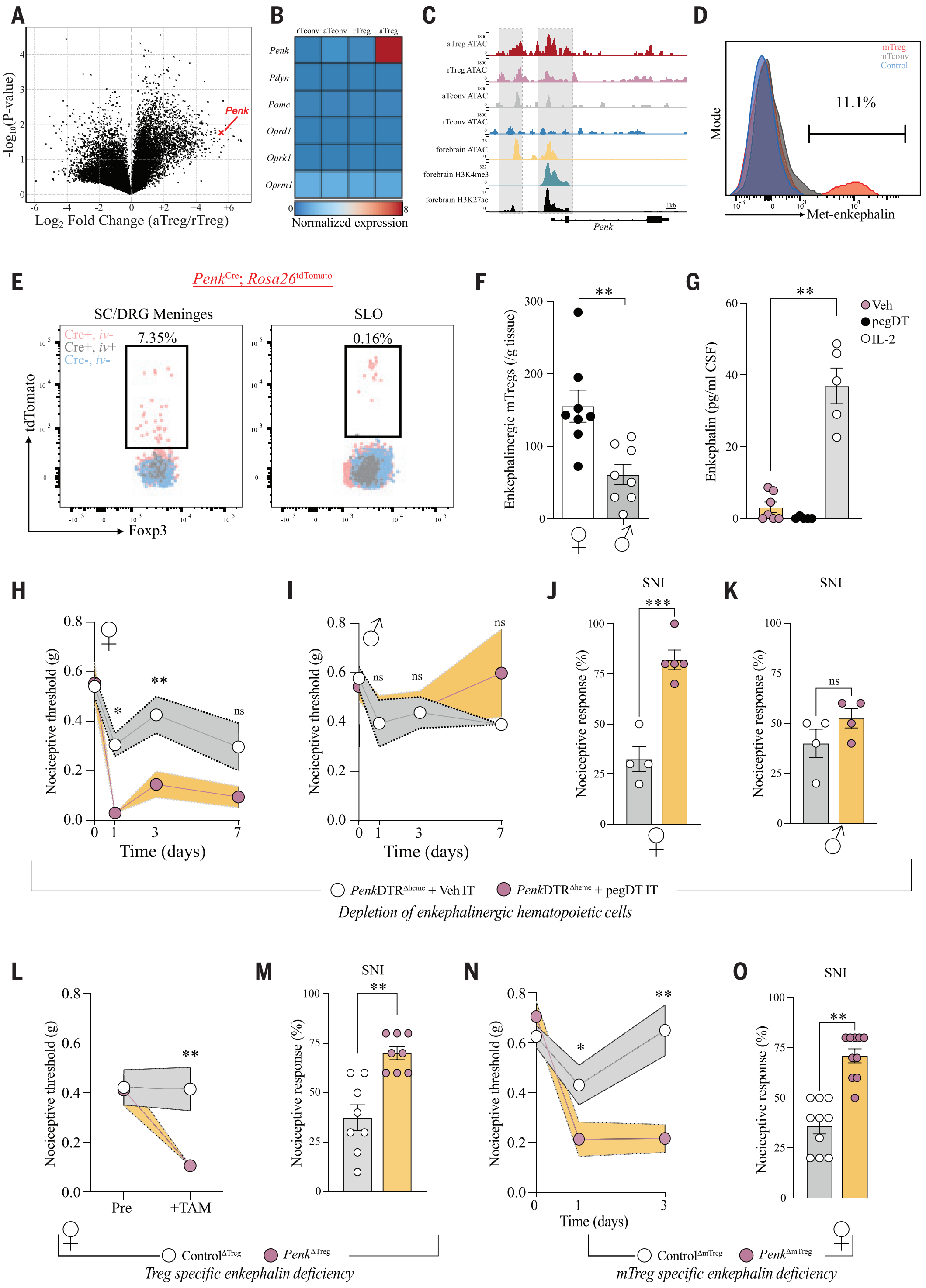

Fig. 3. mT$_{reg}$ cell–derived enkephalin gates nociception. (**A** and **B**) Volcano plot of transcription fold change of activated T$_{reg}$ (aT$_{reg}$) versus resting T$_{reg}$ (rT$_{reg}$) cells (A) and heatmap of relative expression value of aT$_{reg}$, rT$_{reg}$, and activated and resting CD4^{+} CD25^{-} conventional T cells (aT$_{conv}$ and rT$_{conv}$ cells) from public dataset GSE154680 (*n* = 3) (B). (**C**) Averaged ATAC-seq of open chromatin accessibility peaks on the *Penk* locus in different T cell subsets (*n* = 4 per group; GSE154680) compared with ATAC-seq and histone modification chromatin immunoprecipitation with sequencing (ChIP-seq) from public ENCODE dataset of the p0 developing forebrain, a known enkephalinergic region. (**D**) Representative stimulated mT$_{reg}$ cells, meningeal CD4^{+} T cells (mT$_{conv}$ cells) from WT mice, or *Penk*$^{-/-}$ mT$_{reg}$ cells (control). (**E**) Representative flow cytometry plots (from *n* = 5 mice) of T$_{reg}$ cells from meninges or secondary lymphoid organs (SLOs) from *Penk*^{Cre}*Rosa26*^{tdTomato} mice. Pink represents nonvascular tissue T$_{reg}$ cells from transgenic *Penk* lineage reporter mice, gray represents vascular T$_{reg}$ cells in reporter mice, and blue corresponds to tissue T$_{reg}$ cells from nontransgenic control mice. Gating strategy is provided in fig. S1. (**F**) Number of enkephalin lineage fate reporter–positive tissue mT$_{reg}$ cells in male and female mice; *n* = 8 mice per group. (**G**) Quantification of enkephalin in mouse CSF after vehicle (pink) IT SLO injection, two pegDT (black) IT injections, or three IL-2 (white) IT injections in *Foxp3*-DTR female mice. Each circle represents samples pooled from five mice with *n* = 5 to 7 pooled samples per group. (**H** to **K**) Bone marrow chimera of *Penk*^{Cre}*Rosa26*^{DTR} bone marrow → WT recipients. Nociceptive thresholds after a single pegDT (pink) or vehicle (white) IT injection in female (*n* = 4 to 5 mice per group) (H) and male (*n* = 4 mice per group) (I) mice. Nociceptive response to 0.008 g of von Frey filament after SNI and pegDT (pink) or vehicle (white) IT injection in female (*n* = 4 to 5 mice per group) (J) and male (*n* = 4 mice per group) (K) mice. (**L** and **M**) Female *Foxp3*$^{Cre\text{-}ERT2/Cre\text{-}ERT2}$;*Penk*$^{fl/fl}$ mice. Nociceptive thresholds of mice before and after tamoxifen injections (L) and percent nociceptive responses after SNI (M). *n* = 8 mice per group in (L) and (M). (**N** and **O**) Female mixed bone marrow chimeras of *Foxp3*-DTR + *Penk*$^{-/-}$ (1:1) bone marrow → WT recipients. (N) Nociceptive thresholds of mice after a single pegDT (pink) or vehicle (white) IT; *n* = 9 to 10 per group. (O) Percent nociceptive responses in SNI mice after pegDT (pink) or vehicle (white) IT injections; *n* = 10 mice per group. In graphs (F), (G), (J), (K), (M), and (O), individual data points show data for one mouse, and bars show means ± SEMs. In graphs (H), (I), (L), and (N), individual data points show means ± SEMs. Statistics were calculated by unpaired two-tailed Mann-Whitney test [(F), (J), (K), (M), and (O)], Kruskal-Wallis with Dunn's multiple comparisons test (G), or two-way ANOVA with Sidak's test for multiple comparisons [(H), (I), (L), and (N)]. ns, not significant; $^{*}P < 0.05$; $^{**}P < 0.01$; $^{***}P < 0.001$.

Administering pegDT IT to *Penk*DTR$^{\Delta\text{heme}}$ chimeric mice decreased mT$_{\text{reg}}$ cell numbers (fig. S5, J to L) and led to a profound female-specific mechanical hypersensitivity in both uninjured and nerve-injured states (Fig. 3, H to K).

Having established a female-specific contribution of hematopoietic enkephalinergic cells to nociception, we used female mice to dissect the mechanism of pain regulation by mT$_{\text{reg}}$ cells. To establish whether bone marrow–derived enkephalin was required for the regulation of nociceptive thresholds, we generated chimeric mice in which *Penk*-deficient bone marrow was transplanted into irradiated hosts (*Penk*$^{\Delta\text{heme}}$ mice). *Penk*$^{\Delta\text{heme}}$ mice displayed decreased mechanical nociceptive thresholds in the uninjured state compared with controls (fig. S5M). Adoptive transfer of *Penk*-sufficient CD4$^+$ T cells into *Rag2*$^{-/-}$ female mice with SNI induced robust antinociception, and deltorphin II, a δOR agonist, successfully reversed the mechanical hypersensitivity that followed mT$_{\text{reg}}$ cell depletion (fig. S5, N and O). On the basis of these studies, we concluded that hematopoietic cell–derived enkephalin regulates δOR signaling and was downstream of meningeal T$_{\text{reg}}$ cell–derived enkephalin release.

To investigate the contribution of T$_{\text{reg}}$ cell–derived enkephalin in mediating mechanical nociceptive thresholds, we generated *Foxp3*$^{\text{Cre-ERT2/Cre-ERT2}}$;*Penk*$^{\text{fl/fl}}$ (*Penk*$^{\Delta\text{Treg}}$) mice. Female *Penk*$^{\Delta\text{Treg}}$ mice displayed increased mechanical hypersensitivity both in non–nerve-injured and nerve-injured states, which suggests that T$_{\text{reg}}$ cell–derived enkephalin controls nociception (Fig. 3, L and M). We generated mice with mixed bone marrow chimeras using a 1:1 ratio of *Foxp3*-DTR and *Penk*$^{-/-}$ bone marrows transplanted into irradiated WT mice. IT pegDT injection into these mice resulted in mT$_{\text{reg}}$ cell–specific *Penk* deficiency (*Penk*$^{\Delta\text{mTreg}}$ mice) because all *Penk*$^{+/+}$ T$_{\text{reg}}$ cells express DTR and are thus ablated by DT administration. Non–nerve-injured, uninjected mixed chimeric mice exhibited similar mechanical thresholds as those of irradiated WT mice transplanted with WT bone marrow (*WT*$^{\Delta\text{heme}}$) (Fig. 3N). PegDT IT injection to deplete mT$_{\text{reg}}$ cells in *Penk*$^{\Delta\text{mTreg}}$ mice increased mechanical sensitivity in uninjured and nerve-injury conditions compared with controls (Fig. 3, N and O). Thus, these data supported the conclusion that mT$_{\text{reg}}$ cell–derived enkephalin controls nociception.

T$_{\text{reg}}$ cell–derived enkephalin is dispensable for immune suppression

Enkephalin has been linked to skewing of the inflammatory response or tissue injury (*27*, *28*). To test the possibility that T$_{\text{reg}}$ cell–derived enkephalin mediates the suppression of nociception by modulating immunological responses, we tested the mechanical nociceptive thresholds of lymphocyte-deficient *Rag2*$^{-/-}$ female mice compared with immunocompetent littermates. We observed decreased mechanical pain thresholds in *Rag2*$^{-/-}$ mice compared with their *Rag2*$^{+/+}$ and *Rag2*$^{+/-}$ littermates (fig. S6A). This finding suggested a mechanism of T$_{\text{reg}}$ cell–mediated control of nociceptive thresholds that is independent of lymphocyte-driven inflammation. Because macrophages also contribute to nociception (*29*), we depleted macrophages in mice using liposomal clodronate. Depletion of macrophages did not reverse the mechanical hypersensitivity observed in female mice deficient in mT$_{\text{reg}}$ cells (fig. S6B).

Further, we observed no difference in the suppressive capacity of *Penk*$^{-/-}$ T$_{\text{reg}}$ cells compared with control T$_{\text{reg}}$ cells in suppressing T$_{\text{conv}}$ cell proliferation in vitro (fig. S6, C and D). We also did not observe a competitive advantage or disadvantage among *Penk*$^{-/-}$ CD4$^+$ T cells across various tissues after SNI (fig. S6, E to G). There were no differences in effector or regulatory T cell differentiation between the *Penk*-sufficient or -deficient T cells (fig. S6H). Similarly, *Penk*$^{\Delta\text{Treg}}$ mice showed no alterations in CD4$^+$ T cell differentiation, spleen size, or weight changes after SNI (fig. S6, I to M).

Using a graft-versus-host disease (GVHD) model, we assessed whether T$_{\text{reg}}$ cell–derived enkephalin was required for suppressing immune responses. T helper responses, as judged by the expression of IL-17 or interferon-γ (IFN-γ) by T$_{\text{conv}}$ cells, were induced in mice transferred with activated T$_{\text{conv}}$ cells in the absence of T$_{\text{reg}}$ cells (fig. S6N). Mice that received additional transfers of either *Penk*$^{+/+}$ or *Penk*$^{-/-}$ T$_{\text{reg}}$ cells equally suppressed the frequency of T$_{\text{conv}}$ cells expressing IL-17A or IFN-γ and mitigated weight loss (fig. S6, N and O). Neither hematopoietic cell–derived enkephalin nor enkephalinergic bone marrow hematopoietic cells were required to restrain T cell differentiation, spleen size, or weight loss after GVHD or SNI (fig. S7, A to H). Rather, we proposed that T$_{\text{reg}}$ cells suppressed pain hypersensitivity through a mechanism independent of their role in immunosuppression.

Tissue compartmentalization of sexually dimorphic T$_{\text{reg}}$ cell–mediated antinociception

Systemic depletion of T$_{\text{reg}}$ cells worsens nociception after nerve injury, regardless of sex (*5*, *6*). *Rag2*$^{-/-}$ female and male mice both demonstrated increased mechanical sensitivity compared with their littermate controls (figs. S6A and S8A). Unlike mT$_{\text{reg}}$ cell depletion, which selectively induces hypersensitivity in females, systemic depletion of T$_{\text{reg}}$ cells induced hypersensitivity in both sexes in the absence of a nerve injury (fig. S8, B and C). Deficiency of enkephalin in all T$_{\text{reg}}$ cells increased mechanical hypersensitivity both before and after nerve injury (fig. S8, D and E). These findings indicated that *Penk* expression in peripheral T$_{\text{reg}}$ cells regulated pain sensing independently of sex but that meningeal T$_{\text{reg}}$ cell expression of *Penk* regulated nociception only in females.

δOR signaling on MrgprD$^+$ neurons orchestrates the antinociceptive function of mT$_{\text{reg}}$ cells

Previously, we have demonstrated a divergence of expression and function of δOR and μOR in mediating distinct pain modalities (*21*). Specifically, the δOR predominates on nonpeptidergic IB4$^+$ unmyelinated as well as myelinated primary afferents and selectively regulates mechanical hypersensitivity (*21*). Conversely, the μOR is expressed on Trpv1$^+$ nociceptors and selectively regulates heat pain hypersensitivity. In addition, spinal δOR-expressing neurons can dampen mechanical hypersensitivity (*30*, *31*). Using a stable cell line expressing the δLight δOR biosensor, an engineered δOR receptor that emits a fluorescent signal upon direct receptor engagement (*20*), we confirmed that deltorphin II and cell culture supernatants from stimulated T$_{\text{reg}}$ cells stimulated through their antigen receptor can engage the δOR (Fig. 4A and fig. S9, A to D). By contrast, supernatant taken from stimulated *Penk*$^{-/-}$ T$_{\text{reg}}$ cells did not induce a signal from the δOR biosensor (Fig. 4A and fig. S9D). Although selective pharmacological blockade of the δOR by IT injection of naltrindole did not alter mechanical sensitivity in uninjured mice, it diminished the antinociceptive efficacy of IL-2 treatment after SNI (Fig. 4B and fig. S9, E and F).

To assess the role of peripheral nervous system (PNS) or CNS δOR (*Oprd1*) circuits in coordinating the antinociceptive effect of mT$_{\text{reg}}$ cells, we intravenously injected δOR-sufficient (*Oprd1*$^{+/+}$) control and *Oprd1*$^{\text{fl/fl}}$ mice with adeno-associated viruses (AAVs) that have preferential neurotropism for the PNS or CNS (*32*). This approach selectively introduces Cre recombinase and targets the deletion of δOR in the PNS or CNS, respectively (fig. S9, G and H). We found that δOR deletion in the nervous system compartments did not alter mechanical nociceptive thresholds in uninjured mice, consistent with the existing literature (fig. S9I) (*33*, *34*). However, mice selectively lacking δOR in the PNS, but not the CNS, lost the capacity to respond to the antinociceptive effect of IL-2 post-SNI (Fig. 4, C and D). We concluded that a sensory neuron–expressed, presynaptic δOR mediated mT$_{\text{reg}}$ cell suppression of mechanical pain hypersensitivity after nerve injury.

Previous studies of δOR expression in DRG neurons using *Oprd1*$^{\text{eGFP}}$ mice have revealed that around half of the reporter-positive cells in the DRGs are myelinated neurons, and ~36% are IB4$^+$ neurons that express the MrgprD receptor (MrgprD$^+$ cells) (*21*). Using published single-cell RNA sequencing data (*35*, *36*), we found that MrgprD$^+$ DRG neurons expressed *Oprd1* and other receptors for ligands expressed by T$_{\text{reg}}$ cells (Fig. 4E). We found that 39% of

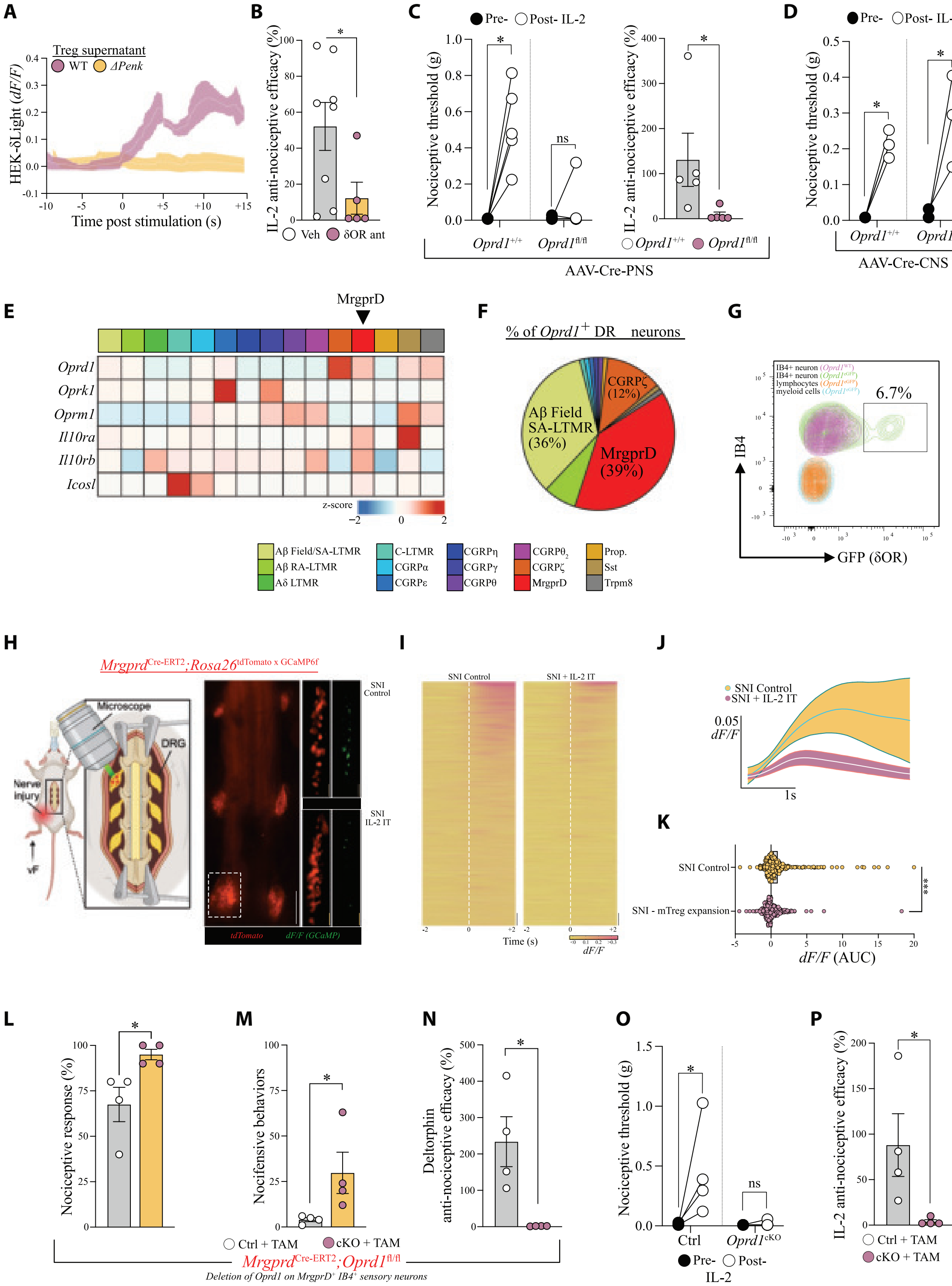

Fig. 4. δOR on MrgprD$^+$ sensory neurons orchestrates mT$_{reg}$ cell–mediated antinociception. (**A**) HEK-δLight activation upon WT (pink) or *Penk*$^{-/-}$ (yellow) T$_{reg}$ cell supernatant application; *n* = 3 biological replicates. (**B**) Antinociceptive efficacy of low-dose IL-2 IT in WT SNI female mice given naltrindole (selective δOR antagonist) or vehicle. Antinociceptive efficacy calculated as ratio of post–IL-2 thresholds compared with preinjury threshold. *n* = 5 to 8 mice per group. (**C**) Nociceptive thresholds and IL-2 antinociceptive efficacy of female mice lacking *Oprd1* in the PNS after mT$_{reg}$ cell expansion compared with controls. *n* = 5 mice per group for all graphs. (**D**) No difference in nociceptive thresholds in female mice lacking *Oprd1* in the CNS after mT$_{reg}$ cell expansion compared with controls. *n* = 3 to 4 mice per group. (**E**) Heatmap of row-normalized expression from DRG sensory neurons clusters from combined GSE139088 and GSE201653. (**F**) Proportions of sensory neuron clusters expressing *Oprd1* from (E). (**G**) Representative flow cytometry plot of δOR-GFP (green) expression on IB4$^+$ MrgprD$^+$ DRG sensory neurons compared with cells from nonreporter mice (purple); *n* = 3 mice. Gating strategy is provided in fig. S9J. Overlaid are lymphoid CD45$^+$ CD90.2$^+$ cells and myeloid CD45$^+$ CD11b$^+$ cells from the DRGs. (**H**) Schematic and representative images of in vivo MrgprD$^+$ sensory neurons of L4 to L6 DRGs showing tdTomato and processed change in GCaMP6 signal after stimulus subtracted by baseline signal

($\Delta F/F$ intensities) in IL-2–treated SNI mice ($n = 4$) compared with controls ($n = 6$). Dashed box represents a whole lumbar DRG shown at 100× magnification on the right. White scale bar, 1 mm; yellow scale bars, 100 μm. (**I**) Heatmap of $\Delta F/F$ neuronal intensities over time of 100 most responsive neurons in IL-2 or vehicle treated SNI mice; 0 represents time of applied von Frey stimulus. Scale bars, 5 neurons. (**J**) Compiled MrgprD$^+$ neuron $\Delta F/F$ time curves post–von Frey stimulus ±90% confidence interval in SNI control (yellow) or mT$_{\text{reg}}$ cell–expanded (pink) SNI mice. (**K**) Area under the curve (AUC) values of all individual neurons imaged in the two groups from (J). (**L** to **P**) *Mrgprd*$^{\text{Cre-ERT2}}$;*Oprd1*$^{\text{fl/fl}}$ female mice. (L) Percent response to 0.008 g of von Frey fiber stimulation after SNI in female mice. (M) Total nocifensive behaviors (withdrawals, shakes, licks) to 0.008 g of von Frey fiber stimulation after SNI in female mice. (N) Antinociceptive efficacy of deltorphin II (selective δOR agonist) in female mice conditionally lacking δOR on MrgprD$^+$ neurons (pink) or controls (white). (O) Nociceptive thresholds after low-dose IL-2 IT in female mice. (P) Antinociceptive efficacy of low-dose IL-2 IT in female mice. $n = 4$ mice per group in (L) to (P). In graphs (B), (C), (D), (L), (M), (N), (O), and (P), individual data points show data for one mouse, and bars show means ± SEMs. In graph (K), individual data points show data for one neuron, and bars show means ± SEMs. In graphs (A) and (J), individual data points show means ± SEMs. Statistics were calculated by unpaired two-tailed Mann-Whitney test [(B) and (C); antinociceptive efficacy: (K), (L), (M), (N), and (P)] or Wilcoxon matched-pairs signed rank test [(C); nociceptive threshold: (D) and (O)]. SA-LTMR, slowly adapting low-threshold mechanoreceptor; RA-LTMR, rapidly adapting low-threshold mechanoreceptor; MrgprD, Mas-related G protein–coupled receptor D; Prop., proprioceptor; SST, somatostatin; Trpm8, transient receptor potential cation channel subfamily M member 8; TAM, tamoxifen; cKO, conditional knockout. ns, not significant; $^*P < 0.05$; $^{**}P < 0.01$; $^{***}P < 0.001$.

sensory neurons expressed the *Oprd1* transcript (Fig. 4F), matching previous proportions determined using *Oprd1*$^{\text{eGFP}}$ reporter mice (*21*). Profiling the expression of the *Oprd1*$^{\text{eGFP}}$ reporter on DRG cells confirmed green fluorescent protein (GFP) expression specifically on IB4$^+$ MrgprD+ sensory neurons. We did not detect *Oprd1*$^{\text{eGFP}}$ expression by broadly defined lymphoid and myeloid cells (Fig. 4G and fig. S9J). Sensory neurons, including the IB4$^+$ subset, which were virally encoded to express the δOR biosensor δLight, were capable of δOR activation using Met-enkephalin in vitro (fig. S9, K and L).

Previously, δOR signaling has been shown to suppress voltage-gated calcium channels in presynaptic sensory neurons, including IB4$^+$ sensory neurons (*31*). We generated mice expressing a genetically encoded calcium indicator coupled to a tdTomato reporter in the MrgprD$^+$ sensory neuron population (Fig. 4H). IT administration of IL-2 reduced calcium activity in MrgprD$^+$ neurons in response to von Frey fiber stimulation of the injured hind paw (Fig. 4, I to K, and fig. S9, M to O). We generated mice in which MrgprD$^+$ neurons lacked expression of the δOR (*Oprd1*$^{\text{cKO}}$). Female *Oprd1*$^{\text{cKO}}$ mice exhibited exaggerated reflexive and spontaneous nocifensive behaviors after SNI compared with controls but not in the uninjured state (Fig. 4, L and M, and fig. S9P). Furthermore, *Oprd1*$^{\text{cKO}}$ female mice with SNI did not respond to the antinociceptive efficacy of deltorphin II and of IL-2 (Fig. 4, N to P). We concluded that mT$_{\text{reg}}$ cell–derived enkephalin acted through the δOR specifically expressed by MrgprD$^+$ sensory neurons, mediating the antinociceptive effect of mT$_{\text{reg}}$ cells after nerve injury.

Discussion

We describe a sexually dimorphic pain inhibitory circuit between T$_{\text{reg}}$ cells residing in the nervous system and sensory neurons. Given the limited number of T$_{\text{reg}}$ cells in the healthy, young CNS parenchyma, we refer to the enkephalinergic T$_{\text{reg}}$ cell population located in the CNS border tissues as mT$_{\text{reg}}$ cells, but we acknowledge their potential ability to migrate between the meninges and the CNS under specific conditions (*37*). Using strategies to deplete or expand T$_{\text{reg}}$ cells within the meningeal compartment, we find that mT$_{\text{reg}}$ cells gate cutaneous mechanical hypersensitivity by modulating nociceptive processing. The pain-modulating function of mT$_{\text{reg}}$ cells is sex selective and regulated by female gonadal hormones.

Although proenkephalin expression by T cells has been identified in various tissues (*16*, *17*), the functional assessment of Met- and Leu-enkephalin in modulating nociception by altering sensory neuron activity has been limited. Recent work has highlighted potential avenues for bidirectional communication between T$_{\text{reg}}$ cells and sensory neurons (*38*, *39*). We conclude that mT$_{\text{reg}}$ cell–secreted enkephalin acts on δORs on primary sensory neurons to selectively reduce neuronal calcium activity and mechanical hypersensitivity. Our analysis uncovered a sensory modality–selective function of mT$_{\text{reg}}$ cells, consistent with prior findings of δOR agonism, specifically providing relief of mechanical but not heat hypersensitivity (*21*). In line with both human and rodent studies, we found that antagonizing or depleting the δOR in the absence of injury or inflammation did not alter mechanical sensitivity, which suggests that there is no endogenous δOR-mediated control of nociception in the absence of nerve injury (*33*, *40*). This suggests that there are other mechanisms to control pain sensing in the naïve state, such as alternative *Penk* peptide splicing by homeostatic T$_{\text{reg}}$ cells, engagement of other opioid receptors by enkephalin at steady state, or the need for an inflammatory stimulus to drive δOR trafficking at the neuronal cell surface (*41*).

The engagement of δOR on MrgprD$^+$ sensory neurons by mT$_{\text{reg}}$ cell–derived enkephalin selectively reduced mechanical hypersensitivity after tissue insult or nerve injury. T$_{\text{reg}}$ cells may further suppress nociception through parallel pathways within peripheral injured tissues (*6*, *35*, *38*). Our findings illustrate a sexually dimorphic pain regulatory mechanism driven by the adaptive immune system and establish mT$_{\text{reg}}$ cells as key regulators of endogenous opioid tone and nociceptive processing.

REFERENCES AND NOTES

1. A. M. Aloisi *et al*., *Pain* **132**, S60–S67 (2007).
2. R. E. Sorge *et al*., *Nat. Neurosci.* **18**, 1081–1083 (2015).
3. J. L. Astarita *et al*., *Clin. Exp. Immunol.* **211**, 176–183 (2023).
4. N. Arpaia *et al*., *Cell* **162**, 1078–1089 (2015).
5. J. G. Lees, S. S. Duffy, C. J. Perera, G. Moalem-Taylor, *Cytokine* **71**, 207–214 (2015).
6. M. Davoli-Ferreira *et al*., *Pain* **161**, 1730–1743 (2020).
7. S. Othy *et al*., *Proc. Natl. Acad. Sci. U.S.A.* **117**, 20088–20099 (2020).
8. J. A. Kuhn *et al*., *eLife* **10**, e69056 (2021).
9. M. M. A. Pereira *et al*., *Nat. Commun.* **8**, 14967 (2017).
10. W. Xie, J. A. Strong, J.-M. Zhang, *eNeuro* **4**, ENEURO.0008-17.2017 (2017).
11. S. R. Chaplan, F. W. Bach, J. W. Pogrel, J. M. Chung, T. L. Yaksh, *J. Neurosci. Methods* **53**, 55–63 (1994).
12. H. Graßhoff *et al*., *Front. Immunol.* **12**, 648408 (2021).
13. J. M. Kim, J. P. Rasmussen, A. Y. Rudensky, *Nat. Immunol.* **8**, 191–197 (2007).
14. C. M. Syrett *et al*., *JCI Insight* **4**, e126751 (2019).
15. A. P. Arnold, X. Chen, *Front. Neuroendocrinol.* **30**, 1–9 (2009).
16. N. Aubert *et al*., *eLife* **13**, RP91359 (2024).
17. H. Shime *et al*., *Proc. Natl. Acad. Sci. U.S.A.* **117**, 20696–20705 (2020).
18. M. Ito *et al*., *Nature* **565**, 246–250 (2019).
19. J. van der Veeken *et al*., *Immunity* **53**, 971–984.e5 (2020).
20. C. Dong *et al*., *Nat. Neurosci.* **27**, 1844–1857 (2024).
21. G. Scherrer *et al*., *Cell* **137**, 1148–1159 (2009).
22. M. Kaag Rasmussen *et al*., *Science* **385**, 80–86 (2024).
23. J. P. Burbach, *Ann. Clin. Biochem.* **19**, 269–277 (1982).
24. K. Alves de Lima *et al*., *Nat. Immunol.* **21**, 1421–1429 (2020).
25. M. M. Santisteban *et al*., *Nat. Neurosci.* **27**, 63–77 (2024).
26. A. Baysoy *et al*., *J. Exp. Med.* **220**, e20222052 (2023).
27. L. Basso *et al*., *J. Neuroinflammation* **13**, 132 (2016).
28. G. Laumet *et al*., *Front. Mol. Neurosci.* **12**, 216 (2019).
29. X. Yu *et al*., *Nat. Commun.* **11**, 264 (2020).
30. D. Wang *et al*., *Neuron* **98**, 90–108.e5 (2018).
31. R. Bardoni *et al*., *Neuron* **81**, 1312–1327 (2014).
32. K. Y. Chan *et al*., *Nat. Neurosci.* **20**, 1172–1179 (2017).
33. G. Corder *et al*., *Science* **341**, 1394–1399 (2013).
34. J. Zhang *et al*., *J. Neurosci.* **42**, 7862–7874 (2022).
35. I. Sankaranarayanan *et al*., *J. Neuroinflammation* **20**, 32 (2023).
36. L. Qi *et al*., *Cell* **187**, 1508–1526.e16 (2024).
37. C. Schläger *et al*., *Nature* **530**, 349–353 (2016).
38. A. Jain *et al*., *Nat. Immunol.* **25**, 1296–1305 (2024).
39. Y. Zhu *et al*., *Science* **385**, eadk1679 (2024).
40. G. Stacher *et al*., *Pain* **34**, 271–276 (1988).
41. C. M. Cahill, A. Morinville, C. Hoffert, D. O'Donnell, A. Beaudet, *Pain* **101**, 199–208 (2003).
42. É. Midavaine *et al*., Meningeal regulatory T cells inhibit nociception in female mice, dataset, Dryad (2025).

ACKNOWLEDGMENTS

Figures were generated with BioRender.com. We thank D. Dubal and her laboratory for the FCG mouse, K. Yackle for *Penk*$^{\text{Cre}}$ mice, A. Molofsky for *Foxp3*$^{\text{Cre-ERT2}}$*Rosa26*$^{\text{tdTomato}}$ mice, A. Pradhan for *Oprd1*$^{\text{eGFP}}$ mice, L. K. Dobbs and A. Zimmer for *Penk*$^{\text{flox}}$, J. Chouinard for HEK293-δLight, and M. Ansonoff for assistance with *Penk*$^{-/-}$ tissue isolation. We thank additional members of the

Basbaum laboratory and UCSF ImmunoX for critical feedback. **Funding:** This study received support from Canadian Institute of Health Research (CIHR) (É.M.); the Fonds de Recherche en Santé-Québec (É.M.); the Sandler Foundation PBBR (É.M. and S.W.K.); the Dermatology Foundation (Career Development Award) (S.W.K.); the Benioff Microbiome Research Program (S.W.K.); a Grunfeld Scholar Award from SFVAMC (S.W.K.); National Institutes of Health (NIH) grant T32AR007175-44 (S.W.K.); São Paulo Research Foundation, 2023/04332-0 (B.C.M.); NIH grant NSR35NS097306 (A.I.B.); and Open Philanthropy (A.I.B.). A.I.D. is supported by an ERC Consolidator Award (ERC-2017 COG 771431), a 2022 Pfizer ASPIRE Global Obesity award, Pfizer no. 70591281, NIH PTE no. 5UM1DK105554-09 sub-award 5000826-5500002717, and BBSRC BB/Y006488/1. **Author contributions:** Conceptualization: É.M., S.W.K.; Critical reagents: L.T., A.I.D., J.E.P.; Funding acquisition: É.M., S.W.K., A.I.B.; Investigation: É.M., B.C.M., J.B., S.R.R., S.W.K.; Methodology: É.M., S.W.K.; Project administration: J.M.B.; Supervision: É.M., S.W.K., A.I.B.; Visualization: É.M., N.P.K., W.L.E., S.W.K.; Writing – original draft: É.M., S.W.K.; Writing – review & editing: É.M., S.W.K., A.I.B. **Competing interests:** The authors declare that they have no competing interests. **Data and materials availability:** All data needed to evaluate the conclusions in the paper are present in the paper or the supplementary materials. Raw data used to generate figures along with the data from the analyses of public datasets are deposited in Dryad (*42*).

SUPPLEMENTARY MATERIALS

science.org/doi/10.1126/science.adq6531
Materials and Methods
Figs. S1 to S9
Table S1
References (*43*–*48*)
MDAR Reproducibility Checklist

Submitted 24 May 2024; resubmitted 11 November 2024
Accepted 6 February 2025
10.1126/science.adq6531

ANIMAL COMMUNICATION

Extensive compositionality in the vocal system of bonobos

M. Berthet[1,2,3]*, M. Surbeck[4,5]†, S. W. Townsend[1,2,3,6]†

Compositionality, the capacity to combine meaningful elements into larger meaningful structures, is a hallmark of human language. Compositionality can be trivial (the combination's meaning is the sum of the meaning of its parts) or nontrivial (one element modifies the meaning of the other element). Recent studies have suggested that animals lack nontrivial compositionality, representing a key discontinuity with language. In this work, using methods borrowed from distributional semantics, we investigated compositionality in wild bonobos and found that not only does each call type of their repertoire occur in at least one compositional combination, but three of these compositional combinations also exhibit nontrivial compositionality. These findings suggest that compositionality is a prominent feature of the bonobo vocal system, revealing stronger parallels with human language than previously thought.

A quintessential feature of human language is the capacity to combine elements. For example, morphemes can be combined into words (e.g., "bio" + "logy" = "biology") or words into sentences ("Biology is interesting"). This is possible because of compositionality, whereby meaningful units are combined into larger structures whose meaning is determined by the meanings of the parts and the way they are combined (*1*, *2*).

Compositionality can take two forms. In its "trivial" (or "intersective") version, each element of the combination contributes to the meaning of the whole independently of the other element, and the combination is interpreted by the conjunction of its parts (*3*–*5*). For example, "blond dancer" refers to a person who is both blond and a dancer; if this person is also a doctor, we can infer that they are a blond doctor as well. However, compositional syntax can also be "nontrivial" (or "nonintersective"): The units constituting a combination do not contribute independent meaning, but instead, they combine so that one part of the combination modifies the other (*3*, *4*). For example, the meaning of the expression "bad dancer" does not refer to a bad person who is also a dancer. Indeed, if this person is also a doctor, we cannot infer that they are a bad doctor. Here, "bad" does not have a meaning independent from "dancer"; rather, it complements it (*3*–*5*).

Compositionality as a phenomenon might not be unique to human language. Numerous studies in birds and primates have demonstrated that animals are capable of combining meaningful vocalizations into trivially compositional structures (*6*–*8*). To our knowledge, however, unambiguous evidence of nontrivial compositionality in animals from systematically collected quantitative data is still lacking (*3*, *9*–*16*).

In this work, we provide robust empirical evidence for the presence of nontrivial compositionality in wild bonobos (*Pan paniscus*). First, we leveraged a framework established by Berthet *et al.* (*2*) that investigates meaning by considering all aspects of context that co-occur with the emission of the signal. This approach defines the meaning of a signal as the set of features of circumstances (FoCs) that appear at a rate greater than chance across the signal's occurrences (*2*). We recorded 700 wild bonobo calls and call combinations (hereafter, vocal utterances; table S1) and systematically collected more than 300 FoCs for each utterance (see materials and methods and table S2). Second, using a method adapted from distributional semantics, a linguistic approach that quantifies meaning similarities between words (*17*), we used these FoCs to map bonobo utterance types within a multidimensional space (hereafter, semantic space) and quantify meaning similarities between utterance types.

Last, to investigate whether the bonobo call system is compositional, we applied a multistep process previously used by Trujillo and Holler to identify nontrivial compositionality in human multimodal communication (*12*). Under this approach, a combination AB is considered compositional if (i) the meaning of A is distinct from that of B, (ii) the meaning of AB is different from that of A and that of B, and (iii) the meaning of AB is derived from the meaning of A and B. The fourth step determines whether a compositional combination is trivial or nontrivial. More precisely, the combination AB represents a nontrivial compositional structure if it is compositional [i.e., it fulfils criteria (i) to (iii)] and if (iv) the meaning of AB is different from the meaning of A+B (see fig. S1 for an explicit visualization of the process). Our study shows that all seven bonobo call types that were considered in our analysis combine into four compositional structures, of which three exhibit nontrivial compositionality.

Results

Semantic space of bonobo utterances

We adapted a distributional semantics framework to investigate the meaning of bonobos' call combinations in relation to single calls. Distributional semantics is based on the distributional hypothesis, which states that words with close meanings are used in similar contexts (*17*). Distributional semantics represents word meaning in a semantic space by converting each word into a vector so that relationships between words can be quantified using geometric relations (*18*). We estimated similarities between single call types and call combinations of wild bonobos using a multiple correspondence analysis (MCA) performed on the FoCs. The MCA is similar to a principal components analysis (PCA) but is conducted on categorical data: It performs a dimension reduction and then quantifies the statistical relationship between a specific utterance type

---

[1]Department of Evolutionary Anthropology, University of Zürich, Zürich, Switzerland. [2]Department of Comparative Language Sciences, University of Zürich, Zürich, Switzerland. [3]Institute for the Interdisciplinary Study of Language Evolution, University of Zürich, Zürich, Switzerland. [4]Department of Human Evolutionary Biology, Harvard University, Cambridge, MA, USA. [5]Department of Human Behavior, Ecology and Culture, Max Planck Institute for Evolutionary Anthropology, Leipzig, Germany. [6]Department of Psychology, University of Warwick, Coventry, UK.
***Corresponding author. Email: melissa.berthet.ac@gmail.com**
†These authors contributed equally to this work.

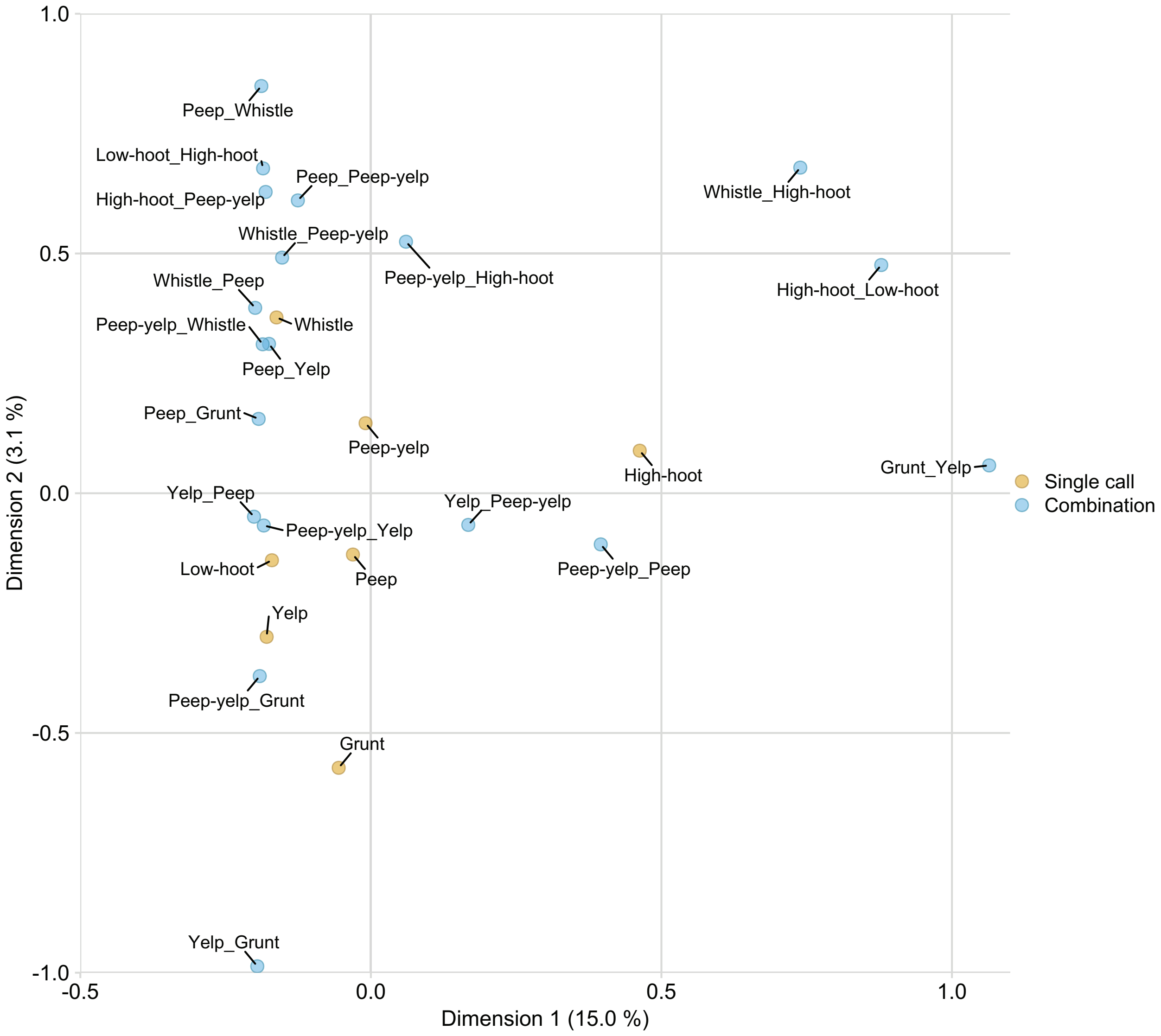

Fig. 1. First two dimensions of the semantic space of bonobos' vocal repertoire. Call types and combinations are plotted in a semantic space based on their inferred meaning (i.e., the FoCs associated with their emission). Utterances that have a similar meaning (i.e., that are emitted in similar contexts) are closer to each other than utterances emitted in different contexts. Combinations (in blue) are in the form A_B.

and several FoCs (*19*) (see materials and methods). We found that the first five dimensions of the MCA explained about 24% of the variance in the data (15.00 + 3.12 + 2.46 + 2.18 + 2.14%). These five dimensions were used to create a semantic space in which each utterance was mapped using five-dimensional coordinates (Fig. 1 and figs. S2 to S4). Utterances with a similar meaning are closer to each other in the semantic space than utterances with a different meaning. These five-dimensional coordinates were used for the remaining analyses.

Compositionality analysis

After mapping the meaning of each call type and each combination, we investigated whether the combinations were nontrivially compositional. For this, we used a step-by-step process described in Trujillo and Holler (*12*).

Chance value

For each call type, we calculated a chance value representing the minimum Euclidian distance required to conclude that another utterance type has a different meaning from that call type. This later allowed us to determine whether distances between call types and/or combinations are greater than expected compared with the natural variance of the meaning of the single calls (table S3 and materials and methods).

(i) The meaning of A is different from the meaning of B

We investigated whether the single calls had significantly different meanings from each other. To do so, we calculated, for each possible pair of single calls, the difference between (i) the Euclidian distance separating the single calls and (ii) the mean of the chance value of the calls. We then assessed whether this difference was overall significantly different from zero using a one-sample *t* test.

The meanings of call types were significantly different from each other ($t_{20} = 4.63$, $p < 0.001$). Specifically, all call types had a different meaning from each other except for three: Low-hoot had a similar meaning to Peep-yelp and Yelp (Fig. 2) because the difference between the pairs of call types and the mean chance value of the calls was less than zero (table S4).

(ii) The meaning of AB is different from the meaning of A and the meaning of B

We then investigated whether the call combinations had a different meaning from that of their constituents. To this end, we calculated, for each possible pair of one combination and one constituting call type of that combination, the difference between (i) the Euclidian distance separating the combination and its constituting call type, and (ii) the chance value of the constituting call type. We then assessed whether this difference was overall significantly different from zero using a one-sample *t* test.

The meaning of combinations was significantly different from the meaning of their constituents ($t_{37} = 7.36$, $p < 0.001$). Specifically, all combinations had a meaning different from their constituting call types, except for two: Peep-yelp_Peep and Peep-yelp_Yelp (Fig. 3 and table S5).

(iii) The meaning of AB is derived from the meaning of A and B

We investigated whether the meaning of the combinations was derived from the meaning of their elements. Following Trujillo and Holler (*12*), we calculated whether the meaning of a combination was closer to that of its constituent elements than any other element. Stated another way, we calculated whether the Euclidean distance between a combination and the call types constituting it was smaller than the distance between a combination and any other call type. For this, we calculated the pairwise Euclidian distance separating every single call from every combination. We then ran a linear model with distance as the dependent variable, and an interaction between the combination type (e.g., Yelp_Grunt) and whether the single call was a part of the combination (here termed the "relationship variable") as independent variables.

The meaning of combinations was closer to that of their constituents at the repertoire level: A likelihood ratio test detected a difference between the full model and its reduced version (i.e., the model without the relationship variable) ($F_{19,95} = 2.13$, $p < 0.01$). Specifically, posthoc analyses revealed that, for four combinations, the distance separating the combination from its constituting call types was smaller than the distance separating the combinations from call types that do not constitute it: High-hoot_Low-hoot ($t_{95} = 2.07$, $p = 0.04$), Peep_Whistle ($t_{95} = 2.70$, $p < 0.01$), Peep-yelp_High-hoot ($t_{95} = 2.17$, $p = 0.03$), and Yelp_Grunt ($t_{95} = 3.17$, $p < 0.01$) (Fig. 4 and table S6). Because these four combinations fulfil criteria (i) to (iii), they are all considered compositional.

(iv) The meaning of AB is different from the meaning of A+B

Finally, we investigated whether the four aforementioned compositional combinations were explained by trivial or nontrivial compositionality (*12*). We expected combinations exhibiting

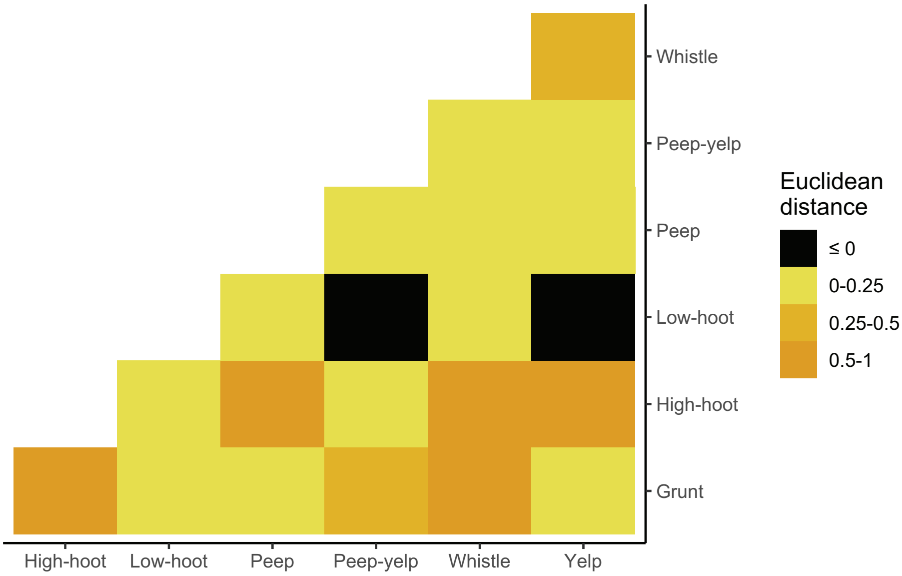

Fig. 2. Meaning differences between call types. The meaning difference is represented by whether the Euclidean distance between two call types is different from the mean of the chance value of these call types. Call types that overlap in meaning have a Euclidian distance of zero or less (in black).

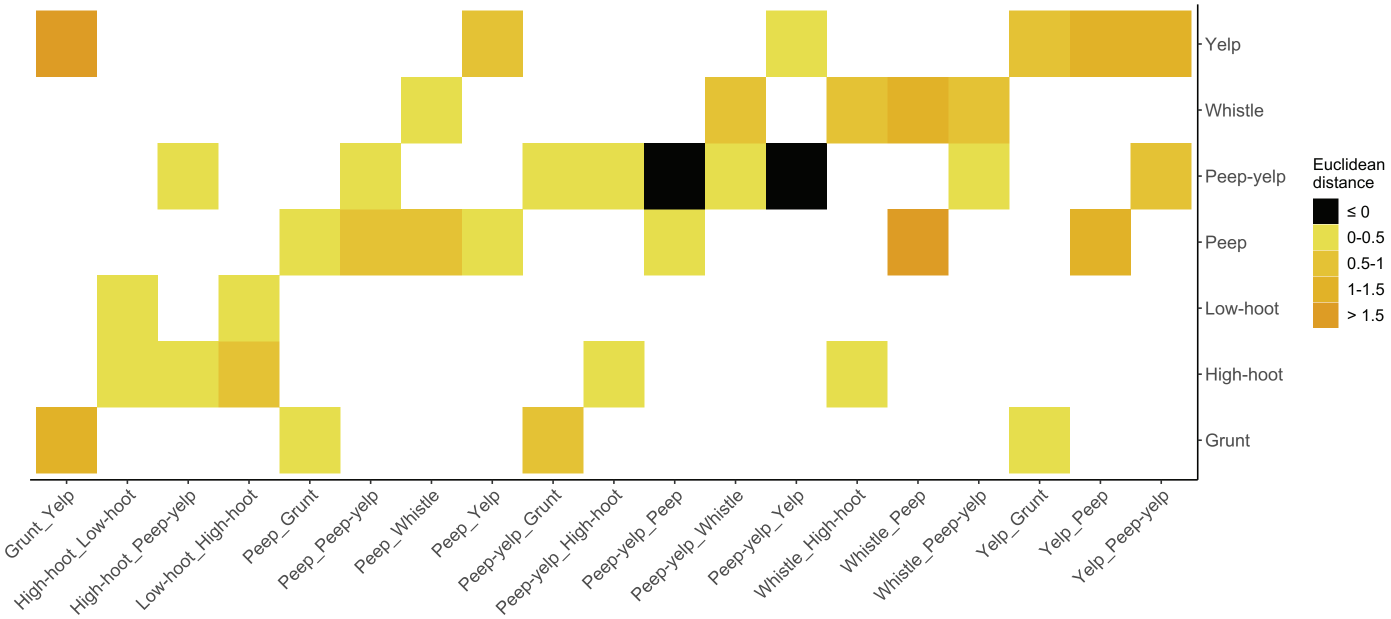

Fig. 3. Meaning differences between a combination A_B and its constituting call types A and B. Meaning differences between a combination A_B (e.g., Grunt_Yelp) (*x* axis) and its constituting call types A (e.g., Grunt) and B (e.g., Yelp) (*y* axis), represented as whether the Euclidean distance between the combination and a constituting call type is different from the chance value of this call type. Combinations whose meaning overlaps with one of its constituting call types have a Euclidian distance of zero or less with that call type (in black).

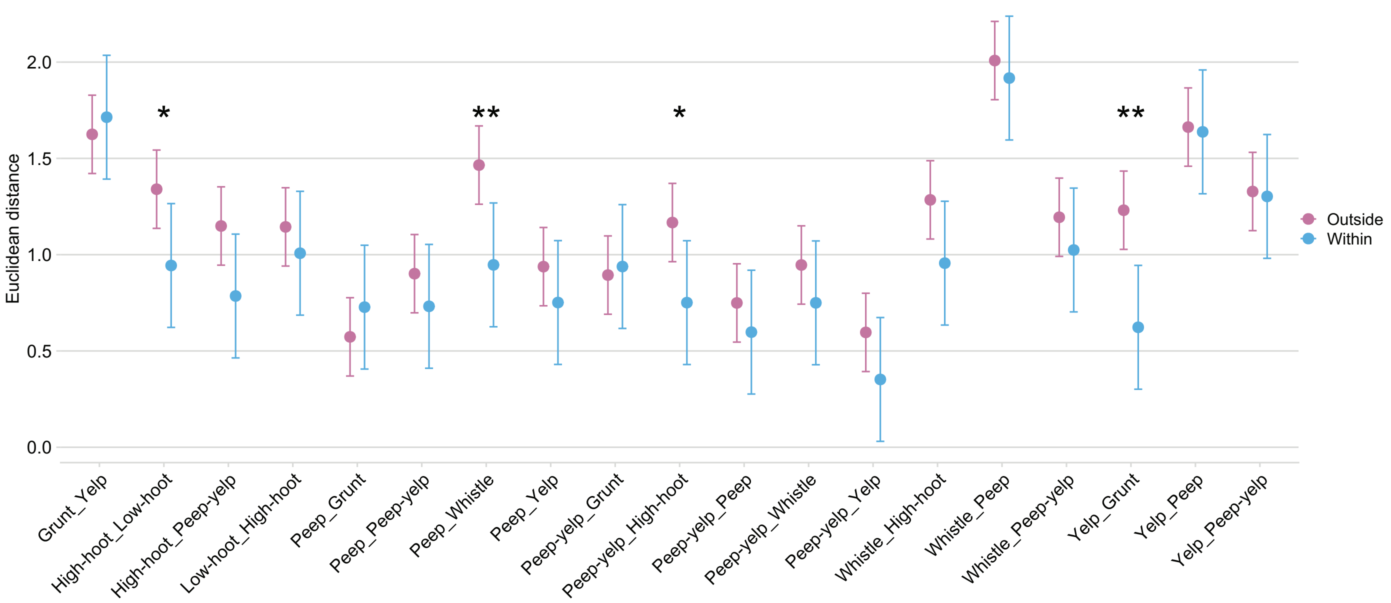

Fig. 4. Meaning difference between a combination A_B and single call types of the repertoire. Distance between the meaning of a given combination and that of its constituting call types (in blue) and between the meaning of a combination and that of call types that do not constitute it (in pink). Boxplots indicate the lower and higher confidence intervals, and dots indicate the estimated marginal means of the model. The symbols indicate significant differences (*$0.01 < p < 0.05$; **$p < 0.01$).

nontrivial compositionality to have a meaning different from adding the meaning of their parts. Following Trujillo *et al.* (*12*), we built a hypothetical additive combination by adding the coordinates of the constituting single call types. We then calculated the difference between (i) the Euclidian distance separating the combination and the additive combination and (ii) the mean chance value of the constituting call types of that combination. If that difference was greater than zero, we concluded that the combination exhibited nontrivial compositionality. Stated another way, we added the coordinates of A and B to create an A+B vector and calculated whether the Euclidean distance between A+B and AB was different from the mean chance value of A and B.

For all compositional combinations except Yelp_Grunt, the difference was greater than zero (High-hoot_Low-hoot: 0.42; Peep_Whistle: 0.36; Peep-yelp_High-hoot: 0.21). For Yelp_Grunt, the distance between the combination and an additive combination was not greater than the mean chance value (–0.02). That is, Yelp_Grunt exhibited trivial compositionality, whereas High-hoot_Low-hoot, Peep_Whistle, and Peep-yelp_High-hoot exhibited nontrivial compositionality.

Meaning of the utterances

In the final step, we derived a tentative meaning for the single calls and the combinations to illustrate how single calls combine into structures whose meaning is derived from the meaning of their parts. We extracted the meaning of each utterance type by determining which set of FoCs is associated with the utterance type at the repertoire level (see materials and methods). Results are summarized in tables S7 and S8.

The semantic analysis of the Grunt suggests that it signals the ongoing activity of the caller. Because Grunts are given in a large variety of contexts (during grooming, resting, moving, feeding), they may signal that others should look at the caller to coordinate activities (“Look at me,” in close interactions). High-hoots are emitted in different contexts and seem to signal the presence or location of the caller, especially in long-distance settings or dangerous situations (“Pay attention to me,” for a larger audience or more considerable distances than the Grunts). The Low-hoots seem related to high-arousal situations, such as the construction of the night nest (*20*) (“I am excited”). The semantic analysis suggests that Yelps and Peeps have similar meanings, used as imperatives to coordinate social activities. However, Peeps seem to be more used as suggestions rather than strong imperatives: They are less associated with changes in behaviors in the audience and sometimes elicit vocal responses, which could suggest a quorum-based or “voting-like” system (“I would like to…”). Conversely, Yelps are associated with changes in the behaviors of the audience and no vocal response, suggesting that Yelps are more of a rigid imperative (“Let’s do that”). The meaning of the Peep-yelp also varies with the context. It is mainly given during group encounters or when building night nests, maybe to coordinate intergroup interactions and encourage other parties to join (“Join!”). Finally, the Whistles seem to coordinate the spatial cohesion of the group (“Let’s stay together”).

The Yelps (“Let’s do that”) and Grunts (“Look at me”) can be combined into the trivial compositional structure Yelp_Grunt, which seems to incite others to build a night nest. The High-hoot (“Pay attention to me”) can be combined with the Low-hoot (“I am excited”) into a nontrivial compositional combination High-hoot_Low-hoot, which is used when another individual is displaying, maybe to elicit a reaction in the audience (recruitment, “Pay attention to me because I am in distress”) or to stop the display behavior of the other individual. The Peep (“I would like to…”) can be combined with the Whistle (“Let’s stay together”) into a nontrivial compositional combination, Peep_Whistle, which is used in sensitive social contexts, for example, during copulations or displays, maybe to attract attention or assert rank. Finally, the Peep-yelp (“Join!”) can be combined with the High-hoot (“Pay attention to me”) into the nontrivial compositional structure Peep-yelp_High-hoot, which seems to be used to coordinate with other parties before traveling.

Discussion

In this study, we assessed whether bonobos combine calls into larger compositional structures. Using a holistic investigation of meaning derived from distributional semantics combined with a method for identifying compositionality in multimodal human language (*12*), we found that bonobos can combine all their calls into four compositional structures, of which one is a case of trivial compositionality (Yelp_Grunt) and three (High-hoot_Low-hoot, Peep_Whistle, Peep-yelp_High-hoot) are cases of nontrivial compositionality.

Our findings have three important implications. In humans, compositionality is essential for generativity, a crucial hallmark of language by which speakers can combine a finite set of elements into an infinite number of combinations that others can understand (*21*). Although most investigations of the compositional capacities of nonhuman species have been limited to one specific combination of a vocal system [for example, (*6*, *7*, *22*, *23*)], our study suggests that, in bonobos, this capacity is not restricted to a few isolated combinations. Indeed, each of the seven call types we investigated here represents a building block of a compositional structure. The first implication of our work is therefore that, akin to human language, compositionality is a pervasive component of bonobos' vocal communication.

Second, our data provide robust empirical evidence that nonhuman animals engage in nontrivial compositionality. In human language, nontrivial compositionality is particularly important in facilitating generativity by allowing meaningful elements to be combined into novel, nonadditive structures like "bad dancer," where the meaning of the whole is more than the meaning of its parts (*12*). Although a number of studies have demonstrated that animals can also combine meaningful vocalizations compositionally [see review in (*8*)], to our knowledge, no study to date has empirically shown that animals engage in complex nontrivial compositionality akin to that observed in human language (*11*, *13*, *24*). Our results indicate that nontrivial compositionality is not limited to humans and that bonobos, our closest living relative, also engage in nontrivial compositionality.

The extent to which our findings can inform the evolutionary roots of linguistic compositionality is yet to be determined. One interpretation of the data could be that nontrivial compositionality can be traced as far back as the last common ancestor of bonobos and humans, 7 million to 13 million years ago (*25*). It is also possible that the absence of evidence in other species has been hampered by the lack of appropriate methods. Indeed, as we show here, detecting (nontrivial) compositionality largely depends on the capacity to reliably assess meaning and detect compositionality across an entire repertoire. Hence, a third important implication of our work is that we present a method for reliably inferring the meaning of all the signals of an animal's repertoire with minimal human judgment. This method can theoretically be applied to any taxa and any communication system (e.g., gestures, facial expressions, multimodal signals) to build a systematic survey of meaning and compositionality across species, ultimately allowing for a comprehensive investigation of the evolutionary pressures driving the evolution of these capacities.

It is worth noting that our study does not come without limitations, which might explain why the meaning of some utterance types (e.g., Low-hoots or Yelp_Grunts) are difficult to translate into human-relevant concepts. First, some meanings might be emotionally expressive (i.e., conveying information about the caller's emotional states), and future research should include FoCs related to the caller's emotional state, using direct emotion measurements such as infrared thermography (*26*). Second, our vocal repertoire might not be of sufficient granularity to capture the full complexity of the system: If some call types have subtle acoustic variants that convey different meanings, we may have misclassified them as one single call type, preventing reliable determination of their meaning. Finally, similar to birdsongs, some call types might have no meaning (*2*), which is not accounted for in our approach; for instance, the High-hoot might function to localize the caller rather than convey a specific message.

Although our focus is on vocal combinations, it is important to note that great apes also combine signals from different modalities, exposing the receiver to an array of additional multimodal information that may refine or modify a signal's meaning (*27*–*31*). For example, bonobos combine Contest-hoots with different gestures that potentially disambiguate the meaning of these vocalizations, that is, whether they intend to play with or challenge another individual (*32*). The extent to which combining vocalizations with other signals also modifies meaning in potentially nontrivial ways remains unknown, but it represents a critical follow-up research avenue to this study (*33*, *34*).

Our results (in particular, Fig. 1 and figs. S2 to S4) suggest that bonobos use call combinations in semantic areas in which single calls do not occur. That is, bonobos seem to combine calls to convey meaning that cannot be conveyed through single calls alone. Testing this hypothesis in the future will help us understand the selective forces that have given rise to compositionality in both animal communication and human language.

REFERENCES AND NOTES

1. B. H. Partee, in *Compositionality in Formal Semantics: Selected Papers* (Blackwell Publishing, 2004), pp. 153–181.
2. M. Berthet, C. Coye, G. Dezecache, J. Kuhn, *Biol. Rev. Camb. Philos. Soc.* **98**, 81–98 (2023).
3. S. Steinert-Threlkeld, *Philos. Sci.* **87**, 897–909 (2020).
4. J. R. Martin, thesis, Harvard University (2022).
5. T. Korbak, J. Zubek, J. Rączaszek-Leonardi, arXiv:2010.15058 [cs.NE] (2020).
6. S. Engesser, A. R. Ridley, S. W. Townsend, *Proc. Natl. Acad. Sci. U.S.A.* **113**, 5976–5981 (2016).
7. M. Leroux *et al.*, *Nat. Commun.* **14**, 2225 (2023).
8. S. W. Townsend, S. Engesser, S. Stoll, K. Zuberbühler, B. Bickel, *PLOS Biol.* **16**, e2006425 (2018).
9. J. Kuhn, S. Keenan, K. Arnold, A. Lemasson, *Linguist. Inq.* **49**, 169–181 (2018).
10. P. Schlenker *et al.*, *Theor. Linguist.* **42**, 1–90 (2016).
11. M. Leroux, *Rev. Primatol.* **14**, 16469 (2023).
12. J. P. Trujillo, J. Holler, *Sci. Rep.* **14**, 2286 (2024).
13. U. Sauerland, *Theor. Linguist.* **42**, 147–153 (2016).
14. P. Schlenker *et al.*, *Biol. Rev. Camb. Philos. Soc.* **99**, 1278–1297 (2024).
15. P. Schlenker, C. Coye, M. Leroux, E. Chemla, *Biol. Rev. Camb. Philos. Soc.* **98**, 1142–1159 (2023).
16. G. J. L. Beckers, M. A. C. Huybregts, M. B. H. Everaert, J. J. Bolhuis, *Front. Psychol.* **15**, 1393895 (2024).
17. Z. S. Harris, *Word* **10**, 146–162 (1954).
18. G. Boleda, *Annu. Rev. Linguist.* **6**, 213–234 (2020).
19. F. Husson, S. Lê, J. Pagès, *Exploratory Multivariate Analysis by Example Using R*, Computer Science & Data Analysis Series (CRC Press, ed. 2, 2017).
20. T. Furuichi, in *Bonobo and Chimpanzee*, Primatology Monographs (Springer, 2019), pp. 1–36.
21. M. C. Corballis, *Cognition* **44**, 197–226 (1992).
22. T. N. Suzuki, D. Wheatcroft, M. Griesser, *Nat. Commun.* **7**, 10986 (2016).
23. K. Ouattara, A. Lemasson, K. Zuberbühler, *PLOS ONE* **4**, e7808 (2009).
24. P. Schlenker, E. Chemla, K. Zuberbühler, *Trends Cogn. Sci.* **20**, 894–904 (2016).
25. K. E. Langergraber *et al.*, *Proc. Natl. Acad. Sci. U.S.A.* **109**, 15716–15721 (2012).
26. G. Dezecache, K. Zuberbühler, M. Davila-Ross, C. D. Dahl, *R. Soc. Open Sci.* **4**, 160816 (2017).
27. L. S. Oña, W. Sandler, K. Liebal, *PeerJ* **7**, e7623 (2019).
28. C. Hobaiter, R. W. Byrne, K. Zuberbühler, *Behav. Ecol. Sociobiol.* **71**, 96 (2017).
29. C. Wilke *et al.*, *Anim. Behav.* **123**, 305–316 (2017).
30. J. G. Mine *et al.*, *Behav. Ecol. Sociobiol.* **78**, 108 (2024).
31. M. Fröhlich, C. P. van Schaik, *Anim. Cogn.* **21**, 619–629 (2018).
32. E. Genty, Z. Clay, C. Hobaiter, K. Zuberbühler, *PLOS ONE* **9**, e84738 (2014).
33. K. Liebal, K. E. Slocombe, B. M. Waller, *Ethol. Ecol. Evol.* **34**, 274–287 (2022).
34. K. E. Slocombe, B. M. Waller, K. Liebal, *Anim. Behav.* **81**, 919–924 (2011).
35. M. Berthet, M. Surbeck, S. W. Townsend, Dataset and R code - Extensive compositionality in the vocal system of bonobos, figshare (2025); https://doi.org/10.6084/m9.figshare.c.7648628.

ACKNOWLEDGMENTS

We thank the people of the villages of Bolamba, Yete, Yomboli, Yasalakose, and Bekungu, who granted us access to their forest; the Ministry of Research in the Democratic Republic of the Congo (DRC); the Institut Conglais pour la Conservation de la Nature; the Bonobo Conservation Initiative; and Vie Sauvage. We also thank the staff of the Kokolopori Bonobo Research Project, as well as L. Zanutto and M. Rohée, for their help and support during data collection. We thank G. Mesbahi and D. da Cruz for logistic support, as well as E. Ahmad, L. Bierhoff, C. H. Chen, L. Fornof, G. Gordon, and J. Vlaeyen for help and support during data collection. We also thank F. Wegdell for conducting an interobserver reliability test. We thank K. Slocombe, M. Leroux, and S. Watson for their comments on the draft and C. Zulberti, A. Bosshard, I. Schamberg, N. Lahiff, and J. Kuhn for insightful discussions. **Funding:** This work was funded by Swiss National Science Foundation grants PP00P3_198912 and 315130_192620 (S.W.T.), NCCR Evolving Language, Swiss National Science Foundation Agreement #51NF40_180888 (S.W.T.), and Startup from Harvard University (M.S.). **Author contributions:** Conceptualization: M.B., S.W.T.; Methodology: M.B., S.W.T., M.S.; Data collection: M.B.; Funding acquisition: S.W.T., M.S.; Supervision: S.W.T., M.S. (fieldwork); Writing – original draft: M.B., S.W.T.; Writing – review & editing: M.B., S.W.T., M.S. **Competing interests:** The authors declare that they have no competing interests. **Data and materials availability:** The dataset analyzed in the current study and the statistical script are available in the figshare repository (*35*).

SUPPLEMENTARY MATERIALS

science.org/doi/10.1126/science.adv1170
Materials and Methods
Figs. S1 to S4
Tables S1 to S9
References (*36*–*63*)

Submitted 6 December 2024; accepted 26 February 2025
10.1126/science.adv1170

CELL BIOLOGY

Tissue-like multicellular development triggered by mechanical compression in archaea

Theopi Rados[1]†‡, Olivia S. Leland[1]†, Pedro Escudeiro[2], John Mallon[1], Katherine Andre[1], Ido Caspy[3], Andriko von Kügelgen[3], Elad Stolovicki[4], Sinead Nguyen[1], Inés Lucía Patop[1]§, L. Thiberio Rangel[5], Sebastian Kadener[1], Lars D. Renner[6], Vera Thiel, Yoav Soen[4], Tanmay A. M. Bharat[3], Vikram Alva[2], Alex Bisson[1]*

The advent of clonal multicellularity is a critical evolutionary milestone, seen often in eukaryotes, rarely in bacteria, and only once in archaea. We show that uniaxial compression induces clonal multicellularity in haloarchaea, forming tissue-like structures. These archaeal tissues are mechanically and molecularly distinct from their unicellular lifestyle, mimicking several eukaryotic features. Archaeal tissues undergo a multinucleate stage followed by tubulin-independent cellularization, orchestrated by active membrane tension at a critical cell size. After cellularization, tissue junction elasticity becomes akin to that of animal tissues, giving rise to two cell types—peripheral (Per) and central scutoid (Scu) cells—with distinct actin and protein glycosylation polarity patterns. Our findings highlight the potential convergent evolution of a biophysical mechanism in the emergence of multicellular systems across domains of life.

Multicellularity has evolved multiple times across the tree of life, fundamentally reshaping Earth's biosphere. Comparative studies across these independent transitions have revealed common selective benefits, including increased size, enhanced mechanical strength, and cellular differentiation—principles later confirmed through experimental evolution (*1*–*4*). Although well documented in eukaryotes and prokaryotes, the extent to which clonal multicellularity contributes to the emergence of structural and functional complexity in bacteria and archaea remains unclear. Once mistaken for bacteria owing to their lack of nuclei, archaea are now recognized as a monophyletic group with eukaryotes (*5*). Most archaea lack a rigid cell wall and are encapsulated by a proteinaceous surface monolayer (S-layer), a two-dimensional (2D) paracrystalline lattice composed of glycoproteins (*6*, *7*). Although the archaeal envelope structure is thought to make cells mechanically vulnerable, it also facilitates close interactions between cells, such as cell-cell contact and fusion, which may have played a role in the emergence of eukaryotes (*8*, *9*). However, the evolution of mechanosensory responses driven by the lack of a rigid cell wall remains elusive owing to the scarcity of in vivo studies. The peculiar combination of genetic and biophysical traits prompted us to investigate the mechanobiology of archaeal cells, leading to the serendipitous discovery of a reversible, clonal, tissue-like multicellular developmental program.

Uniaxial compression gives rise to clonal, tissue-like multicellularity

To gain insights into the mechanobiology of archaeal cells, we performed confinement experiments with the salt-loving *Haloferax volcanii* (*Hvo*), leveraging its straightforward cultivation and genetics (*10*). First, we established a baseline for mechanically unperturbed haloarchaeal cells trapped within ArcCell, a custom microfluidic device (Fig. 1A and fig. S1A). Cells growing in ArcCell showed cell morphologies comparable to those in bulk liquid cultures, indicating no mechanical stress (Fig. 1B, fig. S1B, and movie S1). Next, we imaged cells under agarose pads, a standard technique for microbial immobilization (Fig. 1C). Unlike in ArcCell, agarose pads deformed cells within a single generation (~2.5 hours) at the lowest agarose concentrations, making pad immobilization incompatible with prolonged imaging (fig. S1B and movie S1). To quantify the compressive forces deforming cells, we measured the pad elasticity using dynamic mechanical analysis (*11*). The storage moduli of 0.25 to 3.5% pads revealed that resistance forces of ~10 kPa are sufficient to deform *Hvo* (fig. S1C). These values suggest that *Hvo* cells may have viscoelastic properties close to those of eukaryotic cells, such as amoeba and mammalian cells, but orders of magnitude lower than those of most cell-walled organisms (*12*, *13*).

Given the mechanical sensitivity of haloarchaeal cells under pads, we tested the responses of *Hvo* to compressive forces above 100 kPa, closer to forces experienced in their natural habitat, such as the human gut and salt ponds (*14*–*16*). Following compression under pads with agarose concentrations of 1.5% and higher, cells stopped dividing but continued to grow (Fig. 1D, second panel). After ~12 hours, cellularization occurred via simultaneous septation events (Fig. 1D, third panel), resulting in epithelial-like monolayer structures (Fig. 1E and movie S2). These tissue-like ensembles resemble radial tessellation patterns in leaf tissues and multicellular green algae (*17*, *18*). The morphological development before cellularization also resembles the coenocytic phase of chytrids and chicken embryogenesis, in which cells multiply their nuclei without cell division (*19*, *20*). Time-lapse imaging of cells expressing mNeonGreen-PCNA (DNA sliding clamp) showed continuous replication during development, supporting a coenocytic-like phase preceding cellularization (Fig. 1D and movie S3).

Animal and plant cells often sense and activate biochemical pathways in response to surface curvatures and material properties (*21*, *22*). To test the influence of the pad's stiffness, we immobilized *Hvo* cells under and on top of the same 2.5% agarose pad. As a result, tissues were observed exclusively under the pads (fig. S2A), suggesting that stiffness alone is not sufficient to induce multicellularity. Furthermore, cells compressed by different bilayer "cake" pad setups developed into tissue-like structures only when under compression by at least one stiff surface, ruling out a specific role of the coverslip other than providing a rigid surface for compression (fig. S2, B and C). Finally, tissue formation is independent of gravity (fig. S3A), pad mass, or thickness (fig. S3B) and consistently initiated at the same coenocytic area regardless of pad density (fig. S3C). These analogous features suggest that archaeal tissue development represents an evolved biological program response to compression.

To determine whether cells within multicellular structures retain their S-layer lattice, we cryo-fixed cells from mechanically sheared tissues and imaged individual cells by electron cryotomography (cryo-ET) (fig. S4A). Concomitantly with live-cell staining of glycoproteins (fig. S4B), we concluded that archaeal tissues preserve S-layer material in their intercellular spaces.

Next, we explored the possibility that tissues arise from cell compaction. Three-dimensional (3D) imaging revealed extracellular spaces between most unicells but none within tissues (Fig. 1F and movie S4). To probe physical connectivity, we used laser ablation to wound areas at the center of the tissues. Following ablation, we observed directional movement of cells toward the wounds in tissues, but not in unicells, at speeds of 0.62 ± 0.27 μm/min (Fig. 1G, fig. S4C, and movie S5), comparable to those seen in

---

[1]Brandeis University, Department of Biology, Waltham, MA, USA. [2]Department of Protein Evolution, Max Planck Institute for Biology Tübingen, Tübingen, Germany. [3]Structural Studies Division, MRC Laboratory of Molecular Biology, Cambridge, UK. [4]Department of Biomolecular Sciences, Weizmann Institute of Science, Rehovot, Israel. [5]Department of Earth, Atmospheric, and Planetary Sciences, Massachusetts Institute of Technology, Cambridge, MA, USA. [6]Leibniz Institute of Polymer Research and the Max Bergmann Center of Biomaterials, Dresden, Germany. [7]Department of Microorganisms, Leibniz Institute DSMZ–German Collection of Microorganisms and Cell Cultures GmbH, Braunschweig, Germany.
***Corresponding author. Email: bisson@brandeis.edu**

†These authors contributed equally to this work.

‡Present address: Department of Molecular Microbiology and Immunology, Brown University, Providence, RI, USA.

§Present address: Harvard Medical School, Boston, MA, USA.

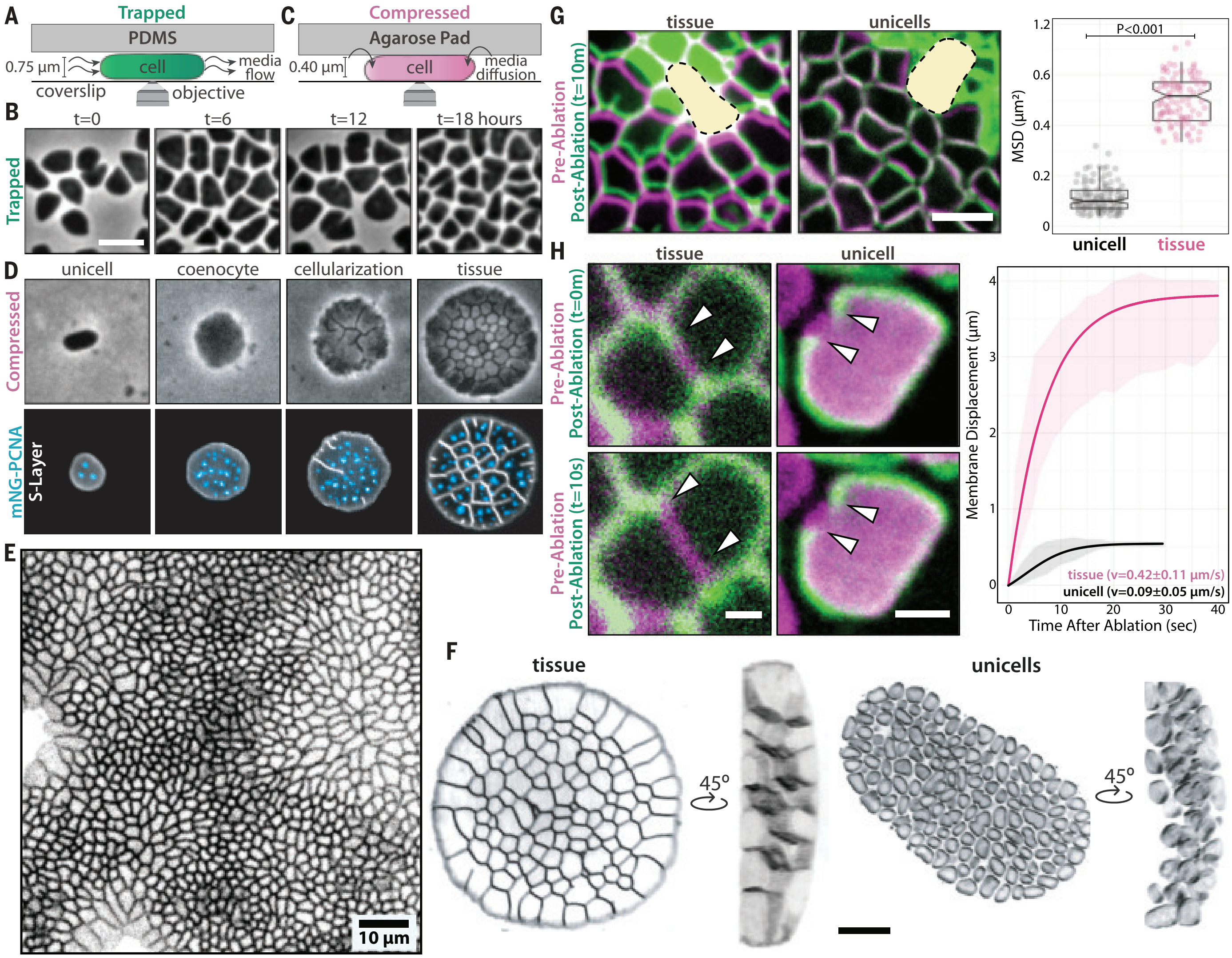

Fig. 1. Uniaxial compression triggers multicellular development in *Hfx. volcanii*. (**A**) Schematic of cells trapped and (**B**) phase-contrast time-lapse images of cells growing in the ArcCell microfluidic device. (**C**) Schematic of compressed cells under 2.5% agarose pads. (**D**) Phase-contrast (top row) and spinning-disk confocal (bottom row) time-lapse images of compressed cells across ~6 generations. msfGFP-PCNA foci (blue) represent replication sites. (**E**) Stretched and compressed areas comprise large monolayers of epithelia-like tissues. (**F**) 3D-SoRa microscopy images of a tissue (left) and unicells (right). (**G**) Laser ablation of tissue regions. False-color overlays of tissues before (magenta) and 10 min after (green) ablation. Yellow areas indicate the ablated area. Directional motion from cells was calculated from mean square displacement (MSD) curves. (**H**) Laser ablation of cell membranes. False-colored overlays of tissues and cells before (magenta) and after (green) ablation. White arrowheads indicate the membrane recoil retraction. Unless specified, scale bars represent 2 µm.

wounded animal tissues, which can vary between 0.2 and 1.0 µm/min (*23*, *24*). Because archaea lack canonical cytoskeleton motors such as myosin (*25*), the synchronous cell migration suggests that archaeal and animal tissues have similar membrane elastic properties. We tested this idea by measuring the retraction rates after ablating the cell envelope in unicells and archaeal tissues, observing a membrane recoil in archaeal tissues (0.42 ± 0.11 µm/s) (Fig. 1H and movie S6) similar to those reported in animal tissues (~0.3 µm/s) (*26*). The apparent higher membrane tension in archaeal tissues compared to compacted unicells (0.09 ± 0.05 µm/s) implies the presence of junctional load-bearing structures, placing archaeal tissues as a new class of prokaryotic multicellularity, exhibiting material properties typical of eukaryotic tissues.

Archaeal tissues are widespread in Haloarchaea and countercorrelate with biofilm production

To understand the evolutionary diversity of haloarchaeal tissues, we constructed a phylogenomic tree spanning 57 genera, representing all haloarchaeal orders (data S1), imaging compressed cells from 52 species across 14 genera (fig. S5). Regardless of cell size or growth rate (fig. S6A), 61.6% of tested haloarchaeal species formed tissues, with at least one instance of tissue development or no multicellularity in every tested genus. Among nonforming tissue strains, we identified cases of cell death (fig. S6B), shape deformation (fig. S6C), and unnoticeable shape deformations under pads (fig. S6D). We also observed three strains—*Htg. salina*, *Ncc. jeotgali*, and *Hka. jeotgali*—that exhibit aggregative multicellularity similar to that of *Methanosarcina*, the only previously reported multicellular archaeon (fig. S6E) (*27*). These results suggest that archaeal tissues emerged early in haloarchaeal evolution and remain dominant in the sampled diversity.

Next, we focused on strains from the *Haloferax* genus, in which *Hfx. prahovense* produced large, deformed tissue structures, whereas *Hfx. mediterranei* (*Hmed*) and *Hfx. gibbonsii* (*Hgib*) failed to develop, growing instead as stacked colonies (Fig. 2A, fig. S7A, and movie S7). Although all three taxa are closely related, *Hmed* is placed on a long branch, suggesting an extended time for adaptation following the loss or gain of genetic material. Under higher compression (5% agarose pads), *Hmed* cells grew larger than *Hvo* coenocytes until they split and swarmed outward (Fig. 2B and movie S7). Because *Hmed*'s swarming-like motion resembles bacterial biofilm-dependent gliding (*28*), we questioned whether their extracellular matrix promoted survival under compression. Supporting this hypothesis, relative biofilm was at least twice as high in *Hmed* as in other *Hfx* strains (fig. S7B). However, it remains unclear whether *Hmed* still hosts the (suppressed) genetic pathways for multicellularity or if it completely lost one or more required components. The diversification of tissue architecture suggests a shared multicellularity origin with occasional losses.

Despite sharing many similar "weed-like" traits, *Hmed* is still outcompeted in nature by other haloarchaea (*29*). To test whether *Hmed*'s lack of multicellularity affects its fitness, we compressed cells under microfabricated pillars intercalated with "relief" zones (Fig. 2C). This setup allowed us to observe how these cells navigated mechanical "escape room" challenges, mimicking their natural habitat. Whereas *Hvo* cells managed to propagate even with low initial cell numbers, *Hmed* showed a 4.3-fold decrease in viability compared to *Hvo* under pillars (Fig. 2, D and E, and movie S8). By contrast, *Hvo* tissues showed only a 1.8-fold and 1.4-fold loss in viability compared to unicells and *Hvo* colonies from agar plates, respectively (fig. S7C).

The survival rates between *Hvo* and *Hmed* suggest that tissues can revert to unicells. To observe the transition to unicells, we shear-shocked tissues by injecting liquid media under pads. Cells detached from tissues and transitioned to motile rods, swimming away from compression zones (movie S9). Our findings suggest that mechano-responsive multicellularity is an adaptive trait and likely beneficial in compressive zones exceeding lethal thresholds in environments such as desiccated salt plates, animal guts, and microbial biofilms (*30*).

Archaeal tissues undergo FtsZ-independent cellularization, resulting in a radial symmetry with distinct cell types

Although compression yielded tissues with larger peripheral cells (Fig. 2D), cell size and shape changes could result from uneven distribution of mechanical forces within the device instead of mechanosensation by specific cells. Because specialized cell types are a hallmark of multicellularity (*31*), we characterized the cellular morphology and cell cycle in different tissue regions. 3D-STED (stimulated emission depletion) micrographs showed two profiles: wider but shorter cells at the periphery and taller cells at the center of tissues (Fig. 3A, Movie S10). 3D-STED projections showed irregular scutoid-like center cell shapes similar to those stabilizing curved epithelia during embryogenesis (*32*). From 3D outline segmented masks, we observed variation in cell neighborhoods across the scutoid regions, suggesting a maximization of packing typical of animal scutoids (Fig. 3B). On the basis of their radial symmetry and position within the tissue, we named tissue cells peripheral (Per) and scutoid (Scu) cells (Fig. 3C).

Moreover, 3D-STED data suggest that Per cells are not in contact with the pad surface, indicating that their lower height is not a direct consequence of compression. By contrast, Scu cells are in physical contact with compression areas, suggesting that they could directly respond to the mechanical compression from

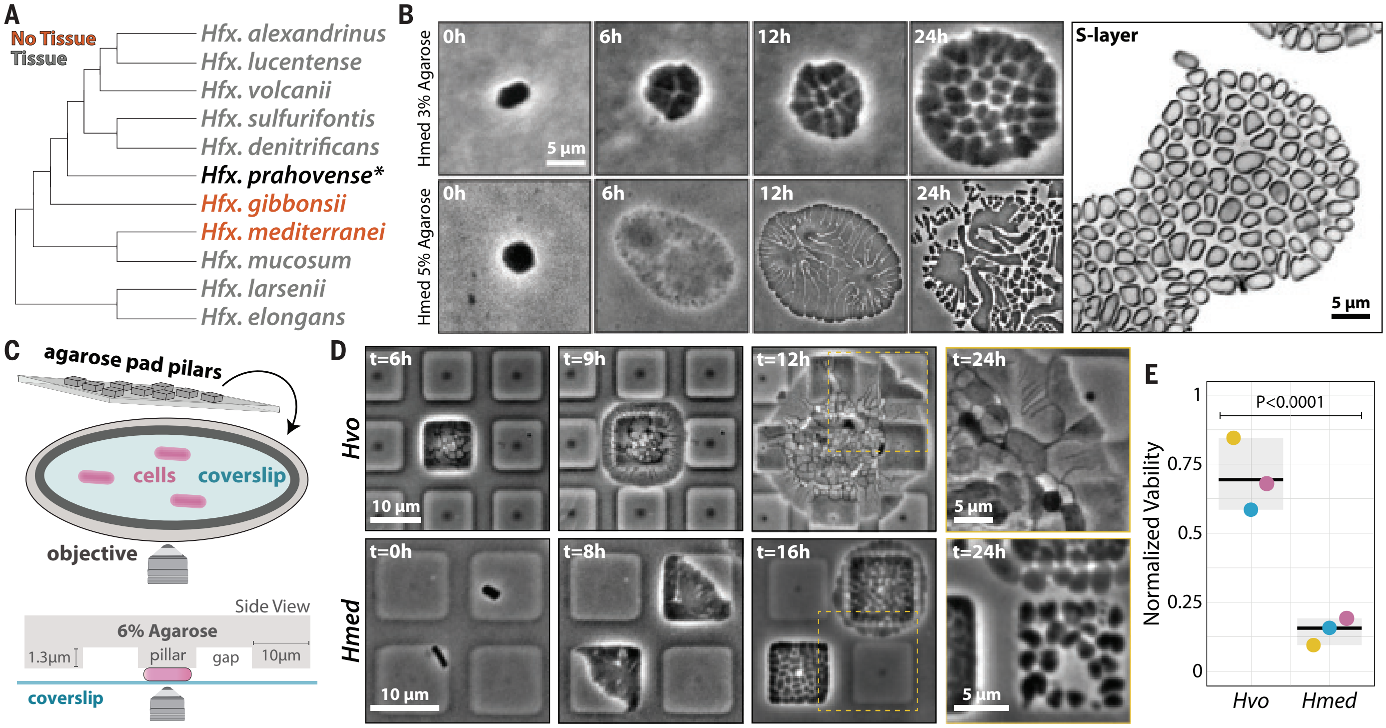

Fig. 2. *Hfx. mediterranei* does not form tissues under compression. (**A**) Cladogram depicting evolutionary relationships between compressed *Haloferax* species. Gray- and red-labeled species represent cells that form or do not form tissues, respectively. *Hfx. prahovense* is marked with an asterisk as it develops to considerably larger, deformed tissues. For a comprehensive phylogenetic tree, see supplementary data S1. (**B**) Phase-contrast time-lapse images (left) of *Hmed* growth under 3% (top) and 5% (bottom) agarose pads. (Right) SoRa microscopy of *Hmed* growth after 24 hours under 3% agarose pads. (**C**) Cartoon representation of microfabricated pillars used in the intermittent compression experiments. (**D**) Phase-contrast time-lapse images of *Hvo* (top) and *Hmed* (bottom) under micropillar devices. The 24-hour data point is represented as a magnified inlet from the yellow area in the previous time point. (**E**) Viability of *Hvo* tissues compared to *Hmed* cells under micropillars measured by colony formation unit. *Hvo* and *Hmed* viabilities were normalized by their respective liquid cultures.

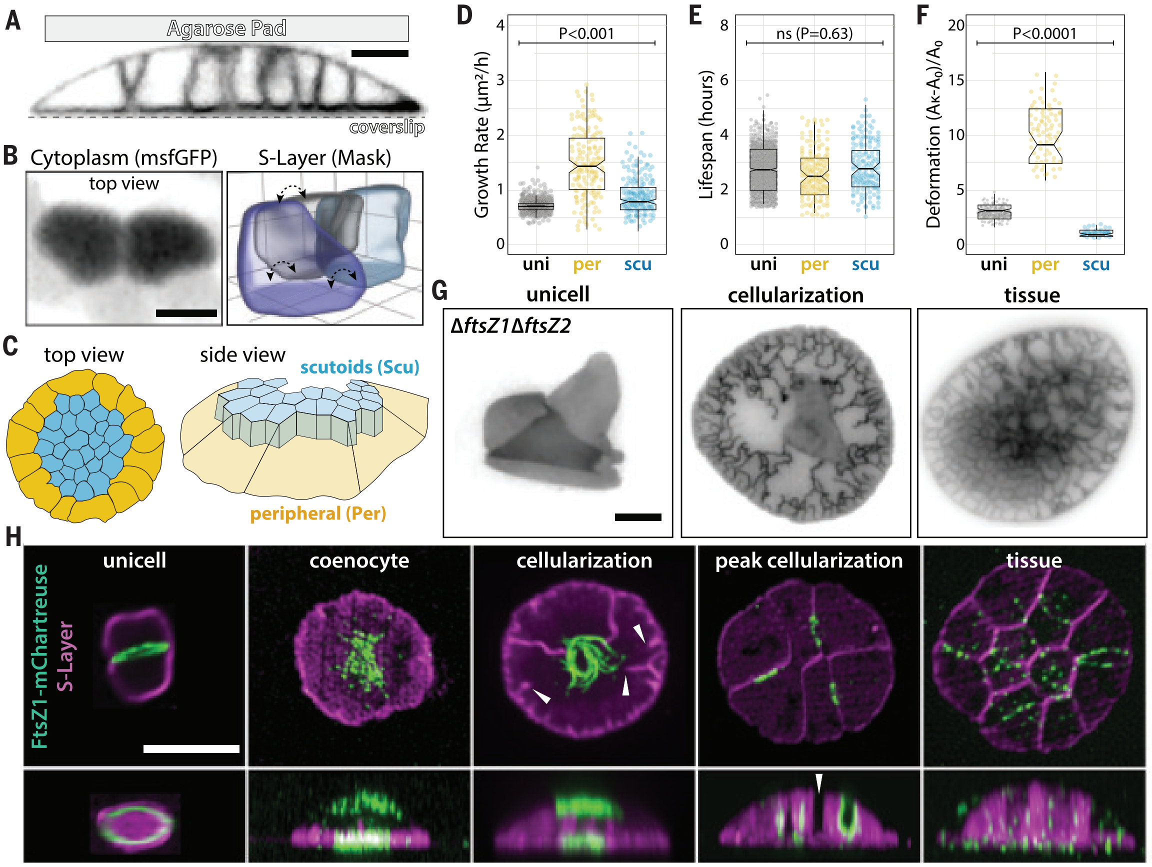

Fig. 3. Cellularization is independent of FtsZs and results in two cell types. (**A**) 3D-STED super-resolution microscopy of the cellularization process. (**B**) (Left) iSIM (instant structured illumination microscopy) of cells expressing cytoplasmic msfGFP and (right) 3D outline masks of scutoid cells segmented from 3D-STED highlights scutoid cells. Dashed arrows indicate the different scutoid surface neighbors across z planes. (**C**) Cartoon representation of top and side views showing Per and Scu cell types within tissues. (**D** to **F**) Area growth rate (D), life span (E), and deformation (F) measurements of unicells, Per, and Scu cells from phase-contrast time-lapse images. (**G**) Epifluorescence microscopy of representative cell division–impaired *ΔftsZ1ΔftsZ2* cells across different developmental stages. Early cellularization represents cells that just entered the cellularization stage. Peak cellularization represents cells at the onset of completing cellularization. (**H**) 3D-SoRa microscopy of representative cells expressing FtsZ1-mChartreuse across different developmental stages. White arrowheads indicate septation sites without FtsZ1 signal. Scale bars, 2 µm.

pads. Inspired by traction force microscopy (*33*), we imaged fluorescent beads embedded in pads, observing an upward displacement of beads over the tissues' Scu but not Per region (fig. S8A).

Another feature of animal scutoid cells is minimizing energy by distributing membrane tension. This led us to determine whether Scu and Per cells maintain a constant surface area–to–volume ratio. Although Per cells have larger volumes and surface areas, Per and Scu surface area–to–volume ratios remained consistent (fig. S8B). Our data suggest that scutoid-like cells may predate eukaryotes.

Mechanically stressed cells are typically smaller, grow more slowly, and have shorter life spans than unstressed cells (*34*). Comparing the growth rates and life spans of Per and Scu to those of unicells, both cell types showed higher growth rates (Fig. 3D) and similar life spans (Fig. 3E) relative to unicells. Our data support the idea that simple physical packing or nutritional stresses cannot summarize Per and Scu cell shape profiles.

To expand on the Per-Scu specialization, we examined whether differences in size and shape could translate to distinct viscoelastic properties. After breaking tissues by mechanical shear, we subjected individual cells to a new compression cycle and measured their deformation. Whereas Per cells were ~3-fold more deformed than unicells, Scu cells were ~2.5 more rigid than unicells (Fig. 3F and movie S11), supporting the model in which stiffer Scu cells counteract compression, so flexible Per cells can escape compression zones.

Specialized cell types in animal tissues often adapt their cytoskeleton to mechanical cues. Although FtsZ1 and FtsZ2 paralogs are required for cell division in unicells (*35*), *ΔftsZ1ΔftsZ2* cells were still capable of cellularization under compression with "zig-zag" askew cell junctions (Fig. 3G). This observation parallels those in animals and holozoans, in which microtubules are dispensable (*36*). Imaging knock-in FtsZ1-mChartreuse cells (*37*) (fig. S9A), we observed continuous FtsZ1 rings that converted to sparse filaments at the top and bottom of the central coenocytic region (Fig. 3H). Supporting the conclusion that cellularization is FtsZ independent, FtsZ1 was absent at 42% of the division furrows (fig. S9B, white arrowheads). Collectively, these observations support a sequential developmental program, with tissues relying on distinct molecular machinery for cell division that is absent in unicells.

Archaeal tissue cellularization is triggered by envelope tension

Evidence from flies and holozoans suggests that the timing of cellularization correlates with a specific threshold ratio between the number of nuclei per cell volume (N/C) (*38*). By imaging *Hvo* cells expressing mNeonGreen-PCNA, we quantified the number of replication sites and the fluorescence intensity within replication sites relative to cell area as a proxy for N/C. If N/C is critical for cellularization, DNA replication would increase faster than cell area. However, mNeonGreen-PCNA at replication sites remained constant relative to cell area, indicating that N/C does not influence cellularization (fig. S10A).

Next, we tracked single-cell parameters such as size, time, and the amount of added cell volume (*39*) at cellularization (Fig. 4, A and B), observing a lower coefficient of variance for cell area (CV = 9.6%) compared to area added and time (CV = 24.2% and 47.1%, respectively) (Fig. 4C). To confirm that cellularization happens at a specific coenocyte size, we compressed larger *ΔftsZ2* unicells, resulting in cellularization ~4.2 times faster and with ~3.7 times less added area compared to wild type, but still at a consistent cell size (Fig. 4C).

Fig. 4. Tissue cellularization is triggered by coenocytic size through a membrane tension threshold. (**A**) Epifluorescence micrographs of wild-type (top) and Δ*ftsZ2* (bottom) cells from compression to cellularization. (**B**) Single-cell growth curves from compression to cellularization onset. (**C**) Time, cell area, and cell area are added at the onset of cellularization. (**D**) Phase-contrast images of unicell and coenocytes and bSpoJ single-molecule tracks overlay false-color images relative to their mean speed. Effective diffusion coefficients are calculated from MSD curves. (**E**) Live-cell generalized polarization measurements of wild-type and *car*$^-$ stained with Laurdan. (**F**) Area at cellularization measurements of wild-type and *car*$^-$ cells from phase-contrast time-lapse images across temperatures. (**G**) Wild-type and *car*$^-$ membrane fluidity calculated by bSpoJ effective diffusion coefficients across developmental stages at 34°C. Correlation between cellularization areas and bSpoJ diffusion in wild-type and *car*$^-$ cells at 34°C. Scale bars, 2 μm.

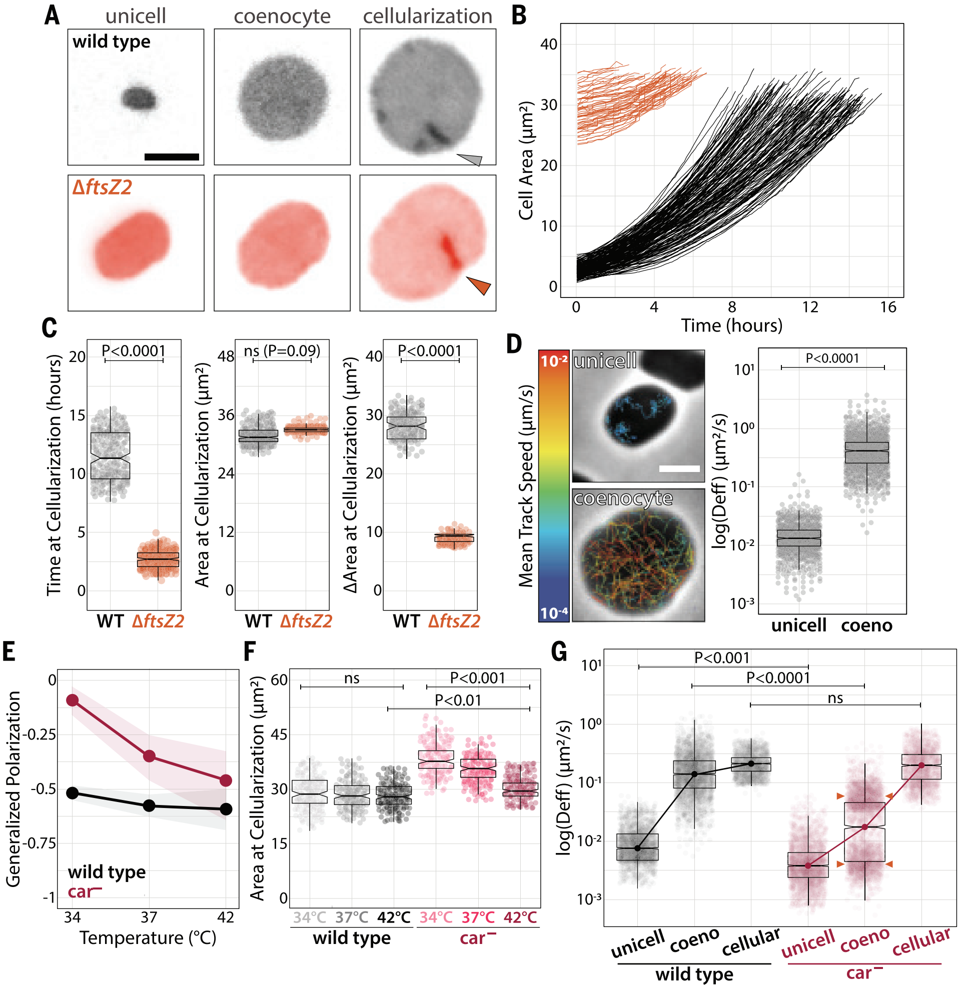

Although cell size is set at cellularization, the underlying mechanism remains unclear. Given the differences in membrane tension between tissues and unicells (Fig. 1H), we hypothesized that cell envelopes accumulate elastic strain as coenocytes grow larger until the critical threshold to initiate cellularization is reached. To measure membrane tension in real time, we created bSpoJ, a single-molecule live-cell membrane fluidity reporter. bSpoJ is a chimeric transmembrane domain of SpoIIIJ from *Bacillus subtilis*, with a secretion signal peptide from *Hvo*, and HaloTag. Particle tracking of bSpoJ in *Hvo* showed a ~30-fold increase in apparent diffusion in coenocytes compared to unicells, an order of magnitude above the ~2.5-fold increase in cell area (Fig. 4D, fig. S10B, and movies S12 and S13).

The disproportionate increase in membrane tension relative to cell area suggests that biochemical changes occur in the coenocytic envelope throughout development. Because carotenoids are thought to play a role in bacteria similar to that of cholesterol in eukaryotes (*40*), we measured membrane fluidity in cells stained with Laurdan, a fluorescent reporter for generalized polarization (*41*). Despite the lack of obvious phenotypic defects in *car*$^-$ unicells at higher or lower temperatures (fig. S10C), *car*$^-$ showed a weaker membrane fluidity homeostasis than wild type at lower temperatures (Fig. 4E and fig. S10D). Consistently, *car*$^-$ showed decreased coenocytic viability (fig. S10E). Colony pigmentation also appeared attenuated in *Hmed* and tissue-defective strains (figs. S10F and S11), suggesting a positive correlation between carotenoids and tissue development in opposition to biofilm production.

The loss of *car*$^-$ membrane fluidity control implies that coenocytes fail to trigger cellularization below critical tension thresholds. Hence, we expect changes in cellularization cell sizes among survivors. As predicted, we observed increased cell area at cellularization (Fig. 4F), suggesting that *car*$^-$ can only match membrane tension threshold at larger coenocyte areas. To directly probe membrane fluidity at cellularization, we compared bSpoJ diffusion between wild type and *car*$^-$ at 34°C (Fig. 4G). Again, we observed lower membrane fluidity in *car*$^-$ unicells compared to wild type as recorded by generalized polarization. bSpoJ diffusion at tissue cellularization was similar in wild type and *car*$^-$, supporting a tension control mechanism. Curiously, we observed a bimodal distribution in *car*$^-$ coenocytes (orange arrowheads). We speculate that one subpopulation with higher bSpoJ diffusion rates reaches the membrane tension threshold only at a larger cell size. By contrast, the second group stochastically fails to meet the tension-area ratio requirement and undergoes lysis. These results highlight a mechanoresponsive mechanism whereby cells regulate membrane fluidity to secure precise cellularization timing.

Actin and N-glycosylation are fiducial markers for archaeal tissue polarity

To identify multicellular factors, we performed RNA sequencing (RNA-seq) across developmental stages (Fig. 5A). Gene expression profiles revealed that coenocytes showed twice as many repressed compared to up-regulated genes, possibly involving pathways related to stress response and cell division arrest (fig. S12A). Although the number of differentially expressed genes (~28% of the genome) is distributed equally across the genome (fig. S12B), most of the genes with highest expression levels in tissues are clustered in the third quarter of the main chromosome between the HVO_2134 and HVO_2150

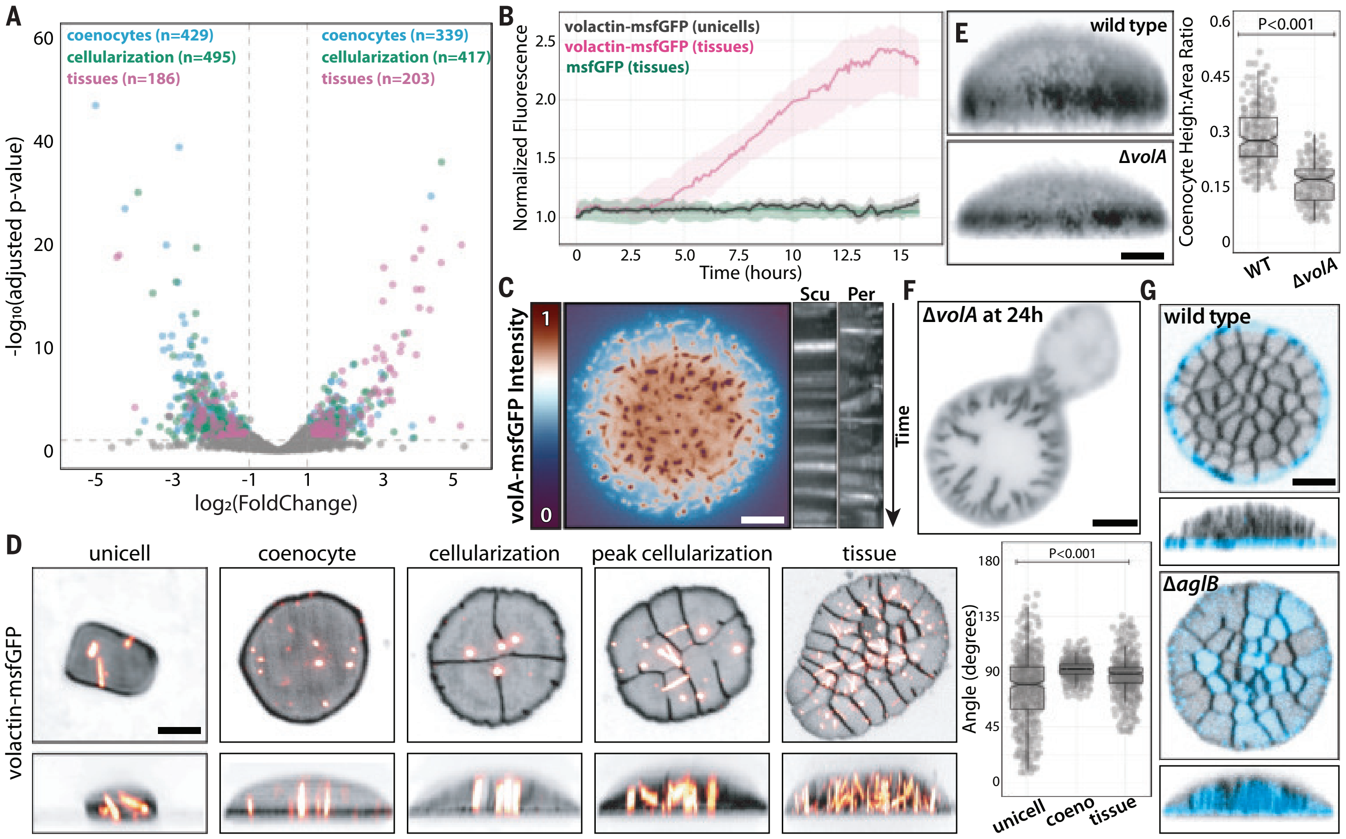

Fig. 5. Volactin and N-glycosylation are tissue-specific polarity markers. (**A**) Volcano plot overlays from RNA-seq datasets collected across developmental stages and normalized by liquid unicellular cultures. Numbers in parentheses indicate the number of candidates above the arbitrary cutoff. (**B**) Normalized fluorescence by cell area of volA-msfGFP and constitutively expressed cytoplasmic msfGFP from confocal time-lapse images. (**C**) Epifluorescence micrograph of a false-colored tissue relative to volA-msfGFP fluorescence (left) and dynamics of volA-msfGFP polymers represented by kymographs (right) from Per and Scu regions. (**D**) 3D-SoRa projections of representative cells expressing volA-msfGFP across developmental stages (left) and volA cable angle measurements relative to the coverslip plane (right). (**E**) Height measurements of wild-type and Δ*volA* coenocytes from 3D-SoRa projections. (**F**) Representative epifluorescence micrograph of a Δ*volA* cell stalled at cellularization. (**G**) 3D-confocal projections of cell surface N-glycosylated proteins in wild-type (top) and Δ*aglB* (bottom) tissues stained by ConA-Alexa488. Scale bars, 2 μm.

loci (fig. S12C). This pattern suggests the existence of possible transferable islands related to the emergence of multicellularity. We also observed an enrichment of proteins with cytochrome-related and photosynthetic reaction center (PRC) domains, which were shown to have structural cell division roles (*42*, *43*). Hence, the above paralogs could represent tissue-specific cell cycle factors.

From our gene candidate list, we focused on four groups: cell surface, cytoskeleton and mechanosensing, signaling, and cell cycle (data S2). Given the importance of actin in eukaryotic tissue biogenesis, we investigated the role of volactin (volA), the only identified actin homolog in *Hvo* (*44*), which is up-regulated ~1.6-fold in tissues. Time-lapse imaging showed increased volA-msfGFP signal during development, reaching a steady state by the end of cellularization (Fig. 5B and movie S14). By contrast, unicells showed unaltered volA-msfGFP levels, as did tissues expressing cytoplasmic msfGFP. Moreover, volactin polymers were less abundant but highly dynamic in uncompressed Per cells than in unicells and Scu cells (Fig. 5C and movie S15). VolA also displayed changes in structural patterns, with cables aligning in coenocytes and Scu cells (Fig. 5D and movie S16). Compression of Δ*volA* cells resulted in shorter coenocytes than the wild-type counterpart (Fig. 5E) and delayed or stalled tissue maturation (Fig. 5F). Because volA is implicated in regulating the development of rod-shaped (motile) and disk-shaped (sessile) cell types (*44*, *45*), we propose that volactin may mirror eukaryotic actin's multifunctional roles as a mechanosensing cytoskeleton and polarity factor in tissues (*46*).

Comparative genomics leveraging of the differences in tissue formation across *Hfx* species showed substantial overrepresentation of orthologous groups (orthogroups) related to protein glycosylation, sugar metabolism, and transport in presence or absence datasets among (i) *Hvo* and *Hmed* (fig. S12D and data S3); (ii) 4 *Hfx* species (fig. S12E and data S4); and (iii) orthogroups enriched in species that form tissues (data S5). Protein glycosylation has historically been studied in haloarchaea for its role in mating and envelope biogenesis (*47*). In eukaryotes, N-glycosylation is crucial for cell identity, polarity, junctions, and adhesion (*48*). To explore the role of N-glycosylation, we labeled cells with ConA-Alexa488, a cell-impermeable fluorescent lectin conjugate that binds mannose glycol groups. Although ConA-Alexa488 did not stain unicells (fig. S13A), it exhibited a radial localization at the outline of Per cells (Fig. 5G and movie S17). To test whether patterns are formed by biofilm accumulation in the extracellular matrix, we examined a Δ*pibD* mutant, blocking all pili-dependent secretion (*49*). We observed no significant differences in ConA-Alexa488 localization between wild-type and Δ*pibD* tissues (fig. S13A), indicating that biofilm is not critical for cell junctions. Next, we imaged tissues of different N-glycosylation mutants, finding that Δ*aglB* is the only one to disrupt ConA-Alexa488 halos, resulting in staining of the whole tissue surface (Fig. 5G and fig. S13B). Therefore, we propose that AglB, the main oligosaccharyltransferase required for S-layer N-glycosylation (*47*), acts as an inhibitor of N-glycosylation in Scu cells, directing tissue cell-surface polarity. The apparent dichotomous nature of AglB in archaeal tissues adds to the list of cell surface N-glycosylation functions such as morphogenesis and mating.

The discovery of clonal, tissue-like multicellularity in archaea highlights the potential of archaeal mechanobiology to shed light on the emergence of complexity in nature. Nevertheless, this is not the first developmental program identified in haloarchaea, joining the rod-shaped (motile) and disk-shaped (sessile) shape-shift transitions (*45*). These cell types are connected by volactin, which is also required for disk formation (*44*). The coordinated alignment of volactin cables indicates that actin cables might sense membrane curvature or mechanically support coenocytic and Scu cells. Although these scenarios are not mutually exclusive, volA's roles in different developmental programs, combined with the FtsZ-independent tissue cellularization, underscore a developmental transition from tubulin-dependent to actin-dependent cellularization (*25*, *46*).

An integrative evo-devo mechanobiology approach offers a framework for understanding the link between microbial biofilms and membrane homeostasis, which may regulate the transition between different multicellularity modalities. Our findings also suggest the need to revisit past evidence for the origin of eukaryotic multicellularity, such as fossils identified as holozoans (*50*). On the basis of their size and absence of definitive eukaryotic features, these fossils may represent ancestors of archaeal tissues. Future studies should uncover the biochemical and structural nature of archaeal cell junctions and expand the presence of archaeal tissues in phyla evolutionarily closer to eukaryotes, such as the Asgard archaea.

REFERENCES AND NOTES

1. M. D. Herron *et al*., *Sci. Rep.* **9**, 2328 (2019).
2. S. Jacobeen *et al*., *Nat. Phys.* **14**, 286–290 (2018).
3. T. Brunet *et al*., *eLife* **10**, e61037 (2021).
4. O. Dudin, S. Wielgoss, A. M. New, I. Ruiz-Trillo, *PLOS Biol.* **20**, e3001551 (2022).
5. B. Baum, A. Spang, *Microbiol. Mol. Biol. Rev.* **87**, e0018621 (2023).
6. T. A. M. Bharat, A. von Kügelgen, V. Alva, *Trends Microbiol.* **29**, 405–415 (2021).
7. M. F. Abdul-Halim *et al*., *mBio* **11**, e00349-20 (2020).
8. D. Moi *et al*., *Nat. Commun.* **13**, 3880 (2022).
9. B. Baum, D. A. Baum, *BMC Biol.* **18**, 72 (2020).
10. M. Pohlschroder, S. Schulze, *Trends Microbiol.* **27**, 86–87 (2019).
11. K. P. Menard, N. Menard, *Dynamic Mechanical Analysis* (CRC Press, ed. 3, 2020).
12. J.-P. Rieu, H. Delanoë-Ayari, S. Takagi, Y. Tanaka, T. Nakagaki, *J. R. Soc. Interface* **12**, 20150099 (2015).
13. J. Lee *et al*., *ACS Biomater. Sci. Eng.* **10**, 2956–2966 (2024).
14. C. M. Chibani *et al*., *Nat. Microbiol.* **7**, 48–61 (2022).
15. C. F. Guimarães, L. Gasperini, A. P. Marques, R. L. Reis, *Nat. Rev. Mater.* **5**, 351–370 (2020).
16. S. Shad, N. Razaghi, D. Zivar, S. Mellat, *Petroleum* **9**, 508–525 (2022).
17. B. E. Shapiro *et al*., Tessellations and pattern formation in plant growth and development, arXiv [q-bio.CB] (2012). http://arxiv.org/abs/1209.2937.
18. L. Dupuy, J. Mackenzie, J. Haseloff, *Proc. Natl. Acad. Sci. U.S.A.* **107**, 2711–2716 (2010).
19. E. M. Medina, N. E. Buchler, *Curr. Biol.* **30**, R516–R520 (2020).
20. Y. S. Hwang *et al*., *Gigascience* **7**, 1–9 (2018).
21. O. Hamant, E. S. Haswell, *BMC Biol.* **15**, 59 (2017).
22. C. Villeneuve *et al*., *Nat. Cell Biol.* **26**, 207–218 (2024).
23. D. Kuipers *et al*., *J. Cell Sci.* **127**, 1229–1241 (2014).
24. S. R. K. Vedula *et al*., *Nat. Commun.* **6**, 6111 (2015).
25. J. A. Theriot, *BMC Biol.* **11**, 119 (2013).
26. W. Kong *et al*., *Sci. Rep.* **9**, 14647 (2019).
27. L. E. Mayerhofer, A. J. Macario, E. Conway de Macario, *J. Bacteriol.* **174**, 309–314 (1992).
28. N. Wadhwa, H. C. Berg, *Nat. Rev. Microbiol.* **20**, 161–173 (2022).
29. A. Oren, *FEMS Microbiol. Lett.* **364**, fnx070 (2017).
30. S. Kim, M. Pochitaloff, G. A. Stooke-Vaughan, O. Campàs, *Nat. Phys.* **17**, 859–866 (2021).
31. E. P. Bingham, W. C. Ratcliff, *Proc. Natl. Acad. Sci. U.S.A.* **121**, e2319840121 (2024).
32. P. Gómez-Gálvez *et al*., *Nat. Commun.* **9**, 2960 (2018).
33. L. Hazlett *et al*., *Sci. Rep.* **10**, 16599 (2020).
34. B. I. Shraiman, *Proc. Natl. Acad. Sci. U.S.A.* **102**, 3318–3323 (2005).
35. S. Ithurbide, S. Gribaldo, S.-V. Albers, N. Pende, *Trends Microbiol.* **30**, 665–678 (2022).
36. O. Dudin *et al*., *eLife* **8**, e49801 (2019).
37. N. Fraikin, A. Couturier, C. Lesterlin, bioRxiv (2024) p. 2024.03.28.587235.
38. M. Olivetta, O. Dudin, *Curr. Biol.* **33**, 1597–1605.e3 (2023).
39. A. Ondracka, O. Dudin, I. Ruiz-Trillo, *Curr. Biol.* **28**, 1964–1969.e2 (2018).
40. W. Seel *et al*., *Sci. Rep.* **10**, 330 (2020).
41. S. A. Sanchez, M. A. Tricerri, E. Gratton, *Proc. Natl. Acad. Sci. U.S.A.* **109**, 7314–7319 (2012).
42. S. Zhao *et al*., Widespread PRC barrel proteins play critical roles in archaeal cell division, bioRxivorg (2023). https://doi.org/10.1101/2023.03.28.534520.
43. P. Nußbaum *et al*., *Nat. Microbiol.* **9**, 698–711 (2024).
44. H. Schiller *et al*., *Nat. Commun.* **15**, 1414 (2024).
45. Z. Curtis *et al*., *Proc. Natl. Acad. Sci. U.S.A.* **121**, e2401583121 (2024).
46. A. Charles-Orszag, N. A. Petek-Seoane, R. D. Mullins, *J. Bacteriol.* **206**, e0034823 (2024).
47. S. Schulze, F. Pfeiffer, B. A. Garcia, M. Pohlschroder, *PLOS Biol.* **19**, e3001277 (2021).
48. T. Brunet, D. S. Booth, *Curr. Top. Dev. Biol.* **154**, 1–36 (2023).
49. R. N. Esquivel, S. Schulze, R. Xu, M. Hippler, M. Pohlschroder, *J. Biol. Chem.* **291**, 10602–10614 (2016).
50. P. K. Strother *et al*., *Curr. Biol.* **31**, 2658–2665.e2 (2021).
51. Moore–Simons Project on the Origin of the Eukaryotic Cell.
52. Bisson Lab, Scripts and models used in "Tissue-Like Multicellular Development Triggered by Mechanical Compression in Archaea," Zenodo (2024); https://doi.org/10.1101/2024.10.19.619234.

ACKNOWLEDGMENTS

The Bisson Lab thanks B. Goode (Brandeis University) for access to the SoRa microscope, and O. Dudin (University of Geneva), A. Rodal (Brandeis University), B. Baum (MRC-LMB), and H. Erickson (Duke University) for constructive suggestions on the manuscript. STED and spectral confocal microscopy were performed at the Brandeis Light Microscopy Core Facility. We thank S. Bruckbauer for the chromosomal mNeonGreen-PCNA strain and A. Stone (Brandeis University) for support in generating scutoid masks. A.B. acknowledges support from the archaeal community, particularly M. Pohlschröder (University of Pennsylvania), J. Eichler (Ben-Gurion University), T. Allers (University of Nottingham), J. Soppa (University of Frankfurt), and I. Duggin (University of Technology Sydney) for sharing published and unpublished strains. T.R. thanks the MBL Woods Hole Physiology Course and Biovis for iSIM use. We are grateful to the Scientific Community Image Forum and the Center for Open Bioimage Analysis (COBA) for fostering an invaluable intellectual community dedicated to training microscopists in image analysis. The Soen lab thanks L. Tunik and the staff of the Nanofabrication unit at the Weizmann Institute for support in the fabrication of microfluidics chips. We acknowledge the MRC-LMB electron microscopy facility for sample preparation and data collection. V.A. thanks A. Lupas (MPI Tübingen) for continued support. **Funding:** This work was supported by the NIH grant 1S10OD034223-01 for the Abberior Facility Line STED microscope, housed in the Brandeis Light Microscopy Core Facility; Moore–Simons Project on the Origin of the Eukaryotic Cell (*51*) awarded to A.B.; the Human Frontiers Science Program (RGY0074/2021) awarded to A.B., T.A.M.B., and V.A.; and the Brandeis National Science Foundation (NSF) Materials Research Science and Engineering Center (MRSEC) Bioinspired Soft Materials (NSF-DMR 2011846). A.B. is the recipient of an NSF grant (NSF-MBC2222076) and is a Pew Scholar in the Biomedical Sciences, supported by The Pew Charitable Trusts. This work was supported by the Medical Research Council as part of United Kingdom Research and Innovation (programme MC_UP_1201/31 to T.A.M.B.). T.A.M.B. thanks the European Molecular Biology Organization, the Wellcome Trust (grant 225317/Z/22/Z), and the Leverhulme Trust. I.C. was supported by an EMBO Long-Term Fellowship (ALTF 92-2022). E.S. and Y.S. were supported by the Sir John Templeton Foundation (764 61122). K.A. was supported by the NIH T32GM139798 Predoctoral Training Grant. This work was partly supported by institutional funds of the Max Planck Society. **Author contributions:** Conceptualization: T.R., O.S.L., A.B. Methodology: T.R., O.S.L., P.E., J.M., K.A., E.S., S.N., I.L.P., L.T.R., L.D.R., Y.S., A.B. Investigation: T.R., O.S.L., P.E., J.M., K.A., I.C., A.v.K., S.N., L.T.R., T.A.M.B., V.A., A.B. Visualization: T.R., O.S.L., P.E., K.A., A.B. Funding acquisition: A.B., V.A., T.A.M.B. Project administration: A.B. Supervision: T.R., S.K., Y.S., T.A.M.B., V.A., A.B. Writing – original draft: T.R., O.S.L., A.B. Writing – review & editing: T.R., O.S.L., P.E., J.M., K.A., I.C., A.v.K., E.S., S.N., I.P., S.K., L.T.R., L.D.R., V.T., Y.S., T.A.M.B., V.A., A.B. **Competing interests:** The authors declare that they have no competing interests. **Data and materials availability:** All custom software developed in this work is publicly available without restrictions in a Zenodo repository (*52*). The complete raw RNA-seq datasets presented in this study can be found in NCBI GEO online repository PRJNA1165275. Haloarchaeal strains are available from the Leibniz Institute DSMZ-German Collection of Microorganisms and Cell Cultures GmbH (DSMZ) strain bank.

SUPPLEMENTARY MATERIALS

science.org/doi/10.1126/science.adu0047
Materials and Methods
Figs. S1 to S13
Tables S1 to S7
References (*53–151*)
MDAR Reproducibility Checklist
Movies S1 to S17
Data S1 to S5

Submitted 19 October 2024; accepted 5 February 2025
10.1126/science.adu0047

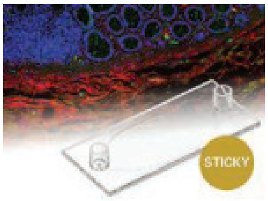

Sticky-Slide Tissue

Standard tissue-treatment workflows, for applications such as immunohistochemistry, multiplexing, and spatial omics applications, often suffer from time-consuming protocols that yield varying results. ibidi's sticky-Slide Tissue streamlines and regulates this process. Designed to fit on standard microscopy slides, the sticky-Slide Tissue can easily be included in pre-established workflows to improve imaging results. When combined with a slide or a coverslip, it creates a reservoir with a small and defined volume on top of FFPE- or cryo-sections for convenient staining and liquid exchange. Two Luer ports make the staining reservoir accessible manually, or by automatization, using perfusion systems for high-throughput or multiplexing experiments. The sticky-Slide Tissue is designed to achieve reproducible results, even for super-resolution microscopy, when using the high-precision (1.5H) Coverslips for the sticky-Slide Tissue, Glass.

ibidi GmbH
For info: +49 89 520 46 17-0
www.ibidi.com

FlowMAb™

FlowMAb™ fluorescently conjugated antibodies from Bio X Cell set a new benchmark for conjugated antibody quality and specificity. Delivering the unmatched performance of Bio X Cell antibodies and optimized for precise detection, across numerous targets, FlowMAb™ antibodies are engineered with fluorophores such as APC, FITC, and PE—ensuring exceptional signal clarity and reliability across flow cytometry, FACS, and other immunoassays. Weak signal detection and background noise often compromise flow cytometry results. FlowMAb™ overcomes these challenges with validated markers, built on the best-in-class clones trusted by researchers worldwide. Whether in immuno-oncology, stem cell biology, or infectious disease research, FlowMAb™ delivers reproducible, high-fidelity data to streamline workflows and accelerate scientific breakthroughs.

Bio X Cell
For info: +1 866-787-3444
www.bioxcell.com

Gyrolab HEK293 HCP Type SN and Type CL Kit Reagents

Gyros Protein Technologies, a pioneer in automated nanoliter-scale immunoassays and leading provider of peptide synthesizers, today announced the introduction of its Gyrolab® HEK293 HCP Type SN Kit Reagents and Gyrolab HEK293 HCP Type CL Kit Reagents. Developed with antibodies from BioGenes GmbH, a global leader in host cell protein (HCP) assay development, the new kits enable rapid detection of HCPs from HEK293 cell lines, adding to Gyros Protein Technologies' growing portfolio of ready-to-use host cell protein impurity kits. Removal of HCP is a critical step in biotherapeutic development to ensure quality, consistency and stability. Importantly, HCP can trigger immune responses in patients, potentially causing adverse effects ranging from mild allergic reactions to severe immunological complications and must therefore be removed for patient safety. The introduction of these two new kits provides a fully validated solution for detection of critical host cell proteins in biotherapeutics expressed in HEK293 cells, offering greater sensitivity and excellent coverage. Although the Gyrolab platform was already compatible with BioGenes' antibodies for detection of HEK293 host cell proteins, the introduction of off-the-shelf, plug and play kits enables reliable and reproducible detection on the automated Gyrolab immunoassay platform, with reduced sample volume and reagent consumption, improving analytical output and workflow productivity. BioGenes' 360-HCP antibodies are developed using an innovative approach that ensures they provide the broadest possible antigen coverage. These antibodies are produced by immunizing multiple species, leveraging a refined process for antigen and antibody preparation, and utilizing an optimized purification strategy. This results in multiple high-quality antibody preparations.

Gyros Protein Technologies
For info : +31 6 34735894
www.gyrosproteintechnologies.com

MatriMix for PDX

MatriMix for PDX, is a fully defined extracellular matrix (ECM) hydrogel comprising of collagen, laminin-511 E8 fragments and hyaluronic acid optimized to support patient-derived xenograft (PDX) studies. A PDX model uses a patient's tumor tissue to create a growing tumor in an immunodeficient mouse. They retain the histological and genetic characteristics of the patient's original tumor, offering a superior platform for studying cancer biology and drug responses, allowing researchers to develop new treatments through drug screening and toxicology studies. Comprising a mixture of fully defined collagen type I, laminin-511 E8 fragments, and hyaluronic acid, MatriMix for PDX is a ready-to-use 3D culture substrate product optimized for culturing patient derived cancer cells. Proven to facilitate excellent cell organization and accurately replicate in vivo conditions, MatriMix for PDX is the ultimate solution for culturing even difficult-to-grow cancer cell types as xenograft. The high lot-to-lot consistency of MatriMix for PDX enables researchers to routinely obtain highly reproducible results. The types and concentrations of the individual components in MatriMix for PDX have been optimized to provide an optimal extracellular environment for target cells. Through its use of medical grade porcine collagens, MatriMix for PDX streamlines the transition from basic to clinical research unlike any existing natural hydrogel. Supplied frozen, MatriMix for PDX transitions to a clear gel when warmed to physiological temperature (37ºC). This feature allows superior visualization possibilities, making it valuable for applications requiring real-time monitoring of tumor growth, invasion, and drug response assays. MatriMix for PDX comes as a single, all-in-one vial. MatriMix is also available in a tunable three-vial format, allowing end-users to optimize for their specific 3D cell culture or organoid models.

AMS Biotechnology
For info: +44-1235-828200
www.amsbio.com

Electronically submit your new product description or product literature information! Go to www.science.org/about/new-products-section for more information.


CAREER
PLANNING

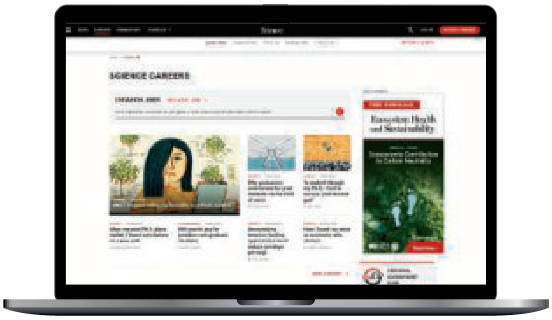

WORKING LIFE

By **Melanie Ortiz Alvarez De La Campa**

Taking flight

The email came 2 weeks after Hurricane Maria ravaged Puerto Rico. I was an undergraduate student at the University of Puerto Rico-Río Piedras and my honors program wanted to know whether I would be interested in an opportunity to temporarily continue my studies elsewhere. Brown University, a school I'd never heard of, was offering 30 of us the chance to take classes there while our university recovered. Amid the devastating news of thousands of deaths and billions of dollars in damage to the island, the offer seemed too good to be true. However, my family encouraged me to go, and soon I found myself on a private flight to Rhode Island. The hurricane had blown me off my planned course, and set me on an unexpected path toward a Ph.D.

"Unexpected challenges can create opportunities for growth and redirection."

I started college dreaming of becoming a forensic pathologist. I wanted to help give a voice to those who could no longer speak. I would need a medical degree, so I enrolled as a premed biology major and focused on my first-year coursework. Research wasn't on my radar, partly because such opportunities in Puerto Rico were limited.

The following year, the hurricane hit. I felt oddly optimistic before the storm—thinking we'd get a few days off and life would go on, just as it always had. Instead, the Category 5 monster leveled our communities, leaving people without power or water for months. Days passed before we could reconnect with loved ones. When I finally saw my grandmother, she hugged me tightly, crying, "I was so scared something happened to you."

On the flight north, which was chartered by Brown, everything felt surreal—leather seats, fresh fruit, and, after landing, a reception in a mansion. I felt conflicted. Here I was, feeling joy and wonder at a new experience, while everyone back home struggled.

Brown set us up with classes, books, dorm rooms, and funds to purchase winter clothes. It was in one of those classes, an introductory biology course, that my trajectory began to shift. I was captivated by the professor's lecture and, on a whim, reached out after class. To my surprise, he immediately offered me a research position in his lab.

I was assigned to work on a project that involved modeling how climate change could alter the distributions of plants across North America. The research opened my eyes to the important work scientists were doing to address urgent, relevant questions.

I began to see a path in science beyond medicine, and at Brown I had the resources to follow it. I had direct access to faculty, state-of-the-art research facilities, and a supportive academic environment. As the academic year came to a close, I stayed on to do a summer research program, where I fell in love with microbiology.

I began to think a Ph.D. was what I wanted. Yet, despite the excitement, I felt doubtful, anxious, and guilty. I struggled to reconcile my new opportunities with the devastation back home. I also worried about leaving behind my dream of medicine to pursue a path that I was excited about but that might not lead to a job in Puerto Rico.

Before I left Brown, my summer research mentor told me, "If you ever want to pursue a Ph.D., I'd be honored to mentor you." After I confided in him about my conflicted feelings on the future, he replied: "There's nothing better than doing what excites you." The words felt like permission to follow my passion.

Back in Puerto Rico, I spent my final years doing all I could to get myself admitted to graduate school. And 3 years later, I returned to Brown—this time as a Ph.D. student. Fittingly, my first weekend back brought a hurricane to Rhode Island. It felt oddly like home.

Now that I'm in the fourth year of my Ph.D., my journey has taught me that unexpected challenges can create opportunities for growth and redirection. My pivot from medicine to research wasn't a loss, but an acknowledgement of where I could have the greatest impact while still doing something that excites me. ■

Melanie Ortiz Alvarez De La Campa is a Ph.D. candidate at Brown University. They are also co-founder of Ciencia Pa' Todes, a Caribbean science communication initiative.

ILLUSTRATION: ROBERT NEUBECKER

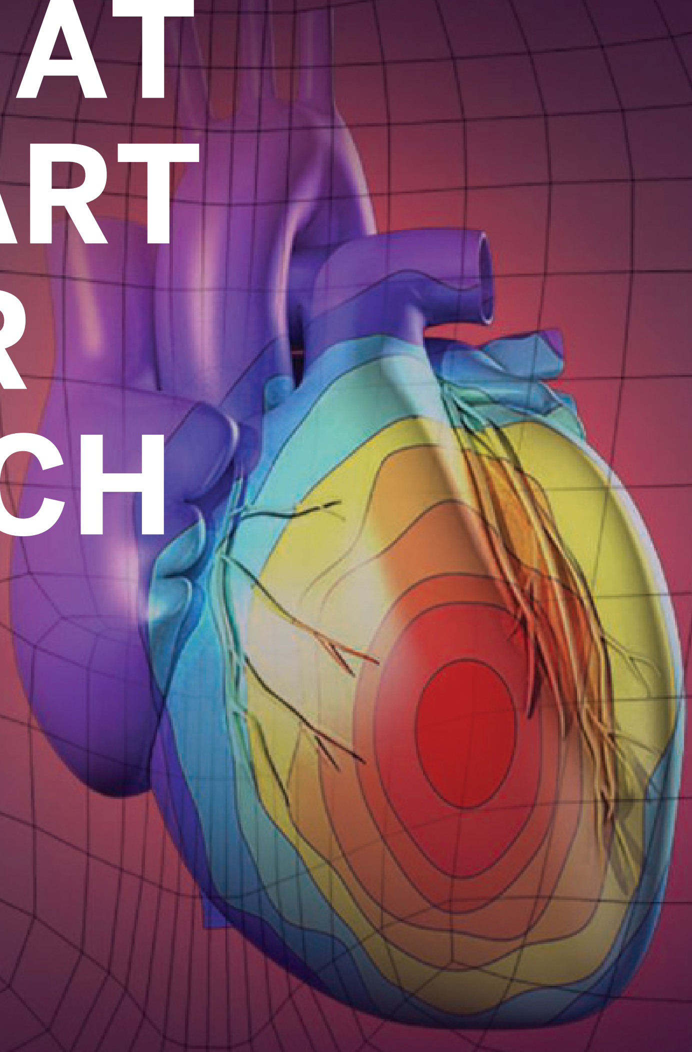

CALL FOR PAPERS

SCIENCE PARTNER JOURNALS

Research

OPEN ACCESS

Research is a Science Partner Journal (SPJ) distributed by the **American Association for the Advancement of Science (AAAS)** in association with Science and Technology Review Publishing House, the publishing house under the leadership of **China Association for Science and Technology (CAST)**. *Research* provides an international platform for academic exchange, research collaboration, and technological advancements. The journal publishes fundamental research in the life and physical sciences as well as important findings or issues in engineering and applied science.

Submit your manuscripts to *Research* today!
Learn more at **spj.science.org/research**

The Science Partner Journals (SPJ) program was established by the American Association for the Advancement of Science (AAAS), the non-profit publisher of the *Science* family of journals. The SPJ program features high-quality, online-only, Open-Access publications produced in collaboration with international research institutions, foundations, funders, and societies. Through these collaborations, AAAS furthers its mission to communicate science broadly and for the benefit of all people by providing top-tier international research organizations with the technology, visibility, and publishing expertise that AAAS is uniquely positioned to offer as the world's largest general science membership society.
Learn more at **spj.science.org**

@SPJournals **@SPJournals** **@SPJournals**